Modification, Design, and Degradation Mechanisms of Nickel-Rich Layered Oxide Cathodes for High-Capacity Lithium-Ion Batteries

A Dissertation
Submitted to the Faculty
of the
WORCESTER POLYTECHNIC INSTITUTE

In partial fulfillment of the requirements for the
Degree of Doctor of Philosophy
in
Materials Science and Engineering

By
Luqman Azhari
August 2022

APPROVED by:

_____

Dr. Yan Wang, Advisor, William Smith Dean's Professor of Mechanical & Materials Engineering, Worcester Polytechnic Institute

_____

Dr. Yu Zhong, Associate Professor of Mechanical & Materials Engineering, Worcester Polytechnic Institute

_____

Dr. Adam Powell, Associate Professor of Mechanical & Materials Engineering, Worcester Polytechnic Institute

_____

Dr. Pratap M. Rao, Associate Professor of Mechanical & Materials Engineering, Worcester Polytechnic Institute

Acknowledgements

My PhD thesis on lithium-ion battery cathodes has been a challenging and rewarding journey. As with most difficult challenges, I could not have achieved any success without the support and guidance from so many others, and I express my gratitude towards them.

First of all, I deeply thank my advisor Professor Yan Wang for his continued support over the last four years. I have always been appreciative of his consistent efforts and availability to his students. His understanding of the direction of the battery industry and technology development has been critical in setting up my research goals from my first year here and has helped prepare me to pursue my career goals. His dedication to his lab and students is admirable and is a characteristic I intend to emulate. It has been an honor and a pleasure to have been a part of his lab group and directly observe our progress and growth.

A special thanks to Renata Arsenault at Ford Motor Company, for her additional guidance and supervision, and without whom and funding support from Ford Motor Company, my projects could not have been realized.

I am also grateful to Dr. Boquan Li for his assistance on operating equipment and troubleshooting whenever issues arose. My progress, along with the research progress of many others, could not have been made possible without his constant assistance and maintenance of critical research equipment at WPI.

I am also grateful to all the other faculty members in the Mechanical & Materials Engineering Department I have interacted with that have helped me in various ways, from being a student or TA for their courses, to casual discussions. I thank my committee members in particular, Professors Brajendra Mishra, Adam Powell, Yu Zhong, and Pratap Rao, for being a part of my PhD progress.

Lastly, I am thankful to the numerous colleagues and friends at WPI, particularly those in our group. They have been so vital in my progress here and have been a source of support during my time here.

Table of Contents

List of Tables

List of Figures

Summary

To meet the energy capacity demands of next generation electric vehicles and other high energy use devices, significant developments in lithium-ion battery (LIB) cathodes will be required. Compositions which provide higher specific capacities need to be proven, and battery materials costs need to be reduced. Moving on from traditional cobalt-rich cathodes and towards nickel-rich compositions is the clearest and most impactful pathway towards these goals. As such, the implementation of transition metal layered oxide cathodes with high fractions of nickel is highly desired with capacities around 200mAh/g and has thus become a particularly popular topic of research in the past several years. By all expectations, commercial LIBs will be composed of nickel-rich cathodes within the next decade, provided that the inherent drawbacks and limitations are addressed. Herein, we choose to focus on LIB layered oxide cathodes with nickel contents of 80% and greater, and pathways towards practical industrial application. In **Chapter 1**, we establish the motivation and limitations of Ni-rich NMC cathodes and touch upon previously demonstrated designs towards resolving these limitations, specifically surrounding the typical polycrystalline secondary particle structure.

In **Chapter 2**, we explore effects of extended aqueous processing of NMC cathodes of various compositions. Aqueous slurry processing is a desirable milestone for battery manufacturers, its success would eliminate the use of expensive and potentially harmful N-Methyl-2-pyrrolidone organic solvents. While isolating on the effects of water processing on solely the NMC cathode, longer processing timescales are utilized which are closer to those used in industry, contrary to shorter washing steps investigated in other works. We demonstrate that at these timescales, extensive fracture along grain boundaries occurs, with the severity of fracture positively

correlated with the nickel fraction in the material. The removal of surface lithium residues and contact with water resulted in localized delithiation of the NMC surface and subsequent surface reconstruction along grain boundaries to rock-salt like ordering. It was also determined that the treated materials are more mechanically compromised, which adds risk for additional particle pulverization during calendaring processes. Lastly, electrochemical performance severely suffers from aqueous processing due to the resistive surface reconstruction layer and increased surface area, exhibiting higher capacity fade and reduced capacity at high charge/discharge rates. This work demonstrates the importance of surface modifications in order to utilize aqueous slurry processes at relevant scale.

In **Chapter 3**, we look to develop a method to address the chemical instability and improve the performance of $LiNi_{0.8}Mn_{0.1}Co_{0.1}O_2$ (NMC811) while solely utilizing a coprecipitation method. NMC811 is well demonstrated to have reversible capacities ~200mAh/g when cycled to an upper voltage cutoff of 4.5V vs Li/Li^+. However, surface-initiated instabilities caused by high valence Ni ions result in capacity fade, rendering it impractical for many applications. Based on the well documented electrochemical stability of Mn-rich oxides, we aimed for the synthesis of a heterogenous hydroxide precursor with a nickel-rich core and manganese-rich coating layer. Due to the importance of coprecipitation for high throughput synthesis, it was critical to maintain the entirety of the precursor synthesis within the coprecipitation reactor, with no post-precipitation modification steps outside of standard lithiation. This can be achieved through careful tuning of the reactor feedstocks and pH regulation, taking advantage of the high driving force for precipitation of transition metal hydroxides and the influence of pH on the coprecipitation process. After lithiation, the resulting cathode should be composed of an NMC811 core and Mn-

rich spinel exterior. Commonly utilized electrochemical tests demonstrate a marked improvement in the electrochemical performance of the resulting cathode when compared to its uncoated version, especially in capacity retention at elevated temperatures and suppression of impedance growth.

In **Chapter 4**, we explore the impact of minor amounts of lithium halides added to the lithium source during the calcination of NMC811. While extensive investigations have been conducted into cation doping of Ni-rich cathodes, less work is involved on anion doping. In this work, we demonstrate that minor additions of LiCl and LiBr result in significant morphology alterations, resulting in a porous cathode with ~3x more specific surface area than an undoped analogue. 5mol% Cl and Br doped samples exhibited significantly improved capacity retention and capacity under high charge/discharge rates, while F doping had negligible observed impact. The improvements in performance for Cl and Br doped samples were attributed to the onset of lithiation at lower temperature and formation of a compact and dense protective CEI layer upon cycling, which was investigated using surface sensitive techniques and supported by electron density-of-states calculations. This work demonstrates a new approach to Ni-rich cathode modifications through use of anion doping and tuning of the lithium source to affect the lithium melting temperatures.

In **Chapter 5**, we attempt to synthesize large single-crystalline NMC811 cathode powders. NMC cathodes and other Ni-rich layered oxides are well documented to go through large anisotropic volume changes when brought to the highly charged state, with the structural changes occurring due to the significant level of withdrawal of lithium from the host structure during deep

lithiation. Most NMC cathodes are typically comprised of micron sized spherical particles, which themselves are comprised of numerous nanosized primary particles with various orientations. Such changes in crystal lattice volume can initiate and exacerbate intergranular cracking in these polycrystalline secondary particles and lead to rapid capacity fade from electrical disconnection and continued exposure of reactive surfaces to electrolyte penetration. By removing the polycrystalline feature from the cathode, intergranular fracturing as a degradation mechanism is virtually eliminated. Single crystal NMC811 powders are synthesized through a facile molten salt method, utilizing lithium sulfate and sodium sulfate eutectics as a flux for crystal growth. The resulting powder is composed of micron sized single crystals of octahedral shapes. The shape and morphology are highly dependent on the initial molten salt content, composition, and sintering temperature/time. The eutectic salts are easily removed with water due to their high solubility, and the initial reversible capacity is comparable to typical polycrystalline NMC811 with excellent crystallinity. However, single crystal NMC811 suffers from rapid capacity fade, and failure mechanisms were investigated to be from intragranular cracking and planar gliding along the weaker (003) plane, which within the first cycle at high states of charge and exposes new surfaces to electrolyte-cathode interactions. Along with the growth of a thick CEI layer due to the more reactive (012) enclosed facets, cells suffer from rapidly increasing polarization at moderate levels of delithiation, with rapid irreversibility of the H2 to H3 transitions. This work demonstrates the effectiveness of flux growth for single crystal Ni-rich cathodes, while also exploring newly developed failure mechanisms and the need for further modifications for Ni-rich single crystal cathodes.

In **Chapter 6**, we discuss recommendations and directions for future work, which includes preliminary data of doped single crystal cathodes and doped ultrahigh nickel-rich cathodes. In ultrahigh nickel-rich cathodes nickel content is pushed beyond 90mol% and cobalt content reduced to ~ 2.5mol%. In commercial considerations, increasing the Ni content and decreasing the Co content further lowers materials cost while improving reversible capacity. The resulting cathode of the composition $LiNi_{0.95}Mn_{0.025}Co_{0.025}O_2$ demonstrates a reversible capacity >200mAh/g when cycled to an upper voltage cutoff of 4.3V, which is higher than that of NMC811. Cyclic voltammograms demonstrate that increasing the nickel content to this extent results in much more severe transformations not observed in NMC811 or other cathodes with lower nickel content, with the H2 to H3 transition also occurring at a lower voltage. The much more reactive ultrahigh nickel-rich material thus exhibits severe capacity fade during galvanostatic charge/discharge cycling, with rapid fading attributed to a combination of mechanical vulnerability and surface-initiated degradation mechanisms leading to fast impedance growth. Usage of dopants is aimed towards improving the capacity retention of the cathode to acceptable level. Magnesium dopant at ~1mol% is demonstrated to be effective for suppressing capacity fade, especially when cycling at an elevated temperature of 60˚C. Additional improvements can be obtained through a combined doping and microstructural modification approach, with minor addition of boron being effective in tuning the primary particle growth. 1mol% of boron is effective in growing elongated, radially oriented primary particles from influence of boron atoms on the surface energy of the (003) plane and resulting in preferential orientations that are more effective in suppressing intergranular cracking.

Chapter 1. Introduction

1.1 Lithium-ion battery (LIBs)

Lithium-ion batteries are critical in powering many different devices used across the world, from small portable devices such as cell phones and laptops, to the larger electric vehicles and drones. Many of these devices are limited by the battery that powers them, whether by weight, cost, or reversible capacity. This is especially true for electric vehicles, with their range limited mainly by the battery's specific capacity. All the while, lithium-ion battery production has increased significantly over the past few decades, and demand is expected to continue to increase [1-3]. Therefore, significant improvements to the performance and cost of lithium-ion batteries are continuously sought.

A typical LIB, as shown in **Figure 1**, is an electrochemical energy storage device, which converts chemical energy to electrical energy during discharge, and vice versa during charge. This is achieved through decoupling of the chemical reaction between the two electrodes, referred to as the anode and cathode, into ionic and electronic components. When a suitable electric connection is made, ideally connected to the desired load, the inherent chemical potential between the two electrodes leads to the transport of lithium ions from the anode into the cathode via an electrolyte. This is associated with discharging of the battery and reduction and oxidation (redox) reactions at the cathode and anode, respectively. During charging, the opposite occurs, in which an applied potential facilitates transport of lithium ions and electrons from the cathode to the anode. A solid electrically insulating but ion permeable membrane between the two electrodes prevents shorting of the cell and potential safety hazards such as thermal runaway.

The voltage, or potential, of the battery is based on the inherent electrochemical potential between the two electrodes. This potential is also referred to as the Nernst potential and is materials dependent, being associated with the energy difference between the half reactions that occur at each electrode [4]. The practical performance of a lithium-ion battery under different electrical loads, such as power, capacity, and high current performance, is highly dependent on the electrode materials, microstructural characteristics of the electrodes, and electrolyte characteristics and design of the battery.

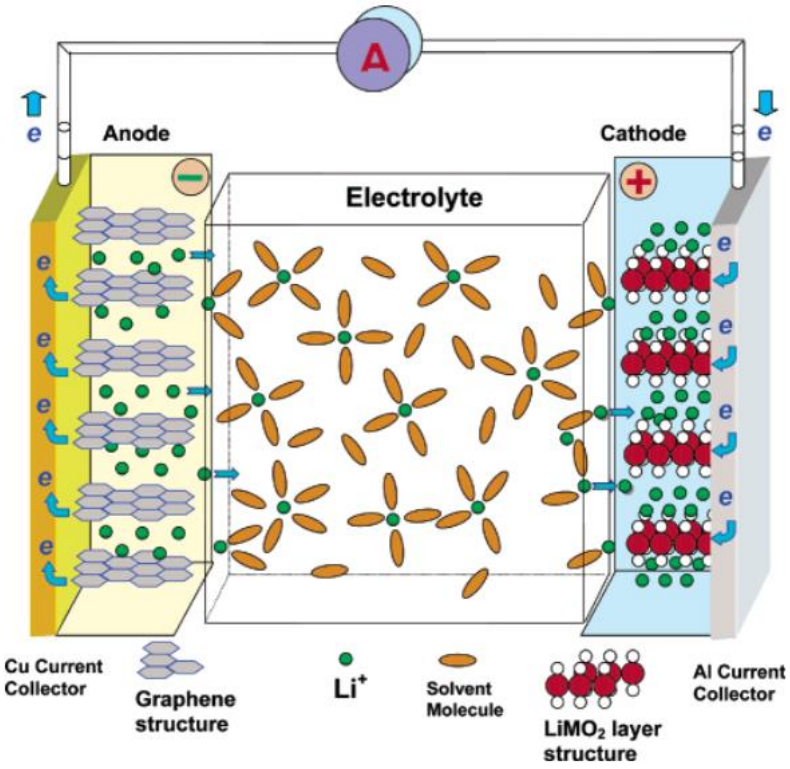

Figure 1: Schematic of a typical lithium-ion battery, with a graphite anode and $LiCoO_2$ cathode, taken from Ref. [5]. Lithium is transported between the electrodes during charge and discharge facilitated by a lithium salt-based electrolyte. The cathode is associated with the electrode that undergoes reduction during discharge, and the anode being oxidized.

1.1.1 Layered oxide cathodes (LCO)

The modern lithium-ion battery was commercialized in the mid-1990s by Sony, and was based on the work of John Goodenough, Stanley Whittingham, and Akira Yoshino, to whom the 2019 Nobel Prize in Chemistry was awarded [6]. This LIB utilized a cathode that was comprised of a transition metal layered oxide of the composition $LiCoO_2$ (LCO) and graphite anode [7]. The cathode was synthesized through a simple solid-state route, utilizing high temperature calcination of lithium salts and cobalt oxide to form the layered lithiated oxide. This cathode exhibited significant improvements over the existing battery systems at the time, such as high power due to relatively fast kinetics with high electronic and ionic conductivity, combined with a high working voltage of ~3.6V versus Li/Li^+ [7,8]. A high specific capacity could also be achieved due to use of the small Li^+ ion, and based on the crystal structure, a theoretical capacity of ~270mAh/g. However only 140mAh/g could be practically achieved based on limitations that will discussed in a later section. During charge and discharge, the electrochemical reactions and transport of lithium is accommodated by oxidation or reduction of the transition metal ion. This can be represented by the following redox reactions at the cathode:

During charge,

$$LiCoO_2 \rightarrow Li_{1-x}CoO_2 + x \cdot Li^+ + x \cdot e^- \quad (1)$$

and discharge,

$$Li_{1-x}CoO_2 + x \cdot Li^+ + x \cdot e^- \rightarrow LiCoO_2 \quad (2)$$

The lithium deficient oxide structure generated in (I) is accommodated by partial oxidation of Co^{3+} to Co^{4+}, fulfilling proper charge balance of the host structure. Lithium is then stored at the anode, whether by lithium intercalation or formation of solid solutions, until discharge of the cell by equation (II), where Co^{4+} is naturally reduced to Co^{3+} with the intercalation of lithium.

LCO is the basis for many other layered oxide cathodes of the general formula A_xMO_2, which take on the R-3m crystal structure. As shown in **Figure 2**, this is a hexagonal crystal structure that is well defined by alternating layers of transition metal and lithium cations, with a layer of oxygen anions in between, when viewed along the (001) plane. As such, this class of cathodes with a composition based on $LiMO_2$ (M being a transition metal) are often referred to as "layered oxides." Transition metal ions at the 3b Wyckoff position, with lithium ions residing in the 3b position. Oxygen anions are coordinated with the metal cations, forming the alternating layers of LiO_6 and MO_6 edge-sharing octahedra [9,10]. This structure is also commonly referred to as O3 structure or by their prototype structure: α-$NaFeO_2$. Within this structure, lithium ions in the "Li slab" are able to intercalate to and from the host structure through a vacancy hopping mechanism to adjacent sites. This is proposed to occur through either intermediate tetrahedral site hopping, or oxygen-dumbbell hopping [11,12]. It is this high fraction of lithium, combined with the close-packed oxygen framework, that realizes the desirable volumetric and specific capacity for layered oxide cathodes.

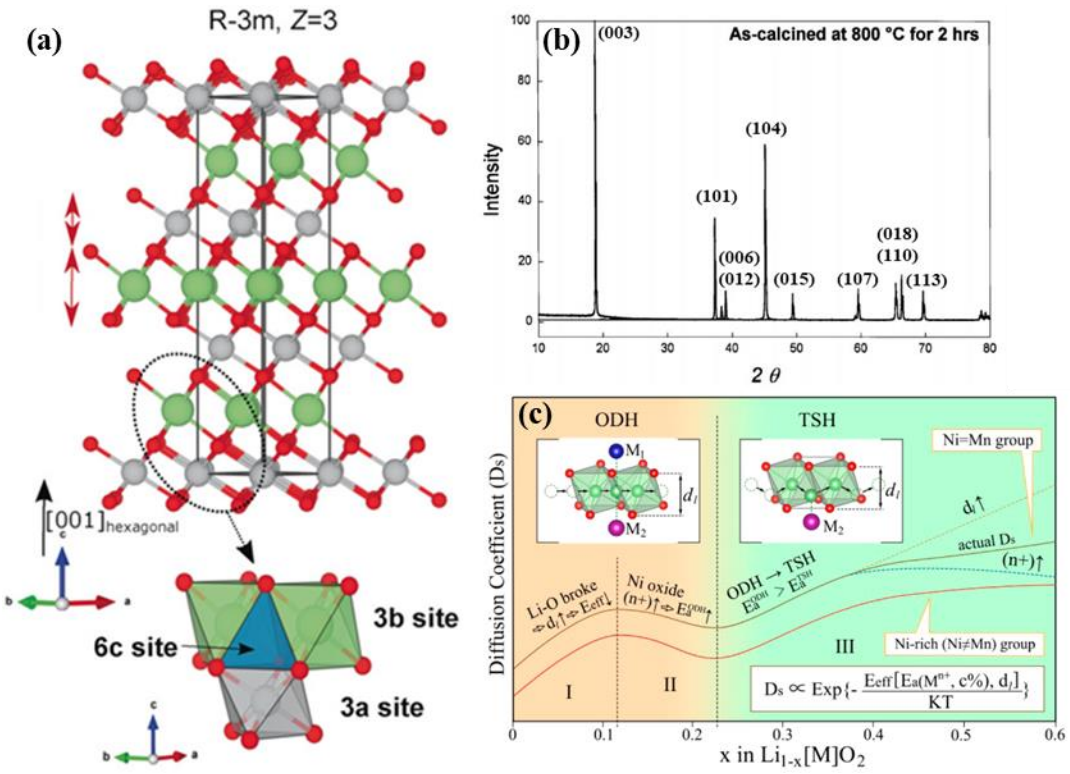

Figure 2: (a) Representation of the layered R-3m crystal structure of $LiCoO_2$ from Ref. [10], with red, gray, and green spheres representing oxygen, transition metal, and lithium ions, respectively. (b) Corresponding powder XRD profile of $LiCoO_2$, scanned using a Cu kα X-ray source (λ = 1.5406Å), taken from Ref. [12], with corresponding planar spacings identified. (c) Schematic of Li intercalation/diffusion through tetrahedral site (TSH) and oxygen dumbbell hopping (ODH) routes, taken from Ref. [11].

While LCO has been the predominant choice of cathode for LIBs for the past few decades, limitations in capacity and costs have begun to render this cathode insufficient for present and upcoming requirements. As mentioned previously, while having a theoretical capacity of ~270mAh/g, only ~140mAh/g can be practically accessible. This is due to the instability of the LCO crystal structure when more than 50% of the available Li is extracted, which occurs at an upper voltage cutoff of ~4.2V vs Li/Li^+ [13-15]. The resulting structural instability in the form of undesirable structural distortions from a hexagonal to monoclinic structure. This is also accompanied by a release in lattice oxygen, theorized to be due to the overlap between the

$Co^{3+/4+}$ band and the top of the O^{2-} 2p band as shown in **Figure 3a**, which threatens safety when considering possible oxidation of the organic solvents in the electrolyte [15-18]. The observed result of attempting to extract beyond 0.5 Li per formula unit is severe capacity fade and premature cell failure. Therefore, practical capacity is limited to 140mAh/g [14].

Aside from performance related limitations, the recent materials costs of cobalt have been volatile, with the cost per metric ton having fluctuated between ~$20,000 and ~$95,000 just within the past decade [19], with a general overall increase in price (**Figure 3b**). Part of this has to do with the current global supply chains mostly located in Central Africa, which are considered high risk along with posing ethical concerns as a conflict resource [20]. Lastly, cobalt in certain forms is toxic to humans [21]. Considering that LIB cathodes comprise ~40% of the total battery cost, moving away from cobalt would result in materials costs would lead to significant savings for manufacturers, more stable supply chains, and safer working environments [20-22].

1.1.2 Layered oxide cathodes (NMC)

In the mid-2000s, work by the Lu, MacNeil, and Dahn at doping the LCO crystal structure with nickel and manganese led to the development and patent of "NMC" cathodes, which have the composition $LiNi_{1-x-y}Mn_xCo_yO_2$ [23, 24]. While reducing the total materials cost of the cathode by cobalt fraction reduction, the desirable layered structure is still maintained and significant improvements in performance are also demonstrated. $LiNi_{1/3}Mn_{1/3}Co_{1/3}O_2$, also referred to as NMC111, was found to be an exceptional cathode material, exhibiting good cycle stability while also improving the practical reversible capacity to 160mAh/g at 4.3V vs Li/Li^+ compared to $LiCoO_2$ [25]. The relationship between nickel and manganese on the layered oxide cathode as

summarized in **Figure 3c**. Nickel generally increases the accessible capacity of the cathode by allowing for deeper levels of delithation, with around 80% of Li ions accessible for certain compositions when charged to 4.3V vs Li/Li^+ [25-27]. Part of this is attributed to reduced overlap between the $Ni^{3+/4+}$ redox and O^{2-} p bands (**Figure 3a**), allowing for further oxidation of Ni^{3+} to Ni^{4+} and subsequently deeper delithiation without the onset of detrimental effects related to lattice oxygen release [18, 28]. Manganese was found to improve the chemical stability of the cathode due to the high Mn^{3+}/Mn^{4+} redox energy, resulting in an electrochemically inactive Mn^{4+} valence state when added in moderate amounts, while also being relatively low cost and very abundant when compared to cobalt [29-33]. Since the development of NMC cathodes, much work has revolved around altering the Ni, Mn, and Co fractions to achieve desirable traits and balance materials costs and performance (**Figure 3d**).

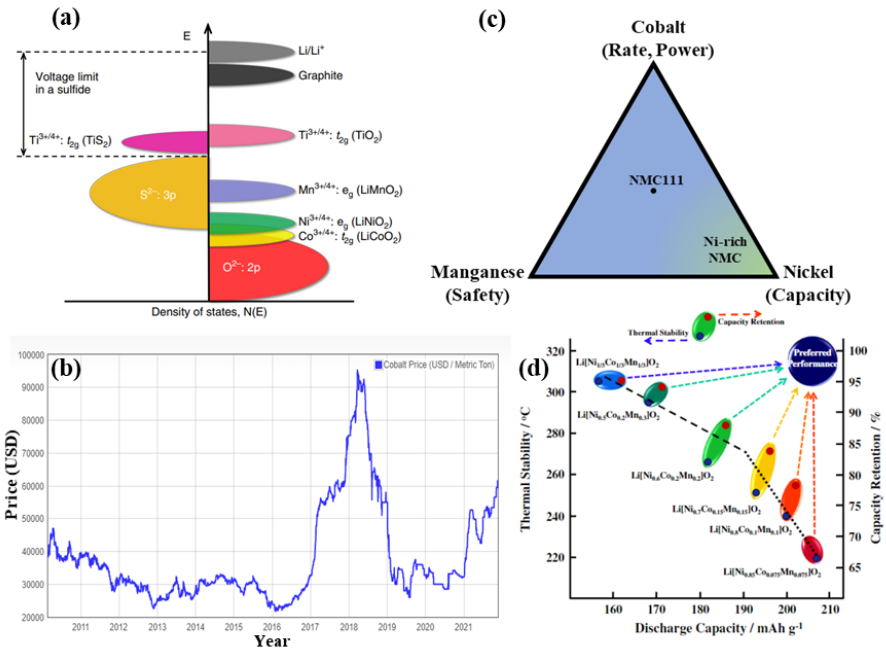

Figure 3: a) Position of the redox energies of Ni, Mn, and Co relative to the O2- p band, taken from Ref. [18]. (b) historical materials cost of cobalt in $/metric ton from 2010 to present, from Ref. [19]. (c) General relationship and contributions of Ni, Mn, and Co towards cathode performance characteristics. (d) Reversible capacities and thermal stabilities of different NMC compositions, taken from Ref. 25.

1.2 Nickel-rich NMC cathodes

Recently traction has gained on the application of nickel-rich NMC cathodes, which is a layered oxide cathode defined by a nickel fraction of over 60%. Specifically, the composition $LiNi_{0.8}Mn_{0.1}Co_{0.1}O_2$ (NMC811), is of significant interest due to a high demonstrated capacity of ~200mAh/g when cycled to an upper voltage cutoff of 4.5V vs Li/Li^+ [33-35]. In addition, the exceptionally low 10% cobalt content allows for an even cheaper materials cost compared to LCO or NMC111, which is a step towards to DOE targets of $100/kWh [36]. More importantly, successful application and commercialization of NMC811 cathodes would be able to meet the DOE 2025 target of 235Wh/kg for electric vehicle battery packs [37]. Thus, it is expected that nickel rich NMC cathodes will become important for next generation batteries and is currently the focus of multiple research efforts.

1.2.1 Limitations from Surface Instability

However, as the nickel content increases for NMC along with reduction in Co and Mn, the cathode become inherently more unstable, especially in the deeply delithiated state at higher voltages. In the charged state, high valence Ni^{4+} is fairly reactive and demonstrates a level of reactivity with the organic electrolytes commonly used for LIBs [38-40]. This reactivity typically results Ni reduction and subsequent outgassing via loss of lattice oxygen [40,41]. The release of oxygen can further oxidize the organic electrolyte, leading to exothermic heat release and posing a safety issue with thermal runaway hazards [40-42]. It is well demonstrated that NMC cathodes with higher nickel compositions exhibit thermal runaway at lower onset temperatures, along with higher peak heat release, when compared to those with lower nickel compositions (**Figure 3d**).

In addition to the lower thermal stability, irreversible phase transformations can occur associated with increased cation mixing during prolonged cycling. This occurs due to Ni^{2+} ion mobility combined with Li site vacancies in the charged state and facilitated by the similar ionic radius of Ni^{2+} and Li^{+} (0.69Å and 0.72Å, respectively) [44,45]. Excessive cation mixing, especially at the surface, drives the undesirable formation of spinel-like phases such as $Li_xNi_2O_4$ (Fd3-m structure) and to eventually a resistive rocksalt-like NiO (Fm3-m structure) [45-48]. This can be represented by the following reactions, which demonstrate phase transformations in delithiated $LiNiO_2$ and the outgassing of lattice oxygen:

$$3 \cdot Li_xNiO_2 \rightarrow Li_xNi_2O_4 + NiO + x \cdot Li_2O \quad (3)$$

$$Li_xNi_2O_4 \rightarrow 2 \cdot NiO + x/2 \cdot Li_2O + (4-x)/2 \cdot O_2 \quad (4)$$

$$3 \cdot Li_xNiO_2 \rightarrow 3 \cdot NiO + 3x/2 \cdot Li_2O + (6-3x)/4 \cdot O_2 \quad (5)$$

Due to the inherent surface sensitivity of Ni-rich NMCs, most of these phase transformations are typically observed near the surface of the secondary particle but can also occur in the bulk. In addition, the Ni^{2+} ions in the lithium sites can still oxidize further to Ni^{3+} and Ni^{4+} valence states, and the smaller ionic radius can facilitate partial structural collapse in this layer, further mitigating Li^{+} diffusion [49]. The increase in cation mixing over time, along with the development of an NiO-like resistive layer at the surface, is associated with impedance growth, severely hindering Li ion diffusion, and reducing the overall reversable capacity and cycle life of the electrochemical cell.

Ni-rich NMC compositions have also been found to be more sensitive to environmental conditions compared to its Ni-deficient counterparts. Typically, Ni-rich cathodes are prepared via calcination of hydroxide or carbonate precursors with a stoichiometric excess of lithium salt

in order to counterbalance lithium volatilization and ensure adequately low levels of cation mixing [18]. The remaining active Li_2O easily reacts with ambient H_2O and CO_2 to form LiOH and Li_2CO_3, respectively, and are colloquially referred to as "residual lithium" [51-53]. These salts naturally act as a form of resistive layer and detrimentally affect electrochemical performance. Furthermore, these salts can additionally react and hydrolyze the $LiPF_6$ electrolyte to form various compounds such as Li_3PO_4, LiF, MF_2, and HF, the latter of which can etch the layered oxide and exacerbate cathode degradation [54]. Even with negligible amounts of residual lithium, lattice lithium in Ni-rich cathodes was found to be able to react with ambient species to form surface residual salts via a Li^+/H^+ exchange mechanism [51-53,55]. This not only forms the resistive salt layer, but also exhausts lithium from the lattice and induces NiO formation, which can be represented via the following reaction:

$$3 \cdot LiMO_2 + 2x \cdot H_2O + x \cdot CO_2 \rightarrow 3 \cdot Li_{1-x}H_xMO_2 + x \cdot LiOH + x \cdot Li_2CO_3 \qquad (6)$$

1.2.2 Stabilization via coating methods

As most of these degradation mechanisms are surface initiated, a straightforward approach is to modify the surface of NMC811. A commonly utilized method is by applying a protective coating around the cathode particles. Whether electrochemically active or inactive, the surface is somewhat passivated by providing a barrier between the Ni-rich cathode surface and electrolyte or ambient air, preventing the degradation mechanisms initiated by high valence nickel reactivity or inherent surface sensitivity. A variety of approaches have been demonstrated, revolving around surface coatings applied pre- or post-sintering, as well as core-shell and gradient structures developed during the precursor synthesis. In terms of coatings applied post-cathode synthesis, a wide range of coating compositions have also been well demonstrated in literature,

ranging from various oxide-based coatings [56-60], phosphates [61-63], and even conducting polymers [64,65].

Coatings applied via rotary evaporation rely on the dissolution of a coating precursor salt, followed by gradual solvent evaporation along with mechanical agitation. The supersaturation results in the precipitation of the coating precursor on the surfaces of the NMC precursor or cathode, ideally with good encapsulation. The Cho and Shen groups have demonstrated several facile methods centered around rotary evaporation of Mn-based compounds to develop spinel coated cathodes, as Mn-based materials tend to exhibit excellent chemical stability [66,67]. After rotary evaporation processes, the material is subsequently heat treated to form the coating layer, which in their case is a spinel layer, as lithiated Mn-rich compounds are stable in the spinel structure. As mentioned before, Mn-rich spinels are electrochemically stable and were demonstrated to function well as protective coatings for Ni-rich cathodes (**Figure 4a**) [66-68].

ALD methods have also been utilized to form coatings, such as Liang et al. to deposit Li-Nb-O based coatings [59]. In each case, the coatings are chosen for their superior electrochemical stability, and can stabilize the Ni-rich core under high voltage or high temperature cycling by inhibiting surface reactions. The ALD process allows for uniform and dense nanoscale coatings along with the ability to coat materials which are difficult to process by other means. In addition, effective particle encapsulation can be achieved, sometimes assisted through agitation of the powder during the deposition process.

Dry mixing the NMC material with the coating material in the form of nanopowders is the lowest cost method towards coating cathode materials. The process simply involves thoroughly mixing nanopowders with either the NMC precursor or already lithiated cathode material using planetary rollers or ball milling equipment, followed by a heat treatment step to coalesce the nanoparticles into a coating formation to reduce surface energy. While straightforward with low processing cost, it should be taken into consideration that uniform and dense coatings can sometimes be difficult to achieve through this method [103]. Additionally, the prior production or acquisition of nano powders as a coating material incurs a non-negligible cost, as well as potential safety and environmental hazards associated with the handling of nano powders [104].

ALD and rotary evaporation methods, while able to form good coatings at the lab scale, are not scalable processes, limiting the ability to synthesize modified cathode material on an industrially relevant scale. The most common high throughput process for developing Ni-rich cathodes is via coprecipitation. This process is centered around the high driving force of metal hydroxide precipitation in an alkaline environment. Typically, solutions of transition metal sulfates are dropped dropwise into a continuously stirring solution of ammonia, with the pH maintained anywhere between 10-11.3 depending on the desired composition. NaOH is used as a buffer solution to maintain the pH, as well as provide the necessary precipitating OH^- counter ion. Metal ions react with the hydroxide ions to precipitate out of solution as $M(OH)_2$ compounds, with the ammonia contributing as a chelating or complexing agent to control the precipitation rate and form dense spherical secondary particle (**Figure 4b**) [69,70]. This process is suitable since intimate elemental mixing can be achieved and reactor setups can either be set for large batch reactors or continuously flowing reactors. As a result, it is more suitable to utilize coprecipitation

processes as part of a modification process. The relevant metal-ammonia complexing and metal hydroxide precipitation reactions during the coprecipitation processes are as followed:

$$M^{2+} + n \cdot NH_3 \rightarrow [M(NH_3)_n]^{2+} \quad (6)$$

$$[M(NH_3)_n]^{2+} + 2 \cdot OH^- \rightarrow M(OH)_2 + n \cdot NH_3 \quad (7)$$

Several attempts have been demonstrated in modifying Ni-rich NMC cathodes utilizing coprecipitation, specifically by forming core-shell or concentration gradient metal hydroxides [71-74]. In a core-shell structure, a Ni-rich composition is precipitated for a fixed amount of time. Afterwards, the metal sulfate feedstock is changed into a composition that is more Ni-deficient, but still typically containing moderate amounts of nickel. This was well demonstrated by the Manthiram group in which an $Ni_{0.9}Co_{0.1}(OH)_2$ core was initially precipitated, then coated with two shells of NMC721 and NMC541 hydroxides, with each shell being at around 1-2μm in thickness [75]. Sun et al. and Maeng et al. also demonstrated similar methods, using a Ni-rich core and a shell composed of $LiNi_{0.5}Mn_{0.5}O_2$ or $LiNi_{1/3}Mn_{1/3}Co_{1/3}O_2$, respectively (**Figure 4c)** [71, 72].

However, the presence of thick shells of different compositions can lead to issues related at the interfaces, as strain can build based on differences in lithium diffusion rates and mechanical properties [76,77]. As a result, concentration gradient cathodes were developed, where the composition from core to surface is gradually changed from an Ni-rich composition to a Ni-deficient composition. This was well demonstrated by the Amine group, where a standard coprecipitation reaction was modified by slowly pumping in a Ni-deficient metal sulfate solution into the metal sulfate feedstock that fed directly into the reactor [73]. The resulting material has a linearly decreasing nickel concentration from core to surface, and exhibited the high capacity associated with Ni-rich compositions, while also improving the capacity retention (**Figure 1d**).

However, it is worth noting that this method of producing concentration gradient cathodes is limited to batch reactor systems and is complicated to achieve in a continuously flowing coprecipitation reactor system.

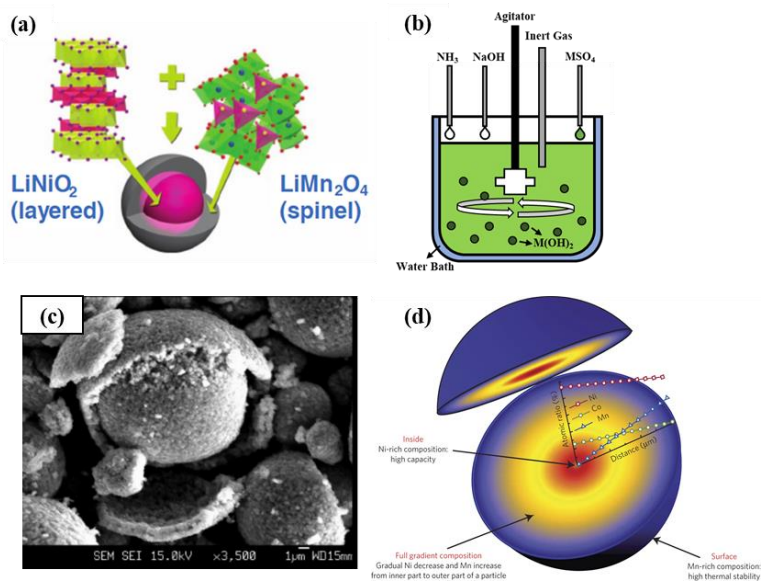

Figure 4: (a) Schematic of spinel coating NMC811, taken from Ref. [77]. (b) Schematic of coprecipitation process. (c) SEM image of a Core-shell cathode, with an NMC811 core and $LiNi_{0.5}Mn_{0.5}O_2$ shell, partially broken at the interface, taken from Ref. 71]. (d) Schematic representation of a full concentration gradient cathode, showing linearly decreasing nickel concentration from core to surface, taken from Ref. [78].

Thus, it is imperative to apply coatings to Ni-rich cathodes while meeting the following conditions: 1) utilizes a high throughput process, ideally coprecipitation of hydroxide precursors, 2) coating must be thin so as not to cause strain-related issues, 3) must not significantly reduce the accessible capacity and rate performance.

We propose that such a method can be achieved by focusing on the concepts of coprecipitation to produce a thin nanoscale coating. It is well demonstrated that pH is the most influential parameter towards morphological control in the coprecipitation process. At too low of a pH,

metal hydroxides do not precipitate as readily, and growth is diffusion controlled in the form of thickening of primary particles [69,70]. Increasing the pH increases the driving energy towards precipitation of metal hydroxides. By increasing the pH beyond the typically demonstrated levels, we expect that the increase in the thermodynamic driving force results in the rapid precipitation of metal hydroxides in the form of nanoparticles. Therefore, after the initial precipitation of NMC811 hydroxides (and subsequent depletion of Ni species in the reactor), a nanoscale coating of Mn-rich spinel precursors can be achieved by changing the feedstock solution to an Mn-rich composition, while also increasing the pH of the reactor to facilitate nanoparticle formation. Utilizing this process method, a heterogenous precursor composed of a NMC811 hydroxide core with a uniform coating of Mn-rich nanoparticles can be produced. Based on the stable state of Mn-rich oxides being the spinel structure, subsequent lithiation and calcination of the heterogenous precursor should result in a cathode composed of NMC811 coated with a nanolayer of spinel. Based on existing literature, it is expected that this cathode would exhibit improved electrochemical performance, with the additional advantage being that this synthesis method remains viable for both batch and continuously flowing reactor setups, alongside mitigating the risk of handling nanopowders.

1.2.3 Limitations from Bulk Instability

Alongside reactivity of the nickel-rich surface, several studies have pointed to the volume changes of nickel-rich cathodes upon lithiation/delithiation as a major contribution to capacity fade and cell failure. More specifically, during delithiation of the cathode, several bulk structural changes occur [79-83]. During initial delithiation of NMC811 from $0 < Li < 0.24$, the cathode structure changes from a hexagonal H1 phase to a monoclinic M phase. From $0.24 < Li < 0.60$, a

second phase change occurs from the M phase to another hexagonal H2 phase. Lastly, above Li > 0.60, a phase change from H2 to another hexagonal H3 phase occurs. These changes can be observed in cyclic voltammetry or differential capacity experiments, as three distinct redox pairs are observed during charging/discharging, as shown in **Figures 5a, b** [83]. These intermediate phases, as shown in **Figure 5c** are created due to lithium leaving the structure in preferential manner based on site activation energy and is also referred to as lithium vacancy ordering [84,85]. The subsequent changes in the crystal structure have a significant impact on the specific unit cell structure and corresponding lattice parameters.

Of these phase changes, the H2 to H3 phase change is considered the most destructive, as it is correlated with an abrupt volume change of the unit cell. During delithiation before the H2 to H3 transition, the *a* and *c* lattice parameters of the unit cell change in value; as transition metal ions such as nickel or cobalt get oxidized to higher valence states, the reduction in cation size and increased covalency (and subsequently decreased bond length distance) with oxygen anions results in shrinking of the *a* lattice parameter. Additionally, as lithium ions leave the structure, reduced shielding effects between the oxygen layers result in increased repulsion and gradual increase of the *c* lattice parameter, in particular a widening of the Li slab, is observed (**Figure 5b)** [82,86]. Based on work by the Grey group utilizing in-situ XRD of NMC811 samples, shrinkage of the *a* lattice parameter and expansion of the *c* lattice parameter reached a minimum and maximum of ~2.1%, respectively, compared to the fully discharged state [83]. However, during the H2 to H3 transition, a level of deep delithiation around 80% causes an interlayer collapse of the Li slab and is realized by a sharp contraction in the *c* lattice parameter and overall unit cell volume. This was hypothesized to be caused by depletion of the effective charge of

oxygen anions and subsequent reduction of repulsion between oxygen planes due to a charge transfer mechanism between high valence Ni and O leading to higher covalency [87]. As a result, the *c* lattice parameter has been observed to decrease by around 4-5% within this small composition/voltage region, shrinking to a value even lower than that of the fully discharged state (~14.5Å to 13.95Å reported by the Grey group for NMC811) [83].

This phenomenon is consistently observed through use of cyclic voltammetry, differential capacity profiles, and in-situ XRD analysis of cathode samples at incremental values of state-of-charge ("SOC") [79,83,86]. While this occurs for all NMC compositions, the voltage at which the H2 to H3 transition occurs tends to decrease with increasing nickel content, as it is mostly dependent on the % Li removal and Ni-rich cathodes can reach deeper levels of delithiation at lower voltages [89]. For NMC811, this phase change occurs at ~ 4.2V vs Li/Li^+, which is well within the voltage range of typically cycled Li-ion batteries. For contrast, this voltage occurs at 4.4V vs Li/Li^+ for NMC622 and even higher for NMC111. Detrimental effects related to this phenomenon include mechanical strain and decreased lithium diffusion coefficients [80,81]. The former is considered especially detrimental for Ni-rich cathodes in use for long term cycling; it is suggested that the repeating mechanical strains leads to intergranular cracking between the randomly oriented primary particles within typical polycrystalline cathode powders, facilitating electrical disconnection, particle pulverization, and electrolyte infiltration, as shown in **Figure 5d**. Thus, many works are focused on different ways to address the structural vulnerability of Ni-rich cathodes.

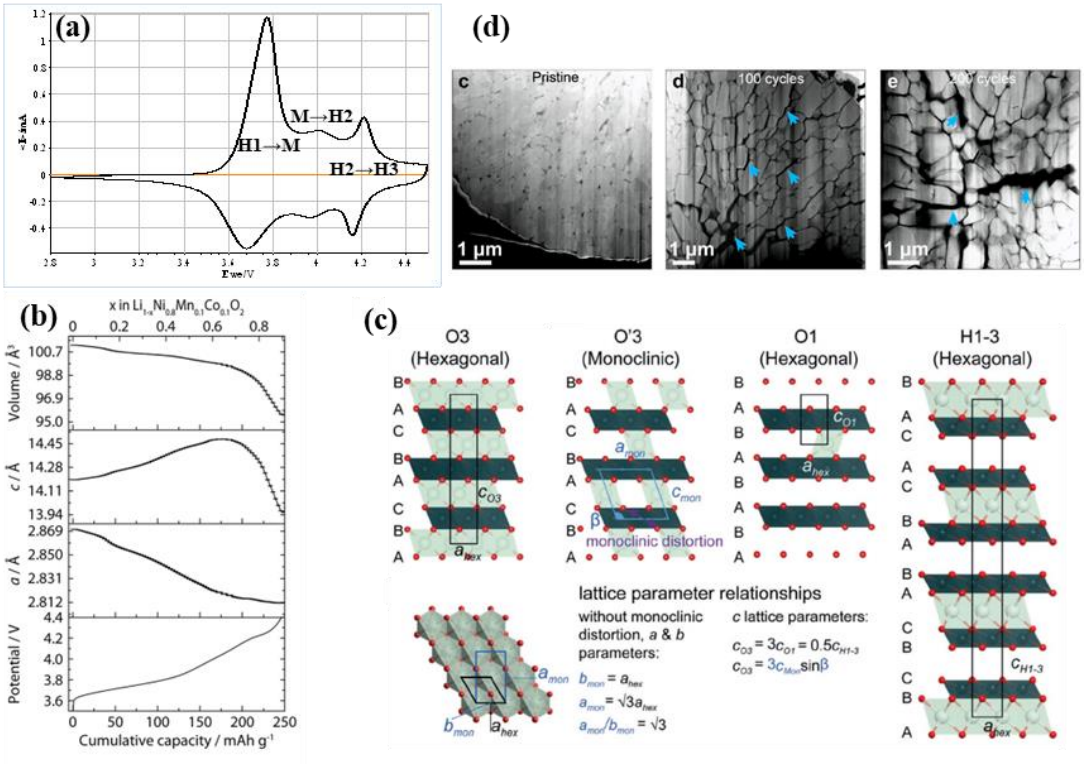

Figure 5: (a) Cyclic voltammetry profile of NMC811, representing the phase transitions between 2.8 and 4.5V. (b) Change in a, c lattice parameters and overall unit cell volume of Ni-rich cathode at different voltages/state-of-charge, taken from Ref. [83]. (c) Illustration of crystal structures of intermediate phase changes during cathode delithiation, with lithium, transition metal, and oxygen atoms in light green, dark green, and red, respectively, taken from Ref. [84]. (d) Cross section SEM image of intergranular cracking of NMC811 cathode after galvanostatic cycling to 4.5V vs Li/Li+, due to repeated volume changes, taken from Ref. [80]

1.2.4 Pathways towards single crystal synthesis

While dopants can provide some sort of suppression of this phenomenon, a recently popular solution towards resolving issues related to intergranular fracture and secondary particle pulverization is via microstructural modification of the cathode powder. More specifically, the elimination of polycrystalline secondary particles and use of large, single crystalline cathode particles (**Figure 6a**) [90-92]. With the absence of grain boundaries and interfaces between primary particles, issues related to intergranular fracture are effectively eliminated, ideally improving

long term cyclability while still utilizing levels of deep lithiation. These larger crystals can successfully accommodate the volume changes associated with the H2 to H3 transition during typical cycling without cracking, although with some limitations in size; work by Qian et al. determined that a critical crystal size exists, in which the internal strains caused by coherency stresses are large enough to initiate intragranular fracture [90]. This was also found to occur if pushing the level of delithiation even higher, as when single crystalline NMC622 was cycled to 4.8V vs Li/Li^+. A secondary benefit when utilizing single crystalline morphology is that typically a lower surface to volume ratio is achieved compared to polycrystalline counterparts and would overall suppress the severity of degradation mechanisms related to surface/electrolyte interactions. This was demonstrated by TGA/DSC experiments on mixtures of electrolyte and single crystalline NMC in the discharged state; the single crystal morphology significantly suppressed gas evolution compared to the polycrystalline counterpart [93].

Some of the main challenges towards the development single-crystalline cathode powders typically revolve around synthesis. Various methods are documented in literature and represented in **Figure 6a**, from simple high temperature sintering to multi-step sintering/lithiation steps [48], to ball milling [95-97], to flux assisted growth using additives such as molten salts [90,92-94]. Higher than typical sintering temperatures are often utilized based on the relationship between temperature and solid-state diffusion [94]. Of these methods, flux assisted growth via molten salts hold significant promise, as it is a scalable process that doesn't involve additional high energy processes such as milling or multiple calcination steps. In addition, multiple variables can be controlled to modify the singly crystal size and morphology [98], which will be discussed in the next section. It should also be noted that in milling steps or other

processes involving breakage of secondary particles, it is difficult to control the single crystal size and morphology.

Several works document the successful synthesis of large single crystalline NMC particles, such as work by Kimjima, where flux growth of single crystal NMC111 was achieved using molybdate flux or sodium sulfate and carbonate fluxes [92]. Kim et al. utilized various molten salts such as NaCl or KCl combined high sintering temperatures to grow faceted micron-sized crystals of NMC811 [93]. Although electrochemical performance was not reported or subpar in these works, they demonstrated that dominant facets during crystal growth and final crystal size can be tuned based on the temperature, sintering environment, and molten salt utilized, thus demonstrating the effectiveness of molten salts in synthesizing uniform single crystals (**Figure 6d**).

Crystal growth was proposed to be driven by Ostwald ripening principles related to liquid phase sintering, with a dissolution/recrystallization process of the oxide material facilitated by the molten salt flux [92]. In particular, these oxides were reported to have higher solubility in fluxes containing either sulfate anions or large alkali cations due to their effectiveness in solvating O^{2-} anions [99,100]. In addition, facet control was theorized to be a result of capping effects, where specific anions or cations can preferentially adsorb onto certain surfaces, inhibiting growth along those directions. In the case of Na-containing flux, Na^+ ions were suspected to adsorb onto the {001} surfaces due to a higher adsorption enthalpy compared to Li^+, resulting in Li^+ ions forced to migrate and precipitate along other surfaces resulting in the aforementioned anisotropic crystals [92,93].

However, many of these works utilize NMC chemistries with low nickel content or are unable to demonstrate favorable electrochemical performance, if they report electrochemical performance at all [92,95]. There has been some documented success in synthesizing single crystalline NMC622, utilizing a eutectic molten salt of LiOH and Li_2SO_4, as it was found that sulfate salts were particularly effective at inhibiting particle agglomeration while growing crystals via the proposed dissolution/recrystallization process [90]. In addition, LiOH and Li_2SO_4 are very soluble in water and excess salts were easily washed away. Significant improvements of traditional polycrystalline NMC622 were demonstrated, with the single-crystalline cathode exhibiting similar reversible capacity but with a noticeable improvement in capacity retention. Post-mortem analysis demonstrated the difference due to intergranular fracturing for the polycrystalline sample (**Figure 6b, c**).

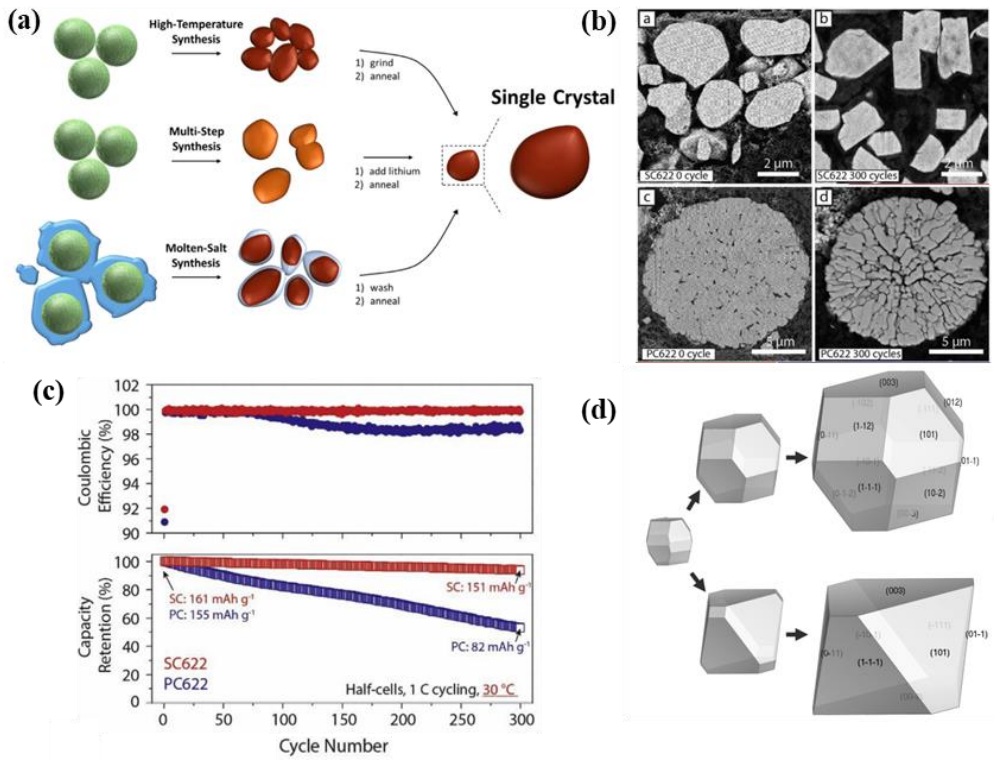

Figure 6: (a) Graphical illustration single crystalline cathode and various synthesis approaches, taken from Ref. [102]. (b) Cross section SEM images of single crystalline and polycrystalline NMC622 after 300 cycles and (c) performance comparison with polycrystalline counterpart during 1C cycling from 2.8-4.3V vs Li/Li+, taken from Ref. [90]. (d) Different dominant facets of single crystal NMC111 due to different flux composition (top: KCl, bottom: NaCl), taken from Ref. [98].

Currently there is a lack of study on single-crystalline NMC cathodes with higher nickel content, particularly in the case of Ni ≥ 80%. In recent years, several works related to large single crystalline Ni-rich cathodes were reported, such as NMC811 and NCA. Multi-step lithiation and high temperature sintering steps combined with ball milling successful in synthesizing micron sized crystals of NCA, with Ni > 80% [95,100]. Although it appears that uniform composition was achieved with no observed impurity phases, the resulting powders did not exhibit uniform size or morphology distributions. In addition, performance was unable to match that of their traditional

polycrystalline cathode counterpart nor provide performance advantages, even with the utilization of different electrolyte additives [91,101].

It is suspected that high temperature sintering is detrimental towards the performance of Ni-rich cathode materials, as it can facilitate a higher increase in cation mixing and potential formation of rock-salt structures at the surfaces [103,104]. With Ni-rich compositions, increasing the temperature facilitates lithium deficiencies in the final structure due to the relatively high vapor pressure of lithium oxide leading to vaporization. In addition, higher temperatures facilities formation of NiO as the equilibrium phase, which is electrochemically resistive and severely detrimental towards cathode performance. Therefore, it is recommended to utilize lower sintering temperatures, typically below 800°C as is the case with most reported studies of Ni-rich compositions [81,82,85,87,102-105]. However, as temperature is a significant driver of diffusion-limited grain growth, it can be difficult to obtain desirable micron sized crystals at lower sintering temperatures. One such demonstrated solution is through temperature swing synthesis, in which a short, high temperature sintering step is followed by a longer sintering step at lower temperature. This was demonstrated recently for NMC622 with some success and relies on the initial high temperature step of 1000°C lasting 3hrs for most of the grain growth/single crystal formation, with a secondary longer step at 900°C for 10hrs to facilitate structural ordering of the bulk material [52]. However, this process method has not been proven for higher Ni-rich cathode chemistries and has not yet been demonstrated beyond this work.

Existing works related to single crystalline NMC cathodes typically utilize a high excess of Li salts to accommodate vaporization during sintering, or molten salts as a flux for crystal growth.

In both cases, these salts are soluble and typically need to be washed away before forming cathode films, as excess residue can function as a resistive layer and result in undesirable electrochemical performance [105,106]. Excess LiOH is also known to be an impediment towards cathode processing, as it can contribute to high slurry alkalinity, which can facilitate corrosion of the typically used aluminum current collector [107]. While a washing process with deionized water is acceptable and documented in the case of NMC with low nickel contents [108], washing with water can be very detrimental towards nickel-rich cathodes. In polycrystalline NMC811 samples, simple stirring in deionized water led to fracturing of secondary particles and was attributed to reactivity between the Ni-rich NMC surface and water [109,110]. Upon extended immersion, the surface was found to degrade severely through proposed mechanisms of H^+/Li^+ exchange and release of lattice oxygen accompanied with Ni reduction. Subsequently, the particle surfaces and along grain boundaries is converted from the layered structure to rock salt-like structures. These mechanisms are identical to that of Ni-rich NMC stored in ambient conditions over long period of time, but in this case, are quickly developed through immersion at the timescale of hours instead of weeks. The resulting surface degradation increases impedance by suppressing lithium diffusion, as well as causing internal strains in the case of secondary particles. While intergranular fracture is not a concern for single crystal cathodes, conversion of the surface/sub-surface regions to resistive rock-salt phases would result in unattractive electrochemical performance, especially since single crystal cathodes generally have reduced performance at high charge/discharge due to inherently lower specific surface compared to their polycrystalline counterparts. Therefore, while excess Li salts and molten salts are critical for the synthesis of large single crystals, the washing step must be carefully optimized, which includes the washing time, choice of solvent, solvent volume, and solvent temperature. In some cases, a

reheating/annealing step post washing can be beneficial to restore the surface structure back to the layered phase, with some works reporting that adding additional Li sources can further help oxidize the surface and replenish any lost lithium [111].

We propose the synthesis of single crystalline Ni-rich NMC compounds, mainly NMC811, using a molten salt eutectic. Like other molten salt methods, crystal growth is facilitated by dissolution/recrystallization of the oxide and liquid phase diffusion. However, use of a molten salt eutectic composition can dramatically decrease the required temperature for liquid phase flux. In comparison to pure NaCl, which has a melting point of ~800°C, Na_2SO_4-NaCl eutectic composition has a significantly lower melting point at 620°C, far below that of either component in their pure phase. This also holds true with various other alkali salts, such as LiOH-Li_2SO_4 or Li_2SO_4-Na_2SO_4, the latter of which has a melting point of~590°C and contains Li^+, Na^+, and SO_4^{2-} ions, all of which can significantly affect crystal morphology whether though common ion effects, capping agents, or facilitating solvation [92,93,99]. The molten salt method is a scalable process with relatively simple steps, and the flux materials are expected to be able to be recovered and reusable to an extent, through a simple washing and evaporation process. Demonstrating the synthesis of single crystalline Ni-rich compositions while maintaining acceptable performance would be a significant step towards improved stability and longevity of Ni-rich cathodes.

1.3 References

[1] Pillot, C. (2017, January). Lithium ion battery raw material supply & demand 2016–2025. In Proceedings of the Advanced Automotive Battery Conference, Mainz, Germany (Vol. 30).

[2] Bernhart, W. (2019). Challenges and opportunities in lithium-ion battery supply. Future Lithium-ion Batteries, 316-334.

[3] Vikström, H., Davidsson, S., & Höök, M. (2013). Lithium availability and future production outlooks. Applied Energy, 110, 252-266.

[4] Bard, A. J., & Faulkner, L. R. (2001). Fundamentals and applications. Electrochemical methods, 2(482), 580-632.

[5] Xu, K. (2004). Nonaqueous liquid electrolytes for lithium-based rechargeable batteries. Chemical reviews, 104(10), 4303-4418.

[6] Bredas, J. L., Buriak, J. M., Caruso, F., Choi, K. S., Korgel, B. A., Palacin, M. R., ... & Ward, M. D. (2019). An electrifying choice for the 2019 chemistry Nobel Prize: Goodenough, Whittingham, and Yoshino.

[7] Mizushima, K., Jones, P. C., Wiseman, P. J., & Goodenough, J. B. (1981). LixCoO2 (0< x⩽ 1): A new cathode material for batteries of high energy density. Solid State Ionics, 3, 171-174.

[8] Wang, X., Wang, X., & Lu, Y. (2019). Realizing high voltage lithium cobalt oxide in lithium-ion batteries. Industrial & Engineering Chemistry Research, 58(24), 10119-10139.

[9] Dyer, L. D., Borie Jr, B. S., & Smith, G. P. (1954). Alkali metal-nickel oxides of the type MNiO2. Journal of the American Chemical Society, 76(6), 1499-1503.

[10] Bianchini, M., Roca-Ayats, M., Hartmann, P., Brezesinski, T., & Janek, J. (2019). There and back again—the journey of LiNiO2 as a cathode active material. Angewandte Chemie International Edition, 58(31), 10434-10458.

[11] Wei, Y., Zheng, J., Cui, S., Song, X., Su, Y., Deng, W., Wu, Z., Wang, X., Wang, W., Rao, M., Kub, Y., Wang, C., Amine, K., & Pan, F. (2015). Kinetics tuning of Li-ion diffusion in layered Li (Ni x Mn y Co z) O2. Journal of the American Chemical Society, 137(26), 8364-8367.

[12] Hong, C., Leng, Q., Zhu, J., Zheng, S., He, H., Li, Y., ... & Yang, Y. (2020). Revealing the correlation between structural evolution and Li+ diffusion kinetics of nickel-rich cathode materials in Li-ion batteries. Journal of Materials Chemistry A, 8(17), 8540-8547.

[13] Kannan, A. M., Rabenberg, L., & Manthiram, A. (2002). High capacity surface-modified LiCoO2 cathodes for lithium-ion batteries. Electrochemical and Solid State Letters, 6(1), A16.

[14] Wang, H., Jang, Y. I., Huang, B., Sadoway, D. R., & Chiang, Y. M. (1999). Electron microscopic characterization of electrochemically cycled LiCoO2 and Li (Al, Co) O2 battery cathodes. Journal of Power Sources, 81, 594-598.

[15] Hirooka, M., Sekiya, T., Omomo, Y., Yamada, M., Katayama, H., Okumura, T., ... & Ariyoshi, K. (2019). Degradation mechanism of LiCoO2 under float charge conditions and high temperatures. Electrochimica Acta, 320, 134596.

[16] Sharifi-Asl, S., Soto, F. A., Foroozan, T., Asadi, M., Yuan, Y., Deivanayagam, R., ... & Shahbazian-Yassar, R. (2019). Anti-Oxygen Leaking LiCoO2. Advanced Functional Materials, 29(23), 1901110.

[17] Sun, C., Liao, X., Xia, F., Zhao, Y., Zhang, L., Mu, S., Shi, S., Li, Y., Peng, H., Van Tendeloo, G., Zhao, K., & Wu, J. (2020). High-voltage cycling induced thermal vulnerability in LiCoO2 cathode: cation loss and oxygen release driven by oxygen vacancy migration. ACS nano, 14(5), 6181-6190.

[18] Manthiram, A. (2020). A reflection on lithium-ion battery cathode chemistry. Nature communications, 11(1), 1-9.

[19] Cobalt price 2020. Metalary. (2020, March 11). Retrieved November 28, 2021, from https://www.metalary.com/cobalt-price/.

[20] Cohen, L., Matich, T., Gautneb, H., & Rodger, M.. Top Cobalt Production by Country. Retrieved February 18, 2020, from https://investingnews.com/daily/resource-investing/battery-metals-investing/cobalt-investing/top-cobalt-producing-countries-congo-china-canada-russia-australia/

[21] Santana, I. L., Moreira, T. F. M., Lelis, M. F. F., & Freitas, M. B. J. G. (2017). Photocatalytic properties of Co3O4/LiCoO2 recycled from spent lithium-ion batteries using citric acid as leaching agent. Materials Chemistry and Physics, 190, 38-44.

[22] Ahmed, S., Nelson, P. A., Gallagher, K. G., Susarla, N., & Dees, D. W. (2017). Cost and energy demand of producing nickel manganese cobalt cathode material for lithium ion batteries. Journal of Power Sources, 342, 733-740.

[23] Lu, Z., & Dahn, J. R. (2005). U.S. Patent No. 6,964,828. Washington, DC: U.S. Patent and Trademark Office.

[24] Lu, Z., MacNeil, D. D., & Dahn, J. R. (2001). Layered cathode materials Li [Ni x Li (1/3− 2x/3) Mn (2/3− x/3)] O 2 for lithium-ion batteries. Electrochemical and Solid State Letters, 4(11), A191.

[25] Noh, H. J., Youn, S., Yoon, C. S., & Sun, Y. K. (2013). Comparison of the structural and electrochemical properties of layered Li [NixCoyMnz] O2 (x= 1/3, 0.5, 0.6, 0.7, 0.8 and 0.85) cathode material for lithium-ion batteries. Journal of power sources, 233, 121-130.

[26] Myung, S. T., Maglia, F., Park, K. J., Yoon, C. S., Lamp, P., Kim, S. J., & Sun, Y. K. (2017). Nickel-rich layered cathode materials for automotive lithium-ion batteries: achievements and perspectives. ACS Energy Letters, 2(1), 196-223.

[27] Manthiram, A., Song, B., & Li, W. (2017). A perspective on nickel-rich layered oxide cathodes for lithium-ion batteries. Energy Storage Materials, 6, 125-139.

[28] Manthiram, A. V. M. A., Murugan, A. V., Sarkar, A., & Muraliganth, T. (2008). Nanostructured electrode materials for electrochemical energy storage and conversion. Energy & Environmental Science, 1(6), 621-638.

[29] Liu, X., Xu, G. L., Yin, L., Hwang, I., Li, Y., Lu, L., Xu, W., Zhang, X., Chen, Y., Ren, Y., Sun, C.J., Chen, Z., Ouyang, M., & Amine, K. (2020). Probing the thermal-driven structural and chemical degradation of Ni-rich layered cathodes by Co/Mn exchange. Journal of the American Chemical Society, 142(46), 19745-19753.

[30] Sun, H. H., Choi, W., Lee, J. K., Oh, I. H., & Jung, H. G. (2015). Control of electrochemical properties of nickel-rich layered cathode materials for lithium ion batteries by variation of the manganese to cobalt ratio. Journal of Power Sources, 275, 877-883.

[31] Liu, Z., Yu, A., & Lee, J. Y. (1999). Synthesis and characterization of LiNi1− x− yCoxMnyO2 as the cathode materials of secondary lithium batteries. Journal of Power Sources, 81, 416-419.

[32] Bak, S. M., Hu, E., Zhou, Y., Yu, X., Senanayake, S. D., Cho, S. J., Kim, K.B., Chung, K.Y., Yang, X. Q., & Nam, K. W. (2014). Structural changes and thermal stability of charged LiNi x Mn y Co z O2 cathode materials studied by combined in situ time-resolved XRD and mass spectroscopy. ACS applied materials & interfaces, 6(24), 22594-22601.

[33] Olivetti, E. A., Ceder, G., Gaustad, G. G., & Fu, X. (2017). Lithium-ion battery supply chain considerations: analysis of potential bottlenecks in critical metals. Joule, 1(2), 229-243.

[34] Manthiram, A., Knight, J. C., Myung, S.-T., Oh, S.-M., & Sun, Y.-K. (2015). Nickel-Rich and Lithium-Rich Layered Oxide Cathodes: Progress and Perspectives. Advanced Energy Materials, 6(1), 1501010.

[35] Xia, Y., Zheng, J., Wang, C., & Gu, M. (2018). Designing principle for Ni-rich cathode materials with high energy density for practical applications. Nano Energy, 49, 434-452.

[36] Kim, J., Lee, H., Cha, H., Yoon, M., Park, M., & Cho, J. (2018). Prospect and Reality of Ni-Rich Cathode for Commercialization. Advanced Energy Materials, 8(6), 1702028.

[37] Hsieh, I. Y. L., Pan, M. S., Chiang, Y. M., & Green, W. H. (2019). Learning only buys you so much: Practical limits on battery price reduction. *Applied Energy*, *239*, 218-224.

[38] DRIVE, U. (2017). US DRIVE Electrochemical Energy Storage Technical Team Roadmap.

[39] Sari, H. M. K., & Li, X. (2019). Batteries: Controllable Cathode–Electrolyte Interface of Li[Ni 0.8 Co 0.1 Mn 0.1]O 2 for Lithium Ion Batteries: A Review (Adv. Energy Mater. 39/2019). Advanced Energy Materials, 9(39), 1970151.

[40] Zhang, X., Jia, H., Zou, L., Xu, Y., Mu, L., Yang, Z., ... & Xu, W. (2021). Electrolyte Regulating toward Stabilization of Cobalt-Free Ultrahigh-Nickel Layered Oxide Cathode in Lithium-Ion Batteries. *ACS Energy Letters*, *6*(4), 1324-1332.

[41] Li, T., Yuan, X.-Z., Zhang, L., Song, D., Shi, K., & Bock, C. (2019). Degradation Mechanisms and Mitigation Strategies of Nickel-Rich NMC-Based Lithium-Ion Batteries. Electrochemical Energy Reviews, 3(1), 43–80.

[42] Jung, R., Metzger, M., Maglia, F., Stinner, C., & Gasteiger, H. A. (2017). Oxygen release and its effect on the cycling stability of LiNixMnyCozO2 (NMC) cathode materials for Li-ion batteries. Journal of The Electrochemical Society, 164(7), A1361-A1377.

[43] Geng, L., Liu, J., Wood III, D. L., Qin, Y., Lu, W., Jafta, C. J., ... & Belharouak, I. (2020). Probing Thermal Stability of Li-Ion Battery Ni-Rich Layered Oxide Cathodes by Means of Operando Gas Analysis and Neutron Diffraction. *ACS Applied Energy Materials*, *3*(7), 7058-7065.

[44] Zhang, X., Jiang, W. J., Mauger, A., Gendron, F., & Julien, C. M. (2010). Minimization of the cation mixing in Li1+ x (NMC) 1− xO2 as cathode material. *Journal of Power Sources*, *195*(5), 1292-1301.

[45] Peres, J. P., Delmas, C., Rougier, A., Broussely, M., Perton, F., Biensan, P., & Willmann, P. (1996). The relationship between the composition of lithium nickel oxide and the loss of reversibility during the first cycle. *Journal of Physics and Chemistry of Solids*, *57*(6-8), 1057-1060.

[46] Lin, F., Markus, I. M., Nordlund, D., Weng, T. C., Asta, M. D., Xin, H. L., & Doeff, M. M. (2014). Surface reconstruction and chemical evolution of stoichiometric layered cathode materials for lithium-ion batteries. *Nature communications*, *5*(1), 1-9.

[47] Bak, S. M., Hu, E., Zhou, Y., Yu, X., Senanayake, S. D., Cho, S. J., Kim, K.B., Chung, K.Y., Yang, X.Q., & Nam, K. W. (2014). Structural changes and thermal stability of charged LiNi x Mn y Co z O2 cathode materials studied by combined in situ time-resolved XRD and mass spectroscopy. *ACS applied materials & interfaces*, *6*(24), 22594-22601.

[48] Kim, N. Y., Yim, T., Song, J. H., Yu, J. S., & Lee, Z. (2016). Microstructural study on degradation mechanism of layered LiNi0. 6Co0. 2Mn0. 2O2 cathode materials by analytical transmission electron microscopy. *Journal of power sources*, *307*, 641-648.

[49] Dixit, M., Markovsky, B., Schipper, F., Aurbach, D., & Major, D. T. (2017). Origin of structural degradation during cycling and low thermal stability of Ni-rich layered transition metal-based electrode materials. *The journal of physical chemistry C*, *121*(41), 22628-22636.

[50] Delmas, C., Peres, J. P., Rougier, A., Demourgues, A., Weill, F., Chadwick, A., ... & Willmann, P. (1997). On the behavior of the LixNiO2 system: an electrochemical and structural overview. *Journal of Power Sources*, *68*(1), 120-125.

[51] Arai, H., Okada, S., Ohtsuka, H., Ichimura, M., & Yamaki, J. (1995). Characterization and cathode performance of Li1− xNi1+ xO2 prepared with the excess lithium method. *Solid State Ionics*, *80*(3-4), 261-269.

[52] Jung, R., Morasch, R., Karayaylali, P., Phillips, K., Maglia, F., Stinner, C., ... & Gasteiger, H. A. (2018). Effect of ambient storage on the degradation of Ni-rich positive electrode materials (NMC811) for Li-ion batteries. *Journal of The Electrochemical Society*, *165*(2), A132.

[53] Mu, L., Yang, Z., Tao, L., Waters, C. K., Xu, Z., Li, L., Saino, S., Du, Y., Xin, H., Nordlund, D., & Lin, F. (2020). The sensitive surface chemistry of Co-free, Ni-rich layered oxides: identifying experimental conditions that influence characterization results. *Journal of Materials Chemistry A*, *8*(34), 17487-17497.

[54] Busà, C., Belekoukia, M., & Loveridge, M. J. (2021). The effects of ambient storage conditions on the structural and electrochemical properties of NMC-811 cathodes for Li-ion batteries. *Electrochimica Acta*, *366*, 137358.

[55] Kim, K., Kim, Y., Park, S., Yang, H. J., Park, S. J., Shin, K., Woo, J.J., Kim, S., Hong, S.Y., & Choi, N. S. (2018). Dual-function ethyl 4, 4, 4-trifluorobutyrate additive for high-performance Ni-rich cathodes and stable graphite anodes. *Journal of Power Sources*, *396*, 276-287.

[56] Shkrob, I. A., Gilbert, J. A., Phillips, P. J., Klie, R., Haasch, R. T., Bareño, J., & Abraham, D. P. (2017). Chemical weathering of layered Ni-rich oxide electrode materials: evidence for cation exchange. *Journal of The Electrochemical Society*, *164*(7), A1489.

[57] Han, B., Key, B., Lapidus, S. H., Garcia, J. C., Iddir, H., Vaughey, J. T., & Dogan, F. (2017). From coating to dopant: how the transition metal composition affects alumina coatings on Ni-rich cathodes. *ACS applied materials & interfaces*, *9*(47), 41291-41302.

[58] Han, B., Key, B., Lipton, A. S., Vaughey, J. T., Hughes, B., Trevey, J., & Dogan, F. (2019). Influence of coating protocols on alumina-coated cathode material: atomic layer deposition versus wet-chemical coating. *Journal of the Electrochemical Society*, *166*(15), A3679.

[59] Liu, S., Dang, Z., Liu, D., Zhang, C., Huang, T., & Yu, A. (2018). Comparative studies of zirconium doping and coating on LiNi0. 6Co0. 2Mn0. 2O2 cathode material at elevated temperatures. *Journal of Power Sources*, *396*, 288-296.

[60] Liang, J., Hwang, S., Li, S., Luo, J., Sun, Y., Zhao, Y., ... & Sun, X. (2020). Stabilizing and understanding the interface between nickel-rich cathode and PEO-based electrolyte by lithium niobium oxide coating for high-performance all-solid-state batteries. *Nano Energy*, *78*, 105107.

[61] Herzog, M. J., Gauquelin, N., Esken, D., Verbeeck, J., & Janek, J. (2021). Increased Performance Improvement of Lithium-Ion Batteries by Dry Powder Coating of High-Nickel NMC with Nanostructured Fumed Ternary Lithium Metal Oxides. *ACS Applied Energy Materials*, *4*(9), 8832-8848.

[62] Henderick, L., Hamed, H., Mattelaer, F., Minjauw, M., Nisula, M., Meersschaut, J., ... & Detavernier, C. (2021). Plasma enhanced atomic layer deposition of a (nitrogen doped) Ti phosphate coating for improved energy storage in Li-ion batteries. *Journal of Power Sources*, *497*, 229866.

[63] Gan, Q., Qin, N., Wang, Z., Li, Z., Zhu, Y., Li, Y., ... & Lu, Z. (2020). Revealing Mechanism of Li3PO4 Coating Suppressed Surface Oxygen Release for Commercial Ni-Rich Layered Cathodes. *ACS Applied Energy Materials*, *3*(8), 7445-7455.

[64] Kim, D. J., Ko, H. S., & Lee, J. W. (2015). Lithium silicate–lithium phosphate (xLi4SiO4−(1− x) Li3PO4) coating on lithium nickel manganese oxide (LiNi0. 7Mn0. 3O2) with a layered structure. *Solid State Ionics*, *278*, 239-244.

[65] Gan, Q., Qin, N., Zhu, Y., Huang, Z., Zhang, F., Gu, S., ... & Lu, Z. (2019). Polyvinylpyrrolidone-induced uniform surface-conductive polymer coating endows Ni-rich LiNi0. 8Co0. 1Mn0. 1O2 with enhanced cyclability for lithium-ion batteries. *ACS applied materials & interfaces*, *11*(13), 12594-12604.

[66] Ju, S. H., Kang, I. S., Lee, Y. S., Shin, W. K., Kim, S., Shin, K., & Kim, D. W. (2014). Improvement of the cycling performance of LiNi0. 6Co0. 2Mn0. 2O2 cathode active materials by a dual-conductive polymer coating. *ACS applied materials & interfaces*, *6*(4), 2546-2552.

[67] Wu, F., Li, N., Su, Y., Shou, H., Bao, L., Yang, W., Zhang, L., An, R., & Chen, S. (2013). Spinel/Layered Heterostructured Cathode Material for High-Capacity and High-Rate Li-Ion Batteries. Advanced Materials, 25(27), 3722–3726.

[68] Cho, Y., Lee, S., Lee, Y., Hong, T., & Cho, J. (2011). Spinel-Layered Core-Shell Cathode Materials for Li-Ion Batteries. Advanced Energy Materials, 1(5), 821–828.

[69] Zhang, J., Yang, Z., Gao, R., Gu, L., Hu, Z., & Liu, X. (2017). Suppressing the Structure Deterioration of Ni-Rich LiNi0.8Co0.1Mn0.1O2 through Atom-Scale Interfacial Integration of Self-Forming Hierarchical Spinel Layer with Ni Gradient Concentration. ACS Applied Materials & Interfaces, 9(35), 29794–29803.

[70] Ngoepe, N., Gutierrez, A., Barai, P., Chen, J., Ngoepe, P. E., & Croy, J. R. (2021). The effects of process parameters on the properties of manganese-rich carbonate precursors: A study of co-precipitation synthesis using semi-batch reactors. *Chemical Engineering Science*, *241*, 116694.

[71] Van Bommel, A., & Dahn, J. R. (2009). Analysis of the growth mechanism of coprecipitated spherical and dense nickel, manganese, and cobalt-containing hydroxides in the presence of aqueous ammonia. *Chemistry of Materials*, *21*(8), 1500-1503.

[72] Sun, Y. K., Myung, S. T., Kim, M. H., Prakash, J., & Amine, K. (2005). Synthesis and characterization of Li [(Ni0. 8Co0. 1Mn0. 1) 0.8 (Ni0. 5Mn0. 5) 0.2] O2 with the microscale core− shell structure as the positive electrode material for lithium batteries. *Journal of the American Chemical Society*, *127*(38), 13411-13418..

[73] Maeng, S., Chung, Y., Min, S., & Shin, Y. (2020). Enhanced mechanical strength and electrochemical performance of core–shell structured high–nickel cathode material. *Journal of Power Sources*, *448*, 227395.

[74] Sun, Y.-K., Kim, D.-H., Yoon, C. S., Myung, S.-T., Prakash, J., & Amine, K. (2010). A Novel Cathode Material with a Concentration-Gradient for High-Energy and Safe Lithium-Ion Batteries. Advanced Functional Materials, 20(3), 485–491.

[75] Mohanty, D., Dahlberg, K., King, D. M., David, L. A., Sefat, A. S., Wood, D. L., Daniel, C., Dhar, S., Mahajan, V., Lee, M., & Albano, F. (2016). Modification of Ni-rich FCG NMC and NCA cathodes by atomic layer deposition: preventing surface phase transitions for high-voltage lithium-ion batteries. Scientific reports, 6, 26532.

[76] Liao, J. Y., Oh, S. M., & Manthiram, A. (2016). Core/double-shell type gradient Ni-rich LiNi0. 76Co0. 10Mn0. 14O2 with high capacity and long cycle life for lithium-ion batteries. *ACS applied materials & interfaces*, *8*(37), 24543-24549.

[77] Wu, B., & Lu, W. (2017). Mechanical modeling of particles with active core–shell structures for lithium-ion battery electrodes. *The Journal of Physical Chemistry C*, *121*(35), 19022-19030.

[78] Liu, B., Wang, X., Chen, H. S., Chen, S., Yang, H., Xu, J., ... & Fang, D. N. (2019). A simultaneous multiscale and multiphysics model and numerical implementation of a core-shell model for lithium-ion full-cell batteries. *Journal of Applied Mechanics*, *86*(4).

[79] Sun, Y. K., Chen, Z., Noh, H. J., Lee, D. J., Jung, H. G., Ren, Y., Wang, S., Yoon, C.S., Myung, S.T., & Amine, K. (2012). Nanostructured high-energy cathode materials for advanced lithium batteries. *Nature materials*, *11*(11), 942-947.

[80] Li, W., Reimers, J. N., & Dahn, J. R. (1993). In situ x-ray diffraction and electrochemical studies of Li1− xNiO2. *Solid State Ionics*, *67*(1-2), 123-130.

[81] Lin, Q., Guan, W., Zhou, J., Meng, J., Huang, W., Chen, T., Gao, Q., Wei, X., Zeng, Y., Li, J., & Zhang, Z. (2020). Ni–Li anti-site defect induced intragranular cracking in Ni-rich layer-structured cathode. *Nano Energy*, *76*, 105021.

[82] Li, H., Liu, A., Zhang, N., Wang, Y., Yin, S., Wu, H., & Dahn, J. R. (2019). An unavoidable challenge for Ni-rich positive electrode materials for lithium-ion batteries. *Chemistry of Materials*, *31*(18), 7574-7583.

[83] Zheng, S., Hong, C., Guan, X., Xiang, Y., Liu, X., Xu, G. L., Liu, R., Zhong, G., Zheng, F., Li, Y., Zhang, X., Ren, Y., Chen, Z., Amine, K., & Yang, Y. (2019). Correlation between long range and local structural changes in Ni-rich layered materials during charge and discharge process. *Journal of Power Sources*, *412*, 336-343.

[84] Märker, K., Reeves, P. J., Xu, C., Griffith, K. J., & Grey, C. P. (2019). Evolution of structure and lithium dynamics in LiNi0. 8Mn0. 1Co0. 1O2 (NMC811) cathodes during electrochemical cycling. *Chemistry of Materials*, *31*(7), 2545-2554.

[85] Delmas, C., Fouassier, C., & Hagenmuller, P. (1980). Structural classification and properties of the layered oxides. *Physica B+ c*, *99*(1-4), 81-85.

[86] Xu, C., Reeves, P. J., Jacquet, Q., & Grey, C. P. (2021). Phase Behavior during Electrochemical Cycling of Ni-Rich Cathode Materials for Li-Ion Batteries. *Advanced Energy Materials*, *11*(7), 2003404.

[87] Li, W., Reimers, J. N., & Dahn, J. R. (1993). In situ x-ray diffraction and electrochemical studies of Li1− xNiO2. *Solid State Ionics*, *67*(1-2), 123-130.

[88] Croguennec, L., Pouillerie, C., Mansour, A. N., & Delmas, C. (2001). Structural characterisation of the highly deintercalated LixNi1. 02O2 phases (with x≤ 0.30) Basis of a presentation given at Materials Discussion No. 3, 26–29 September, 2000, University of Cambridge, UK. *Journal of Materials Chemistry*, *11*(1), 131-141.

[89] Xie, Q., Cui, Z., & Manthiram, A. (2021). Unveiling the Stabilities of Nickel-Based Layered Oxide Cathodes at an Identical Degree of Delithiation in Lithium-Based Batteries. *Advanced Materials*, *33*(32), 2100804.

[90] Jung, R., Metzger, M., Maglia, F., Stinner, C., & Gasteiger, H. A. (2017). Oxygen release and its effect on the cycling stability of LiNixMnyCozO2 (NMC) cathode materials for Li-ion batteries. *Journal of The Electrochemical Society*, *164*(7), A1361.

[91] Qian, G., Zhang, Y., Li, L., Zhang, R., Xu, J., Cheng, Z., XIe, S., Wang,H., Rao, Q., He, Y., She, Y., Chen, L., Tang, M., & Ma, Z. F. (2020). Single-crystal nickel-rich layered-

oxide battery cathode materials: synthesis, electrochemistry, and intra-granular fracture. *Energy Storage Materials*, *27*, 140-149.

[92] Li, J., Cameron, A. R., Li, H., Glazier, S., Xiong, D., Chatzidakis, M., Allen, J., Botton, G.A., & Dahn, J. R. (2017). Comparison of single crystal and polycrystalline LiNi0. 5Mn0. 3Co0. 2O2 positive electrode materials for high voltage Li-ion cells. *Journal of The Electrochemical Society*, *164*(7), A1534.

[93] Kimijima, T., Zettsu, N., & Teshima, K. (2016). Growth manner of octahedral-shaped Li (Ni1/3Co1/3Mn1/3) O2 single crystals in molten Na2SO4. *Crystal Growth & Design*, *16*(5), 2618-2623.

[94] Kim, Y. (2012). Lithium nickel cobalt manganese oxide synthesized using alkali chloride flux: morphology and performance as a cathode material for lithium ion batteries. *ACS applied materials & interfaces*, *4*(5), 2329-2333.

[95] Qian, G., Li, Z., Meng, D., Liu, J. B., He, Y. S., Rao, Q., Lio, Y., Ma, Z.F., & Li, L. (2021). Temperature-Swing Synthesis of Large-Size Single-Crystal LiNi0. 6Mn0. 2Co0. 2O2 Cathode Materials. *Journal of the Electrochemical Society*, *168*(1), 010534.

[96] Liu, A., Zhang, N., Stark, J. E., Arab, P., Li, H., & Dahn, J. R. (2021). Synthesis of Co-Free Ni-Rich Single Crystal Positive Electrode Materials for Lithium Ion Batteries: Part I. Two-Step Lithiation Method for Al-or Mg-Doped LiNiO2. *Journal of The Electrochemical Society*, *168*(4), 040531.

[97] Zheng, L., Bennett, J. C., & Obrovac, M. N. (2020). All-Dry Synthesis of Single Crystal NMC Cathode Materials for Li-Ion Batteries. *Journal of The Electrochemical Society*, *167*(13), 130536.

[98] Huang, B., Wang, M., Zuo, Y., Zhao, Z., Zhang, X., & Gu, Y. (2020). The effects of reheating process on the electrochemical properties of single crystal LiNi0. 6Mn0. 2Co0. 2O2. *Solid State Ionics*, *345*, 115200.

[99] Zhu, J., & Chen, G. (2019). Single-crystal based studies for correlating the properties and high-voltage performance of Li [Ni x Mn y Co 1− x− y] O 2 cathodes. *Journal of Materials Chemistry A*, *7*(10), 5463-5474.

[100] Xiao, X., Hayashi, F., Yubuta, K., Selloni, A., & Teshima, K. (2017). Effects of alkali cations and sulfate/chloride anions on the flux growth of {001}-faceted β-Li2TiO3 crystals. *Crystal Growth & Design*, *17*(3), 1118-1124.

[101] Liu, A., Zhang, N., Stark, J. E., Arab, P., Li, H., & Dahn, J. R. (2021). Synthesis of Co-Free Ni-Rich Single Crystal Positive Electrode Materials for Lithium Ion Batteries: Part II. One-Step Lithiation Method of Mg-Doped LiNiO2. *Journal of The Electrochemical Society*, *168*(5), 050506.

[102] Li, H., Li, J., Zaker, N., Zhang, N., Botton, G. A., & Dahn, J. R. (2019). Synthesis of single crystal LiNi0. 88Co0. 09Al0. 03O2 with a two-step lithiation method. *Journal of The Electrochemical Society*, *166*(10), A1956.

[103] Ronduda, H., Zybert, M., Szczęsna-Chrzan, A., Trzeciak, T., Ostrowski, A., Szymański, D., Wieczorek, W., Rarog-Pilecka, W., & Marcinek, M. (2020). On the Sensitivity of the Ni-rich Layered Cathode Materials for Li-ion Batteries to the Different Calcination Conditions. *Nanomaterials*, *10*(10), 2018.

[104] Tang, L., Cheng, X., Wu, R., Cao, T., Lu, J., Zhang, Y., & Zhang, Z. (2022). Monitoring the morphology evolution of LiNi0. 8Mn0. 1Co0. 1O2 during high-temperature solid state synthesis via in situ SEM. *Journal of Energy Chemistry*, *66*, 9-15.

[105] Wang, T., Ren, K., Xiao, W., Dong, W., Qiao, H., Duan, A., Pan, H., Yang, Y., & Wang, H. (2020). Tuning the Li/Ni disorder of the NMC811 cathode by thermally driven competition between lattice ordering and structure decomposition. *The Journal of Physical Chemistry C*, *124*(10), 5600-5607.

[106] Arai, H., Okada, S., Ohtsuka, H., Ichimura, M., & Yamaki, J. (1995). Characterization and cathode performance of Li1− xNi1+ xO2 prepared with the excess lithium method. *Solid State Ionics*, *80*(3-4), 261-269.

[107] Lee, W., Lee, D., Kim, Y., Choi, W., & Yoon, W. S. (2020). Enhancing the structural durability of Ni-rich layered materials by post-process: washing and heat-treatment. *Journal of Materials Chemistry A*, *8*(20), 10206-10216.

[108] Li, S. Y., & Church, B. C. (2016). Effect of aqueous-based cathode slurry pH and immersion time on corrosion of aluminum current collector in lithium-ion batteries. *Materials and Corrosion*, *67*(9), 978-987.

[109] Jo, M., Ku, H., Park, S., Song, J., & Kwon, K. (2018). Effects of Residual Lithium in the precursors of Li [Ni1/3Co1/3Mn1/3] O2 on their lithium-ion battery performance. *Journal of Physics and Chemistry of Solids*, *118*, 47-52.

[110] Azhari, L., Zhou, X., Sousa, B., Yang, Z., Gao, G., & Wang, Y. (2020). Effects of Extended Aqueous Processing on Structure, Chemistry, and Performance of Polycrystalline LiNi x Mn y Co z O2 Cathode Powders. *ACS Applied Materials & Interfaces*, *12*(52), 57963-57974.

[111] Hamam, I., Zhang, N., Liu, A., Johnson, M. B., & Dahn, J. R. (2020). Study of the reactions between Ni-rich positive electrode materials and aqueous solutions and their relation to the failure of Li-ion cells. *Journal of The Electrochemical Society*, *167*(13), 130521.

[112] Zhang, F., Lou, S., Li, S., Yu, Z., Liu, Q., Dai, A., Cao, C., Toney, M.F., Ge, M., Xiao, X., Lee, W.H., Yao, Y., Den, J., Liu, T., Tang, Y., Yin, G., Lu, J., Su, D., & Wang, J. (2020). Surface regulation enables high stability of single-crystal lithium-ion cathodes at high voltage. *Nature communications*, *11*(1), 1-11.

[113] Langdon, J., & Manthiram, A. (2021). A perspective on single-crystal layered oxide cathodes for lithium-ion batteries. *Energy Storage Materials*.

[114] Herzog, M. J., Gauquelin, N., Esken, D., Verbeeck, J., & Janek, J. (2021). Facile Dry Coating Method of High-Nickel Cathode Material by Nanostructured Fumed Alumina (Al2O3) Improving the Performance of Lithium-Ion Batteries. Energy Technology, 9(4), 2100028.

[115] Sarkar, A., Ghosh, M., & Sil, P. C. (2014). Nanotoxicity: oxidative stress mediated toxicity of metal and metal oxide nanoparticles. Journal of nanoscience and nanotechnology, 14(1), 730-743.

Chapter 2. Effects of Extended Aqueous Processing on Structure, Chemistry, and Performance of Polycrystalline LiNixMnyCozO2 Cathode Powders

Luqman Azhari[1], Xiangyu Zhou[1], Bryer Sousa[1], Zhenzhen Yang[2], Guanhui Gao[3], Yan Wang[*]

1 Department of Materials Science and Engineering, Worcester Polytechnic Institute, 100 Institute Road, Worcester, MA, 01609, USA

2 Chemical Science and Engineering Division, Argonne National Laboratory, 9700 S. Cass Avenue, Lemont, Illinois 60439, United States

3 Rice Electron Microscopy Center, Rice University, 6100 Main Street, Houston, Texas, USA 77005

Published as: Azhari, L., Zhou, X., Sousa, B., Yang, Z., Gao, G., & Wang, Y. (2020). Effects of Extended Aqueous Processing on Structure, Chemistry, and Performance of Polycrystalline LiNi x Mn y Co z O2 Cathode Powders. ACS Applied Materials & Interfaces, 12(52), 57963-57974.

The prospect of aqueous processing of $LiNi_xMn_yCo_zO_2$ (NMC) cathodes has significant appeal to battery manufacturers for the reduction in materials cost, toxicological risk, and environmental impact compared to conventional NMP based processing. However, the effects of aqueous processing of NMC powders at industrial timescales are not well studied, with prior studies mostly focusing on relatively brief water washing processes. In this work, we investigate the bulk and surface impacts of extended aqueous processing of polycrystalline NMC powders with different compositions. We demonstrate that at timescales of several hours, polycrystalline NMC is susceptible to intergranular fracture, with the severity of fracture scaling with the NMC nickel

content. While bulk crystallinity and composition are unchanged, surface sensitive techniques such as x-ray photoelectron spectroscopy (XPS) and transmission electron microscopy (TEM) indicate that the exposure of water leads to a level of delithiation, nickel reduction, and reconstruction from the layered to rock-salt structure at the surface of individual grains. Dynamic single NMC microparticle compression testing suggests that the resulting mechanical stresses weaken the integrity of the polycrystalline particle and increases susceptibility of intergranular fracture. The initially degraded surfaces along with the increased surface area leads to faster capacity fade and impedance growth during electrochemical cycling. From this work, it is demonstrated that NMC powders require surface or grain boundary modifications in order to make industrial-scale aqueous cathode processing viable, especially for next generation nickel-rich NMC chemistries.

2.1 Introduction

Li-ion batteries are widely used across the world as an integral part of life, powering many of our common electronics. While the market share for Li-ion batteries has continued to steadily grow for the past several years, projections indicate a sharp rise in Li-ion battery demand and utilization as new applications, such as electric vehicles, continue to be adopted [1,2]. With the ever-increasing production needed from battery manufacturers, any reduction in processing or materials costs can be significant. One significant alternative being considered is the aqueous processing of $LiNi_xMn_yCo_{1-x-y}O_2$ (NMC) slurries for cathode fabrication. Due to the insolubility of conventional polyvinylidene fluoride (PVDF) binder in water, cathode slurry processing typically involves the use of organic solvents, mainly N-methyl-2-pyrrolidone, which is often abbreviated as NMP [3,4]. However, NMP is relatively expensive at a price of ~ \$1.25 L^{-1} and

typically requires additional costs for solvent recovery during electrode drying processes [3-5]. In addition, there are serious toxicological, environmental, and health hazards associated with NMP [5,6]. Therefore, there are strong incentives surrounding the replacement of NMP with safer and cheaper water-based solvents. Accordingly, several studies have been performed concerning water-based binders, such as carboxymethyl cellulose (CMC), among other polymeric compounds for cathode applications [7-10].

However, there are concerns surrounding the potentially deleterious effects of water processing on typical NMC cathode materials. Previous studies have shown that increasing the stoichiometric proportion of Ni in NMC cathodes can make the material more susceptible to surface initiated degradation in humid air environments, demonstrating the negative effects of moisture for NMC materials in which $x > 0.5$ [11,12]. Specifically, it is suggested that H_2O and CO_2 in air can be adsorbed onto the NMC surface and interact with nickel and lithium ions to form a surface layer of nickel and lithium carbonates and hydroxides that contributes to high impedance, reduces average discharge voltage, and causes off gassing and swelling of the cell from decomposition during electrochemical operation [11,12]. While NMC compositions with higher Mn contents are observed to be more resistant to this form of degradation, current cathode development is trending towards Ni-rich compositions due to the lower materials costs associated with the increased use of Ni over Co, and the higher specific capacities near 200 mAh/g observed with Ni-rich cathodes [13-15].

In addition to the effects of ambient and humid air exposure on NMC, there are several studies focused on water washing processes on NMC material or aqueous slurry processing at the lab

scale, where moderate improvements towards capacity retention is observed due to removal of lithium residual species at the expense of some initial capacity [16-21]. However, since industrial slurry mixing and electrode drying processes typically take several hours or even days depending on the processing equipment [22-25], it is important to focus on the effects of NMC immersion in water at industrial timescales rather than preliminary lab-based conditions in which mixing times can be on the scale of minutes. One such study demonstrated that stirring NMC532 in distilled water for an hour led to increased cation mixing in the surface layer and the formation of lithium compounds from lithium leached from the NMC surface, thus severely impairing electrochemical performance [26]. It has also been demonstrated that NMC-water interactions can be influenced by the pH of the solution, with ion-exchange mechanisms occurring at high pH, and dissolution at lower pH [20]. However, another study concluded that aqueous slurry processing appears to not have major effects on NMC811 bulk material nor its electrochemical performance in pouch cells, with only slight changes to the surface [27].

In this work, we further explore the effects of water immersion on polycrystalline NMC powders of various compositions. Under different conditions for water immersion, the cathode powders are studied for changes in surface and bulk chemistry, crystallinity, mechanical behavior, and morphology. By utilizing different surface and bulk characterization techniques, we demonstrate that at industrial timescales of 6-24 hrs, immersing polycrystalline NMC into deionized water will degrade the particle surfaces and weaken the integrity of the secondary particles at the grain boundaries, leading to intergranular fracturing into smaller agglomerates or even individual primary particles when subjected to mechanical agitation such as stirring. Surface chemistry and crystallinity is severely compromised by surface Li leaching, reduction of Ni, and the formation

of a rock-salt layer, leading to decreased reversible capacity and impedance growth during galvanostatic charge/discharge cycling. This work provides valuable insights into the limitations of commercial-scale aqueous cathode processing, and demonstrates that in order to achieve successful aqueous processing of Ni-rich NMC, significant modifications to the NMC material are required in order to prevent fracturing of the secondary particle, preserve surface integrity, and maintain adequate electrochemical performance.

2.2 Materials and Methods

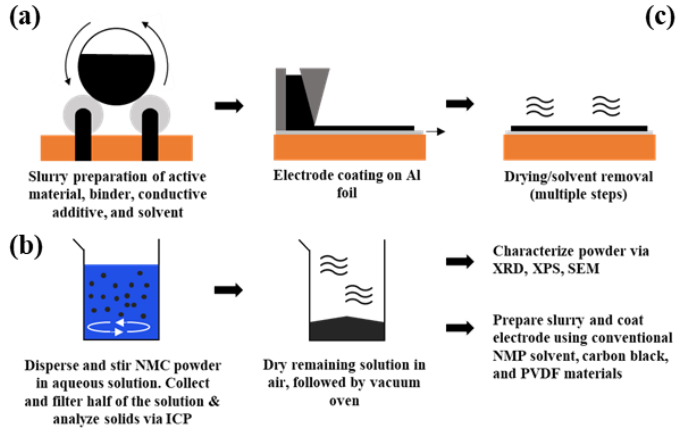

(c)

Sample #	NMC Type	Solids Loading	Stir speed (RPM)	Exposure time (hrs)	Solution
1	NMC111	N/A	N/A	0	N/A
2	NMC622	N/A	N/A	0	N/A
3	NMC811	N/A	N/A	0	N/A
4	NMC111	10%	500	1	DI Water
5	NMC622	10%	500	1	DI Water
6	NMC811	10%	500	1	DI Water
7	NMC111	10%	500	6	DI Water
8	NMC622	10%	500	6	DI Water
9	NMC811	10%	500	6	DI Water
10	NMC111	10%	500	24	DI Water
11	NMC622	10%	500	24	DI Water
12	NMC811	10%	500	24	DI Water
13	NMC811	10%	0	24	DI Water
14	NMC811	10%	1000	24	DI Water
15	NMC811	50%	500	24	DI Water
16	NMC811	10%	500	24	Ethanol

Figure 7: (a) Schematic of typical industrial cathode fabrication steps. (b) Experimental design, imitating equivalent steps of an industrial process while isolating the active material for characterization methods. (c) Summary of experiments and parameters.

$LiNi_{0.33}Mn_{0.33}Co_{0.33}O_2$ (NMC111), $LiNi_{0.60}Mn_{0.20}Co_{0.20}O_2$ (NMC622), and $LiNi_{0.80}Mn_{0.10}Co_{0.10}O_2$ (NMC811) powders were obtained from commercial suppliers (BASF, Targray) and are used as received. Each powder in its pristine state was characterized through inductively coupled plasma optical emission spectrometry (ICP-OES), scanning electron microscopy (SEM), energy

dispersive x-ray spectroscopy (EDS), powder x-ray diffraction (XRD), and various electrochemical methods to establish a baseline for composition, structure, crystallinity, and electrochemical performance. To test the effects of water on the various NMC powders, a predetermined amount of powder was dispersed in 10 mL of deionized water within a 50 mL beaker and stirred at a fixed RPM for a predetermined length of time. The level of solids loading was typically set to 1 g/10mL to allow for an excess of water to exacerbate the water-NMC interaction. One sample was tested at a solids loading of 50% to represent a ratio closer to realistic slurry compositions. The level of stirring/agitation was set to either 0 RPM, 500 RPM, or 1000 RPM, and the time of agitation was set to 0hrs, 1hrs, 6hrs, or 24hrs, which represent reasonable times scales for industrial cathode slurry processing [22-25]. Due to the clear influence of Ni content on the results observed in the initial experiments, more focus was placed on NMC111 and NMC811, as they represented low and high levels of nickel content, with the behavior of NMC622 exhibiting characteristics in between that of NMC111 and NMC811. The different parameters and experiments conducted on each of the NMC cathode types considered are summarized in the table in **Figure 7c**.

After stirring for a given set of time, the suspension was split into two samples where half of the suspension was collected and within this half, the solids and solution were separated through vacuum filtration. The filtered solids were collected and analyzed via ICP-OES to determine the composition of the NMC solids and the degree of metal ion leaching into solution achieved based on the given experimental parameters. The other half of the suspension was left to dry in air at 80°C until the water has evaporated, followed by further drying overnight in a vacuum oven at 80°C to remove all residual water. This was conducted to allow the solvent present in the

slurry to dry in contact with the NMC powder, so that any potential precipitates from the solvent would remain in the slurry or on the NMC surface [23]. This would be representative of the NMC environment processed in a typical slurry coating process (**Figure 7a**). However, in this work, aqueous based binders and additives, such as CMC and carbon black, were not included in the aqueous processing step in order to isolate the explicit NMC-water interaction behaviors. After drying, the resulting cathode powder was gently ground to remove agglomerates, followed by XRD, SEM, and electrochemical characterization. Select samples were further analyzed via x-ray photoelectron spectroscopy (XPS). A schematic of the experimental process is detailed in **Figure 7b.**

To test the electrochemical performance, all tested samples were mixed with Super C65 carbon black and PVDF binder dissolved in NMP (6 wt%). The mass ratio of active material to conductive carbon and PVDF is 8:1:1, respectively. Conventional solvents and binders were chosen over their aqueous counterparts to avoid potential corrosion of the current collector due to slurry alkalinity [24, 28-30]. In addition, water-soluble binders can have different binder coverage properties than PVDF, which can affect electrochemical performance [31]. Therefore, the selection of NMP and PVDF further focuses on the explicit and direct effects of water on NMC cathode powder properties. The slurry was cast onto 15 μm Al foil with a 150 μm doctor blade and dried in air at 60 °C for several hours until visibly dry, followed by further drying in a vacuum oven at 80 °C overnight to remove any residual solvent and possible moisture. Afterwards the resulting electrode was calendared to a total thickness of approximately 35-40 μm, punched into 14 mm discs, and assembled in an argon glovebox into 2032-coin cells with lithium metal as the anode, 1M $LiPF_6$ in EC/EMC 3:7 wt ratio as the electrolyte, and a Celgard

separator. Active mass loading for the cells tested were calculated to be in the range of 3.5-4.3 mg/cm^2. Cells were tested for rate performance and galvanostatic charge/discharge cycling in the range of 2.8-4.3 V. Cyclic voltammetry profiles and EIS spectra were obtained for cells after 0.05 C formation cycles and post 100 cycles at 0.5 C.

2.3 Characterization Methods

XRD profiles of the NMC precursor and sintered cathode were obtained using a PANalytical Empyrean X-ray Diffractometer and Cu Kα radiation source, using a step size of 0.017 °/step. Crystallographic lattice parameters and $I_{(003)}/I_{(104)}$ ratios were determined using the Rietveld refinement technique via FullProf Suite software. Surface and bulk morphology were examined using SEM and EDS analysis via a JEOL JSM-700F SEM at 10 kV accelerating voltage. High-resolution transmission electron microscopy (HRTEM), high angle annular dark-field imaging (HAADF), and EDS mapping were performed with a double correctors Titan cubed Themis 300 operated at 300 kV from the Electron Microscopy Center (EMC), equipped with a Ceta camera, Gatan Quantum 966 energy filter and an electron monochromator. Quantitative chemical compositions were determined through ICP-OES,using a Perkin-Elmer Optima ICP-OES 8000 instrument. XPS data was acquired using PHI 5000 VersaProbe II system (Physical Electronics) that attached to an argon-atmosphere glovebox to avoid any contamination of moisture and air. The individual scans at the Li 1s, O 1s, C 1s, Co 2p3, Mn 2p3, and Ni 2p3 peaks were collected at a pass energy of 23.50eV and electron escape angle of 45^o to the sample plane. The high-resolution spectra were used to examine surface oxidation states of specific elements on the particles. The spot size for X-ray beam was set to 100 μm. XPS survey scans collected at a pass energy of 117.4eV were utilized to determine surface atomic composition.

Electrochemical charge/discharge cycles were conducted on a LANDT CT2001A from 2.8-4.3 V at a C-Rate of C/2 at room temperature. High C-rate capacity was tested using an Arbin Battery tester under a voltage range of 2.8-4.3 V at 0.1 C, 0.2 C, 0.5 C, 1 C, 2 C, 3 C, and 5 C. Cyclic voltammetry (CV) profiles and electrochemical impedance spectra (EIS) were obtained using a Bio-logic VMP3 multi-channel Potentiostat maintained at 25 °C ± 1 °C. CV and EIS data were obtained for cells before and after 100 galvanostatic charge/discharge cycles at 0.5 C. CV profiles were obtained at scan rates of 0.1 mV/s, 0.2 mV/s, 0.5 mV/s, and 1 mV/s from 2.8-4.3 V. EIS was obtained by holding cells to a desired voltage for 2 hours before application of a 10 mV sinusoidal amplitude from a frequency range of 1 Mhz to 20 mHz. Before testing, all coin cells were subjected to two initial formation cycles at a rate of 0.05 C from 2.8-4.3 V.

Load-compression curves were obtained with a modified dynamic single particle compression testing protocol originally developed by Nanomechanics, Inc. (Oak Ride, TN, USA) with a maximum applied load of 50 mN [32, 33]. The methodology was employed using an iMicro Pro with an InForce 1000 mN actuator and a 75-um diameter flat-punch diamond nanoindentation tip from Synton-MDP (Switzerland). To inspect and compare the dynamic mechanical behavior of pristine and water immersed NMC811 powders, secondary particles of similar diameters were targeted during single particle compression testing. Prior to compression, the NMC811 powders were mechanically dispersed upon a flat plate of fused Si glass. Outliers were removed from the data which occurred when the microscope-to-indenter coordinates were misaligned.

2.4 Results and Discussion

2.4.1 Bulk Morphology, Structure, and Chemistry

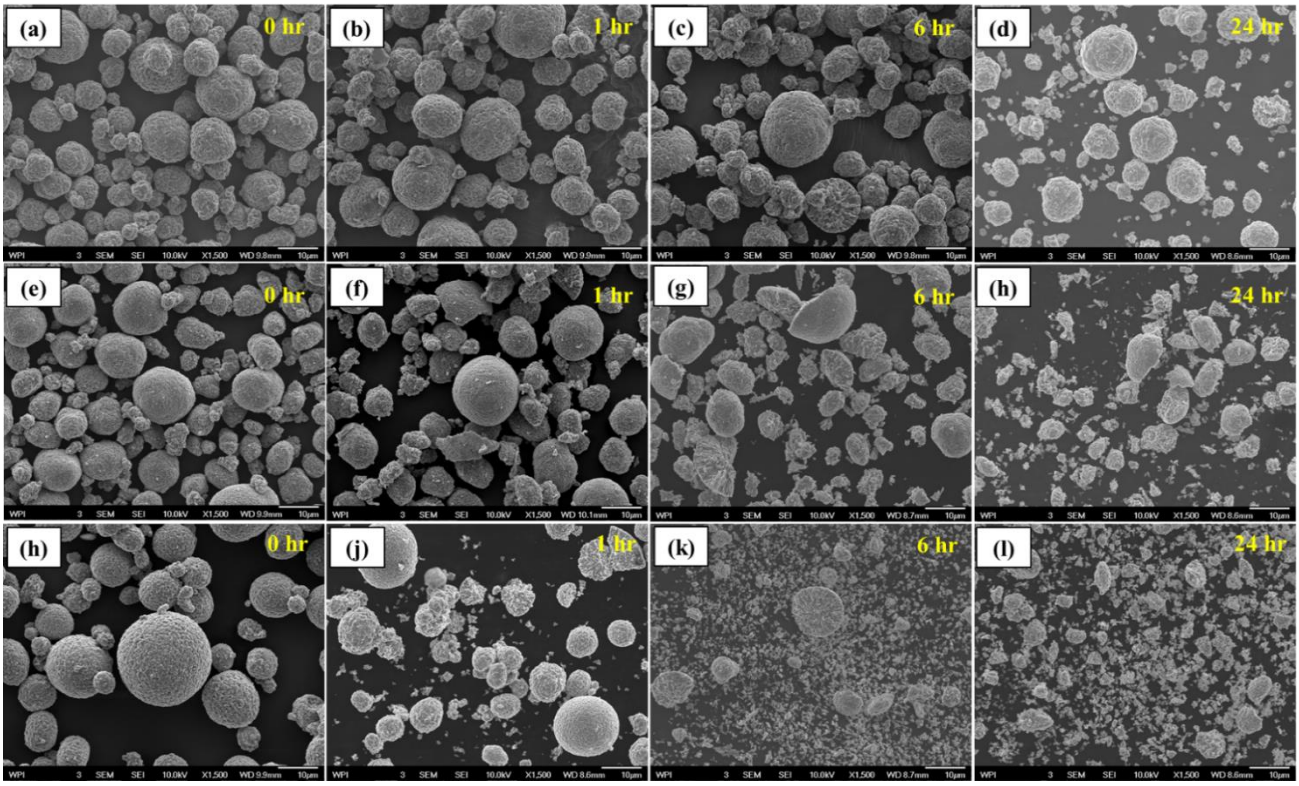

Figure 8: SEM images of commercially obtained powders of (a-d) NMC111, (e-h) NMC622, and (h-l) NMC811 after stirring in water at 500rpm at room temperature for 0, 1, 6, and 24hrs. Images correspond to samples 1-12 in the table in Figure 1c. All images were taken at the same magnification.

SEM images shown in **Figure 8** reveal a significant correlation between nickel content and the time of agitation. In the pristine, as-received state, all powders were observed to be polycrystalline, consisting mostly of spherical secondary particles ~10 µm in diameter, with some smaller secondary particles ~2 µm as well. The secondary particles themselves were composed of elongated block-like primary particles sub-micron in size. As agitation time increased from 1 hr to 24 hrs, it was generally observed that the NMC secondary particles cracked and broke apart into smaller irregular agglomerates or even into individual primary

particles. For NMC compositions with higher Ni content, the severity of secondary particle cracking increases; NMC111, shown in **Figure 8a-d**, displayed very little fracturing at timescales $\leqslant$ 6 hrs. Even at 24 hrs, most of the secondary particles remained intact. NMC811, however, was already extensively fractured after 6 hrs, with significant amounts of individual primary particles having separated from the secondary particle structure. This is supported by particle size analysis in **Figures S1b, d**, where NMC811 showed significant reduction in the d50 size at the 24 hr mark and significant shift in the particle size distribution. While the d50 for NMC111 decreased moderately at 24hrs, it is worth noting the existence of a small peak ~2 µm in the particle size distribution and a sharp decrease in the d5 value (**Figures S1a, c)**. NMC622 displayed a level of fracture in between NMC111 and NMC811, which is expected due to the intermediate level of nickel content and correlation between nickel content and severity of fracture. Increasing the agitation rate from 500 rpm to 1000 rpm expectedly led to even higher levels of fracture, as shown in **Figure S2**. The increased surface area from fracturing is expected to exacerbate surface-initiated reactions during storage, electrode drying, and during electrochemical cycling.

As the only significant difference between the powders was the NMC composition, the degree of cracking was attributed to the Ni rich compositions having increased surface reactivity; existing literature has shown that increasing the nickel content in NMC leads to higher surface reactivity and more susceptibility to degradation in humid environments, such as by delithiation at the surface of the NMC and subsequent formation of lithium compounds such as LiOH and Li_2CO_3 on the surface [11,34-36]. It has also been reported that Ni^{3+} at the surface is prone to reduction and subsequent loss of active lattice oxygen, leading to surface-initiated phase transformations from

the layered R-3m phase to cubic rock-salt Fd3m phase [11, 36]. These degradation mechanisms observed in ambient or humid air are thought to be driven predominantly by NMC-water vapor interactions rather than NMC-CO_2 interactions [36]. Compared to ambient air, aqueous processing intensifies these mechanisms, with the resulting mechanical stresses residing primarily at surfaces and grain boundaries and weakening the integrity of the secondary particle, with increasing Ni content further exacerbating this phenomenon.

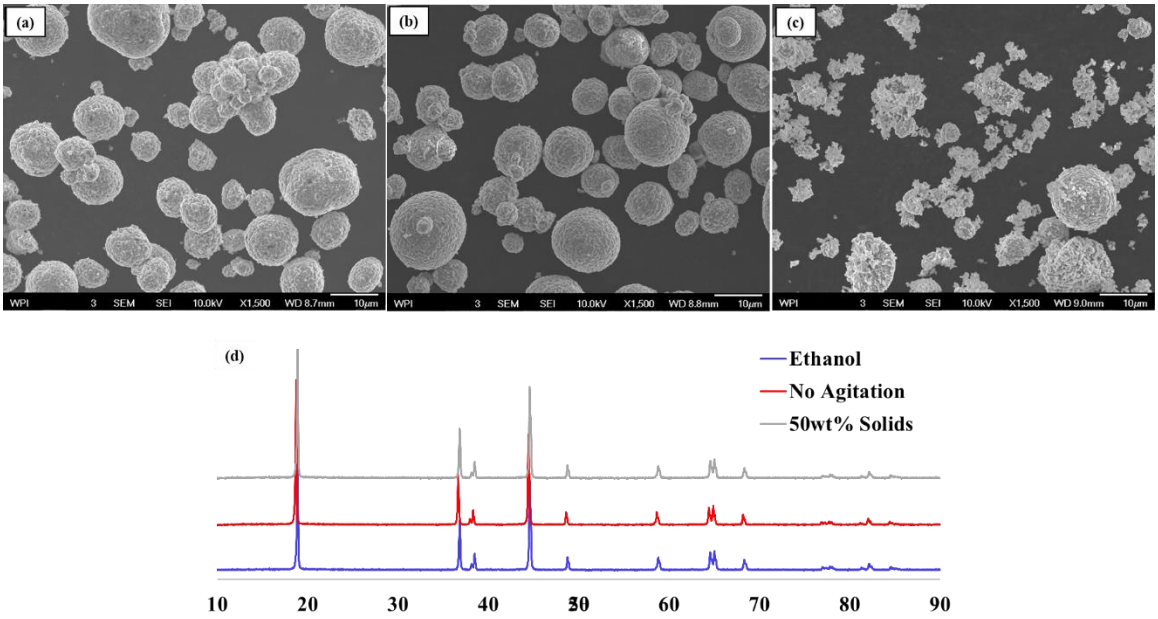

Figure 9: SEM images of NMC811 (a) dispersed for 24 hours in ethanol with agitation of 500rpm, (b) immersed in DI water without agitation, and (c) dispersed in DI water with agitation at 500rpm at a solids loading of 50wt%. (d) XRD profiles of the corresponding powders shown in the SEM images (obtained via Cu Kα X-ray source).

Figure 9 represents experiments 14,17, and 18 in the table of **Figure 7**, focused on isolating the differences of water exposure, mechanical agitation, and solids content. NMC811 was selected for these experiments due to its increased sensitivity to aqueous processing as observed in **Figures 8, S1, and S2**. NMC811 was either immersed into water without mechanical agitation,

dispersed into ethanol with agitation, or dispersed into water with agitation at a solids loading closer to typical slurry compositions. Ethanol is nonreactive towards NMC compounds, having been demonstrated in prior studies to wash away LiOH & Li_2O residue to an extent without destroying the bulk and surface morphology of NCA particles [37]. It was observed that despite the same duration and level of agitation conducted in **Figure 8l**, there was no significant fracturing of the secondary particles in **Figure 9a**, and the powder appeared identical to that of pristine NMC811 under SEM imaging and particle size analysis in **Figure S3**. The nonreactive solvents such as ethanol or NMP would not cause reduction of surface Ni species, delithiation of the surface, nor the subsequent surface phase transformations that could weaken the mechanical integrity of the secondary particle, allowing the secondary particles to remain intact under mechanical agitation.

Lack of intergranular fracture was also observed in NMC811 when immersed in water for 24 hrs without agitation, shown in **Figure 8b.** It appears that the high levels of intergranular fracture of the secondary particle only occurs from a combination of water immersion and mechanical agitation. Even with exposure to water, without a certain level of shear stress from agitation, the depth of degradation remained limited to the surface primary particles and particle size distributions are not impacted. This is analogous to NMC which degrades from exposure to ambient air; surface primary particles may degrade based on the aforementioned mechanisms but are unable to break off and expose new surfaces and grain boundaries to further degradation. However, it would be difficult to avoid intergranular fracture in a traditional slurry making process utilizing aqueous solvent as NMC, water, and other additives would typically be placed on a high-speed mixer or planetary mill on the timescale of several hours. This is represented by

Figure 8c, where under 50wt% solids loading, aqueous processing for 24 hrs with agitation still caused severe levels of intergranular fracturing, significantly affecting the particle size distribution, shown in **Figure S3.** In practice, nickel-rich powders processed with conventional industrial slurry mixing methods may appear closer to those in **Figure 8j-l**.

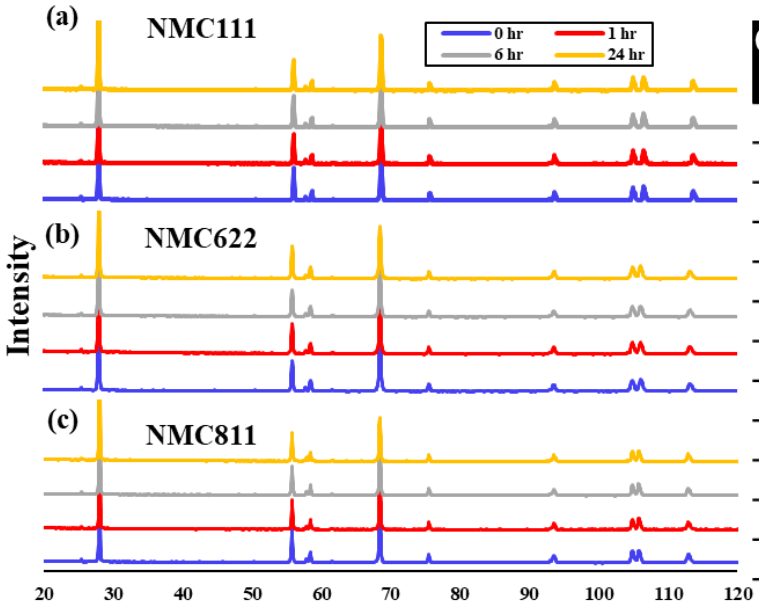

(d)

Sample #	FWHM (104)	I(003) / I(104)	*a*, *b* (Å)	*c* (Å)
NMC111-0hrs	0.249	1.390	2.859	14.231
NMC111-1hrs	0.244	1.430	2.859	14.233
NMC111-6hrs	0.246	1.407	2.860	14.230
NMC111-24hrs	0.250	1.406	2.860	14.229
NMC622-0hrs	0.334	1.386	2.868	14.218
NMC622-1hrs	0.309	1.406	2.867	14.216
NMC622-6hrs	0.314	1.470	2.867	14.215
NMC622-24hrs	0.313	1.370	2.867	14.217
NMC811-0hrs	0.281	1.427	2.871	14.207
NMC811-1hrs	0.263	1.474	2.872	14.202
NMC811-6hrs	0.265	1.579	2.872	14.201
NMC811-24hrs	0.260	1.612	2.872	14.201

Figure 10: XRD profiles of (a) NMC111, (b) NMC622, and (c) NMC811 in the pristine state and after 1, 6, and 24hrs of stirring in water (obtained via Cr Kα X-ray source). (d) FWHMs of the (104) peaks for each condition, along with characteristic $I_{(003)}/I_{(104)}$ ratio and refined lattice parameters.

From the XRD profiles shown in **Figures 10a-c**, no major changes in bulk crystallinity nor the appearance of secondary phases were observed. All NMC samples stirred in DI water appear comparable to their pristine counterpart, with similar quality of peak splitting. Utilizing Fullprof Suite software and the Rietveld Refinement method, we also observed no change in several key parameters, summarized in the table in **Figure 10d**. FWHMs taken from the (104) peaks across all samples are similar, indicating negligible change in the mean coherence length as per Scherrer's equation [38,39]. The mean coherence length is assumed to be on the order of a primary

particle diameter; therefore, we confirm that fracturing is indeed intergranular rather than intragranular. $I_{(003)}/I_{(104)}$ ratios, which are usually seen as a gauge on the degree of cation mixing [40,41], also remained above 1.2 for each NMC sample, indicating low levels of cation mixing regardless of immersion time. For NMC811, the increase in this ratio with exposure time was attributed to the breaking and packing of the anisotropic primary particles resulting in favored orientation during XRD sample preparation. Lastly, there was no change or correlation between immersion time and the lattice parameters, further indicating that water immersion has negligible impact on the bulk crystallinity regardless of nickel content, and effects are localized to the surface of the NMC particles.

Table 1: ICP-OES analysis of NMC samples' stoichiometry, calculated by adjusting the analyzed molar fractions based on $LiMO_2$, where M = Ni + Mn + Co = 1

Sample #	Li	Ni	Mn	Co
NMC111-0hrs	1.069	0.338	0.342	0.319
NMC111-1hrs	1.017	0.348	0.320	0.332
NMC111-6hrs	1.033	0.345	0.323	0.332
NMC111-24hrs	1.029	0.346	0.323	0.331
NMC622-0hrs	0.997	0.619	0.192	0.190
NMC622-1hrs	0.956	0.613	0.193	0.193
NMC622-6hrs	0.960	0.614	0.197	0.189
NMC622-24hrs	0.943	0.619	0.192	0.189
NMC811-0hrs	1.064	0.806	0.098	0.095
NMC811-1hrs	0.964	0.810	0.095	0.095
NMC811-6hrs	0.972	0.810	0.094	0.096
NMC811-24hrs	0.978	0.810	0.095	0.095

ICP-OES analysis of the aqueous processed powders in **Table 1** (after solvent removal via filtration) revealed no noticeable correlation between NMC composition and time of water exposure. However, there was an observed drop in the lithium content from the pristine sample

to the water-processed samples. This observation is attributed to residual lithium compounds that remain on the surface of the NMC after traditional lithiation and sintering processes and/or initial passivation reactions with ambient environment. The presence of lithium compounds is well documented and are comprised mostly of soluble lithium hydroxides and lithium carbonates [11,13,27]. Under water exposure, these soluble compounds were quickly dissolved in the solvent, leading to the sudden drop in Li content observed in the ICP data. This is also demonstrated in previous works that observe an immediate rise in pH value upon dispersion into water, correlated to the dissolving of lithium compounds [18,19,27]. Although there were no changes to the bulk composition, chemical changes such as delithiation and small levels of TM dissolution occur at the surface at levels not discernable through ICP-OES, requiring surface sensitive techniques [24], described in the next section.

2.4.2 Surface Morphology, Structure, and Chemistry

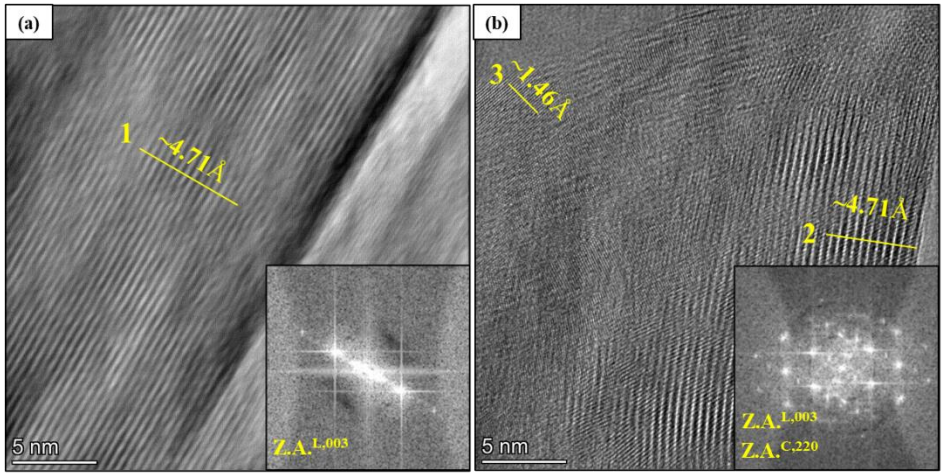

Figure 11: TEM images of (a) NMC811 dispersed in ethanol for 24hrs at 500rpm, (b) NMC811 immersed for 24hrs in DI water without agitation. Line profiles indicate lattice spacings measured in the corresponding region. Insets represent FFT patterns of the corresponding HRTEM image, relating to either the layered "L" or cubic "C" structures.

The TEM images shown in **Figure 11** reveal the significant impact of water immersion on the surface morphology of NMC. The sample dispersed in ethanol [**Figure 11a**] maintained its original crystallinity as expected, with the layered structure intact at the surface and subsurface of a primary particle. FFT patterns in the inset, along with a measured planar spacing ~4.71 Å, matched well with the (003) zone axis of the R-3m hexagonal structure of NMC811. This was expected when considering the nonreactivity of ethanol on the NMC material. In addition, negligible amounts of amorphous lithium residual compounds at the surface were observed, which are typically seen in NMC samples to some degree. This was attributed to the partial solubility of lithium hydroxide in ethanol, with the washing process able to remove this layer with some effectiveness without damaging the underlying structure [37].

In contrast, the samples immersed in water without agitation [**Figure 11b]** suffered a significant amount of degradation at the surface and sub-surface of a primary particle in the form of localized surface reconstruction. The HRTEM image revealed several nano-sized domains within the same primary particle, exhibiting multiple lattice spacings and directions in contrast to the overall layered phase that the NMC sample originally displayed. Line 2 in **Figure 10b** has a lattice spacing ~4.71 Å, matching well with the original R-3m hexagonal structure of NMC811 at the (003) zone axis. However, line 3 reveals a much tighter planar packing of 1.46 Å in one of the nano-sized domains observed throughout the primary particle. This lattice spacing closely matches the planar spacing of the cubic rick-salt NiO phase when viewed from the (220) zone axis, and the FFT patten in the inset shows the existence of multiple phases. This surface reconstruction is proposed to be caused by the reactivity of surface nickel, which has been demonstrated to undergo reduction from Ni^{3+} to Ni^{2+} in environments containing carbon dioxide

and/or water [41,42]. This consequently can facilitate the leaching of lithium into the aqueous solution, subsequent loss of lattice oxygen, and migration of surface nickel from the TM layer into the lithium layer due to the created lithium deficiency [41-45]. The result is the formation of cubic NiO at the surface/subsurface regions, with the overall suggested surface reaction for NMC811 represented by the following equation:

$$LiNi_{0.8}Mn_{0.1}Co_{0.1}O_{2\,(s)} + x/2\cdot H_2O_{\,(l)} \rightarrow$$

$$Li_{1-x}Ni_{0.8-x}Mn_{0.1}Co_{0.1}O_{2-2x\,(s)} + x\cdot NiO_{\,(s)} + x\cdot LiOH_{\,(aq)} + x/4\cdot O_{2\,(g)} \qquad (8)$$

Due to the high pH of the solution during processing, it is also proposed that surface reconstruction can alternatively occur via an H^+/Li^+ ion exchange mechanism at exposed NMC surfaces, which is documented in literature for various lithiated transition metal oxides [20]. This mechanism does not involve any dissolution of transition metals, and also results in the contraction of the layered structure in the (001) direction due to the presence of the smaller H^+ ion in the lithium layer [20]. This would also introduce a degree of mechanical strain at grain boundaries. Subsequent drying processes could initiate the loss of hydrogen and lattice oxygen as water vapor while initiating surface reconstruction to the cubic rocksalt phase. This degradation pathway is demonstrated by the following proposed equations for H^+/Li^+ exchange and thermal decomposition, respectively:

$$LiNi_{0.8}Mn_{0.1}Co_{0.1}O_{2\,(s)} + x\cdot H_2O_{\,(l)} \rightarrow Li_{1-x}H_xNi_{0.8}Mn_{0.1}Co_{0.1}O_{2\,(s)} + x\cdot LiOH_{\,(aq)} \qquad (9)$$

$$Li_{1-x}H_xNi_{0.8}Mn_{0.1}Co_{0.1}O_{2\,(s)} \rightarrow$$

$$Li_{1-x}Ni_{0.8-x}Mn_{0.1}Co_{0.1}O_{2-2x\,(s)} + x\cdot NiO + x/2\cdot H_2O_{\,(g)} + x/4\cdot O_{2\,(g)} \qquad (10)$$

While it is not confirmed which degradation mechanism dominates during the aqueous processing, the degradation observed appears to be only limited to the surface regions of the primary particles, as we have shown that bulk composition and crystallinity remains unchanged. These surface reconstructions induce a level of mechanical stress between primary particles at the grain boundaries, jeopardizing mechanical integrity and facilitating intergranular fracture when under shear stresses as observed in the SEM images in **Figure 8**.

Table 2: Surface composition of the NMC powders, calculated from the XPS survey scan.

Sample	Li 1s	C 1s	O 1s	Mn 2p3	Co 2p3	Ni 2p3
Pristine NMC811	25.22%	39.65%	32.94%	0.96%	0.07%	1.15%
24hr, DI water	14.43%	47.66%	27.79%	2.64%	1.27%	6.20%
24hr, Ethanol	17.68%	38.96%	35.44%	2.50%	1.33%	3.47%
24hr, No Agitation	8.74%	29.21%	44.41%	4.76%	0.99%	11.89%

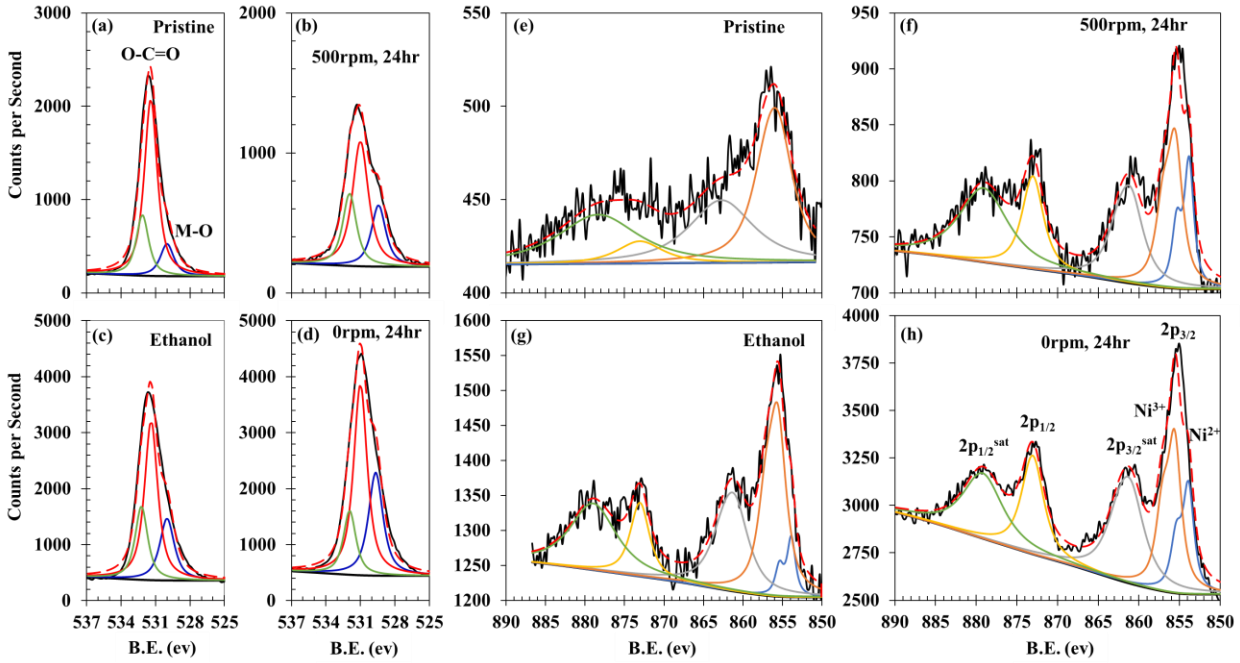

Figure 12: XPS spectra and fitted peaks of (a-d) oxygen 1s binding energies and (e-h) nickel $2p_{3/2}$ and $2p_{1/2}$ binding energies of (a, e) pristine NMC811, (b, f) NMC811 after dispersion for 24hrs in DI water, (c, g) NMC811 are dispersion for 24hrs in ethanol, and (d, h) NMC811 immersed in DI water without agitation. Peak labels for the oxygen 1s spectra and Ni 2p spectra are listed in (a) and (h), respectively. While the metal carbonate related peak at 531.5eV is prominent, this binding energy overlaps with several other chemical states.

XPS analysis of the oxygen 1s spectrum shown in **Figure 12a-d** reveals significant differences in the level of surface residue of pristine NMC811 and those treated by ethanol or DI water. In **Figure 12a**, pristine NMC811 has a weak peak ~530 eV, which is related to the metal oxide chemical state. The low relative intensity of this signal compared to the carbonate peak at ~531.5eV is attributed to the presence of a surface layer of LiOH and Li_2CO_3 that typically forms after NMC lithiation and exposure to ambient air [41-44,47]. Ethanol or water treated NMC811 in **Figures 12b-d** exhibited a much more prominent contribution of the metal oxide chemical state relative to the carbonate peak, indicative of the removal of the lithium residual layer to a degree. This is also supported by XPS spectra of the carbon peak (**Figure S4)** and the surface atomic

compositions determined by a survey scan, shown in **Table 2**, where the lithium content at the surface was the highest for pristine NMC811, and the transition metal content highest for the solution processed samples. It is notable that the sample immersed in DI water without agitation exhibited a lower amount of lithium compared to the sample stirred in DI water. This can be explained by the intergranular fracturing observed in agitated samples; fracturing allowed for delithiation to occur from newly exposed and fully lithiated surfaces, while under only immersion, lithium continued to leach out of mostly primary particles at the surface of the secondary particle. As a result, the sample immersed in DI water without agitation suffered greater surface delithiation and contained less overall lithium in the surface/subsurface compared to the sample stirred in DI water. It is also notable that the metal oxide signal increased, despite allowing the aqueous or ethanol solvents to dry within the same beaker. We attribute this to a level of segregation during solvent evaporation, where a portion of lithium salts precipitated on the beaker walls or segregated pieces rather than a uniform layer on the particle surfaces. In an industrial slurry coating process, this precipitate could cause issues with slurry alkalinity and corrosion of the aluminum current collector [28-30].

The nickel 2p spectra are shown in **Figures 12e-h**. For the pristine NMC811, the nickel peak intensity is relatively low, which is again correlated to the lithium residual layer reducing the signal intensity of the underlying NMC material. Although signal intensity is low, peak fitting indicates mostly Ni^{3+} character, which is expected for pristine NMC811 and evidenced by the dominant orange $2p_{3/2}$ peak at ~855.6 eV [46, 48]. In contrast, NMC811 samples exposed to DI water whether under agitation or only immersion (**Figure 12f, h)**, exhibited approximately 57% and 59% of Ni^{2+} character, respectively, by analyzing the integrated area contribution of the blue

$2p_{3/2}$ peak at ~853.9 eV [43,46]. The portion of reduced nickel due to water exposure is attributed to the formation of nickel carbonate species and rock-salt NiO from delithiation of the surface regions [11]. The NMC811 sample washed with ethanol shown in **Figure 2g** also displayed a portion of ~18% Ni^{2+} character- not nearly as high as those exposed to water. This is attributed to the formation of nickel carbonate species resulting from the washing away of the passivating lithium salt layer and exposure of fresh NMC811 surfaces to ambient air during drying processes, as observed in prior studies [11].

2.4.3 Electrochemical Performance

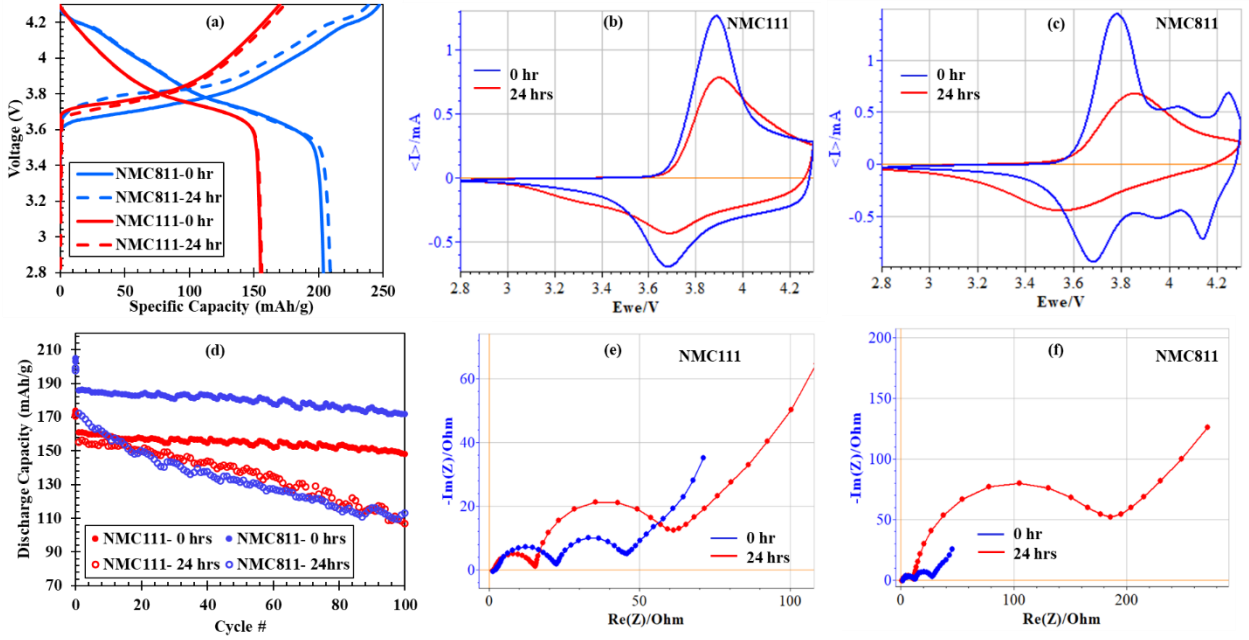

Figure 13: (a) First cycle charge and discharge curve of NMC111 and NMC811 in the initially pristine condition and after stirring in DI water for 24hrs. CV profiles of (b) NMC111 and (c) NMC811 in the initially pristine condition and after stirring in DI water, after 100 cycles. (d) Galvanostatic charge/discharge cycling from 2.8-4.3V at C/2 of NMC111 and NMC811 in the initially pristine condition and after stirring in DI water. EIS profiles of (e) NMC111 and (f) NMC811 in the initially pristine condition and after stirring in DI water, taken at 4.3V after 100 cycles.

Figure 13 summarizes the electrochemical performances of NMC111 and NMC811 in the pristine state and after 24hrs of water exposure with agitation. This represents two different extremes of water exposure and nickel content, with the expectation that NMC622 would exhibit performance characteristics in between NMC111 and NMC811. In the voltage-capacity curves for the first formation cycle in **Figure 13a**, initial charge and discharge capacities for NMC111 and NMC811 were similar between their pristine and water treated counterparts. In addition, the voltage curves do not appear to have any significant changes due to the water treatment. This is in line with other analysis, as we have shown that bulk composition and crystallinity were unaffected by the aqueous processing. As such, formation cycle charge/discharge curves would be expected to remain nearly identical.

However, under galvanostatic cycling in **Figure 13d**, water exposed samples suffered from lower initial cycling capacity and significantly enhanced capacity fade during cycling at a rate of 0.5 C. As expected, the degradation rate was much more severe for NMC811, with the water treated sample retaining only 66% of its original capacity after 100 cycles, compared to 92% for the pristine sample. NMC111 retained 69% and 92% of its original capacity for the water treated sample and pristine sample, respectively. The sharp capacity fade for water treated NMC811 is attributed to a combination of both the initially degraded surface and significantly increased surface area due to intergranular fracture, which exacerbated the well-known undesirable side reactions of Ni-rich NMC during electrochemical cycling [49-54]. The increased capacity fade for water treated NMC111 must also be attributed to surface level degradation, impacting the kinetics of lithium diffusion, and causing impedance growth over prolonged cycling.

In order to verify this, cyclic voltammetry profiles and impedance spectra were taken after 100 cycles at 0.5 C. CV profiles in **Figures 13b, c** reveal that the water treatment process led to a significant broadening and flattening of the main oxidation/reduction peaks for both NMC111 and NMC811. This likely indicates loss of active material as well as the growth of a resistive layer [56] and is supported by the impedance spectra in **Figures 13e, f**, which show a much larger second semicircle for the water treated samples. This second semicircle is usually attributed to charge-transfer resistance and can increase due to surface/subsurface reconstruction from the layered phase to the rock-salt cubic phase, which was observed in TEM and XPS analysis in pre-cycled NMC811, and may exhibit continued thickening during prolonged cycling [57, 58]. In addition, the larger surface areas of water-treated samples typically hasten any surface-initiated degradation mechanisms. This indicates that the observed capacity fade for water treated samples under prolonged cycling was due to the presence of a resistive rock-salt layer from surface delithiation during water treatment, which grows in thickness during cycling and leads to large impedance growth. Although NMC111 did not suffer the same degree of cracking as NMC811, it is believed that the NMC111 also became susceptible to surface reconstruction due to water exposure.

Electrochemical performances of NMC811 treated in ethanol, in water without agitation, and in water at 50 wt% solids loading, are shown in **Figure S5**. Both NMC811 samples exposed to water performed worse than those treated with ethanol. It is notably observed that NMC811 immersed in water without agitation exhibited the worst capacity fade of the three different processes, evidenced by an exceptionally higher charge transfer resistance and flattened cyclic voltammetry curve. We attribute this to a thicker surface reconstruction layer due to the deeper

initial level of delithiation of surface primary particles, as discussed by the XPS analysis from **Table 2** and **Figure 12**. Ethanol treated NMC811 is also found to perform worse than pristine NMC811. Based on the XPS Ni2p and C1s spectra revealing a degree of Ni^{2+} and carbonate character, respectively, this could be explained by the formation of new lithium and transition metal hydroxides and/or carbonates on the newly exposed surfaces during the drying process, which would contribute to the higher initial impedance and continued impedance growth [11].

2.4.4 Mechanical Behavior of Secondary Particles

Single particle compression was employed to evaluate and compare the mechanical integrity of pristine NMC811 powder with NMC811 powder immersed in DI water for 24 hours without agitation. NMC811 was chosen due to the increased sensitivity to aqueous processing compared to compositions with lower nickel fractions, as apparent in **Figures 8, S1, and S2**. The resulting load-compression curves obtained are shown in **Figure 14**. Ethanol treated samples were not tested, due to the focus of this work on aqueous processed NMC powders.

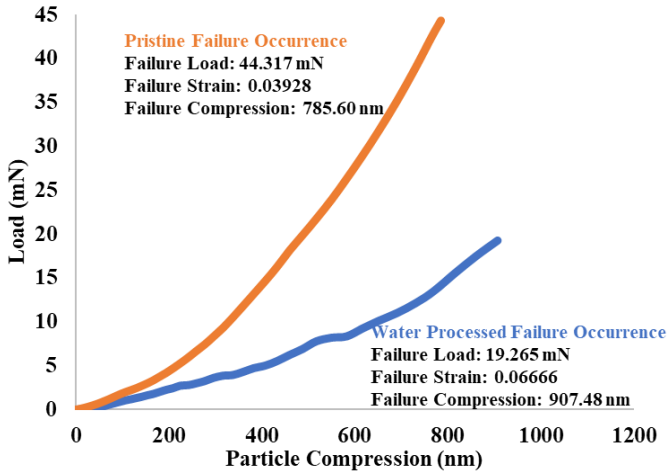

Figure 14: Load-compression curves obtained from dynamic single particle compression testing of secondary particles of pristine NMC811 secondary particles (orange) and DI water immersed NMC811 without agitation (blue). The average critical failure loads, critical failure strain and critical failure particle compression values are embedded within the figure.

It is demonstrated that critical failure of pristine NMC811 secondary particles occurred at an average compressive load of 44.317 mN, more than two times that of the same NMC811 powder processed via 24 hours of DI water immersion without agitation. Given the fact that particles were of similar diameters as shown in **Figure S3** or comparing **Figures 8h and 9b**, critical failure strains and critical failure compression measurements were comparable across the two NMC811 conditions. It is also shown that although the pristine NMC811 critically failed at a greater applied compressive force than DI water immersed NMC811, pristine NMC811 exhibited a lower critical failure strain and particle compression than DI water immersed NMC811. This is consistent with DI water immersed sample being more susceptible to plastic deformation, with reduced overall mechanical strength. Prior to performing single particle compression testing, NMC811 powder particles in the pristine state and immersed in DI water without agitation exhibited highly similar particle shape and size irrespective of their processed condition.

The surface degradation and subsurface reconstruction of primary particles in DI water immersed NMC811 demonstrated from HRTEM and XPS data in **Figures 11 and 12** are consistent with the reduced critical failure load measured in **Figure 14**. The level of surface delithiation of the DI water immersed samples [**Table 2**] may also impact the compressive strength of the secondary particles, with the Li concentration gradient from the bulk to the surface contributing to mismatch strain and generating stresses [58-60]. The weakened surface facilitates crack propagation into the "pristine" interior of the secondary particle by reducing the energy needed to initiate intergranular crack propagation within the brittle NMC particle. Similar mechanisms have been observed in NMC cathode in the deeply delithiated state within working electrochemical cells [59]. Overall, the data supports the hypothesis that surface-initiated reactions from NMC-water interactions induced deleterious mechanical stress formation between primary particles (i.e., grain boundaries), which compromised the mechanical integrity of the secondary particle and enabling intergranular failure at significantly lower loads than pristine NMC811.

2.5 Conclusion

Aqueous based processing of lithium-ion battery cathodes has garnered a fair share of interest, due to the potential for eliminating the use of toxic and costly NMP. However, as cathode chemistries strongly trend towards the utilization of Ni-rich NMC compositions, aqueous processing can be exceptionally harmful towards battery performance. In the work, it is shown that NMC exposure to water and agitation can lead severe levels of intergranular fracture, which scaled with the level of nickel in the NMC. At timescales similar to industrial slurry making techniques, this resulted in a significant increase in surface area, which upon exposure to water, further exacerbates surface-initiated reactions. These reactions include the removal of surface

lithium species such as lithium hydroxides, carbonates, and lattice lithium near the surface via leaching into the aqueous solvent. In addition, localized surface reconstruction is observed at the surface and subsurface, with nanosized domains of different structures such as cubic rock-salt phases within the layered host structure. These surface phase transformations combined with mechanical agitation are theorized to induce mechanical stress at the grain boundaries, compromising the mechanical integrity of the secondary particle. In addition, surface reconstruction negatively impacted electrochemical performance, as the resulting cathodes displayed fast capacity fade from enhanced impedance growth and polarization, presumably from the thickening of the surface rock-salt phase. Without agitation, Ni-rich NMC still suffered from deep levels of surface delithiation and reconstruction during water immersion, which also severely impacted electrochemical performance. Ethanol-based processing, while found to be nonreactive to the NMC compounds, can also negatively impact the NMC material due to the prolonged exposure of fresh NMC surfaces in ambient air during the drying timescales in typical industrial cathode processing.

To realize the potential of aqueous based NMC processing, it is vital to stabilize the NMC particle from surface-initiated degradation mechanisms and/or enhance the mechanical stability of the secondary particle. This can be achieved in a variety of ways, such as coatings, dopants, and/or grain boundary engineering. There have already been several approaches demonstrating that dopants such as aluminum can improve the mechanical integrity of secondary particles [61]. There have also been successful methods utilizing ALD and heat treatment processes to deposit lithium phosphate at grain boundaries [62], although in both cases, the resulting materials resistance to intergranular fracture was not explored in detail. Coatings, core shell structures, and

full gradient compositions may also be beneficial in mitigating water-related degradation by utilizing chemically stable outer surfaces such as Mn-rich NMC compositions or other metal oxides [63-65]. Additives within the slurry may also be of interest for further studies, as certain acid additives have been previously demonstrated to address current collector corrosion due to slurry alkalinity [66]. If this limitation can be remedied in a practical manner, aqueous based NMC slurry processing at the industrial level becomes one step closer to realization, opening new pathways towards cheaper and safer cathode manufacturing processes.

2.6 Supporting information

Particle size analysis for NMC samples after different levels of aqueous processing and other processing conditions, SEM image of NMC811 sample under higher stirring speeds, XPS survey scans, XPS C1s spectra, and electrochemical performance for NMC811 samples in the pristine condition, ethanol processed, water immersed without agitation, and at 50% solids loading.

2.7 Acknowledgement

We thank Qing Yin at Battery Resourcers, 54 Rockdale St, Worcester, MA, 01606, USA, for collecting the particle size analysis data used in this work

2.8 References

[1] Richa, K., Babbitt, C. W., Gaustad, G., & Wang, X. (2014). A future perspective on lithium-ion battery waste flows from electric vehicles. *Resources, Conservation and Recycling*, *83*, 63-76.

[2] Nykvist, B., & Nilsson, M. (2015). Rapidly falling costs of battery packs for electric vehicles. *Nature climate change*, *5*(4), 329-332.

[3] Zhang, Z., Zeng, T., Lai, Y., Jia, M., & Li, J. (2014). A comparative study of different binders and their effects on electrochemical properties of LiMn2O4 cathode in lithium ion batteries. *Journal of Power Sources*, *247*, 1-8.

[4] Wood III, D. L., Li, J., & Daniel, C. (2015). Prospects for reducing the processing cost of lithium ion batteries. *Journal of Power Sources*, *275*, 234-242.

[5] Lee, K. P., Chromey, N. C., Culik, R., Barnes, J. R., & Schneider, P. W. (1987). Toxicity of N-methyl-2-pyrrolidone (NMP): teratogenic, subchronic, and two-year inhalation studies. *Fundamental and Applied Toxicology*, *9*(2), 222-235.

[6] Keener, S. A., Wrbitzky, R., & Bader, M. (2007). Human volunteer study on the influence of exposure duration and dilution of dermally applied N-methyl-2-pyrrolidone (NMP) on the urinary elimination of NMP metabolites. *International archives of occupational and environmental health*, *80*(4), 327-334.

[7] Xu, J., Chou, S. L., Gu, Q. F., Liu, H. K., & Dou, S. X. (2013). The effect of different binders on electrochemical properties of LiNi1/3Mn1/3Co1/3O2 cathode material in lithium ion batteries. *Journal of Power Sources*, *225*, 172-178.

[8] Kazzazi, A., Bresser, D., Birrozzi, A., von Zamory, J., Hekmatfar, M., & Passerini, S. (2018). Comparative analysis of aqueous binders for high-energy li-rich NMC as a Lithium-Ion cathode and the impact of adding phosphoric acid. *ACS applied materials & interfaces*, *10*(20), 17214-17222.

[9] Li, C. C., & Wang, Y. W. (2013). Importance of binder compositions to the dispersion and electrochemical properties of water-based LiCoO2 cathodes. *Journal of power sources*, *227*, 204-210.

[10] Wang, Z., Dupre, N., Gaillot, A. C., Lestriez, B., Martin, J. F., Daniel, L., ... & Guyomard, D. (2012). CMC as a binder in LiNi0. 4Mn1. 6O4 5 V cathodes and their electrochemical performance for Li-ion batteries. *Electrochimica acta*, *62*, 77-83.

[11] Jung, R., Morasch, R., Karayaylali, P., Phillips, K., Maglia, F., Stinner, C., ... & Gasteiger, H. A. (2018). Effect of ambient storage on the degradation of Ni-rich positive electrode materials (NMC811) for Li-ion batteries. *Journal of The Electrochemical Society*, *165*(2), A132-A141.

[12] Doo, S. W., Lee, S., Kim, H., Choi, J. H., & Lee, K. T. (2019). Hydrophobic Ni-rich layered oxides as cathode materials for lithium-ion batteries. *ACS Applied Energy Materials*, *2*(9), 6246-6253.

[13] Zhao, J., Wang, Z., Wang, J., Guo, H., Li, X., Yan, G., ... & Chen, N. (2018). The role of a MnO2 functional layer on the surface of Ni-rich cathode materials: towards enhanced chemical stability on exposure to air. *Ceramics International*, *44*(11), 13341-13348.

[14] Manthiram, A., Knight, J. C., Myung, S. T., Oh, S. M., & Sun, Y. K. (2016). Nickel-rich and lithium-rich layered oxide cathodes: progress and perspectives. *Advanced Energy Materials*, *6*(1), 1501010.

[15] Kim, J., Lee, H., Cha, H., Yoon, M., Park, M., & Cho, J. (2018). Prospect and Reality of Ni-Rich Cathode for Commercialization. *Advanced Energy Materials*, *8*(6), 1702028.

[16] Xiong, X., Wang, Z., Yue, P., Guo, H., Wu, F., Wang, J., & Li, X. (2013). Washing effects on electrochemical performance and storage characteristics of LiNi0. 8Co0. 1Mn0. 1O2 as cathode material for lithium-ion batteries. *Journal of power sources*, *222*, 318-325.

[17] Kim, J., Hong, Y., Ryu, K. S., Kim, M. G., & Cho, J. (2005). Washing effect of a LiNi0. 83Co0. 15Al0. 02O2 cathode in water. *Electrochemical and Solid State Letters*, *9*(1), A19-A23.

[18] Loeffler, N., Kopel, T., Kim, G. T., & Passerini, S. (2015). Polyurethane binder for aqueous processing of Li-ion battery electrodes. *Journal of the Electrochemical Society*, *162*(14), A2692-A2698.

[19] Doberdò, I., Löffler, N., Laszczynski, N., Cericola, D., Penazzi, N., Bodoardo, S., ... & Passerini, S. (2014). Enabling aqueous binders for lithium battery cathodes–Carbon coating of aluminum current collector. *Journal of power sources*, *248*, 1000-1006.

[20] Hamam, I., Zhang, N., Liu, A., Johnson, M. B., & Dahn, J. R. (2020). Study of the Reactions between Ni-Rich Positive Electrode Materials and Aqueous Solutions and their Relation to the Failure of Li-Ion Cells. *Journal of The Electrochemical Society*, *167*(13), 130521.

[21] Çetinel, F. A., & Bauer, W. (2014). Processing of water-based LiNi 1/3 Mn 1/3 Co 1/3 O 2 pastes for manufacturing lithium ion battery cathodes. *Bulletin of Materials Science*, *37*(7), 1685-1690.

[22] Chu, M. Y. (1998). *U.S. Patent No. 5,814,420*. Washington, DC: U.S. Patent and Trademark Office.

[23] Ludwig, B., Zheng, Z., Shou, W., Wang, Y., & Pan, H. (2016). Solvent-free manufacturing of electrodes for lithium-ion batteries. *Scientific reports*, *6*, 23150.

[24] Liu, D., Chen, L.-C., Liu, T.-J., Fan, T., Tsou, E.-Y. and Tiu, C. (2014) An Effective Mixing for Lithium Ion Battery Slurries. Advances in Chemical Engineering and Science, 4, 515-528.

[25] Li, C. C., & Wang, Y. W. (2013). Importance of binder compositions to the dispersion and electrochemical properties of water-based LiCoO2 cathodes. *Journal of power sources*, *227*, 204-210.

[26] Bichon, M., Sotta, D., Dupré, N., De Vito, E., Boulineau, A., Porcher, W., & Lestriez, B. (2019). Study of immersion of LiNi0. 5Mn0. 3Co0. 2O2 material in water for aqueous

processing of positive electrode for Li-ion batteries. *ACS applied materials & interfaces*, *11*(20), 18331-18341.

[27] Wood, M., Li, J., Ruther, R. E., Du, Z., Self, E. C., Meyer III, H. M., ... & Wood III, D. L. (2020). Chemical stability and long-term cell performance of low-cobalt, Ni-Rich cathodes prepared by aqueous processing for high-energy Li-Ion batteries. *Energy Storage Materials*, *24*, 188-197.

[28] Bauer, W., Çetinel, F. A., Müller, M., & Kaufmann, U. (2019). Effects of pH control by acid addition at the aqueous processing of cathodes for lithium ion batteries. *Electrochimica Acta*, *317*, 112-119.

[29] Church, B. C., Kaminski, D. T., & Jiang, J. (2014). Corrosion of aluminum electrodes in aqueous slurries for lithium-ion batteries. *Journal of materials science*, *49*(8), 3234-3241.

[30] Carvalho, D. V., Loeffler, N., Kim, G. T., Marinaro, M., Wohlfahrt-Mehrens, M., & Passerini, S. (2016). Study of water-based lithium titanate electrode processing: the role of pH and binder molecular structure. *Polymers*, *8*(8), 276.

[31] Phillip, N. D., Daniel, C., & Veith, G. M. (2020). Influence of Binder Coverage on Interfacial Chemistry of Thin Film LiNi0. 6Mn0. 2Co0. 2O2 Cathodes. *Journal of The Electrochemical Society*, *167*(4), 040521.

[32] Nanoindentation Instruments: InSEM, iNano, iMicro Nanoindenters: Lab Analysis Hardness Testing. (n.d.). Retrieved from http://nanomechanicsinc.com/

[33] Sousa, B. C., Gleason, M. A., Haddad, B., Champagne Jr, V. K., Nardi, A. T., & Cote, D. L. (2020). Nanomechanical Characterization for Cold Spray: From Feedstock to Consolidated Material Properties. *Metals*, *10*(9), 1195.

[34] Xie, Q., & Manthiram, A. (2020). Long-Life, Ultrahigh-Nickel Cathodes with Excellent Air Storage Stability for High-Energy Density Lithium-Based Batteries. *Chemistry of Materials*, *32*(17), 7413-7424.

[35] Li, Y., Deng, S., Chen, Y., Gao, J., Zhu, J., Xue, L., ... & Wang, S. (2019). Dual functions of residue Li-reactive coating with C4H6CoO4 on high-performance LiNiO2 cathode material. *Electrochimica Acta*, *300*, 26-35.

[36] Zou, L., He, Y., Liu, Z., Jia, H., Zhu, J., Zheng, J., ... & Zhang, J. G. (2020). Unlocking the passivation nature of the cathode–air interfacial reactions in lithium ion batteries. *Nature communications*, *11*(1), 1-8.

[37] Liu, W. M., Qin, M. L., Lü, X. U., Su, Y. I., Deng, J. Y., & Huang, Z. H. (2018). Washing effect on properties of LiNi0. 8Co0. 15Al0. 05O2 cathode material by ethanol solvent. *Transactions of Nonferrous Metals Society of China*, *28*(8), 1626-1631.

[38] Zhang, X., Jiang, W. J., Mauger, A., Gendron, F., & Julien, C. M. (2010). Minimization of the cation mixing in Li1+ x (NMC) 1− xO2 as cathode material. *Journal of Power Sources*, *195*(5), 1292-1301.

[39] Zukalova, M., Prochazka, J., Laskova, B. P., Zukal, A., & Kavan, L. (2018). Layered LiNi1/3Mn1/3Co1/3O2 (NMC) with Optimized Morphology for Li-Ion Batteries. *ECS Transactions*, *87*(1), 67-75.

[40] Pimenta, V., Sathiya, M., Batuk, D., Abakumov, A. M., Giaume, D., Cassaignon, S., ... & Tarascon, J. M. (2017). Synthesis of Li-rich NMC: a comprehensive study. Chemistry of Materials, 29(23), 9923-9936.

[41] Liu, H. S., Zhang, Z. R., Gong, Z. L., & Yang, Y. (2004). Origin of deterioration for LiNiO2 cathode material during storage in air. *Electrochemical and Solid State Letters*, *7*(7), A190-A193.

[42] Liu, H., Yang, Y., & Zhang, J. (2006). Investigation and improvement on the storage property of LiNi0. 8Co0. 2O2 as a cathode material for lithium-ion batteries. *Journal of power sources*, *162*(1), 644-650.

[43] Ye, D., Zeng, G., Nogita, K., Ozawa, K., Hankel, M., Searles, D. J., & Wang, L. (2015). Understanding the Origin of Li2MnO3 Activation in Li-Rich Cathode Materials for Lithium-Ion Batteries. Advanced Functional Materials, 25(48), 7488-7496.

[44] Li, T., Yuan, X. Z., Zhang, L., Song, D., Shi, K., & Bock, C. (2020). Degradation mechanisms and mitigation strategies of nickel-rich NMC-based lithium-ion batteries. *Electrochemical Energy reviews*, *3*(1), 43-80.

[45] Duan, Y., Yang, L., Zhang, M. J., Chen, Z., Bai, J., Amine, K., ... & Wang, F. (2019). Insights into Li/Ni ordering and surface reconstruction during synthesis of Ni-rich layered oxides. *Journal of Materials Chemistry A*, *7*(2), 513-519.

[46] Fu, Z., Hu, J., Hu, W., Yang, S., & Luo, Y. (2018). Quantitative analysis of Ni2+/Ni3+ in Li [NixMnyCoz] O2 cathode materials: Non-linear least-squares fitting of XPS spectra. *Applied Surface Science*, *441*, 1048-1056.

[47] https://xpssimplified.com/elements/oxygen.php

[48] Haik, O., Leifer, N., Samuk-Fromovich, Z., Zinigrad, E., Markovsky, B., Larush, L., ... & Aurbach, D. (2010). On the surface chemistry of LiMO2 cathode materials (M=[MnNi] and [MnNiCo]): electrochemical, spectroscopic, and calorimetric studies. *Journal of The Electrochemical Society*, *157*(10), A1099-A1107.

[49] Zheng, X., Li, X., Wang, Z., Guo, H., Huang, Z., Yan, G., & Wang, D. (2016). Investigation and improvement on the electrochemical performance and storage characteristics of LiNiO2-based materials for lithium ion battery. *Electrochimica Acta*, *191*, 832-840.

[50] Chen, Z., Wang, J., Chao, D., Baikie, T., Bai, L., Chen, S., ... & Shen, Z. (2016). Hierarchical porous LiNi 1/3 Co 1/3 Mn 1/3 O 2 nano-/micro spherical cathode material: minimized cation mixing and improved Li+ mobility for enhanced electrochemical performance. *Scientific reports*, *6*, 25771.

[51] Manthiram, A., Knight, J. C., Myung, S.-T., Oh, S.-M., & Sun, Y.-K. (2015). Nickel-Rich and Lithium-Rich Layered Oxide Cathodes: Progress and Perspectives. *Advanced Energy Materials*, 6(1), 1501010.

[52] Li, T., Yuan, X.-Z., Zhang, L., Song, D., Shi, K., & Bock, C. (2019). Degradation Mechanisms and Mitigation Strategies of Nickel-Rich NMC-Based Lithium-Ion Batteries. *Electrochemical Energy Reviews*, 3(1), 43–80.

[53] Xia, Y., Zheng, J., Wang, C., & Gu, M. (2018). Designing principle for Ni-rich cathode materials with high energy density for practical applications. *Nano Energy*, 49, 434-452.

[54] Kim, J., Lee, H., Cha, H., Yoon, M., Park, M., & Cho, J. (2018). Prospect and Reality of Ni-Rich Cathode for Commercialization. *Advanced Energy Materials*, 8(6), 1702028.

[55] Maleki Kheimeh Sari, H., & Li, X. (2019). Controllable cathode–electrolyte interface of Li [Ni0. 8Co0. 1Mn0. 1] O2 for lithium ion batteries: a review. *Advanced Energy Materials*, *9*(39), 1901597.

[56] Mohanty, D., Dahlberg, K., King, D. M., David, L. A., Sefat, A. S., Wood, D. L., Daniel, C., Dhar, S., Mahajan, V. Lee, M., & Albano, F. (2016). Modification of Ni-rich FCG NMC and NCA cathodes by atomic layer deposition: preventing surface phase transitions for high-voltage lithium-ion batteries. *Scientific reports*, 6, 26532.

[57] Li, J., Li, W., You, Y., & Manthiram, A. (2018). Extending the service life of high-Ni layered oxides by tuning the electrode–electrolyte interphase. *Advanced Energy Materials*, 8(29), 1801957.

[58] Xu, R., Sun, H., de Vasconcelos, L. S., & Zhao, K. (2017). Mechanical and structural degradation of LiNixMnyCozO2 cathode in Li-ion batteries: an experimental study. *Journal of The Electrochemical Society*, 164(13), A3333-A3341.

[59] Mao, Y., Wang, X., Xia, S., Zhang, K., Wei, C., Bak, S., ... & Pianetta, P. (2019). High-Voltage Charging-Induced Strain, Heterogeneity, and Micro-Cracks in Secondary Particles of a Nickel-Rich Layered Cathode Material. *Advanced Functional Materials*, *29*(18), 1900247.

[60] Xu, R. (2019). *Theories and Experiments on the Electro-Chemo-Mechanics of Battery Materials* (Doctoral dissertation, Purdue University Graduate School).

[61] Kim, U. H., Kuo, L. Y., Kaghazchi, P., Yoon, C. S., & Sun, Y. K. (2019). Quaternary layered Ni-rich NCMA cathode for lithium-ion batteries. *ACS Energy Letters*, *4*(2), 576-582.

[62] Yan, P., Zheng, J., Liu, J., Wang, B., Cheng, X., Zhang, Y., ... & Zhang, J. G. (2018). Tailoring grain boundary structures and chemistry of Ni-rich layered cathodes for enhanced cycle stability of lithium-ion batteries. *Nature energy*, *3*(7), 600-605.

[63] Dong, X., Yao, J., Zhu, W., Huang, X., Kuai, X., Tang, J., … Zhao, J. (2019). Enhanced high-voltage cycling stability of Ni-rich cathode materials via the self-assembly of Mn-rich shells. *Journal of Materials Chemistry A*, 7(35), 20262–20273.

[64] Sun, Y.-K., Kim, D.-H., Yoon, C. S., Myung, S.-T., Prakash, J., & Amine, K. (2010). A Novel Cathode Material with a Concentration-Gradient for High-Energy and Safe Lithium-Ion Batteries. *Advanced Functional Materials*, 20(3), 485–491.

[65] Lim, B.-B., Myung, S.-T., Yoon, C. S., & Sun, Y.-K. (2016). Comparative Study of Ni-Rich Layered Cathodes for Rechargeable Lithium Batteries: Li[Ni0.85Co0.11Al0.04]O2 and Li[Ni0.84Co0.06Mn0.09Al0.01]O2 with Two-Step Full Concentration Gradients. *ACS Energy Letters*, 1(1), 283–289.

[66] Kazzazi, A., Bresser, D., Birrozzi, A., von Zamory, J., Hekmatfar, M., & Passerini, S. (2018). Comparative analysis of aqueous binders for high-energy li-rich NMC as a Lithium-Ion cathode and the impact of adding phosphoric acid. *ACS applied materials & interfaces*, *10*(20), 17214-17222.

Chapter 3. Modified Nickel-rich Cathodes via Conformal Nanoparticle Coating of Precursors using Single Reactor Process

Luqman Azhari[1], Renata Arsenault[2], Guanhui Gao[3], Yan Wang[1]

[1]Department of Mechanical Engineering, Worcester Polytechnic Institute, Worcester, MA, 01609, USA

[2]Energy Storage & Materials Research, Research and Innovation Center, Ford Motor Company, 2101 Village Rd., Dearborn, MI, 48120, USA

[3]Department of Materials Science and Nano-Engineering, Rice University, Houston, TX, 77005, USA

Published as: Azhari, L., Arsenault, R., Gao, G., & Wang, Y. (2021). Modified Nickel-Rich Cathodes via Conformal Nanoparticle Coating of Precursors Using a Single Reactor Process. ACS Applied Energy Materials, 4(12), 14618-14627.

Ni-rich $LiNi_{0.8}Mn_{0.1}Co_{0.1}O_2$ (NMC811) cathode materials, with a higher energy density compared to current commercial cathodes, are looked upon as the next improvement in lithium-ion batteries. However, modifications are needed to address issues of capacity fade due to a variety of degradation mechanisms, most of which initiate at the cathode/electrolyte interface. In this work, this issue is addressed by modifying a typical co-precipitation method to develop a heterogenous precursor composed of transition-metal hydroxides coated with nanoparticles of composition $Mn_{2.7}Co_{0.3}O_4$. Reactor conditions and feedstocks are altered to induce nanoparticle formation directly after NMC811 hydroxide secondary particle formation, with pH, feedstock

solution, and reaction time being significant factors. The lithiated and sintered cathode maintains a high initial capacity of ~ 215mAh/g due to the Ni-rich base material, and an improvement of capacity retention of over 40% at both 25°C and 55°C temperatures due to a conformal nanoscale coating of $LiMn_{1.8}Co_{0.2}O_4$ spinel material. Electrochemical analysis combined with TEM indicates that improvements are attributed to suppression of impedance growth by reducing undesirable reactions between the Ni-rich cathode and electrolyte in the highly discharged state. This work demonstrates a practical method for synthesizing spinel-coated NMC during initial precursor synthesis as a step towards high throughput commercialization of Ni-rich NMC cathodes.

3.1 Introduction

Driven by the rapid interest and development in electric vehicles, drones, and personal electronics, industry must meet the demands for longer lasting and cheaper lithium-ion batteries. One of the way manufacturers look to fulfill this growing demand is by implementing nickel rich $LiNi_xMn_{1-x-y}Co_yO_2$ as a cathode materials. $LiNi_{0.8}Mn_{0.1}Co_{0.1}O_2$, commonly referred to as "NMC811" is a composition of significant interest as the next generation cathode due to its exceptionally high nickel content resulting in a high capacity of 200mAh/g and average discharge potential of 3.8V vs Li/Li^+ [1-5]. In addition, the low cobalt content reduces the materials cost and mitigates supply chain concerns, as prices have fluctuated wildly over the past decade, with a large fraction of world supply sourced from ethically questionable sources [6,7]. However, several obstacles must be overcome to achieve successful commercialization; Ni-rich cathode materials are inherently unstable during electrochemical cycling, especially at upper voltage cutoffs > 4.3V vs Li/Li^+. These instabilities are due to a combination of increasing cation

mixing between Ni^{2+} and Li^{+} with cycling, reactivity of high valence Ni^{4+} with conventional electrolytes, release of lattice oxygen in the highly charged state, structural changes from layered R-3m to spinel and rock-salt phases, onset of thermal runaway, and intergranular cracking due to anisotropic volume changes during cycling [1-5,8-10]. These mechanisms lead to severe capacity fading and can jeopardize operational safety, barriers which must be overcome to enable broad-scale implementation of Ni-rich NMC cathodes for lithium-ion batteries in commercial use.

Existing literature has shown that many of these degradation mechanisms typically initiate at the surface of the NMC particles, where the reactive Ni-rich material is in direct contact with the electrolyte [5,11-15]. Surface-initiated phase transformations from hexagonal layered, to cubic spinel, then cubic rock-salt phases have been well documented, with a thickening of this layer with continued charge/discharge cycles and subsequent impedance growth [5,11-15]. In order to inhibit degradation, much work has been focused on reducing the contact between the Ni-rich material and electrolyte through a variety of means, typically by having an electrochemically stable material on the outer surface. It is also desirable to use materials that are non-toxic and low cost. Some examples of protective materials that have been demonstrated in recent work includes alumina oxide [16], conductive polymers [17], gradient or shell NMC with lower Ni/Mn ratios [18-21], and spinel compounds [22-26]. Mn-rich materials are especially favored for their low toxicity, high chemical stability, and affordable cost [18-26].

In this work, an "MC91 spinel" nanoscale coating, composed of $LiMn_{1.8}Co_{0.2}O_4$, is applied onto NMC811 to stabilize the cathode material and inhibit degradation and capacity fade. Mn-rich compositions promote thermal and electrochemical stability at high working voltages, with the

spinel structure allowing for good lithium diffusion characteristics [22-26]. In addition, partial cobalt substitution for Mn-rich spinel has been found to further improve charge-transfer kinetics and structural stability by inhibiting detrimental Jahn-Teller distortions [24-26]. The coating precursor, composed of a layer of $Mn_{2.7}Co_{0.3}O_4$ nanoparticles, is synthesized and applied immediately after formation of the NMC811 hydroxide precursor via a co-precipitation method within the same single reactor, an industrially viable process that is well established for the synthesis of high quality spherical and homogeneous NMC precursors [28-32]. After sintering, the nanoparticles convert to a conformal nanoscale coating on NMC811. To our knowledge, this is a new approach of forming a heterogeneous cathode precursor composed of both precursors for core layered and surface spinel components via nanoparticle deposition at the coprecipitation step. This contrasts with gradient or core-shell structures, in which only $M(OH)_2$ particles of different transition metal ion "M" ratios are synthesized [18-21]. In concentration gradient precursor synthesis, the resulting cathode(s) from these works are still comprised solely of layered metal oxides. In addition, concentration gradient precursor is difficult to achieve in continuously stirred coprecipitation reactor processes, which is a standard industrial method for producing large quantities of NMC precursor. Core-shell structures can also suffer from issues concerning the interface between the core and shell. Typically, the shell layer is relatively thick (> 1um), which poses potential strain at the interface during lithiation/delithiation and can be jeopardized by debonding [22]. Thus, it is desirable to achieve thinner sub-micron coatings that are well bonded to the core material. This method also contrasts with other established methods that utilize spinel coatings, where the coating is applied to cathode powders post calcination/lithiation, by methods such as ALD or rotary evaporation [23-27], which are not practical for high volume industrial processes. Thus, synthesis of spinel-coated NMC811 using a

coprecipitation method allows for larger scale production of modified Ni-rich cathode for better cycle stability.

The Mn-rich coating has a negligible effect on capacity, while also noticeably improving capacity retention over 100 cycles at both room temperature and an elevated temperature of 55°C, maintaining 92.88% and 91.47% of initial capacity, vs 81.81% and 84.87% for the uncoated NMC811, respectively. This improvement in performance is attributed to inhibition of surface-initiated degradation and subsequent suppression of impedance growth. This process can also easily be adapted to a two-reactor continuous output system, demonstrating a pathway towards stabilization of Ni-rich NMC can be achieved via nanoscale Mn-rich coating using by modifying a co-precipitation method without sacrificing significant charge/discharge capacity or productional output capability.

3.2 Experimental Methods

Transition metal hydroxide precursors are synthesized using a co-precipitation route in a 1L glass jacketed reactor, utilizing solutions of transition metal sulfates, ammonia, and sodium hydroxide as reactants. A 3.5M solution of ammonia functions as a chelating agent, complexing with transition metal ions to control the rate of metal hydroxide precipitation to allow for the formation of dense spherical secondary particles [29,30]. The initial 1.8M metal sulfate feedstock solution is composed of $NiSO_4$, $MnSO_4$, and $CoSO_4$ dissolved in deionized water in an 8:1:1 molar ratio. The 1L reactor is initially filled with 500mL of a 2.75M solution of ammonia and stirred at 650 RPM at 55°C with nitrogen gas continuously bubbled into the reactor to establish an inert atmosphere. The 3.5M solution of ammonia and 1.8M metal sulfate solution are then

added dropwise into the reactor at 0.17mL/min and 0.55mL/min, respectively. The pH is maintained at a constant value of 11.0 ± 0.1 using a pH controller and a 5M solution of sodium hydroxide to adjust pH accordingly. To produce NMC811 hydroxide precursors, the reaction is allowed to continue for 6 hours, followed by an aging time of 2 hours in which the pH is kept constant using the NaOH solution with no further metal sulfate or ammonia additions to the reactor. Afterwards, the metal hydroxide product, composed of $Ni_{0.8}Mn_{0.1}Co_{0.1}(OH)_2$, is collected, washed several times with DI water, dried in a convection oven, and filtered through a 38μm sieve.

To synthesize the coated NMC811 (C-NMC811), a similar procedure is followed. However, after the 2-hour aging step, the initial feedstock solution of $Ni_{0.8}Mn_{0.1}Co_{0.1}SO_4$ is changed into a more dilute 0.5M solution of $Mn_{0.9}Co_{0.1}SO_4$. The pH setting is adjusted to 12.5 ± 0.1 and maintained using a 10M solution of sodium hydroxide to increase the reaction driving force and facilitate nanoparticle formation. The new reactant and ammonia are added dropwise for 1 hour and left to age for several hours before collection. The product is washed several times with DI water, dried in a convection oven to remove residual water, then filtered through a 38μm sieve. Upon exposure to air, the Mn-rich hydroxides on the surface are observed to quickly oxidize into $Mn_{2.7}Co_{0.3}O_4$ nanoparticles, visibly turning the powder from a typical light brown in color to a dark brown.

After drying in air, the transition metal precursor is mixed thoroughly with lithium hydroxide monohydrate in a 1.00:1.05 molar ratio. A slight excess of lithium is required to account for partial vaporization of lithium and to minimize cation mixing during initial sintering [33].

Sintering is conducted in a tube furnace under oxygen flow, with a two-step process of 450°C for 6hrs, followed by 775°C for 15hrs. A schematic of the full process is detailed in **Figure 15**. Afterwards the resulting cathode powder is ground gently to remove agglomerates, sieved again through a 38µm sieve, then mixed with Super C65 carbon black and PVDF binder dissolved in NMP (6wt%). The mass ratio of active material to conductive carbon and PVDF is 8:1:1, respectively. The slurry is cast onto a 15µm thick Al foil using a 150µm doctor blade and dried in air at 60°C for several hours, followed by further drying in a vacuum oven at 80°C overnight to remove any residual solvent and possible moisture. Afterwards the resulting electrode is calendared to a total thickness of approximately 35-40µm, punched into 14mm discs, and assembled in an argon glovebox into 2032-coin cells with lithium metal as the anode, 1M $LiPF_6$ in EC/EMC (3:7 weight ratio) as the electrolyte, and a Celgard polyolefin separator. Active mass loading for the cells tested are calculated to be in the range of 3.5-4.3mg/cm^2.

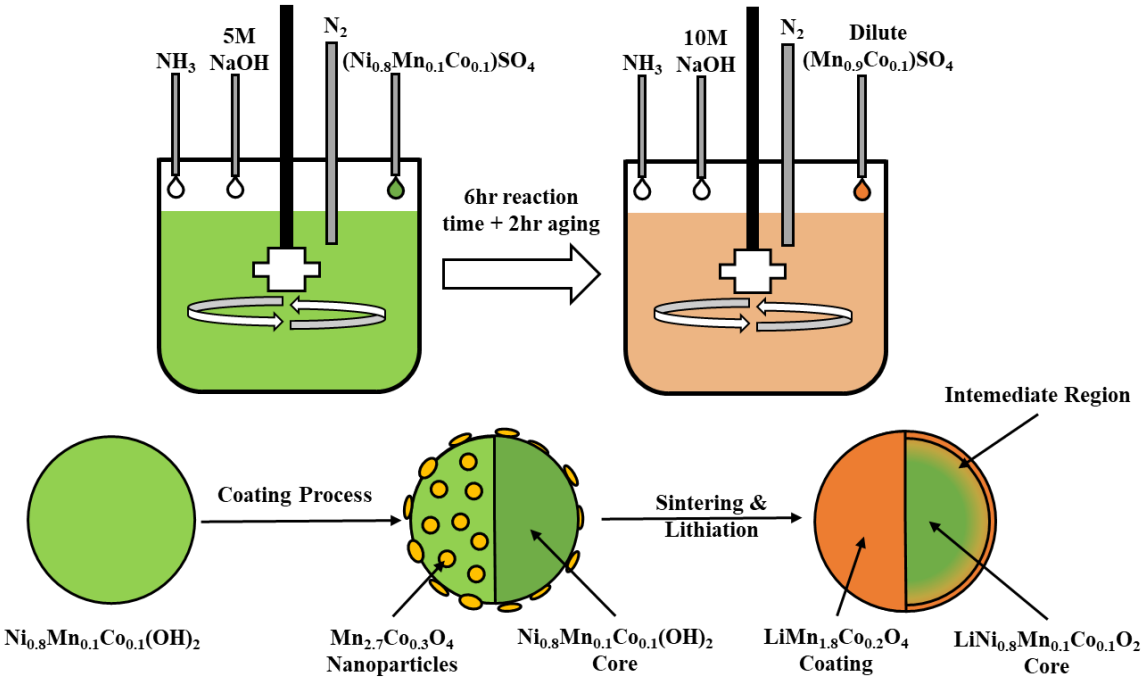

Figure 15: Process schematic of the coating process

3.3 Characterization Methods

X-ray diffraction (XRD) profiles of the NMC hydroxide precursor and sintered cathode powders were obtained using a PANalytical Empyrean X-ray Diffractometer with a Cu Kα radiation source (λ=1.5406Å), using a step size of 0.0167°/step. Crystallographic lattice parameters and intensity ratios of the (003) and (104) peaks were determined using the Rietveld refinement technique via FullProf Suite software, using the R-3m space group as the structural reference. Surface morphology and qualitative chemical information of the hydroxide precursors and sintered cathode were examined using scanning electron microscopy (SEM) and energy dispersive X-ray spectroscopy (EDS) analysis via a JEOL JSM-7000F SEM at 10kV accelerating voltage. High-resolution transmission electron microscopy (HRTEM) and EDS mapping are performed with a double correctors Titan cubed Themis 300 operated at 300 kV, equipped with a Ceta camera, Gatan Quantum 966 energy filter and an electron monochromator. Quantitative chemical compositions were determined through inductively coupled plasma optical emission spectrometry (ICP-OES), using a Perkin-Elmer Optima 8000 ICP-OES instrument and powder samples dissolved prior in a solution of sulfuric acid and hydrogen peroxide. In-situ XRD was conducted using a D8 Advance X-ray Diffractometer (Bruker AXS) equipped with an Mo Kα radiation source, while galvanostatically charging/discharging samples at a rate of C/10 and sampling XRD profiles every hour. Raman spectra of pristine and coated samples were obtained using a Horiba Xplora system with a 532nm green laser light, 1800 grating, at 10% attenuation at 100x magnification.

Electrochemical charge/discharge cycles to were conducted on a LANDT CT2001A from 2.8-4.5V at a C-Rate of C/2 (specific capacity set to 200mAh/g) at either room temperature or 55°C in an oven. High C-rate capacity was tested using an Arbin Battery tester and at a voltage range of

2.8-4.3V with rates of C/10, C/5, C/2, 1C, 2C, 3C, and 5C. A lower upper voltage cutoff was chosen for rate testing to mitigate cathode degradation from affecting the reversible capacity. Cyclic voltammetry (CV) profiles and electrochemical impedance spectra (EIS) were obtained using a Bio-logic SAS VMP3 multi-channel Potentiostat maintained at room temperature (25°C). CV and EIS data were obtained for cells before and after 100 galvanostatic charge/discharge cycles. CV profiles were obtained at different scan rates of 0.1mV/s, 0.2mV/s, 0.5mV/s, and 1mV/s from 2.8-4.5V. EIS was obtained using a 10mV sinusoidal amplitude from a frequency range of 1Mhz to 20mHz. Cells were held at the desired SOC/voltage for approximately 2hrs before EIS analysis. Before all testing, all coin cells were subjected to at least two initial formation cycles at a rate of C/20 from 2.8-4.5V.

3.4 Results and Discussion

3.4.1 Morphology, Composition, and Structure

Following the previously detailed procedure, the obtained NMC811 hydroxide precursor as shown in **Figure 16a, b** displays a narrow size distribution of spherical secondary particles ~6-8um in diameter. Closer examination reveals thin needle-like primary particles. After sintering and lithiation, these needle-like primary particles densify into 100nm block like primary particles [**Figure 16c, d**]. The secondary particle size and shape is maintained after the sintering cycle and ICP results shown in the table in **Table 3** reveals a composition close to the targeted 8:1:1 ratio.

The coated NMC811 precursor in **Figure 16e, f,** referred to as "C-NMC811," displays a similar underlying base material of spherical secondary particles composed of needle-like primary particles. However, small disc-like nanoparticles are observed to be uniformly distributed on the

surfaces of the secondary particles, with a small amount of segregation of nanoparticles and secondary particles. It is assumed that these nanoparticles are composed of $Mn_{0.9}Co_{0.1}(OH)_2$, which oxidizes into $Mn_{2.7}Co_{0.3}O_4$ upon air exposure. To verify this, a separate experiment was performed in which the coating process is conducted without the initial NMC811 precursor formation step. The resulting coating material shown in **Figure S1** is composed of small nanoparticles identical to those found on the C-NMC811 precursor and XRD profiles are well indexed to the tetragonal Mn_3O_4 phase, also known as hausmannite, and a is precursor to $LiMn_2O_4$ [33,35-37]. After sintering, the coating nanoparticles on the surface are no longer observed and C-NMC811 looks identical to NMC811 at the sub-micron scale, with occasional areas of unadhered coating material [**Figure 16g, h**]. It is assumed that during the sintering process, the Mn-rich nanoparticles on the surface partially diffuse and coalesce into a thin spinel coating on the surface of the NMC811 primary particles, with a slightly Mn-rich layered NMC intermediate region as illustrated in **Figure 15**. Other pH conditions were also tested, with lower pH conditions during the coating step leading to the formation of larger, spherical coating particles with less coverage, which can reduce the effectiveness of the coating process [**Figure S2].** Thus, this also indicates that the coverage uniformity and thickness of the coating can be controlled by adjusting the coating time and reactor pH during the coating process. Naturally a longer coating time/higher volume of added coating feedstock will lead to a thicker coating, and a higher pH facilities nucleation of smaller nanoparticles, which improves the overall uniformity and coverage of the coating material onto the NMC811 hydroxide secondary particles. At a low pH, along with the precipitation of larger coating particles, the solubility of metal hydroxides increases based on Le Chatelier principle, and results in less overall coating material being precipitated. This is evident in the table in **Table S1**, where utilizing a pH of 9 results in Mn/(Ni

+ Mn + Co) of 0.132, compared to 0.150 when using a pH of 12.5. The lack of effective coating at low pH would naturally result in less overall protection, while too thick of a coating would result in lower capacity due to the inherently lower specific capacity of the spinel structure. A thicker coating may also result in generation of the aforementioned strain between the coating and core interface, which may compromise the overall structure under repeated cycling [22].

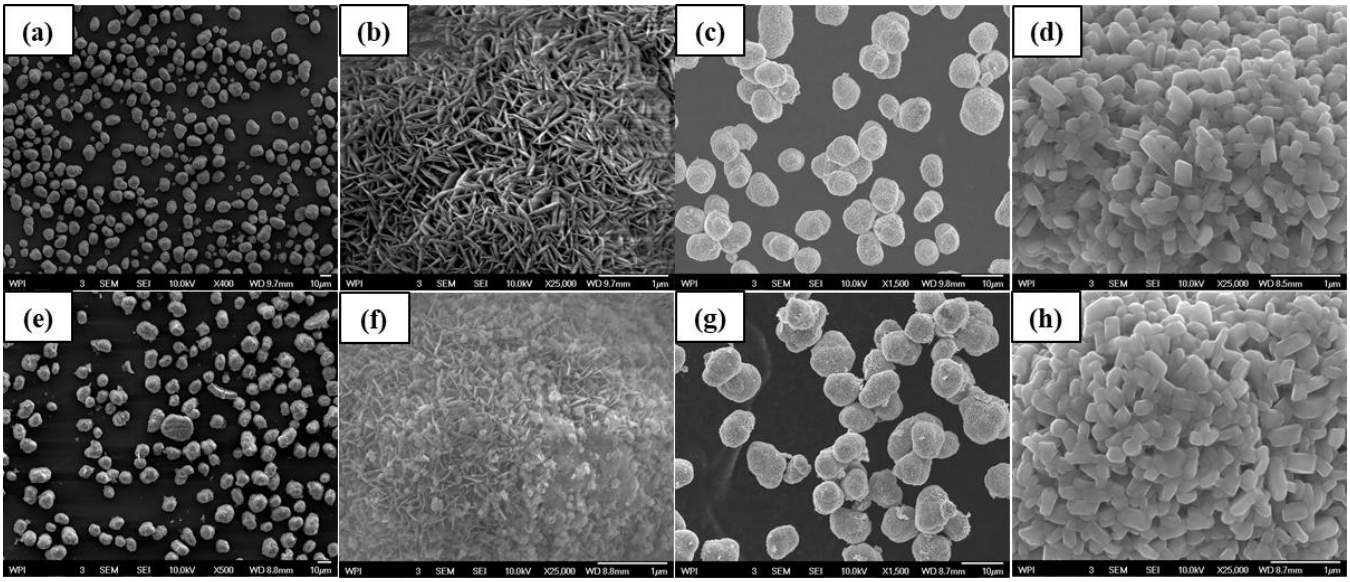

Figure 16: Particle shape, size, and surface morphology of hydroxide precursors for (a,b) NMC811 and (e,f) C-NMC811. Particle shape, size, and surface morphology of sintered cathode powder for (c,d) NMC811 and (g,h) C-NMC811.

Table 3: Elemental composition of sintered cathode material determined by ICP-OES

Sample	Ni	Mn	Co
NMC811	0.813	0.093	0.094
C-NMC811	0.746	0.150	0.104

EDS analysis reveals an expected composition of Ni, Mn, and Co at the surface of NMC811, with a noticeable increase of relative Mn intensity in the case of the C-NMC811, as expected.

Some areas on the C-NMC811 exhibit thicker patches of the coating material, and EDS analysis reveals a degree of coating inhomogeneity [**Figure S3**]. From the ICP results detailed in **Table 3**, an expected higher content of Mn is observed, corroborating the EDS analysis, and it is determined that $Mn_{2.7}Co_{0.3}O_4$ makes up ~2.10 mol%, or ~5.04 wt% of the total precursor mass. Assuming complete conversion of $Mn_{2.7}Co_{0.3}O_4$ to $LiMn_{1.8}Co_{0.2}O_4$, and negligible interdiffusion between the spinel coating and layered base material, this would result in ~3.05 mol%, or ~5.75 wt% of MC91 spinel coating. Using approximate densities of 4.73g/cm^3 for $LiNi_{0.8}Mn_{0.1}Co_{0.1}O_2$ and 4.3g/cm^3 $LiMn_{1.8}Co_{0.2}O_4$, this would correspond to a coating thickness of around 100-150nm. However, the presence of such a thick coating cannot be seen from SEM images in **Figure 16**, so a degree of interdiffusion between the coating and bulk material likely occurs during sintering/lithiation, resulting in a thinner coating, as illustrated in the schematic in **Figure 15.**

TEM/EDS mapping images are shown in **Figure 17**. Uncoated NMC811 exhibits an expected homogeneity of Ni and Mn throughout the sample, with no discernable difference between the particle surface and subsurface areas (**Figure 17a-c)**. In contrast, for C-NMC811, a layer of approximately 50-100nm from the surface is observed to be richer in Mn and deficient Ni (**Figure 17e-g)**. The presence of Ni in the surface regions is indicative of interdiffusion between the Mn-rich coating layer and Ni-rich core during the sintering process. Samples were also allowed to be exposed to ambient air for several weeks, and a significant difference can be observed afterwards at the surface and subsurface regions of NMC811 and C-NMC811 powders, as shown in **Figures 17d, h**. In uncoated NMC811, the surface appears much more rough and significant levels degradation can be observed based on the presence of various irregular

domains with different crystal planes and orientations; areas with different lattice spacings of ~4.76Å and ~2.0Å can be observed. Along with the FFT pattern in the inset of **Figure 17d**, this may correspond to the (003) and (002) reflection planes of layered R-3m and cubic Fm-3m rock-salt structures, respectively [38]. This agrees with prior studies involving exposure of Ni-rich NMC to ambient conditions, which describe the development of surface impurity layers, contraction of the *c* lattice parameter, and rock salt phase formation in subsurface regions due to various surface-initiated reactions with ambient air and moisture [39,40]. In contrast, the surface of C-NMC811 appears to maintain good crystallinity, with no irregularities in the sub surface regions nor surface roughness. Along with the FFT pattern (which is distorted due to being slightly off zone-axis) in the inset of **Figure 17h,** interplanar spacings of ~4.76Å may correspond to (111) reflection plane of a cubic LiM_2O_4 structure [40, 41]. This suggests the presence of a cubic spinel at the surface of C-NMC811 and that the coating process enhances the durability of the active material against surface-initiated degradation mechanisms during long term exposure to air.

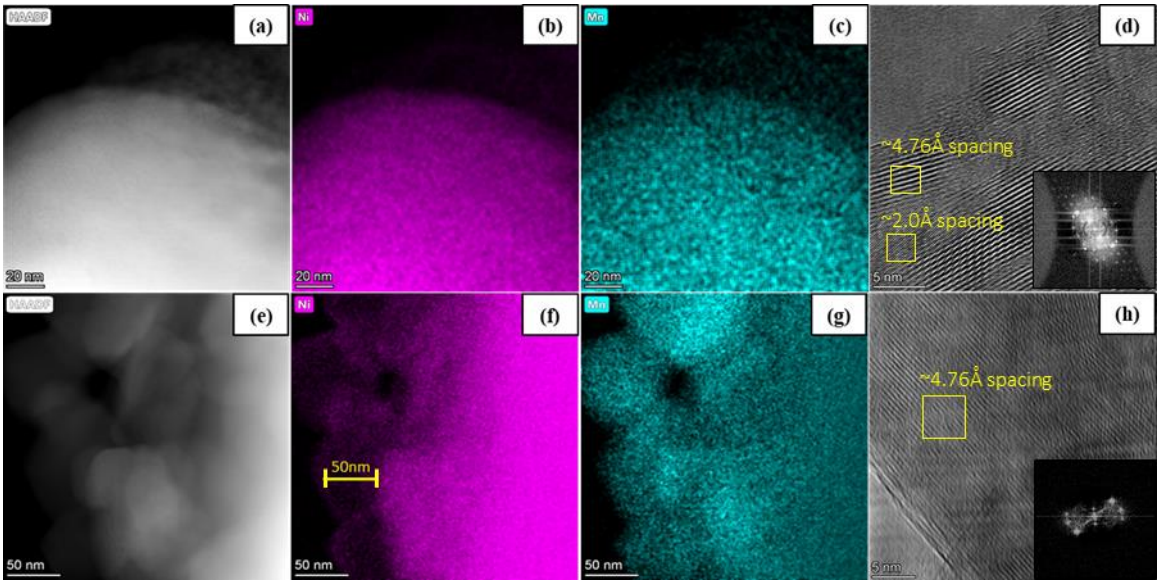

Figure 17: HAADF images and EDS maps of a particle surface cross section for NMC811 (a-c) and C-NMC811 (e-g). HRTEM images of (d) NMC811 and (h) C-NMC811 after extended exposure to ambient air. Inset of (d, h): FFT patterns of subsurface regions of NMC811 and C-NMC811, respectively. Line profiles for interplanar spacing values are shown in Figure S12.

XRD results for both NMC811 and C-NMC811 can be well indexed to the R-3m layered hexagonal structure, with lattice parameters of expected values [**Figure 18a, Table 4]**. No secondary phases are observed in C-NMC811, possibly due to too small of a signal from the coating material as well as some peak overlap. Furthermore, both samples exhibit good crystallinity, as indicated by the well-defined (018) and (110) double peaks and low cation mixing based on a $I_{(003)}/I_{(104)}$ ratio close to 1.2 [43, 44]. It is observed that the intensity ratio for C-NMC811 is slightly lower than that of NMC811. This may be due to incomplete lithiation of the Ni-rich component of the C-NMC811 hydroxide precursor. It is hypothesized that some lithium reacts preferentially with the manganese-rich coating to form a portion of lithium-rich Li_2MnO_3 phase [45]. This would result in a slight lithium-deficiency in the Ni-rich component, which would increase the degree of cation mixing during sintering and subsequently reduce the $I_{(003)}/I_{(104)}$

ratio. This may be evidenced in **Figure S4**, where NMC811 coated in an exceptionally thick layer of coating material, via the previously detailed process but with a 4 hour coating step, exhibits subpar crystallinity, a low $I_{(003)}/I_{(104)}$, and CV peaks characteristic to the activation of the Li_2MnO_3 phase [46, 47].

XRD data provides bulk structural information and is not particularly suitable in probing surface/sub-surface regions of the cathode powders. Raman spectroscopy, however, is useful for probing local structures and transition metal-oxygen bonding characteristics of NMC cathodes below 800cm^{-1}, which may not show up in XRD analysis [48]. From the results shown in **Figure 18c and d**, NMC811 and C-NMC811 exhibit significantly different local structures at the surface. NMC811 displays two main peaks around 557cm^{-1} and 465cm^{-1}, which correspond to the respective A_{1g} stretching and E_g bending modes of Ni-O bonding in the R-3m layered structure, with overall broadening due to the additional contributions of Mn and Co Raman bending and stretching modes [47]. C-NMC811 displays a noticeable shift towards higher wavenumber compared to NMC811, which is clearly demonstrated in **Figure S13**. This difference is associated with the more Mn-rich surface, as Mn A_{1g} and E_g modes in the R-3m layered structure is well demonstrated to appear ~611cm^{-1} [48-50] and would have a larger contribution to the total Raman spectra. However, a noticeable shoulder peak is observed in a higher frequency region around 625-640cm^{-1}. This peak can be attributed to the presence of an Mn-rich spinel structure, as the subsequent shorter Mn-O bonding results in higher frequency Raman modes compared to Mn-O bonding in the layered structure, and is consistent with prior literature [49,50].

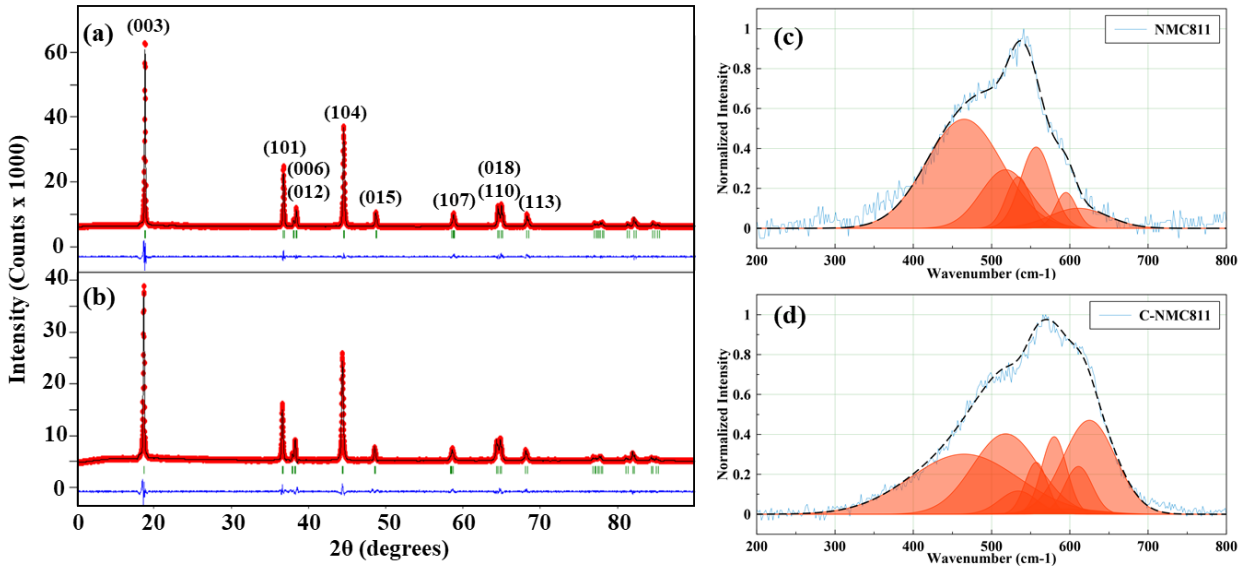

Figure 18: (a) XRD profiles of NMC811 and (b) C-NMC811 fitted to the R-3m structure. (c) Raman Spectra of as synthesized NMC811 and (d) C-NMC811. Raman peaks were deconvoluted into 6 or 8 peaks based on refs 48-50.

Table 4: Refined lattice parameters and characteristic intensity ratio obtained via Rietveld refinement of powder XRD data

Sample	a (Å)	b (Å)	c (Å)	V (Å^3)	χ^2	$I_{(003)}/I_{(104)}$
NMC811	2.8703	2.8703	14.1987	101.3066	4.46	1.25
C-NMC811	2.8726	2.8726	14.2129	101.5689	2.58	1.17

3.4.2 Electrochemical Performance

Under different scan rates from 2.8-4.3V, NMC811 and C-NMC811 display identical reversible capacities, as shown in **Figure 19a**. This contrasts with other results, which claim that the three-dimensional interstitial network for spinel materials would enhance rate performance by means of enhanced lithium diffusion [24]. Our observation may be attributed to the small fraction of coating material, with the main component of layered material being the limiting factor in reversible capacity under high charge/discharge rates tested in this work.

Long term charge/discharge cycling to a high upper voltage cutoff of 4.5V shows that C-NMC811 has a significant improvement in capacity retention over NMC811 [**Figure 19d**]. Both materials show a high initial capacity of ~215mAh/g in the C/20 formation cycles. In the initial C/2 cycling, the C-NMC811 has a slightly lower initial capacity of 190mAh/g, compared to 200mAh/g of NMC811. This difference may be attributed to the mass fraction of spinel coating material, which has a lower reversible capacity of 120mAh/g compared to the layered NMC811 and does not contribute much capacity beyond 4.3V. After 100 cycles at room temperature, the C-NMC811 retains 92.88% of its initial capacity, compared with 81.81% of the NMC811. The fluctuations in capacity seen for both samples are attributed to temperature fluctuations of the room throughout the day, as these fluctuations are not observed during high temperature cycling, which took place in a much more controlled environment with constant temperature. It is also found that the reactor pH significantly influenced the effectiveness of the coating, with reduced capacity retention observed when using a reactor pH of 9 or 10.3 during the coating process [**Figure S2, S5**]. This is attributed to the decreased effectiveness of coverage due to the formation of larger coating particles under lower pH, as well as the overall lessened amount of coating material. Thickly coated cathode material also exhibited subpar capacity, although with exceptional capacity retention [**Figure S5**]. It is likely that the higher fraction of coating material with less inherent capacity, combined with the reduced crystallinity and higher fraction of obstacles in the form of grain boundaries, resulted in significantly lower reversible capacity during charge/discharge cycling. Therefore, it is clear that the amount of coating deposited and the effectiveness of coverage is critical to achieve an optimum balance between specific capacity and capacity fade.

This improved capacity retention of the C-NMC811 is also observed when cycling at 55°C; C-NMC811 retains 91.47% of its initial capacity, compared to 84.87% for the NMC811 [**Figure 19g**]. With the increased temperature, the C-NMC811 displays an improvement in initial cycling capacity, improving from 190mAh/g at room temperature to ~210mAh/g at 55°C. This is attributed to enhanced lithium diffusion kinetics in the layered material, as even the uncoated NMC811 displays an improved initial capacity under this condition.

From the post-formation CV curves, there are three main pairs of oxidation and reduction peaks. The largest oxidation peak occurs around 3.7V, with the other peaks occurring near 4.0V and 4.2V, as shown in **Figures 19b, e, and h.** These peaks correspond to phase changes during delithiation of the host structure, from an initial hexagonal H1 phase to monoclinic M, hexagonal H2, and eventual hexagonal H3 phase [50, 51]. It is observed that both the NMC811 and C-NMC811 display similar redox peaks before cycling. After 100 cycles at room temperature, it is observed that the main redox peak for NMC811 has decreased in intensity and broadened relative to other redox peaks, while those for C-NMC811 remain much closer to its initial post-formation CV profile. This is indicative of greater active material loss and surface degradation for NMC811, and the effectiveness of the protective Mn-rich coating in C-NMC811 in inhibiting such surface degradation [53-55]. This contrast is much more apparent when examining CV profiles after 100 cycles at 55°C, with NMC811 displaying even broader and lower intensity redox peaks compared to C-NMC811 [**Figure 19h**]. Furthermore, the Randles-Sevcik equation, which establishes a linear relationship between peak current and the square root of the scan rate, in which the slope of the line is proportional to the square root of the diffusion coefficient of the

electrochemically active species, highlights the improved performance of C-NMC811 [56]; by examining the peak current vs scan rates of cells after 100 cycles at room temperature in **Figure S6**, the slope for C-NMC811 is larger than that of NMC811, indicating better lithium diffusion characteristics after prolonged cycling due to less surface phase transformations in the Ni-rich layered material [45-47]. Based on a theoretical lithium concentration of 0.0488mol/cm^3, the slopes correspond to lithium diffusion coefficients of $1.053\times10^{-10}cm^2/s$ and $1.623\times10^{-10}cm^2/s$ for NMC811 and C-NMC811, respectively.

EIS data for both NMC811 and coated NMC811 (C-NMC811) show a small semicircle in the high frequency region, followed by a larger semicircle at medium frequencies, followed by a linear region. The high frequency semicircle is attributed to the SEI layer and bulk resistive/capacitive behavior, while the medium frequency semicircle is attributed to charge-transfer resistance and the double layer capacitance at the electrode surface. The linear, low frequency region is typically attributed to the diffusion of lithium ions [57, 58]. Using this understanding, the half-cell is modelled to a circuit with three elements in series: a resistor, two RC elements, and a Warburg element. In **Figure 19c**, it is observed that even after the initial formation cycles, C-NMC811 displays a lower charge transfer resistance than NMC811. The lower charge-transfer resistance in the highly charged state is evidence that the coating is protecting the Ni-rich material from degradation mechanisms with the electrolyte [55, 56]. This is even more evident in impedance behavior after 100 charge/discharge cycles at room temperature and 55°C [**Figure 19f, 19i**]. The medium frequency semicircle has grown significantly larger for NMC811 than for the C-NMC811. This indicates that the applied coating continues to suppress

impedance growth by shielding the Ni-rich material from undesirable reactions with the electrolyte.

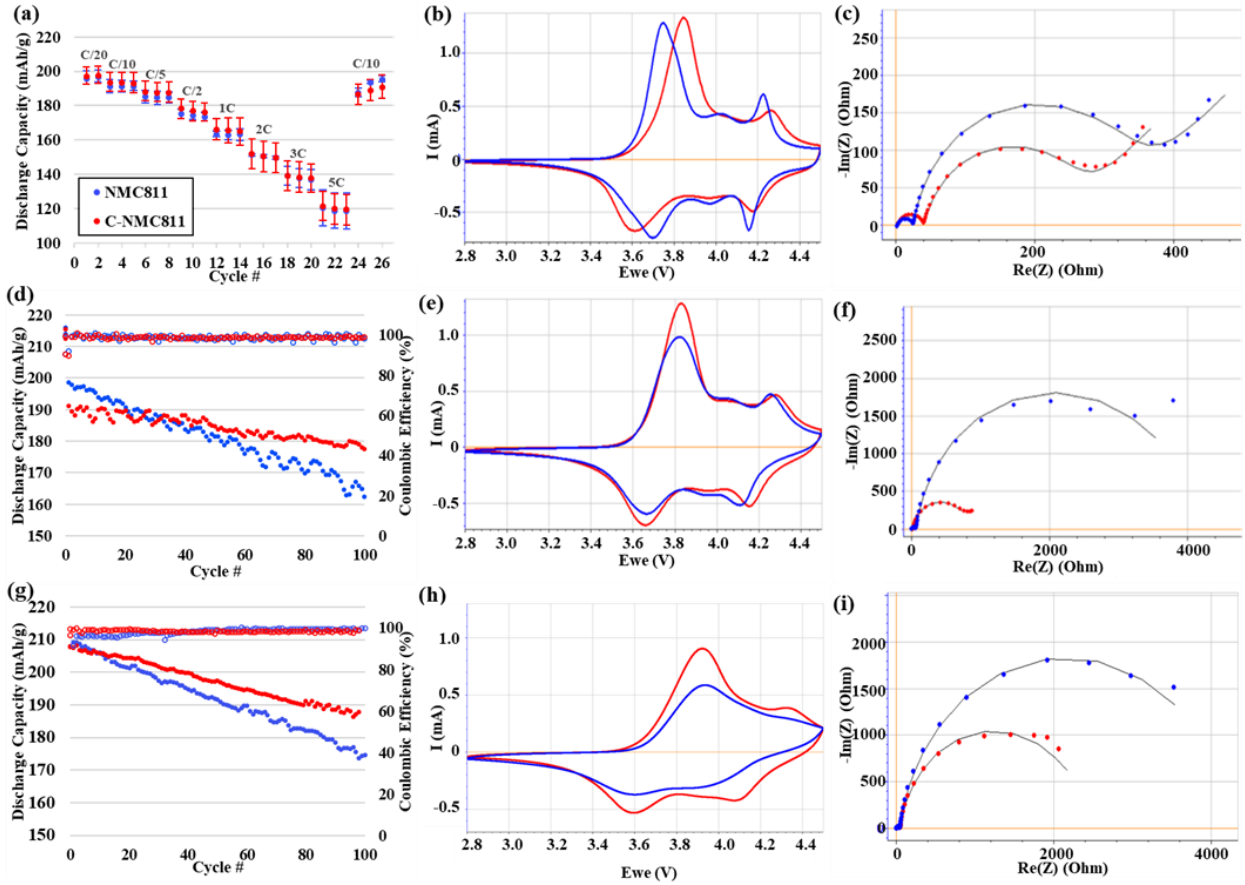

Figure 19: (a) Rate performance of NMC811 and C-NMC811 from 2.8-4.3V. Charge/discharge galvanostatic cycling from 2.8-4.5V at C/2 rate at (d) room temperature and (g) 55°C. Cyclic voltammetry profiles after (b) initial formation cycles, (e) 100 cycles at room temperature, and (h) 100 cycles at 55°C. Electrochemical impedance spectra taken at 4.5V after (c) initial formation cycles, (f) 100 cycles at room temperature, and (i) 100 cycles at 55°C.

3.5 Conclusion

In this work, we demonstrate a novel method of synthesizing a heterogenous two-component precursor. By utilizing a single reactor co-precipitation process and altering feedstock solutions and reactor pH, we develop a precursor composed of NMC811 hydroxide secondary particles

uniformly coated with $Mn_{2.7}Co_{0.3}O_4$ nanoparticles. During subsequent sintering with a Li source, these Mn-rich particles distribute themselves into a conformal nanoscale $LiMn_{1.8}Co_{0.2}O_4$ coating on the surface of the NMC811 material. Good crystallinity, particle morphology/uniformity, and a low degree of cation mixing are obtained. This method is industrially scalable and improves the capacity retention of the resulting cathode material during electrochemical cycling at a 4.5V upper voltage cutoff, at both room temperature and 55°C. Furthermore, there is minimal loss in the initial capacity of the coated sample vs the uncoated sample, especially at higher temperatures. By examining cyclic voltammetry, electrochemical impedance spectra, and TEM data, improvements in electrochemical cycling are attributed to the coating suppressing impedance growth by reducing Ni-rich/electrolyte contact in the highly charged state. The coating uniformity and thickness can feasibly be controlled by altering the reactor pH and/or coating feedstock volume. It is also likely that different nanoparticle coating compositions can be synthesized using this process, as various other metal hydroxides are highly insoluble and readily precipitate in alkaline solutions. Thus, this works demonstrates a new direction towards NMC modification. While reactor conditions could likely be optimized further, this work demonstrates a possible pathway towards the development and commercialization of Ni-rich NMC811 for next generation lithium-ion batteries.

3.6 Supporting Information

SEM images and XRD spectra of coating precipitates, SEM images and EDS spectra of precursors under different conditions, XRD spectra and CV profile of 4hr coated cathode. Cycling performance and chemical composition of cathode coated under different reactor conditions, Current vs scan rate plots, EIS spectra under different SOC, Equivalent EIS circuit,

In-situ XRD data and discussion, Additional TEM images and lattice spacing line profiles, Superimposed Raman spectra of NMC811 and C-NMC811

3.7 Acknowledgements

This work was made possible under the financial support of Ford Motor Company University Research Project. In-situ XRD data was obtained with the help from Yifan Ma and Hailong Chen at the School of Mechanical Engineering, Georgia Institute of Technology, Atlanta, GA. TEM analysis was obtained by Guanhui Gao at the Electron Microscopy Center (EMC) of Shared Equipment Authority (SEA) at Rice University. There is also a patent application based on the research results reported in this paper.

3.8 References

[1] Manthiram, A., Knight, J. C., Myung, S.-T., Oh, S.-M., & Sun, Y.-K. (2015). Nickel-Rich and Lithium-Rich Layered Oxide Cathodes: Progress and Perspectives. Advanced Energy Materials, 6(1), 1501010.

[2] Li, T., Yuan, X.-Z., Zhang, L., Song, D., Shi, K., & Bock, C. (2019). Degradation Mechanisms and Mitigation Strategies of Nickel-Rich NMC-Based Lithium-Ion Batteries. Electrochemical Energy Reviews, 3(1), 43–80.

[3] Xia, Y., Zheng, J., Wang, C., & Gu, M. (2018). Designing principle for Ni-rich cathode materials with high energy density for practical applications. Nano Energy, 49, 434-452.

[4] Kim, J., Lee, H., Cha, H., Yoon, M., Park, M., & Cho, J. (2018). Prospect and Reality of Ni-Rich Cathode for Commercialization. Advanced Energy Materials, 8(6), 1702028.

[5] Sari, H. M. K., & Li, X. (2019). Batteries: Controllable Cathode–Electrolyte Interface of Li[Ni 0.8 Co 0.1 Mn 0.1]O 2 for Lithium Ion Batteries: A Review (Adv. Energy Mater. 39/2019). Advanced Energy Materials, 9(39), 1970151.

[6] Historical Cobalt Prices and Price Chart. Retrieved March 20, 2020, from https://www.infomine.com/investment/metal-prices/cobalt/all/

[7] Cohen, L., Matich, T., Gautneb, H., & Rodger, M.. Top Cobalt Production by Country. Retrieved February 18, 2020, from https://investingnews.com/daily/resource-investing/battery-metals-investing/cobalt-investing/top-cobalt-producing-countries-congo-china-canada-russia-australia/

[8] Cheng, X., Zheng, J., Lu, J., Li, Y., Yan, P., & Zhang, Y. (2019). Realizing superior cycling stability of Ni-Rich layered cathode by combination of grain boundary engineering and surface coating. Nano Energy, 62, 30–37.

[9] Yan, P., Zheng, J., Liu, J., Wang, B., Cheng, X., Zhang, Y., Sun, X., Wang, C., & Zhang, J.-G. (2018). Tailoring grain boundary structures and chemistry of Ni-rich layered cathodes for enhanced cycle stability of lithium-ion batteries. Nature Energy, 3(7), 600–605.

[10] Jung, R., Metzger, M., Maglia, F., Stinner, C., & Gasteiger, H. A. (2017). Oxygen release and its effect on the cycling stability of LiNixMnyCozO2 (NMC) cathode materials for Li-ion batteries. Journal of The Electrochemical Society, 164(7), A1361-A1377.

[11] Li, J., Li, W., You, Y., & Manthiram, A. (2018). Extending the service life of high-Ni layered oxides by tuning the electrode–electrolyte interphase. Advanced Energy Materials, 8(29), 1801957.

[12] Xu, R., Sun, H., de Vasconcelos, L. S., & Zhao, K. (2017). Mechanical and structural degradation of LiNixMnyCozO2 cathode in Li-ion batteries: an experimental study. Journal of The Electrochemical Society, 164(13), A3333-A3341.

[13] Zhao, W., Zheng, J., Zou, L., Jia, H., Liu, B., Wang, H., Engelhard, M., Wang, C., Xu, W., Yang, Y., & Zhang, J. G. (2018). High voltage operation of Ni-rich NMC cathodes enabled by stable electrode/electrolyte interphases. Advanced Energy Materials, 8(19), 1800297.

[14] Ma, L., Nie, M., Xia, J., & Dahn, J. R. (2016). A systematic study on the reactivity of different grades of charged Li [NixMnyCoz] O2 with electrolyte at elevated temperatures using accelerating rate calorimetry. Journal of Power Sources, 327, 145-150.

[15] Tatara, R., Yu, Y., Karayaylali, P., Chan, A. K., Zhang, Y., Jung, R., Maglia, F., Giordana, L., & Shao-Horn, Y. (2019). Enhanced Cycling Performance of Ni-Rich Positive Electrodes (NMC) in Li-Ion Batteries by Reducing Electrolyte Free-Solvent Activity. ACS applied materials & interfaces, 11(38), 34973-34988.

[16] Mohanty, D., Dahlberg, K., King, D. M., David, L. A., Sefat, A. S., Wood, D. L., Daniel, C., Dhar, S., Mahajan, V., Lee, M., & Albano, F. (2016). Modification of Ni-rich FCG NMC and NCA cathodes by atomic layer deposition: preventing surface phase transitions for high-voltage lithium-ion batteries. Scientific reports, 6, 26532.

[17] Li, L., Xu, M., Yao, Q., Chen, Z., Song, L., Zhang, Z., Gao, C., Wang, P., Yu, Z., & Lai, Y. (2016). Alleviating Surface Degradation of Nickel-Rich Layered Oxide Cathode Material by Encapsulating with Nanoscale Li-Ions/Electrons Superionic Conductors Hybrid Membrane for Advanced Li-Ion Batteries. ACS Applied Materials & Interfaces, 8(45), 30879–30889.

[18] Dong, X., Yao, J., Zhu, W., Huang, X., Kuai, X., Tang, J., Li, X., Dai, S., Shen, L., Yang, R., Gao, K., Zhao, J. (2019). Enhanced high-voltage cycling stability of Ni-rich cathode materials via the self-assembly of Mn-rich shells. Journal of Materials Chemistry A, 7(35), 20262–20273.

[19] Sun, Y.-K., Kim, D.-H., Yoon, C. S., Myung, S.-T., Prakash, J., & Amine, K. (2010). A Novel Cathode Material with a Concentration-Gradient for High-Energy and Safe Lithium-Ion Batteries. Advanced Functional Materials, 20(3), 485–491.

[20] Lim, B.-B., Myung, S.-T., Yoon, C. S., & Sun, Y.-K. (2016). Comparative Study of Ni-Rich Layered Cathodes for Rechargeable Lithium Batteries: Li[Ni0.85Co0.11Al0.04]O2 and Li[Ni0.84Co0.06Mn0.09Al0.01]O2 with Two-Step Full Concentration Gradients. ACS Energy Letters, 1(1), 283–289.

[21] Liao, J.-Y., Oh, S.-M., & Manthiram, A. (2016). Core/Double-Shell Type Gradient Ni-Rich LiNi0.76Co0.10Mn0.14O2 with High Capacity and Long Cycle Life for Lithium-Ion Batteries. ACS Applied Materials & Interfaces, 8(37), 24543–24549.

[22] Wu, B., & Lu, W. (2017). Mechanical modeling of particles with active core–shell structures for lithium-ion battery electrodes. The Journal of Physical Chemistry C, 121(35), 19022-19030.

[23] Zhang, J., Yang, Z., Gao, R., Gu, L., Hu, Z., & Liu, X. (2017). Suppressing the Structure Deterioration of Ni-Rich LiNi0.8Co0.1Mn0.1O2 through Atom-Scale Interfacial Integration of Self-Forming Hierarchical Spinel Layer with Ni Gradient Concentration. ACS Applied Materials & Interfaces, 9(35), 29794–29803.

[24] Wu, F., Li, N., Su, Y., Shou, H., Bao, L., Yang, W., Zhang, L., An, R., & Chen, S. (2013). Spinel/Layered Heterostructured Cathode Material for High-Capacity and High-Rate Li-Ion Batteries. Advanced Materials, 25(27), 3722–3726.

[25] Cho, Y., Lee, S., Lee, Y., Hong, T., & Cho, J. (2011). Spinel-Layered Core-Shell Cathode Materials for Li-Ion Batteries. Advanced Energy Materials, 1(5), 821–828.

[26] Arora, P., Popov, B. N., & White, R. E. (1998). Electrochemical Investigations of Cobalt-Doped LiMn2 O 4 as Cathode Material for Lithium-Ion Batteries. Journal of the electrochemical society, 145(3), 807-815.

[27] Kim, J., Ma, H., Cha, H., Lee, H., Sung, J., Seo, M., Oh, P., Park, M., & Cho, J. (2018). A highly stabilized nickel-rich cathode material by nanoscale epitaxy control for high-energy lithium-ion batteries. Energy & Environmental Science, 11(6), 1449–1459.

[28] Robert Armstrong, A. (1998). The intercalation compound Li (Mn 0.9 Co 0.1) O 2 as a positive electrode for rechargeable lithium batteries. Chemical Communications, (17), 1833-1834.

[29] Zhou, F., Zhao, X., Bommel, A. V., Rowe, A. W., & Dahn, J. R. (2010). Coprecipitation Synthesis of NixMn1−x(OH)2Mixed Hydroxides†. Chemistry of Materials, 22(3), 1015–1021.

[30] Wang, J., Gao, A., Wang, R., Su, Y., Chen, S., & Wu, F. (2018). Effects of complexant concentration in base solution on the structure and electrochemical properties of LiNi0.8Co0.1Mn0.1O2. Proceedings of the 4th Annual International Conference on Material Engineering and Application (ICMEA 2017).

[31] Wang, D., Belharouak, I., Zhou, G., & Amine, K. (2013). Synthesis of lithium and manganese-rich cathode materials via an oxalate co-precipitation method. Journal of The Electrochemical Society, 160(5), A3108-A3112.

[32] Noh, M., & Cho, J. (2013). Optimized synthetic conditions of LiNi0. 5Co0. 2Mn0. 3O2 cathode materials for high rate lithium batteries via co-precipitation method. Journal of the Electrochemical Society, 160(1), A105-A111.

[33] Zhou, F., Zhao, X., Bommel, A. V., Rowe, A. W., & Dahn, J. R. (2010). Coprecipitation Synthesis of NixMn1−x(OH)2Mixed Hydroxides†. Chemistry of Materials, 22(3), 1015–1021.

[34] Wu, F., Tian, J., Su, Y., Wang, J., Zhang, C., Bao, L., He, T., Li, J., & Chen, S. (2015). Effect of Ni2+ content on lithium/nickel disorder for Ni-rich cathode materials. ACS applied materials & interfaces, 7(14), 7702-7708.

[35] Hu, G., Jiang, J., Peng, Z., Du, K., Cao, Y., & Duan, J. (2013). Syntheses of LiMn2O4 Nanoparticles with Nano-Size Precursor and Its Electrochemistry Performance. Journal of nanoscience and nanotechnology, 13(3), 2262-2265.

[36] Jin, G., Qiao, H., Xie, H., Wang, H., He, K., Liu, P., ... & Huang, C. (2014). Synthesis of single-crystalline octahedral LiMn2O4 as high performance cathode for Li-ion battery. Electrochimica Acta, 150, 1-7.

[37] Park, J. P., Kim, S. K., Park, J. Y., Hwang, C. H., Choi, M. H., Kim, J. E., Ok, K.M., Kwak, H.Y., & Shim, I. W. (2009). Syntheses of Mn3O4 and LiMn2O4 nanoparticles by a simple sonochemical method. Materials Letters, 63(26), 2201-2204.

[38] Ruan, Y., Song, X., Fu, Y., Song, C., & Battaglia, V. (2018). Structural evolution and capacity degradation mechanism of LiNi0. 6Mn0. 2Co0. 2O2 cathode materials. *Journal of Power Sources*, *400*, 539-548.

[39] Xu, Y. D., Xiang, W., Wu, Z. G., Xu, C. L., Li, Y. C., Guo, X. D., Lv, G.P., Peng, X., & Zhong, B. H. (2018). Improving cycling performance and rate capability of Ni-rich LiNi0. 8Co0. 1Mn0. 1O2 cathode materials by Li4Ti5O12 coating. Electrochimica Acta, 268, 358-365.

[40] Fu, F., Wang, Q., Deng, Y. P., Shen, C. H., Peng, X. X., Huang, L., & Sun, S. G. (2015). Effect of synthetic routes on the rate performance of Li-rich layered Li 1.2 Mn 0.56 Ni 0.12 Co 0.12 O 2. Journal of Materials Chemistry A, 3(9), 5197-5203.

[41] Yang, X., Qu, F., Niu, H., Wang, Q., Yan, J., & Fan, Z. (2015). High-performance aqueous asymmetric supercapacitor based on spinel LiMn2O4 and nitrogen-doped graphene/porous carbon composite. *Electrochimica Acta*, *180*, 287-294.

[42] Tang, X., Zhou, J., Bai, M., Wu, W., Li, S., & Ma, Y. (2019). *Journal of Materials Chemistry A*, *7*(21), 13364-13371.

[43] Pimenta, V., Sathiya, M., Batuk, D., Abakumov, A. M., Giaume, D., Cassaignon, S., Larcher, D., & Tarascon, J. M. (2017). Synthesis of Li-rich NMC: a comprehensive study. Chemistry of Materials, 29(23), 9923-9936.

[44] Ye, D., Zeng, G., Nogita, K., Ozawa, K., Hankel, M., Searles, D. J., & Wang, L. (2015). Understanding the Origin of Li2MnO3 Activation in Li-Rich Cathode Materials for Lithium-Ion Batteries. Advanced Functional Materials, 25(48), 7488-7496.

[45] Zhao, W., Xiong, L., Xu, Y., Li, H., & Ren, Z. (2017). High performance Li2MnO3/rGO composite cathode for lithium ion batteries. Journal of Power Sources, 349, 11-17.

[46] Mu, L., Lin, R., Xu, R., Han, L., Xia, S., Sokaras, D., Steiner, J., Weng, T., Nordlund, D., Doeff, M., Liu, Y., Zhao, K., Xin, H., & Lin, F. (2018). Oxygen release induced chemomechanical breakdown of layered cathode materials. Nano letters, 18(5), 3241-3249.

[47] Zheng, S., Hong, C., Guan, X., Xiang, Y., Liu, X., Xu, G. L., Liu, R., Zhong, G., Zheng, F., Li, Y., Zhang, X., Ren, Y., Chen, Z., Amine, K., & Yang, Y. (2019). Correlation between long range and local structural changes in Ni-rich layered materials during charge and discharge process. Journal of Power Sources, 412, 336-343.

[48] Li, C. Y.; Tian, Z. Q.; Yu, Y.; Wang, C.; Zhang, Y.; Zheng, S. Y.; Li, J. F.; Maglia, F.; Jung, R.; Shao-Horn, Y. Surface Changes of LiNixMnyCo1-x-YO2 in Li-Ion Batteries Using in Situ Surface-Enhanced Raman Spectroscopy. *J. Phys. Chem. C* **2020**, *124* (7), 4024–4031. https://doi.org/10.1021/acs.jpcc.9b11677

[49] Ramana, C. V.; Massot, M.; Julien, C. M. XPS and Raman Spectroscopic Characterization of LiMn2O 4 Spinels. *Surf. Interface Anal.* **2005**, *37* (4), 412–416. https://doi.org/10.1002/sia.2022

[50] Ruther, R. E., Callender, A. F., Zhou, H., Martha, S. K., & Nanda, J. (2014). Raman microscopy of lithium-manganese-rich transition metal oxide cathodes. Journal of The Electrochemical Society, 162(1), A98-A102.

[51] Li, X., Colclasure, A. M., Finegan, D. P., Ren, D., Shi, Y., Feng, X., Cao, L., Yang, Y., & Smith, K. (2019). Degradation mechanisms of high capacity 18650 cells containing Si-graphite anode and nickel-rich NMC cathode. Electrochimica Acta, 297, 1109-1120.

[52] Chung, S. H., & Manthiram, A. (2013). Lithium–sulfur batteries with superior cycle stability by employing porous current collectors. Electrochimica Acta, 107, 569-576.

[53] Liu, Z., Lee, J. Y., & Lindner, H. J. (2001). Effects of conducting carbon on the electrochemical performance of LiCoO2 and LiMn2O4 cathodes. Journal of power sources, 97, 361-365.

[54] Tang, K., Yu, X., Sun, J., Li, H., & Huang, X. (2011). Kinetic analysis on LiFePO4 thin films by CV, GITT, and EIS. Electrochimica Acta, 56(13), 4869–4875.

[55] Mohanty, D., Dahlberg, K., King, D. M., David, L. A., Sefat, A. S., Wood, D. L., Daniel, C., Dhar, S., Mahajan, V. Lee, M., & Albano, F. (2016). Modification of Ni-rich FCG NMC and NCA cathodes by atomic layer deposition: preventing surface phase transitions for high-voltage lithium-ion batteries. Scientific reports, 6, 26532.

[56] Zhao, W., Zheng, J., Zou, L., Jia, H., Liu, B., Wang, H., Engelhard, M., Wang, C., Xu, W., Yang, Y., & Zhang, J. G. (2018). High voltage operation of Ni-rich NMC cathodes enabled by stable electrode/electrolyte interphases. Advanced Energy Materials, 8(19), 1800297.

[57] Jung, R., Morasch, R., Karayaylali, P., Phillips, K., Maglia, F., Stinner, C., Shao-Horn, Y., & Gasteiger, H. A. (2018). Effect of ambient storage on the degradation of Ni-rich positive electrode materials (NMC811) for Li-ion batteries. Journal of The Electrochemical Society, 165(2), A132-A141.

[58] Shkrob, I. A., Gilbert, J. A., Phillips, P. J., Klie, R., Haasch, R. T., Bareño, J., & Abraham, D. P. (2017). Chemical weathering of layered Ni-rich oxide electrode materials: evidence for cation exchange. Journal of The Electrochemical Society, 164(7), A1489-A1498.

Chapter 4. Stability Enhancement and Microstructural Modification of Ni-rich Cathodes through the Partial Addition of Lithium Halide Salts

Luqman Azhari[1], Bryer Sousa[1], Ridwan Ahmed[1], Rui Wang[1], Zhenzhen Yang[2], Guanhui Gao[3], Yimo Han[3], Yan Wang[1]

1 Department of Mechanical and Materials Engineering, Worcester Polytechnic Institute, 100 Institute Road, Worcester, MA, 01609, USA

2 Chemical Science and Engineering Division, Argonne National Laboratory, 9700 S. Cass Avenue, Lemont, Illinois 60439, United States

3 Rice Electron Microscopy Center, Rice University, 6100 Main Street, Houston, Texas, USA 77005

Submitted to: ACS Applied Materials & Interfaces. Currently in review

Elemental doping is an effective strategy to modify surface and bulk chemistry in NMC cathode materials. By adding small amounts of lithium halide salts during the calcination process, the Ni-rich NMC811 cathode is doped with Br, Cl, or F halogens. The dopant type has a significant impact on the lithiation process and heavily influences the final cathode porosity and surface morphology. Utilizing a variety of electrochemical, surface, and bulk characterization techniques, it is demonstrated that an initial content of 5mol% LiBr or LiCl in the lithium source is effective in improving capacity retention while also providing excellent rate performance. The improvements are attributed to a substantial increase in specific surface area, the formation of a stable CEI layer, and suppressed surface reconstruction. In addition, the particle microstructure is

better equipped to handle cyclic volume changes with increased values of critical crack length. Overall, it is demonstrated that anion doping via addition of lithium halide salts is a facile approach towards Ni-rich NMC modification for enhanced cathode performance.

4.1 Introduction

Over the past several decades, lithium-ion batteries (LIBs) have become essential in powering electronics, from portable devices to electric vehicles. As new technologies become more widely accepted and implemented, the demand for LIB production is expected to scale exponentially [1,2]. The resulting demand is expected to strain manufacturers to provide an adequate supply at a low cost while improving performance, especially when considering the concerns around cobalt, a critical component in currently utilized LIB cathodes. The mining and production of cobalt has considerable supply chain vulnerabilities and historically demonstrated price volatility [3,4]. Manufacturers can resolve these issues by improving the specific capacity and reducing materials costs for next-generation LIBs, mainly through design and modification of the cathode chemistry. Most LIB cathodes utilized today are composed of transition metal layered oxides of the $LiMO_2$ form, with M representing transition metal(s) and typically comprising Ni, Mn, or Co. This stoichiometry commonly forms the layered R-3m structure, defined by alternating TM-O and Li-O octahedra layers with 2D Li^+ diffusion channels [5,6], and demonstrates a class of materials exhibiting among the highest practical specific energies of all cathode chemistries due to a high operating voltage >3.5 V vs Li/Li^+ and specific capacities ranging from 140-200 mAh/g, depending on the chemistry. One such class of materials is referred to as "NMC," defined by the composition $LiNi_xMn_yCo_zO_2$. Significant efforts have been made to develop NMC compositions that reduce the costly cobalt fraction and increase the nickel content, which

typically increases the reversible capacity of the overall material by allowing for deeper levels of delithiation at similar cutoff voltages while also being a cheaper ore to mine [2–4,6,7].

While strides have been made towards shifting from NMC111 to NMC532 and NMC622, shifts to even higher nickel fractions > 80% have been met with much difficulty [3,6,8,9]. For example, NMC811 ($LiNi_{0.8}Mn_{0.1}Co_{0.1}O_2$), with a demonstrated reversible capacity of 200 mAh/g, is challenging to use in practical applications due to its fast capacity fade. Furthermore, as the nickel content in NMC increases, the material becomes more inherently unstable and prone to degradation as it is put through repeated charge and discharge, which results in premature cell failure and safety concerns. These degradation mechanisms have been a subject of extensive investigation and are due to a variety of factors such as reactivity of high valence Ni^{4+} with the electrolyte at the electrode surface [10,11], the release of lattice oxygen [12,13], nickel reduction to Ni^{2+} with subsequent migration to the Li layer [14,15], surface reconstruction from the R-3m layered structure to resistive spinel and subsequent Fd-3m rock-salt phases [12,14–16], and intergranular fracture from sharp anisotropic volume changes [17–19]. There are many challenges concerning Ni-rich cathode materials, and these obstacles must be overcome to enable implementation for commercial use.

The addition of dopants added in concentrations < 10 mol% is a standard modification route toward addressing the limitations of NMC811 by modifying chemical and physical properties, and extensive work has been conducted and studied on doped Ni-rich cathodes [6,9,14,20–24]. For example, Al substituting on the TM site was found to improve the chemical stability of the cathode due to stronger Al-O bonding preventing structural disorder [20,23]. B and Ta dopants

facilitated crystal growth of thin, radially aligned primary particles to inhibit microcracking [25,26]. Other dopants, such as Mg, Zr, Ti, Zn, and Nb, have also been demonstrated for NMC-type cathodes, with various degrees of impact on the cathode properties [14,20,27,28]. However, while cation doping has been extensively studied, anion doping of NMC cathodes is surprisingly not as well explored. Anion doping has inherent advantages in it avoids the substitution of Li or transition metal sites, which is an attribute of cationic doping that can lower the practical energy density by either reducing the content of redox active species or act as obstacles for Li diffusion [14]. In the past several years, some works have demonstrated various types of anion doping on layered oxide cathodes such as F-doping of Li-rich oxides with anionic redox activity to stabilize lattice oxygen [29,30]. Other studies focused on NMC compositions have mostly been limited to NMC111 and other chemical analogues with lower Ni content [31,32]. In addition, several computational studies have been conducted on the incorporation of F, S, and Cl dopants on the $LiNiO_2$ system, showing conflicting roles of anion dopants towards the cathode properties such as cation mixing, lithium mobility, and redox potential, but have not been corroborated with experimental results nor consider the dopant source [33].

In this work, NMC811 is partially doped with Br, Cl, or F halogen ions through the addition of LiX (X = Br, Cl, F) during initial lithiation and calcination, with a doping level of 5 mol% initially targeted. It is demonstrated that the addition of halide salts has significant impacts on the cathode microstructure and surface chemistry, which in turn impacts the electrochemical performance. Lithium chloride and bromide are notably found to improve capacity retention while also increasing the accessible specific capacity by 10% compared to its undoped counterpart. Lithium fluoride did not noticeably improve the capacity fade nor accessible

capacity within the doping ranges tested and in contrast, negatively affected the reversible capacity under increasing charge/discharge rates. Improvements in the case of Cl and Br were attributed to a lower lithiation temperature due to the partial formation of low melting eutectic salt and increased electrochemically active surface area. During extended cycling, disorder and surface reconstruction at the particle surface/subsurface was suppressed due to the formation of a stable and passivating cathode electrolyte interface (CEI). This work demonstrates the viability of anion doping and potential for microstructural modification through the simple addition of lithium halide salts.

4.2 Experimental Methods

4.2.1 Synthesis of the NMC precursor

NMC811 hydroxide precursors were synthesized via a co-precipitation route described in a previous study [34]. Summarily, a solution of transition metal sulfates in the desired stoichiometric ratio is added dropwise to a glass jacked reactor alongside the addition of an ammonia solution that functions as a chelating agent. The reactor pH is maintained at 11.0 ± 0.2 using a pH controller and NaOH buffer solution, which also functions as the precipitating agent. The reaction is allowed to run for 8 hrs under a constant stirring at 55 °C under nitrogen atmosphere. Afterward, the metal hydroxide precipitates are filtered from the solution, washed thoroughly with deionized water, and then dried at 100 °C. The final product consists of spherical transition metal hydroxide precursors approximately 6-8 μm in diameter and composed of thin, plate-like primary particles.

4.2.2 Synthesis of pristine NMC811

Undoped NMC811, referred to as "pristine NMC811" or "PR," is synthesized by mixing the hydroxide precursor described in section 2.1 with lithium hydroxide monohydrate using a mortar and pestle. The molar ratio of transition metal to Li is 1.00:1.05, with the excess lithium needed to account for partial lithium volatilization during sintering [35]. The mixture is sintered in an alumina crucible under 50 sccm flowing oxygen in a two-step process; the mixture is first sintered at 450 °C for 5 hrs then reground to homogenize possible irregularities in the lithium distribution further. Then a second sintering step is performed at 775 °C for 15 hrs to fully lithiate and densify the secondary particles.

4.2.3 Synthesis of the modified cathode

Modified NMC811 samples are synthesized using a similar route as pristine NMC811. However, the mixture differs with partial substitution of the LiOH lithium source with LiX (X = Br, Cl, or F) while maintaining a total 5 mol% excess of Li. The doping content is relative to the number of moles of transition metals. For example, in the 5 mol% chlorine doped sample, the molar ratios of transition metal hydroxide precursor to LiOH to LiCl is 1.00:1.00:0.05. While several doping levels were tested, 5 mol% was the doping concentration chosen for further analysis. Before mixing, LiCl and LiBr were dried thoroughly in a vacuum oven and stored in a desiccator to limit measurement errors in the targeted doping concentration due to the inherent hygroscopic nature of these lithium salts in an ambient environment. The final mixture is sintered according to the same furnace profile used for pristine NMC811. The samples are labeled as 5Br, 5Cl, and 5F representing 5 mol% doping amounts of bromine, chlorine, and fluorine, respectively.

4.2.4 Preparation of cathode and coin cells

Electrode films were prepared using traditional slurry casting methods. The active cathode material was mixed thoroughly with carbon black as a conductive additive and polyvinylidene fluoride (PVDF) as a binder in a weight ratio of 8:1:1, with n-methyl-2-pyrrolidone (NMP) as a solvent. The mixture was homogenized using a FlakTek Speedmixer and subsequently cast onto 15 μm thick aluminum foil with a doctor blade set to 150 μm in height. The electrode is allowed to dry in air at 60 °C overnight, followed by 12 hrs at 120 °C in a vacuum oven to remove residual water and solvent thoroughly. The dried electrode is punched into discs 12.5 mm in diameter, calendared to ~35-38 μm in total thickness, and stored in an argon glovebox until further use. The electrode active mass was maintained between 2.85-3.4 mg/cm^2. 2032-type coin cells were formed using a half cell setup, with lithium metal as the anode and a celgard polyolefin film as the separator. The electrolyte was composed of 1 M $LiPF_6$ in EC/EMC (3:7 weight ratio). The as-prepared coin cells were subjected to a formation procedure consisting of 2 charge/discharge activation cycles between 2.8-4.5 V at C/20.

4.3 Characterization Methods

4.3.1 Physical and Mechanical Properties

The surface morphology of the as-prepared cathode powders was analyzed via scanning electron microscopy (SEM) analysis using a JEOL JSM-7000F SEM with a 10 kV accelerating voltage. Cross-sections were obtained by embedding the powders in resin, followed by polishing, which cleaved the secondary particles to reveal a fractured particle interior. High-resolution transmission electron microscopy (HRTEM) is performed with a double correctors Titan cubed Themis 300 operated at 300 kV, equipped with a Ceta camera, Gatan Quantum 966 energy filter, and an electron monochromator. Dynamic light scattering particle size analysis was conducted

using a SALD-7101 Nano Particle Size Analyzer to determine the d50 values. Specific surface area measurements of the cathode powders were determined via Brunauer-Emmet-Teller (BET) method on a Micromeritics ASAP 2020, with degassing as a pretreatment. TGA/DSC measurements of the mixed lithium salts and hydroxide precursors were conducted using a simultaneous TGA and DSC instrument. Mixtures were placed in uncovered alumina crucibles and heated under dry air flow to an upper temperature of 775°C at a rate of 2°C/min.

X-ray diffraction (XRD) profiles of the loose cathode powders were obtained using a PANalytical Empyrean X-ray Diffractometer with a Cu Kα radiation source (λ = 1.5406 Å) and step size of 0.0167° per step. In addition, crystallographic lattice parameters and degree of cation mixing were determined through the Rietveld refinement method via FullProf Suite software, using the R-3m space group as the structural reference and assuming no secondary impurity phases.

Porosity quantification was achieved via two-dimensional image analysis using ImageJ (National Institutes of Health, Bethesda, MD) protocols. Since each powder studied maintained a significant number of particles that were fully dense under SEM, the porosity analysis only served to quantify the difference in porosity across particles found to contain observable pores. Accordingly, the porosity was measured for at least ten cross-sectioned particles per sample. Once cross-sections were examined using a Zeiss Evo Series Benchtop and W-filament SEM. Secondary emission electron SEM micrographs were obtained between 15-20 kV.

To obtain high-fidelity SEM micrographs, argon ion beam cross-sectional polishing was applied to the cast electrodes associated with each sample. Samples were ion-mill polished using a JEOL IB-19530CP Cross Section Polisher (Tokyo, Japan). Electrodes were first fixed to a sacrificial backing and then milled using argon gas at 8 kV for 2 h (7200 s). Depending on the sample under consideration, this procedure was used, or an alternative procedure was applied, wherein ~6.5-7 kV was applied for 1.25 hrs with a 3-to-5 s on-off alternating cycle employed to prevent binder degradation-induced chamber pressurization.

The fracture strength (σ_f) of the NMC powder particles demonstrating brittle failure under compressive loading was achieved for as synthesized and charged samples for each doped sample. σ_f was obtained using a microparticulate compression testing system (MCT) from Shimadzu wherein <1 mN/s loading rates were applied to at least 15 particles per condition in both the as synthesized and charged state. σ_f measurements were computed as a function of the breakage load and particulate diameter based upon the standard JIS R 1639-5 [36]

4.3.2 Chemical Properties

Chemical compositions were determined through inductively coupled plasma optical emission spectrometry (ICP-OES), using a Perkin-Elmer Optima 8000 ICP-OES system. Chemical mapping of selected particles were obtained using the TEM instrumentation's energy-dispersive X-ray spectroscopy (EDS) functions. X-ray photoelectron spectra (XPS) were collected using a PHI 5000 VersaProbe II system (Physical Electronics). Individual scans at the O 1s, C 1s, Co 2p3, Mn 2p3, Ni 2p3, and relevant halogen peaks were collected at a pass energy of 23.50 eV and electron escape angle of 45^{o} to the sample plane. Ni 2p3 and O 1s spectra were deconvoluted

and fitted using XPSPeak software to analyze surface element oxidation states from powders in the as-synthesized state and electrodes taken from disassembled cells after cycling

4.3.3 Electrochemical Measurements

Electrochemical charge/discharge cycles were conducted at ambient room temperature on a LANDT CT2001A from 2.8-4.5 V (specific capacity set to 200 mAh/g). Extended cycling of cells was conducted at a charge/discharge rate of 0.5 C for up to 100 cycles. Rate performance was tested for each sample, using rates of C/10, C/5, C/2, 1C, 2C, and 3C. Cyclic voltammetry (CV) profiles and electrochemical impedance spectra (EIS) were obtained using a Bio-logic SAS VMP3 multi-channel Potentiostat maintained at 30 °C. CV and EIS data were obtained for cells before and after 100 galvanostatic charge/discharge cycles. CV profiles were obtained at a scan rate of 0.1 mV/s between 2.8-4.5 V vs. Li/Li^+. EIS was obtained using a 10 mV sinusoidal amplitude from 1 MHz to 20 mHz. Galvanostatic intermittent titration technique (GITT) was utilized to determine lithium diffusion coefficients and was conducted using a C/10 current pulse for 0.5 hrs, followed by 1.5 hrs of resting time. GITT measurements for each sample were collected across one full charge cycle.

4.3.4 Computational Methods

Density functional theory calculations were used to evaluate the effect of halogen doping on the electronic structure of the cathode material, using $LiNiO_2$ as a reference model system for simplicity. All calculations were carried out using Quantum Espresso package [37] and the generalized gradient approximation (GGA) of Perdew-Burke-Ernzerhof (PBE) is utilized for the exchange correlation potential. The Hubbard U correction of U_{eff} = 6.37 eV was used for the Ni d

states [38]. The plane wave cut-off energy was set to 450 eV and a k-point of 3 × 3 × 3 grid mesh for the Brillouin zone sampling. The energy convergence criterion of 10^{-6} eV and a value of 0.001 eV/ Å for the force convergence criterion were set for the electronic structural optimization. Doping was realized by constructing a 2 × 2 × 1 supercell from the hexagonal structure (R-3m space group) of $LiNiO_2$ and substituting one of the O atoms in the supercell with a F, Cl, or Br atom.

4.4 Results and Discussion

4.4.1 Morphology, Surface Area, Mechanical Properties

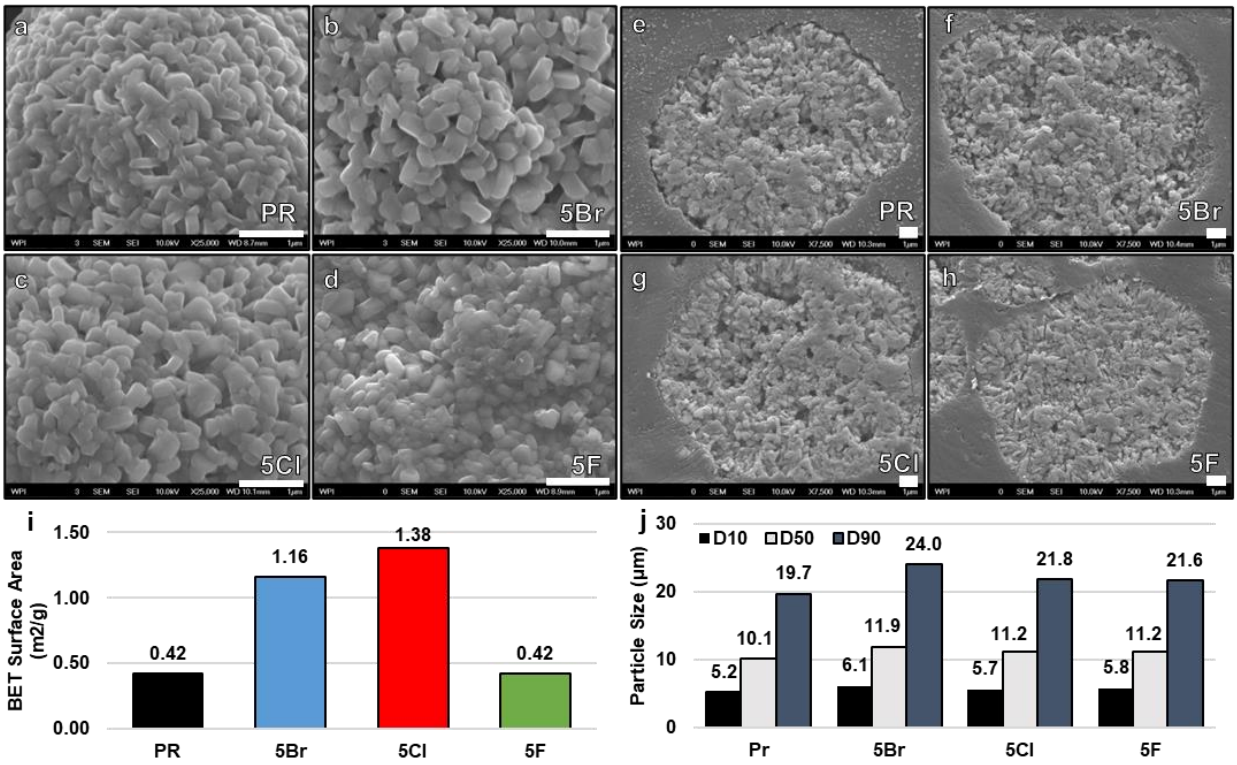

Figure 20: SEM images of the surface morphology and cross sections of (a,e) PR, (b,f) 5Br, (c,g) 5Cl, and (d,h) 5F, as synthesized. Specific surface area determined through BET measurement (i) and corresponding d10, d50, and d90 particle sizes (j). Scale bars are set to 1µm.

As shown in **Figure 20a**, the secondary particle surface for PR is composed of densely packed, slightly elongated block-like particles. This is consistent with the morphologies observed in NMC811 powders synthesized via a coprecipitation route [6,39]. However, an evident change in morphology is observed after adding Br, Cl, or F dopants, as shown in **Figures 20b-d, S1**. The addition of LiBr and LiCl results in substantially more porous surface morphology, with noticeable gaps in between primary particles. In addition, the primary particles for 5Br and 5Cl are slightly larger than those of PR, a result which was also observed in a similar doping study for NMC111[32]. Whereas in the case of LiF, the particle morphology remains dense with smaller block-like primary particles compared to PR. Cross-sections of cleaved secondary particles for each sample were obtained and shown in **Figure 20e-h, S2-4**, which shows that the porosity observed at the surface is also observed in the particle's interior. 5Cl and 5Br samples exhibited more pores and cavities within the interior of the secondary particles, whereas PR and 5F generally exhibited a more uniform, dense packing of primary particles. However, this is a qualitative observation of the particle interior and exact information on pore size and distribution could not be determined without the application of porosimetry techniques. The secondary particles for all samples were consistent, being composed of spherical particles approximately 10 μm in diameter [**Figure S1**]. Increasing the amount of Br or Cl resulted in more porous morphologies, while decreasing the amount expectedly results in a morphology closer to that of PR [**Figure S5**].

A combination of BET measurements and particle size analysis reveal significant differences in the specific surface area across the samples [**Figure 20i, j**]. PR and 5F powders have identical surface areas of 0.42 m^2/g, indicating that fluorine doping has a negligible influence on the

secondary particle surface area. In contrast, 5Br and 5Cl display specific surface areas over two times higher than PR, at 1.16 and 1.38 m^2/g, respectively. This is consistent with the observed surface morphology and interior porosity from SEM imaging. Particle size distributions shown in **Figure 20j and Table S1** demonstrate that secondary particle size is unaffected across all samples, which is to be expected and corroborates the SEM imaging results, verifying that the increase in specific surface area is solely due to changes in the particle morphology/porosity. The increased surface area of the NMC secondary particles is expected to allow for more thorough penetration of electrolyte into the secondary particle surface and a subsequently increase in electrochemically active surface area.

The increase in surface area is hypothesized to be due to a combination of the dopant effect on primary particle growth, molten salt-assisted growth, and gas evolution during the initial calcination. Based on the binary phase diagrams for LiOH-LiBr and LiOH-LiCl, a low eutectic melting point exists at ~260 °C and 270 °C respectively, significantly lower than either component in its pure state [40,41]. Therefore, even with the small addition of LiBr or LiCl in the binary system as demonstrated, a partial melt is predicted to form at or below 300 °C. On the contrary, LiF-LiOH compositions exhibit a eutectic temperature around 425 °C, which is only moderately lower than pure LiOH (460 °C). With the initial Li-salt composition composed of 95.2 mol% LiOH and 4.8 mol% LiX, the partial melt would form near 300 °C in the case of LiBr and 270 °C in the case of LiCl.

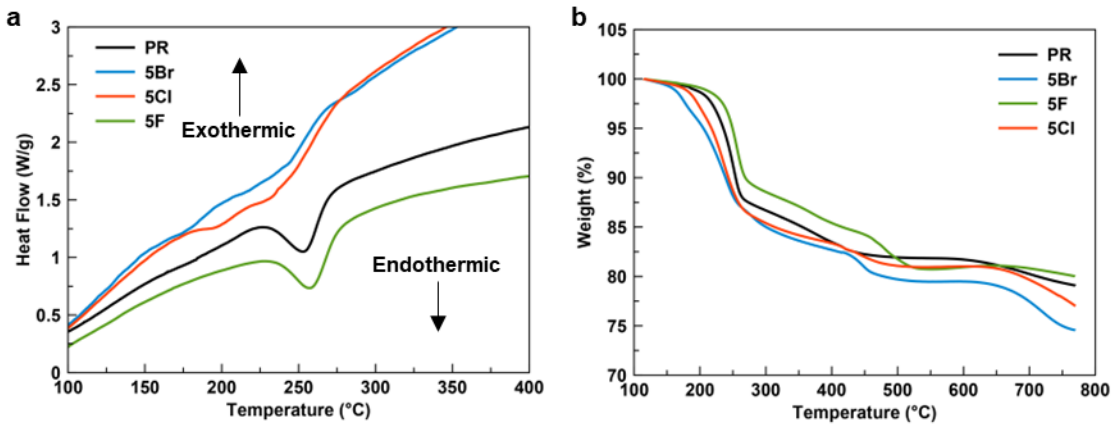

Figure 21: DSC curves of precursor and lithium salt mixtures during initial lithiation (a) and corresponding TGA/weight loss curves (b). The constant increase in the DSC curves is associated with instrument drift.

DSC curves of the initial hydroxide precursor/Li mixtures are shown in **Figure 21a**. A notable difference in the curves can be observed between 150-300 °C. PR and 5F display firm endothermic peaks at ~260 ˚C, which can be attributed to the decomposition of transition metal hydroxides to oxides and subsequent generation of H_2O vapor [42,43]. This conversion typically precedes lithiation, which occurs at or after the melting point of the lithium source (460 ˚C for pure LiOH), although some reports suggested that a solid-state lithiation of the oxide can occur at temperatures below the melting point [44]. In the case of 5Br and 5Cl samples, the endothermic peak intensity is mostly suppressed, which suggests that simultaneous exothermic reaction(s) are occurring within this temperature range. While the partial formation of low-temperature melt is expected to form around this temperature, a more intense endothermic peak should have been observed. Thus, the observation of an exothermic reaction can be attributed to the lithiation reaction of the NMC precursor in this temperature range [44]. This is also corroborated with the DSC curves between 400-500 °C, where melting of LiOH and lithiation would occur [**Figure S6**]; the intensity of the endothermic peak for 5Br and 5Cl is relatively reduced than that of PR

and 5F, indicating that a higher fraction of the Li salts has already been consumed in a lithiation reaction at a lower temperature.

Due to the formation of melt and onset of lithiation occurring at a lower temperature simultaneous with precursor decomposition for 5Br and 5Cl, primary particle growth is enhanced by a molten salt assisted route and longer coarsening time, resulting in the larger primary particles and the formation of gaps and pores in the secondary particle due to the increased coalescence of primary particles. The addition of more LiBr or LiCl naturally furthers this phenomenon by increasing the fraction of melt present, and the formation of faceted primary particles and more intergranular gaps are observed as a product of increased molten salt-assisted growth [45,46] as shown in **Figure S5d, e**.

TGA analysis of precursor/Li-salt mixtures in **Figure 21b** reveals that near the end of the calcination cycle above 650 ˚C, 5Br and 5Cl samples exhibit a faster change in weight loss compared to PR and 5F. It is suspected that this weight loss observed for 5Br and 5Cl may stem from partial volatilization of remaining LiBr or LiCl, resulting in partial gas evolution rather than doping into the structure, although this is not exactly confirmed. Generation of gasses during primary particle growth could also facilitate the formation of the porous secondary particles observed. In contrast, 5F samples exhibit similar weight loss behavior as PR, implying no gas evolution from the halide salt during the lithiation/calcination of the precursor, which would also correlate with the dense secondary particles observed. It is also worth noting that the onset of weight loss between 150-300 ˚C for 5Br and 5Cl occurs at a lower temperature and the initial

loss is much smoother than that of PR and 5F, further indicating the earlier onset of lithiation during the metal hydroxide to oxide transition formation.

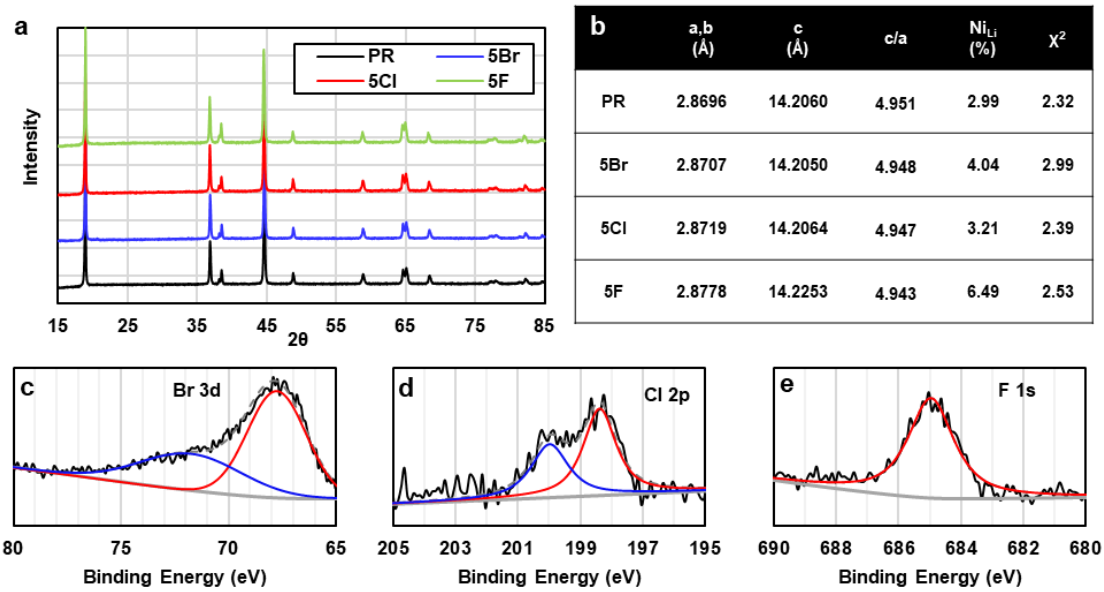

b	a,b (Å)	c (Å)	c/a	Ni_{Li} (%)	X^2
PR	2.8696	14.2060	4.951	2.99	2.32
5Br	2.8707	14.2050	4.948	4.04	2.99
5Cl	2.8719	14.2064	4.947	3.21	2.39
5F	2.8778	14.2253	4.943	6.49	2.53

Figure 22: (a) Powder X-Ray diffraction profiles revealing no noticeable impurity phases and (b) corresponding refined lattice parameters and calculated interlayer mixing concentrations. (c-e) XPS spectra of the relevant halogen binding energy for each anion doped sample

Powder XRD profiles of the as-synthesized powders are shown in **Figure 22a,** and all samples are well indexed to the R-3m layered structure. No impurity phases are detected across all samples, with excellent crystallinity as evidenced by well defined (006)/(102) and (018)/(110) peak separation. However, the doped samples all exhibit slightly reduced ordering quality as evidenced by the lower c/a ratio. Rietveld refinement of the XRD profiles indicate that the doped samples have slightly larger lattice parameters than PR. The *a* lattice parameter is slightly increased for 5Br and 5Cl, which is expected due to a combination of the larger atomic radius of these halogens compared to oxygen and increased partial reduction of transition metal ions for

charge compensation. This is supported by the observed increase in Ni_{Li} shown in the table in **Figure 22b**. 5F, while having a smaller ionic radius than oxygen, was observed to have significantly increased *a* and *c* lattice parameters and can be attributed to the larger degree of cation mixing of 6.49%, compared to 2.99% for PR, and is consistent with previous studies on fluorine doping [33,47,48]. Since a similar halogen doping level should ideally result in similar levels of cation mixing due to charge compensation considerations [49], the noticeably lower degree of cation mixing for 5Br and 5Cl samples compared to 5F may be further evidence of the occurrence of partial volatilization of LiCl or LiBr inferred from TGA/DSC results, which would result in an actual doping level less than the 5 mol% target.

4.4.2 Composition, Surface Chemistry

ICP-OES verifies the chemical compositions of all samples to be close to the targeted NMC811 stoichiometry [**Table S2**]. In addition, the Li/TM ratio is between 1.021-1.054 across all samples, indicating no issues concerning lithium deficiency due to volatilization despite the partial substitution of lithium halide salts. A combination of XPS spectra and EDS mapping shown in **Figures 22c-e and Figure S7** verifies the presence of each respective halide dopant, which is distributed uniformly across the entire particle. EDS signals for Br and Cl elements are notably weaker than that of F, which supports the TGA results and further suggests a degree of volatilization of these halogens and a doping content less than the 5 mol% target. The distribution of Ni, Mn, and Co elements are also uniformly distributed across the primary particles in the expected stoichiometry, and no segregated particles of halide-rich materials were observed in the images taken.

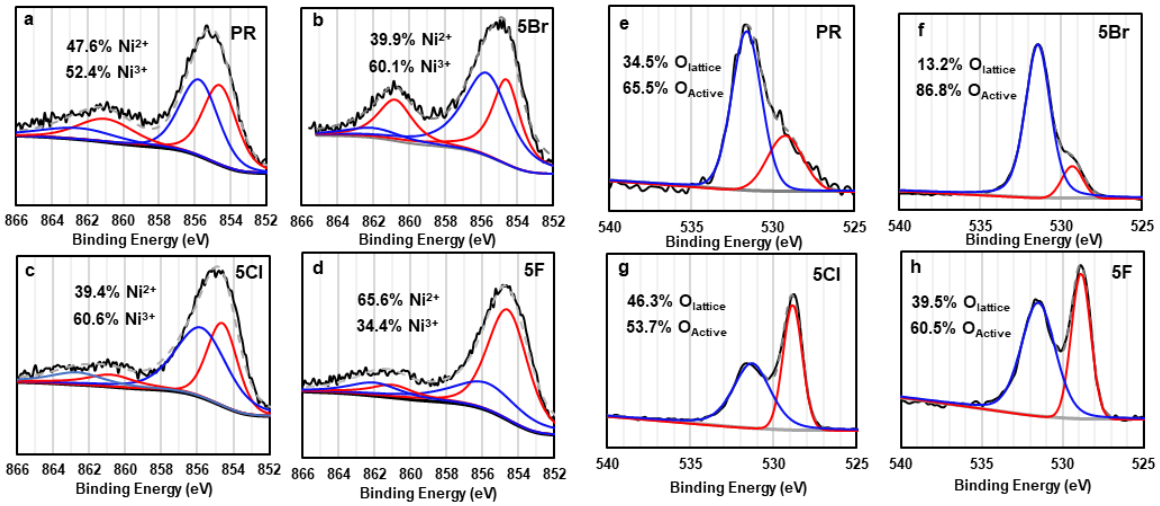

Figure 23: Deconvoluted and fitted XPS peaks of the (a-d) Nickel 2p3/2 and (e-h) Oxygen 1s spectra for the as-synthesized powders

XPS analysis of the nickel and oxygen binding energies is shown in **Figure 23** and is utilized in characterizing the transition metal valence state and oxygen chemical structure. The main nickel $2p^{3/2}$ peak is observed at ~855 eV, with a satellite peak observed at a higher binding energy of ~862 eV. Prior literature has shown that the Ni $2p^{3/2}$ peak and its satellite peak can be deconvoluted and fitted as a combination of Ni^{2+} and Ni^{3+}, centered around binding energies at 854.6 eV and 855.76 eV, respectively, for the main XPS peaks [50,51]. Satellite peaks can be fitted at 861 eV and 862.5eV [50,51]. By comparing the integrated intensity for each contribution, the average valence state analysis can be determined. As shown for the 5Br and 5Cl in **Figure 23a-d**, Ni^{3+} contributes to ~60% of the Ni $2p^{3/2}$ peak, but only 52.4% for PR and even lower for 5F at 34.4%. The low oxidation state for 5F is consistent with previous studies, which demonstrated increased nickel reduction at the surface of F-doped NMC samples [31]. The higher average nickel valence state for 5Br and 5Cl relative to PR is indicative of moderately better crystallinity and ordering at the surface for the doped samples, as nickel ideally remains in the 3+ oxidation state in a nickel rich $LiMO_2$ stoichiometry. Furthermore, the presence of Ni^{2+} in the XPS spectra is

often associated with cation mixing or surface reconstruction, which is a degradation mechanism that has been observed to occur for Ni-rich NMC cathodes when exposed to ambient conditions and has detrimental effects on the electrochemical performance [52,53]. Based on the results shown, it can be expected that the doped samples would have better initial electrochemical performance due to the superior surface quality.

Two distinct peaks can be observed in the O 1s XPS spectra, illustrated in **Figure 23e-h**, and can be identified as the lattice-bonded oxygen and active oxygen at ~529 eV and 531.5 eV, respectively [50]. The active oxygen stems from oxygen defects present near the surface/subsurface structure and is also thought to be the origin of harmful residual lithium compounds often present at the surface of NMC cathodes [24,54]; these residues form after calcination by reacting with carbon dioxide or water vapor via the following reactions.

$$O^{2-}_{active} + H_2O, CO_2 \rightarrow 2OH^-, CO_3^{2-} \quad (11)$$

$$2Li^+ + 2OH^-, CO_3^{2-} \rightarrow 2LiOH, Li_2CO_3 \quad (12)$$

PR contains a high fraction of active oxygen, with ~65% of the total signal correlating to active oxygen. 5F exhibits a similar ratio of active oxygen to lattice oxygen. In contrast, 5Cl exhibits a higher fraction of lattice oxygen, at 46.3%, indicating that a reduced amount of lithium residual compounds would be present compared to PR and 5F. In contrast, 5Br shows the lowest fraction of lattice oxygen and thus the highest fraction of oxygen defects, with only 13.2% of the signal being attributed to the lower energy peak.

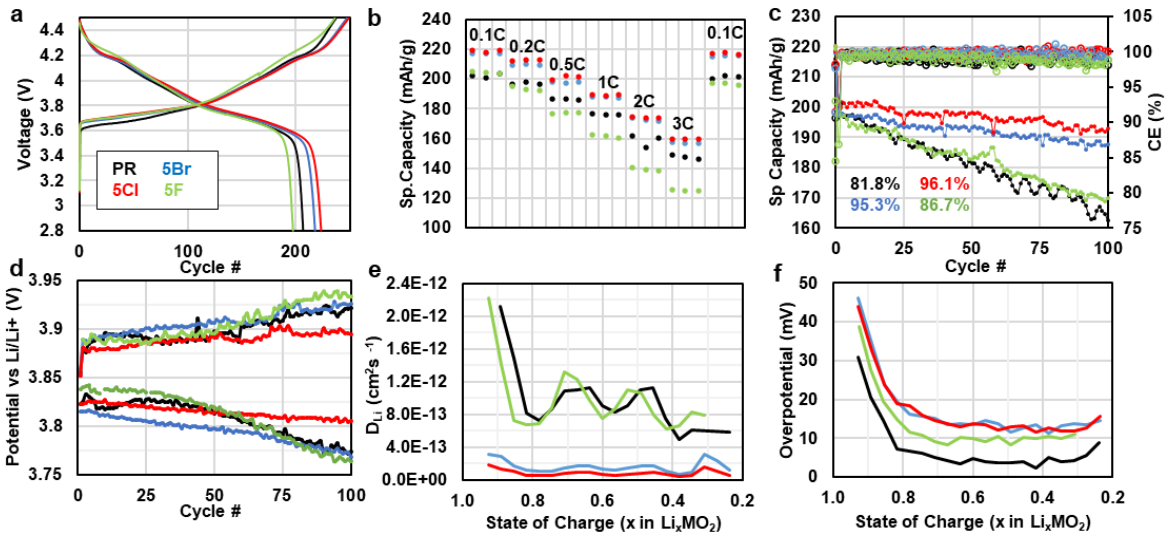

Figure 24: (a) First charge and discharge cycle. (b) Rate performance of samples cycled between 2.8-4.5V. (c) Galvanostatic charge-discharge cycling of half-cells at C/2 rate between 2.8-4.5V and corresponding specific discharge capacity. (d) Mean charge and discharge potential of half-cells over cycling. (e) Lithium diffusion coefficient determined from GITT measurements. Diffusion coefficients at high SOC (x > 0.8) are overestimated due to the rest potential not being fully relaxed before the next current pulse. (f) Potential drop vs SOC, obtained at beginning of current pulse

5Cl and 5Br samples exhibit noticeably increased reversible capacity, with initial discharge capacities of 225 mAh/g and 220 mAh/g at 0.05 C, respectively [**Figure 24a**]. In contrast, PR exhibited a capacity of 200 mAh/g under the same conditions, demonstrating a 10% improvement in accessible capacity through Br and Cl doping. In contrast, no improvement in accessible capacity is observed for 5F, with a slightly lower reversible capacity likely due to the increased fraction of electrochemically inactive Ni^{2+}. The capacity improvement for Br and Cl is also observed in lower and higher doping concentrations, shown in **Figure S8**. However, a significant drop in capacity is observed with increased F concentration, which is consistent with other observations and attributed to a further increase in cation mixing [49]. 5Cl and 5Br also exhibit superior capacity under high charge/discharge rates, with nearly 175 mAh/g at 2C,

compared to 154 mAh/g for PR. In contrast, 5F exhibited lower capacity under increasing charge/discharge rates [**Figure 24b**].

The improvements in reversible capacity for 5Br and 5Cl are attributed to the increased specific surface area, allowing for electrolyte penetration and thus higher electrochemically active sites. Whereas for 5F, the reduced capacity is a result from the significantly increased cation mixing and formation of Ni/Li antisite defects [33,49]. Improvement in rate performance across all modified samples is seen at a doping concentration of 2 mol%. However, there is an optimum upper limit to doping concentration; when increasing the doping content to 8 mol%, the performance of 8Br is similar to that of PR, while 8F has an even lower reversible capacity. 8Cl, in contrast, still maintains an improved rate capacity compared to PR. An optimum concentration clearly exists for each halogen doping regarding rate performance, and such dopant concentration optimization is beyond this work's scope.

Galvanostatic charge/discharge at a C/2 rate in **Figure 24c** demonstrates a significant improvement in capacity retention for 5Br and 5Cl. Whereas PR retains 81.8% of its initial capacity after 100 cycles, 5Cl and 5Br retain 96.1% and 95.3% of their initial capacity after 100 cycles, respectively, while also having a higher initial capacity. The improved capacity retention of 5Br and 5Cl is significant considering these materials' higher specific surface areas, which generally should facilitate faster capacity fade due to the more exposed surfaces detrimentally reacting with electrolyte [52,55,56]. Thus, 5Br and 5Cl samples indicate much better inherent surface stability than PR. 5F also demonstrates slightly improved capacity retention, although not nearly as significant as 5Br and 5Cl. F doping in lower amounts may be more beneficial to

capacity retention, with 1 mol% reported in other works as being effective [57,58]. Mean charge/discharge potentials during extended cycling in **Figure 24d** show that while 5F had an average discharge potential of around 20 mV higher compared to PR, 5Br decreased the average discharge potential by 10 mV, and 5Cl showed no change. After 100 cycles, 5Cl demonstrates superior voltage retention with only moderate change in both charge and discharge potential, while the rest of the samples show more severe potential polarization across 100 cycles.

GITT experiments for a single charge cycle were deconvoluted and interpreted to determine the lithium diffusion coefficients and potential drop vs. SOC. Lithium diffusion coefficients were determined based on the relationship developed by existing work [59] , with surface area estimated from the cell active mass and specific surface area determined from BET analysis. From **Figure 24e**, D_{Li+} for PR and 5F are similar, with a value of ~1.0E-12 cm^2/s across most of the SOC range tested, with some fluctuations due to the experimental conditions used. In contrast, D_{Li+} for 5Br and 5Cl one order of magnitude lower at ~1.0E-13 cm^2/s. Despite the lower diffusion coefficients, 5Cl and 5Br cathodes can maintain higher reversible capacity and improved rate performance attributed to the increased specific surface area. The exact reasons behind Br, Cl, and F doping influence on lithium diffusion would be of interest for future study and are beyond the scope of this work.

4.4.3 Post-Cycling Analysis

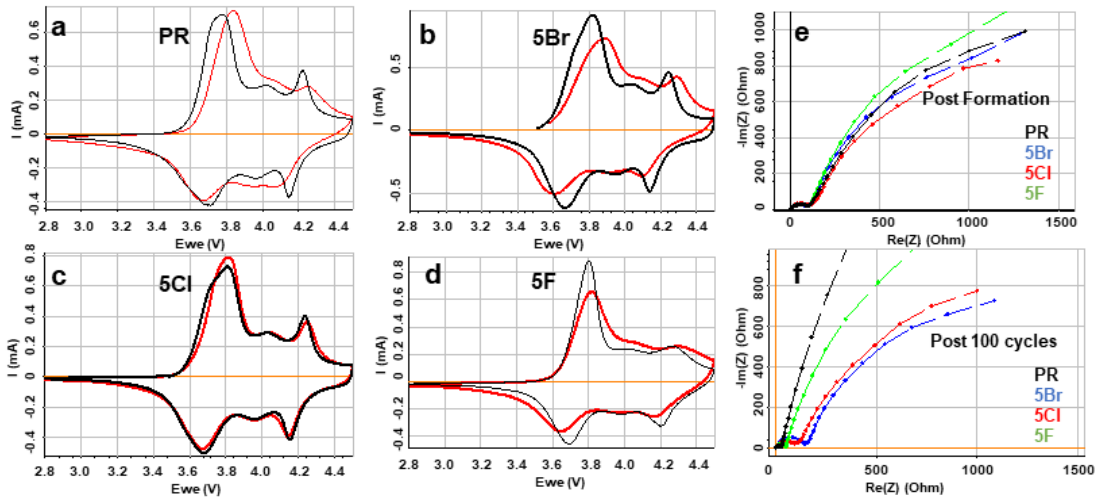

Figure 25: Cyclic voltammetry curves after initial formation cycles (black) and after 100 cycles (red) for pristine and doped samples (a-d). (e) Nyquist plots of samples after (e) initial formation cycles and (f) 100 cycles.

Cyclic voltammetry curves between 2.8-4.5 V exhibit three redox pairs at ~3.7 V, 4.0 V, and 4.2 V vs. Li/Li^+, with multiple reports associating these peaks with the H1→M, M→H2, and H2→H3 structural transitions [17]. Here, **Figure 25a-d** represents the initial state of each sample before and after 100 charge/discharge cycles. As can be seen for PR, the cycled cathode develops a higher polarization evidenced by increased ΔV between respective anodic and cathodic redox pairs and peak flattening and broadening due to degraded Li diffusion kinetics [60]. This is especially evident for the redox peaks in the high voltage region (>4.0 V) associated with the H2→ H3 transition, which is a region of significant degradation due to a combination of sudden volume changes and high nickel and lattice oxygen reactivity with the electrolyte [17].

While the CV profile 5Br still exhibits increased polarization and broadening after cycling, the intensity of the redox peaks at ~4.2 V is much better maintained than PR, indicating better reversibility of the H2 to H3 transition. The increased polarization for 5Br may also be attributed to the formation of a thicker layer of decompositions products from residual lithium, which is supported by the initial higher fraction of active surface oxygen determined from XPS analysis discussed in a previous section. 5Cl shows excellent reversibility, with the CV curve post cycling being nearly identical to that taken after initial formation, with only a small increase in polarization compared to the other samples and is consistent with the superior capacity retention observed. 5F, in contrast, shows similar degradation as PR in the high voltage region with increased polarization and broader, lower intensity peaks.

Impedance curves are also examined in **Figures 25e and f**, which show two distinct semicircles, with the high-frequency semicircle related to surface film resistance and the mid-frequency semicircle primarily related to charge-transfer resistance [61,62]. All samples show similar impedance behavior in the uncycled state, as evidenced by close overlap among all curves. However, after 100 cycles, 5Br and 5Cl exhibit lower impedance mainly by the suppressed growth of charge transfer resistance. There is a noticeable increase in impedance related to surface film, implying the formation of thicker CEI formation compared to PR and 5F. The improved suppression of charge-transfer resistance growth is attributed to the resistance to surface reconstruction, as evidenced by the better Ni^{3+}/Ni^{2+} ratios observed from cycled samples and a protective CEI, which will be discussed in the next section. In contrast, 5F exhibits similar impedance behavior to PR, consistent with the observations from galvanostatic charge/discharge cycling and CV curves.

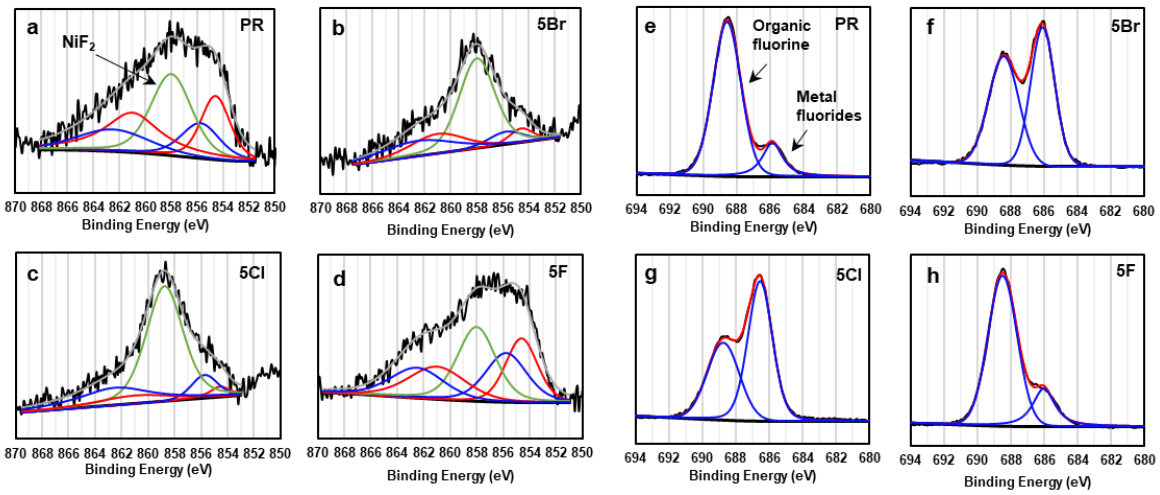

Figure 26: XPS spectra of (a-d) Nickel 2p3 and (e-h) Fluorine 1s peaks of discharged electrodes removed from half-cells after 100 cycles at C/2 from 2.8-4.5 V

XPS spectra taken from disassembled electrodes after cycling demonstrate a stark difference in surface composition for 5Br and 5Cl compared to PR and 5F. From the deconvolution of the Ni 2p3 spectra in **Figures 26a-d**, all samples exhibit a noticeable peak centered around 858 eV that can be indexed as NiF_2 formed by the reactivity of Ni^{4+} at the charged cathode surface and the organic electrolyte or as a byproduct of HF reactivity with the cathode surface [63,64]. While PR and 5F still maintain strong signals related to the lattice Ni as evidenced by the peak contributions at 854.6 and 855.76 eV, the contribution from this signal is mostly subdued for 5Br and 5Cl. NiF_2 dominates the entire signal, suggesting that a dense, uniform NiF_2 layer has formed for the Cl and Br-doped samples during cycling. This is also perceivable when examining the XPS spectra for the F1s binding energies in **Figure 26e-h**, which reveals a much higher ratio of metal fluoride signal (~684.5 eV) compared to organic fluoride signals from PVDF binder (~688 eV)[65]. The formation of an insulative NiF_2 layer would expectedly result in the higher IR drops observed across the entire SOC range in **Figure 24f** and the increased surface film impedance in **Figure 25f**. The formation of a uniform and dense NiF_2 layer can also explain the

improved capacity retention by acting as a protective barrier to reduce surface-initiated degradation mechanisms and inhibit the growth of charge-transfer resistance. This is consistent with several works on NMC532 involving dense, uniform MF_2-based coatings; it was demonstrated that such coatings can suppress interfacial resistance growth and HF attack [63,64,66]. In addition, 5Br and 5Cl samples still maintain better Ni^{3+} /Ni^{2+} ratios than PR and 5F, which indicates that the doped samples effectively suppressed surface reconstruction and further nickel reduction [**Table S4**].

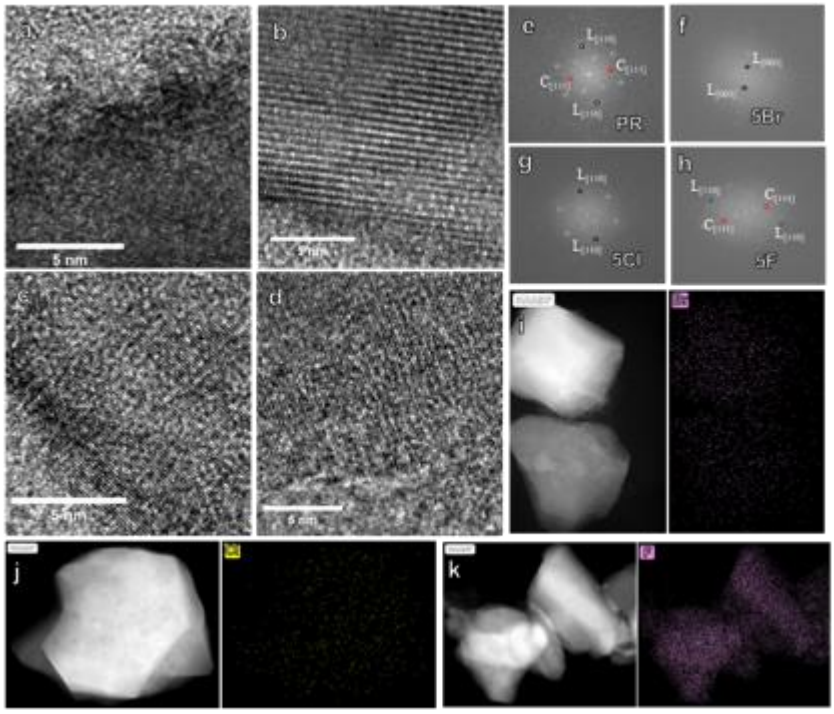

Figure 27: (a-d) HRTEM images of a particle taken from a disassembled electrode after 100 charge/discharge cycles. (e-f) Indexed FFT patterns of the corresponding HRTEM images, with hexagonal layered structure and cubic rock-salt structures labelled as "L" and "C" and associated lattice fringes. (i-k) HAADF images of the anion doped samples and corresponding EDS maps for the relevant halogen. Scale bars are set to 5µm.

HRTEM images of particle edges taken from a cycled electrodes reveal that PR and 5F samples suffer from areas of surface reconstruction, with noticeable changes in lattice spacing in the surface and sub-surface regions [**Figure 27a,d**]. Fast Fourier Transform (FFT) patterns of the TEM images effectively demonstrate that PR and 5F samples develop a significant fraction of cubic rock-salt like phases. While a clear pattern associated with [110] lattice fringes of the layered structure is seen and circled in black, the appearance of a transposed weaker intensity pattern is evident and can be indexed to the [111] lattice fringes of the cubic rock-salt structure [**Figure 27e and 8h]**. In contrast, the selected areas of 5Cl and 5Br samples and their associated FFT patterns reveal only the layered structure, with no noticeable secondary structures evident in the FFT patterns. It should be noted, however, that areas of cation mixing are observed for all samples near the particle edge, and the differences in the FFT patterns are an indication of the severity of cation mixing in the subsurface region. These differences observed further indicate the superior resistance to surface reconstruction in Cl and Br doped samples, which is in line with the observed enhanced capacity retention and XPS spectra.

4.4.4 Mechanical Properties

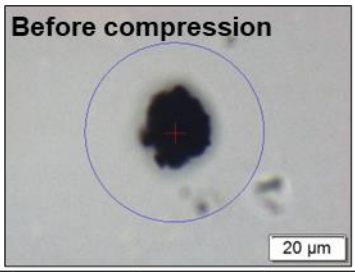

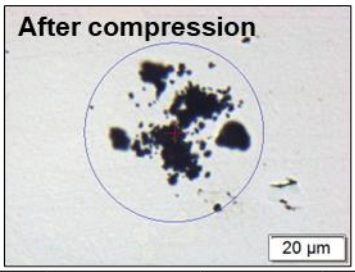

Specimen	Breakage Force [mN]	Breakage Displacement [µm]	Secondary Particle Diameter [µm]	Fracture Strength [MPa]	Avg. Fracture Strain [%]	Est. Critical Crack Length [µm]
PR	19.94 ± 4.01	0.676 ± 0.427	20.038 ± 3.424	40.487 ± 9.666	3.37	4.638
PR - 4.5V	9.04 ± 3.41	1.491 ± 0.893	14.567 ± 1.382	33.363 ± 11.681	10.24	5.319
5F	25.76 ± 7.25	1.276 ± 0.857	16.881 ± 1.112	70.537 ± 13.917	7.56	1.528
5F - 4.5V	7.75 ± 2.62	0.525 ± 0.151	14.726 ± 1.548	28.133 ± 7.721	3.57	7.478
5Cl	9.92 ± 3.24	0.464 ± 0.377	14.322 ± 3.113	39.875 ± 12.256	3.24	4.781
5Cl - 4.5V	6.85 ± 3.21	1.784 ± 1.191	14.74 ± 3.35	23.719 ± 2.352	12.10	10.521
5Br	12.62 ± 5.92	1.080 ± 0.836	18.412 ± 3.498	34.59 ± 11.296	5.87	6.354
5Br - 4.5V	10.07 ± 3.67	1.549 ± 0.733	18.416 ± 2.286	23.035 ± 6.434	8.41	11.155

Blue – Similar PR and 5F pristine-to-charged property evolution
Red – Similar property evolution for 5Cl and 5Br as-is and charged

Figure 28: Mechanical characterization through microparticulate compression testing of the doped NMC powders in the as-synthesized condition and charged to 4.5V vs Li/Li+.

While many improvements surrounding cathode material structural stability have been made to date via efforts dedicated to investigating transition metal dissolution or interfacial surface film formation, research dedicated to the study of structural disorder as well as crack formation and growth– and how mechanical properties correlate with functional performance – remains incomplete and insufficiently studied in the pursuit of dependable Li-based ion batteries [67]. Overwhelming evidence has been invoked to demonstrate that crack or fracture nucleation within cathode materials triggers parasitic reaction, electrochemical disconnection, and jeopardizes structural longevity of cells [67]. As Li^+ ions are inserted and removed within the crystal structure during cycling, the random direction of primary particle volume changes introduces stress-

induced breakage of cathode particles at grain boundaries over a period of charging and discharging events. Utilizing an MCT-based method, an analysis of the fracture strength and other mechanical properties of the doped cathode powders in the fully discharged state and charged to 4.5V is shown in **Figure 28**.

Assuming a constant value for K_{I_C} for all specimens studied pre- and post-charging conditions – $K_{I_C}^{pre} = 0.102 \pm 0.03$ MPa.m$^{1/2}$ and $K_{I_C}^{post} \approx 0.9\left(K_{I_C}^{pre}\right)$, when only cycled once – linear-elastic fracture mechanics and Griffith's criterion for brittle fracture [68] of the critical half penny-shape crack along the midpoint of the microparticles tested can be expressed and approximated as followed [69]:

$$c_{hp} = \left(\frac{K_{I_C}}{0.66\sqrt{\pi}\sigma_r}\right)^2 \qquad (13)$$

$(0.66)\sqrt{\pi}$ holds for reasonably finite cracks relative to the size of the microparticles tested, K_{I_C}'s was assumed based upon prior work surrounding as-synthesized NMC811 secondary particles [70]. Accordingly, c_{hp} values were estimated as a function of the σ_f values obtained, as noted in **Figure 28**, and subsequently tabulated alongside the measurements obtained via microparticulate compression testing of brittle materials with breakage points in general. While the values themselves may have inaccuracies due to the assumptions and estimations utilized, and ceramic samples can exhibit larger standard deviations, a qualitative comparison can be used to interpret the results. For example, the estimated critical crack lengths at 4.5V for 5Cl and 5Br are notably higher than that of PR and 5F, which alludes to higher resistance to particle cracking in the delithiated state. This is especially notable since the delithiated cathode at high SOC is more susceptible to intergranular fracture due to the occurrence of the H2 → H3 transition and

associated volume contraction. SEM observations of cycled electrodes in **Figure S10** supports the MCT results, as the greater cracking was generally observed in the case of the PR and 5F samples. In contrast, cracking was less frequently observed in 5Cl and 5Br samples. The improvement of secondary particle integrity in the delithiated state should be a focus for future study, as it is difficult to elucidate whether the improvement is due to the dopant or simply the porous nature of the secondary particle.

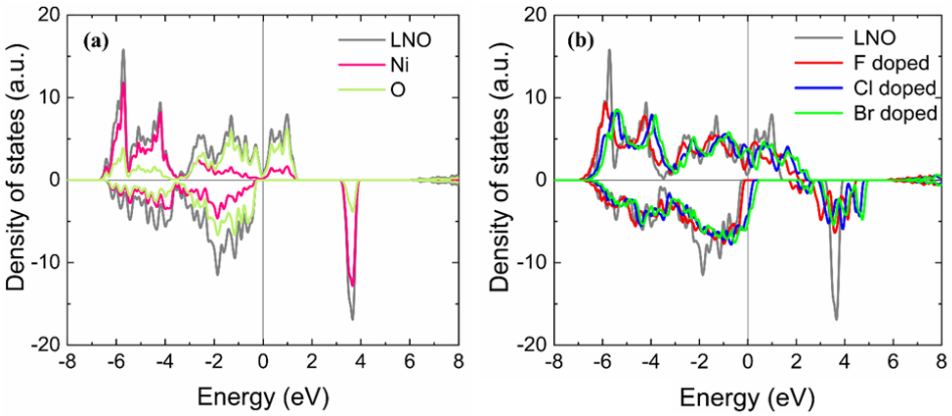

Figure 29: DOS for (a) pure LNO and contributions from Ni and O, and (b) total DOS of LNO and halogen doped LNO

To further understand the effect of anion doping on the electronic structure and performance characteristics of the Ni-rich cathode, the electronic density of states (DOS) for undoped LNO and doped LNO are presented **Figure 29**. LNO was chosen as a representative system to simplify DFT calculations. The near closure of the band gap of LNO in **Figure 29a** reveals the metallic character of Ni-rich cathodes. Previous experiments have also demonstrated significant electrical conductivity from increasing nickel content in the cathode [71]. The DOS plot for F-doped LNO [**Figure 29b**] reveals further closure of the band gap and an upward shift of the Fermi energy. These suggest improved electronic conductivity in the F doped $LiNO_2$, which is consistent with

the previous theoretical prediction [72]. By contrast, Cl and Br doping results in a downward shift of the Fermi level. As a result, the Fermi energy approaches closer to the highest occupied molecular orbital (HOMO) of the electrolyte, with the change in electronic energy possibly facilitating the formation of continuous surface passivation films in Br or Cl -doped Ni rich cathode [73]. This is consistent with the other experimental analysis, where downshifting of the fermi energy in Al-doped cathode surfaces resulted in the formation of a protective CEI [73]. As such, the computational results corroborate the experimental observations where formation of a stable CEI for enhanced cycling stability is better achieved through Cl or Br doping.

4.5 Conclusion

The addition of small amounts of lithium halide salts as dopants during the lithiation and calcination of NMC811 led to significant differences in physical and chemical properties depending on the halide salt. 5 mol% LiF appeared to have negligible to detrimental influence on the NMC811 properties, with higher severity of cation mixing and reduced rate performance. The addition of LiCl and LiBr facilitates lithiation at lower temperatures due to the formation of partial eutectic melt, with a resulting porous secondary particle with nearly 3x higher specific surface area than NMC811 prepared without LiCl or LiBr. As such, 5Br and 5Cl doped samples exhibit enhanced rate performance due to higher electrochemically active area, though it should be noted that the actual doping content is likely lower than the intended concentration due to likely partial volatilization. Capacity retention was also notably improved and attributed to the formation of a uniform CEI protective layer suppressing charge-transfer impedance growth and surface reconstruction, which was confirmed through XPS, TEM, and EIS techniques. These findings suggest that NMC811 properties can be beneficially tuned by adjusting the lithium

source(s) and provides guidance towards future studies to understand further the effects of lithium halide additions on NMC811 synthesis and resulting cathode properties.

4.6 Acknowledgments

This work was made possible under the financial support of the Ford Motor Company University Research Project. BET and PSD analysis was conducted with assistance from Ascend Elements

4.7 Supporting Information

Low magnification SEM imaging. SEM imaging of 2mol% and 8mol% doped samples. LiOH-LiX binary phase diagrams. Full TGA/DSC profile. TEM EDS mapping and line profiles. Rate performance of 2mol% and 8mol% samples. Raw GITT voltage/time profiles. SEM images of cycled electrodes. HR-TEM images of cycled electrodes.

4.8 References

[1] Curry, C. Lithium-ion Battery Costs and Market Squeezed Margins seek Technology Improvements & New Business Models. Bloomberg New Energy Finance 2017, 5, 4-6

[2] Ding, Y.; Cano, Z. P.; Yu, A.; Lu J.; Chen Z. Automotive Li-Ion Batteries: Current Status and Future Perspectives. Electrochemical Energy Reviews 2019, 2, 1–28.

[3] Muralidharan, N.; Self, E.; Dixit, M.; Du, Z.; Essehli, R.; Amin, R.; Nanga, J.; Belharouak, I. Next-Generation Cobalt-Free Cathodes – A Prospective Solution to the Battery Industry's Cobalt Problem. Advanced Energy Materials 2022, 12(9), 2103050.

[4] Gourley, S. W. D.; Or, T.; Chen, Z. Breaking Free from Cobalt Reliance in Lithium-Ion Batteries. iScience 2020, 23, 101505.

[5] Akhilash, M.; Salini, P. S.; John, B.; Mercy, T. D. A Journey through Layered Cathode Materials for Lithium ion cells – From Lithium Cobalt Oxide to Lithium-rich Transition Metal Oxides. Journal of Alloys and Compounds 2021, 869, 159239.

[6] Xia, Y.; Zheng, J.; Wang, C.; Gu, M. Designing Principle for Ni-rich Cathode Materials with high Energy Density for Practical Applications. Nano Energy 2018, 49, 434–452.

[7] Duan J.; Tang X.; Dai H.; Yang Y.; Wu W.; Wei X.; Huang Y. Building Safe Lithium-ion Batteries for Electric Vehicles: a Review. Electrochemical Energy Reviews 2020, 3(1), 1-42.

[8] Kim J.; Lee H.; Cha H.; Yoon M.; Park M.; Cho J. Prospect and Reality of Ni-rich Cathode for Commercialization. Advanced Energy Materials 2018, 8(6), 1702028.

[9] Wang, X.; Ding, Y.; Deng, Y.; Chen, Z.; Ni-Rich/Co-Poor Layered Cathode for Automotive Li-Ion Batteries: Promises and Challenges. Advanced Energy Materials 2020, 10, 1903864.

[10] Dixit, M.; Markovsky, B.; Schipper, F.; Aurbach, D.; Major, D. T. Origin of Structural Degradation During Cycling and Low Thermal Stability of Ni-Rich Layered Transition Metal-Based Electrode Materials. The Journal of Physical Chemistry C 2017, 121, 22628–22636.

[11] Ryu, H.-H.; Park, G.-T.; Yoon, C. S.; Sun, Y.-K. Microstructural Degradation of Ni-Rich Li[Ni x Co y Mn 1 −x−y]O 2 Cathodes During Accelerated Calendar Aging. Small 2018, 14, 1803179.

[12] Zheng, J.; Kan, W. H.; Manthiram, A. Role of Mn Content on the Electrochemical Properties of Nickel-Rich Layered LiNi 0.8– x Co 0.1 Mn 0.1+ x O 2 ($0.0 \leq x \leq 0.08$) Cathodes for Lithium-Ion Batteries. ACS Applied Materials & Interfaces 2015, 7, 6926–6934.

[13] Gan, Q.; Qin, N.; Wang, Z.; Li, Z.; Zhu, Y.; Li, Y.; Gu, S.; Yuan, H.; Luo, W.; Lu, L.; Xu, Z. Revealing Mechanism of Li3PO4 Coating Suppressed Surface Oxygen Release for Commercial Ni-rich Layered cathodes. ACS Applied Energy Materials 2020 3(8), 7445-55.

[14] Li, H.; Zhou, P.; Liu, F.; Li, H.; Cheng, F.; Chen, J. Stabilizing Nickel-rich Layered Oxide Cathodes by Magnesium Doping for Rechargeable Lithium-ion Batteries. Chemical science 2019, 10(5), 1374-9.

[15] Yang, C.; Shao, R.; Wang, Q.; Zhou, T.; Lu, J.; Jiang, N.; Gao, P.; Liu, W.; Yu, Y.; Zhou, H. Bulk and Surface Degradation in Layered Ni-rich Cathode for Li ions Batteries: Defect Proliferation via Chain Reaction Mechanism. Energy Storage Materials 2021, 35, 62-9.

[16] Li, X.; Gao, A.; Tang, Z.; Meng, F.; Shang, T.; Guo, S.; Ding, J.; Luo, Y.; Xiao, D.; Wang, X.; Su, D. Robust Surface Reconstruction Induced by Subsurface Ni/Li Antisites in Ni-Rich Cathodes. Advanced Functional Materials 2021, 31(16), 2010291.

[17] Märker, K.; Reeves, P. J.; Xu, C.; Griffith, K. J.; Grey, C. P. Evolution of Structure and Lithium Dynamics in LiNi 0.8 Mn 0.1 Co 0.1 O 2 (NMC811) Cathodes during Electrochemical Cycling. Chemistry of Materials 2019, 31, 2545–2554.

[18] Qian, G; Zhang, Y; Li, L, Zhang, R; Xu, J; Cheng, Z; Xie, S; Wang, H; Rao, Q; He, Y; Shen, Y; Single-crystal Nickel-rich Layered-oxide Battery Cathode Materials: Synthesis, Electrochemistry, and Intra-granular Fracture. Energy Storage Materials 2020 27, 140-9.

[19] Jeong, S.; Park, J.H.; Park, SY.; Kim, J.; Lee, K.T.; Park, Y.D.; Mun, J. Mass-Scalable Molecular Monolayer for Ni-Rich Cathode Powder: Solution for Microcrack Failure in Lithium-Ion Batteries. ACS Applied Materials & Interfaces 2021, 13(19), 22475-84.

[20] Gao, Y.; Park, J.; Liang, X. Comprehensive Study of Al- and Zr-Modified LiNi 0.8 Mn 0.1 Co 0.1 O 2 through Synergy of Coating and Doping. ACS Applied Energy Materials 2020, 3, 8978–8987.

[21] Steiner, J.D.; Cheng, H.; Walsh, J.; Zhang, Y.; Zydlewski, B.; Mu, L.; Xu, Z.; Rahman, M.M.; Sun, H.; Michel, F.M.; Sun, C.J. Targeted Surface Doping with Reversible Local Environment Improves Oxygen Stability at the Electrochemical Interfaces of Nickel-rich Cathode Materials. ACS Applied Materials & Interfaces 2019, 11(41), 37885-37891.

[22] Li, X.; Zhang, K.; Wang, M.; Liu, Y.; Qu, M.; Zhao, W.; Zheng, J. Dual Functions of Zirconium Modification on Improving the Electrochemical Performance of Ni-rich LiNi 0.8 Co 0.1 Mn 0.1 O 2. Sustainable Energy & Fuels 2018, 2(2), 413-421.

[23] Han, B.; Key, B.; Lapidus, S.H.; Garcia, J.C.; Iddir, H.; Vaughey, J.T.; Dogan, F. From Coating to Dopant: How the Transition Metal Composition affects Alumina Coatings on Ni-Rich Cathodes. ACS Applied Materials & Interfaces 2017, 9(47), 41291-41302.

[24] Yang, H.; Wu, H.H.; Ge, M.; Li, L.; Yuan, Y.; Yao, Q.; Chen, J.; Xia, L.; Zheng, J.; Chen, Z.; Duan, J. Simultaneously Dual Modification of Ni-Rich Layered Oxide Cathode for High-Energy Lithium-Ion Batteries. Advanced Functional Materials 2019, 29(13), 1808825.

[25] Park, K.J.; Jung, H.G.; Kuo, L.Y.; Kaghazchi, P.; Yoon, C.S.; Sun, Y.K.; Improved Cycling Stability of Li [Ni0. 90Co0. 05Mn0. 05] O2 through Microstructure Modification by Boron Doping for Li-Ion Batteries. Advanced Energy Materials 2018, 8(25), 1801202.

[26] Kim, U.H.; Park, G.T.; Son, B.K.; Nam, G.W.; Liu, J.; Kuo, L.Y.; Kaghazchi, P.; Yoon, C.S.; Sun, Y.K.; Heuristic Solution for Achieving Long-Term Cycle Stability for Ni-Rich Layered Cathodes at Full Depth of Discharge. Nature Energy 2020, 5(11), 860-869.

[27] Cui, Z.; Xie, Q.; Manthiram, A. Zinc-Doped High-Nickel, Low-Cobalt Layered Oxide Cathodes for High-Energy-Density Lithium-Ion Batteries. ACS Applied Materials & Interfaces 2021, 13, 15324–15332.

[28] Pagot, G.; Bandiera, M.; Vezzù, K.; Migliori, A.; Bertoncello, R.; Negro, E.; Morandi, V.; Di Noto, V. High Valence Transition Metal-Doped Olivine Cathodes for Superior Energy and Fast Cycling Lithium Batteries. Journal of Materials Chemistry A 2020, 8(48), 25727-25738.

[29] Vanaphuti, P.; Bong, S.; Ma, L.; Ehrlich, S.; Wang, Y. Systematic Study of Different Anion Doping on the Electrochemical Performance of Cobalt-Free Lithium–Manganese-Rich Layered Cathode. ACS Applied Energy Materials 2020, 3, 4852–4859.

[30] Chen, S.; Xie, Y.; Chen, W.; Chen, J.; Yang, W.; Zou, H.; Lin, Z. Enhanced Electrochemical Performance of Li-Rich Cathode Materials by Organic Fluorine Doping and Spinel Li1+ X Ni Y Mn2–Y O4 Coating. ACS Sustainable Chemistry & Engineering 2019, 8(1), 121-128.

[31] Binder, J.O.; Culver, S.P.; Pinedo, R.; Weber, D.A.; Friedrich, M.S.; Gries, K.I.; Volz, K.; Zeier, W.G.; Janek, J. Investigation of Fluorine and Nitrogen as Anionic Dopants in Nickel-Rich Cathode Materials for Lithium-Ion Batteries. ACS Applied Materials & Interfaces 2018, 10(51), 44452-44462.

[32] Zhu, H.; Li, Q.; Gong, X.; Cao, K.; Chen, Z. Enhanced High Voltage Performance of Chlorine/Bromine Co-Doped Lithium Nickel Manganese Cobalt Oxide. Crystals (Basel) 2018, 8, 425.

[33] Kong, F.; Liang, C.; Longo, R.C.; Yeon, D.H.; Zheng, Y.; Park, J.H.; Doo, S.G.; Cho, K. Conflicting Roles of Anion Doping on the Electrochemical Performance of Li-Ion Battery Cathode Materials. Chemistry of Materials 2016, 28(19), 6942-6952.

[34] Azhari, L.; Arsenault, R.; Gao, G.; Wang, Y. Modified Nickel-Rich Cathodes via Conformal Nanoparticle Coating of Precursors Using a Single Reactor Process. ACS Applied Energy Materials 2021, 4, 14618–14627.

[35] Chen, A.; Wang, K.; Li, J.; Mao, Q.; Xiao, Z.; Zhu, D.; Wang, G.; Liao, P.; He, J.; You, Y.; Xia, Y. The Formation, Detriment and Solution of Residual Lithium Compounds on Ni-Rich Layered Oxides in Lithium-Ion Batteries. Frontiers in Energy Research 2020, 8, 593009.

[36] Test Methods of Properties of Fine Ceramic Granules Part 5: Compressive Strength of a Single Granule. Japanese Standards Association (JSA) 2007.

[37] Giannozzi, P.; Baroni, S.; Bonini, N.; Calandra, M.; Car, R.; Cavazzoni, C.; Ceresoli, D.; Chiarotti, G.L.; Cococcioni, M.; Dabo, I.; Dal Corso, A. QUANTUM ESPRESSO: A Modular and Open-Source Software Project for Quantum Simulations of Materials. Journal of Physics: Condensed Matter 2009, 21(39), 395502.

[38] Zhou, F.; Cococcioni, M.; Marianetti, C.A.; Morgan, D.; Ceder, G.; First-Principles Prediction of Redox Potentials in Transition-Metal Compounds with LDA+ U. Physical Review B 2004, 70(23), 235121.

[39] Wang, D.; Belharouak, I.; Ortega, L.H.; Zhang, X.; Xu, R.; Zhou, D.; Zhou, G.; Amine, K.; Synthesis of High Capacity Cathodes for Lithium-Ion Batteries by Morphology-Tailored Hydroxide Co-Precipitation. Journal of Power Sources 2015, 274, 451-457.

[40] FTsalt (2022). FACT Salt Phase Diagrams. FactSage.

[41] Hartwig, P.; Rabenau, A.; Weppner, W.; Lithium Hydroxide Halides: Phase Equilibria and Ionic Conductivities. Journal of the Less Common Metals 1981, 78, 227–233.

[42] Wolfman, M.; Wang, X.; Garcia, J.C.; Barai, P.; Stubbs, J.E.; Eng, P.J.; Kahvecioglu, O.; Kinnibrugh, T.L.; Madsen, K.E.; Iddir, H.; and Srinivasan, V.The Importance of Surface Oxygen for Lithiation and Morphology Evolution during Calcination of High-Nickel NMC Cathodes. Advanced Energy Materials 2022, 12(16), 2102951.

[43] Dong, Q.; Yin, S.; Guo, C.; Wu, X.; Kumada, N.; Takei, T.; Miura, A.; Yonesaki, Y.; Sato, T. Single-crystalline Porous NiO Nanosheets prepared from β-Ni (OH) 2 Nanosheets: Magnetic Property and Photocatalytic Activity. Applied Catalysis B: Environmental 2014, 147, 741-747.

[44] Shi, Y.; Zhang, M.; Meng, Y. S.; Chen, Z. Ambient-Pressure Relithiation of Degraded Li x Ni 0.5 Co 0.2 Mn 0.3 O 2 (0 < x < 1) via Eutectic Solutions for Direct Regeneration of Lithium-Ion Battery Cathodes. Advanced Energy Materials 2019, 9, 1900454.

[45] Zhu, J; Chen, G. Single-Crystal Based Studies for correlating the Properties and High-Voltage Performance of Li[Ni x Mn y Co 1−x−y]O 2 Cathodes. Journal of Materials Chemistry A 2019, 7, 5463–5474.

[46] Kim, Y. Lithium Nickel Cobalt Manganese Oxide Synthesized Using Alkali Chloride Flux: Morphology and Performance As a Cathode Material for Lithium Ion Batteries. ACS Applied Materials & Interfaces 2012 4, 2329–2333.

[47] Wang, D.; Xin, C.; Zhang, M.; Bai, J.; Zheng, J.; Kou, R.; Peter Ko, J.Y.; Huq, A.; Zhong, G.; Sun, C.J.; Yang, Y. Intrinsic Role of Cationic Substitution in Tuning Li/Ni Mixing in High-Ni Layered Oxides. Chemistry of Materials 2019, 31(8), 2731-2740.

[48] Zhang, N.; Stark, J.; Li, H.; Liu, A.; Li, Y.; Hamam, I.; Dahn, J.R. Effects of Fluorine Doping on Nickel-Rich Positive Electrode Materials for Lithium-Ion Batteries. Journal of The Electrochemical Society 2020, 167(8), 080518.

[49] Qiu, Z.; Liu, Z.; Fu, X.; Liu, J.; Zeng, Q. Improving the Cycling Performance of Lini0.8Co0.15Al0.05O2 Cathode Materials via Zirconium and Fluorine Co-Substitution. Journal of Alloys and Compounds 2019, 806, 136–145.

[50] Wang, T.; Ren, K.; Xiao, W.; Dong, W.; Qiao, H.; Duan, A.; Pan, H.; Yang, Y.; Wang, H. Tuning the Li/Ni Disorder of the NMC811 Cathode by Thermally Driven Competition between Lattice Ordering and Structure Decomposition. The Journal of Physical Chemistry C 2020, 124(10), 5600-5607.

[51] Jeong, S.; Choi, K.; Ho, V.C.; Cho, J.; Bae, J.S.; Nam, S.C.; Yim, T.; Mun, J. Crucial Role of Ni-doping to Interfacial Li2MnO3 layer of High-performance Ni-rich layered Cathode in Lithium-Ion Batteries. Chemical Engineering Journal 2022, 434, 134577.

[52] Mu, L.; Yang, Z.; Tao, L.; Waters, C.K.; Xu, Z.; Li, L.; Sainio, S.; Du, Y.; Xin, H.L.; Nordlund, D.; Lin, F. The Sensitive Surface Chemistry of Co-free, Ni-rich Layered

Oxides: Identifying Experimental Conditions that Influence Characterization Results. Journal of Materials Chemistry A 2020, 8(34), 17487-17497.

[53] Jung, R.; Morasch, R.; Karayaylali, P.; Phillips, K.; Maglia, F.; Stinner, C.; Shao-Horn, Y.; Gasteiger, H.A. Effect of Ambient Storage on the Degradation of Ni-Rich Positive Electrode Materials (NMC811) for Li-ion Batteries. Journal of The Electrochemical Society 2018, 165(2), A132.

[54] Li, L.; Chen, J.; Huang, H.; Tan, L.; Song, L.; Wu, H.H.; Wang, C.; Zhao, Z.; Yi, H.; Duan, J.; Dong, T. Role of Residual Li and Oxygen Vacancies in Ni-Rich Cathode Materials. ACS Applied Materials & Interfaces 2021, 13(36), 42554-42563.

[55] Quilty, C.D.; West, P.J.; Li, W.; Dunkin, M.R.; Wheeler, G.P.; Ehrlich, S.; Ma, L.; Jaye, C.; Fischer, D.A.; Takeuchi, E.S.; Takeuchi, K.J. Multimodal Electrochemistry Coupled Microcalorimetric and X-Ray Probing of the Capacity Fade Mechanisms of Nickel Rich NMC–Progress and Outlook. Physical Chemistry Chemical Physics 2022, 24(19), pp.11471-11485.

[56] Heiskanen, S. K.; Laszczynski, N.; Lucht, B. L. Perspective—Surface Reactions of Electrolyte with LiNi x Co y Mn z O 2 Cathodes for Lithium Ion Batteries. Journal of The Electrochemical Society 2020, 167, 100519.

[57] Wang, J.; Liu, C.; Xu, G.; Miao, C.; Wen, M.; Xu, M.; Wang, C.; Xiao, W. Strengthened the Structural Stability of in-Situ F− Doping Ni-Rich Lini0. 8Co0. 15Al0. 05O2 Cathode Materials for Lithium-Ion Batteries. Chemical Engineering Journal 2022, 438, p.135537.

[58] Kim, U.H.; Park, G.T.; Conlin, P.; Ashburn, N.; Cho, K.; Yu, Y.S.; Shapiro, D.A.; Maglia, F.; Kim, S.J.; Lamp, P.; Yoon, C.S. Cation Ordered Ni-Rich Layered Cathode for Ultra-Long Battery Life. Energy & Environmental Science 2021, 14(3), pp.1573-1583.

[59] Weppner, W.; Huggins, R. A.; Determination of the Kinetic Parameters of Mixed-Conducting Electrodes and Application to the System Li3Sb. Journal of The Electrochemical Society 1977, 124, 1569–1578.

[60] Liang, L.; Sun, X.; Wu, C.; Hou, L.; Sun, J.; Zhang, X.; Yuan, C. Nasicon-Type Surface Functional Modification in Core–Shell Lini0. 5Mn0. 3Co0. 2O2@ Nati2 (PO4) 3 Cathode Enhances Its High-Voltage Cycling Stability and Rate Capacity Toward Li-Ion Batteries. ACS Applied Materials & Interfaces 2018, 10(6), 5498-5510.

[61] Nara, H.; Morita, K.; Mukoyama, D.; Yokoshima, T.; Momma, T.; Osaka, T. Impedance Analysis of Lini1/3Mn1/3Co1/3O2 Cathodes with Different Secondary-Particle Size Distribution in Lithium-Ion Battery. Electrochimica Acta 2017, 241, pp.323-330.

[62] Tsai, P.C.; Wen, B.; Wolfman, M.; Choe, M.J.; Pan, M.S.; Su, L.; Thornton, K.; Cabana, J.; Chiang, Y.M. Single-Particle Measurements of Electrochemical Kinetics in NMC and NCA Cathodes for Li-Ion Batteries. Energy & Environmental Science 2018, 11(4), 860-871.

[63] Lee, Y.M.; Nam, K.M.; Hwang, E.H.; Kwon, Y.G.; Kang, D.H.; Kim, S.S.; Song, S.W. Interfacial Origin of Performance Improvement and Fade for 4.6 V Lini0. 5Co0. 2Mn0. 3O2 Battery Cathodes. The Journal of Physical Chemistry C 2014, 118(20), 10631-10639.

[64] Darapaneni, P.; Mane, A. U.; Turczynski, A.; Elam, J. W. Elucidating the Redox Behavior during Atomic Layer Deposition on Lithium-Ion Battery Cathode Materials. Chemistry of Materials 2021, 33, 8079–8088.

[65] Beamson, G. High resolution XPS of Organic Polymers. The Scienta ESCA 300 Database 1992

[66] Gutierrez, A.; Choudhury, D.; Sharifi-Asl, S.; Yonemoto, B.T.; Shahbazian-Yassar, R.; Mane, A.U.; Elam, J.W.; Croy, J. Multifunctional Films Deposited by Atomic Layer Deposition for Tailored Interfaces of Electrochemical Systems. Journal of The Electrochemical Society 2020, 167(14), 140541.

[67] Moon, J.; Jung, J.Y.; Hoang, T.D.; Rhee, D.Y.; Lee, H.B.; Park, M.S.; Yu, J.S. The Correlation Between Particle Hardness and Cycle Performance of Layered Cathode Materials for Lithium-Ion Batteries. Journal of Power Sources 2021, 486, 229359.

[68] Žagar, G.; Pejchal, V.; Mueller, M.G.; Rossoll, A.; Cantoni, M.; Mortensen, A. The Local Strength of Microscopic Alumina Reinforcements. Acta Materialia 2015, 100, 215-223.

[69] Pejchal, V.; Žagar, G.; Charvet, R.; Dénéréaz, C.; Mortensen, A. Compression Testing Spherical Particles for Strength: Theory of the Meridian Crack Test and Implementation for Microscopic Fused Quartz. Journal of the Mechanics and Physics of Solids 2017, 99, 70–92.

[70] Xu, R.; Sun, H.; de Vasconcelos, L. S.; Zhao, K. Mechanical and Structural Degradation of LiNi x Mn y Co z O 2 Cathode in Li-Ion Batteries: An Experimental Study. Journal of The Electrochemical Society 2017, 164, A3333–A3341.

[71] Noh, H.-J.; Youn, S.; Yoon, C. S.; Sun, Y.-K. Comparison of the Structural and Electrochemical Properties of Layered Li[Nixcoymnz]O2 (X = 1/3, 0.5, 0.6, 0.7, 0.8 And 0.85) Cathode Material for Lithium-Ion Batteries. Journal of Power Sources 2013, 233, 121–130.

[72] Fang, L.; Wang, M.; Zhou, Q.; Xu, H.; Hu, W.; Li, H.; Suppressing Cation Mixing and Improving Stability by F Doping in Cathode Material LiNiO2 For Li-Ion Batteries: First-Principles Study. Colloids and Surfaces A: Physicochemical and Engineering Aspects 2020, 600, 124940.

[73] Zou, L.; Li, J.; Liu, Z.; Wang, G.; Manthiram, A.; Wang, C. Lattice Doping Regulated Interfacial Reactions in Cathode for Enhanced Cycling Stability. Nature communications 2019, 10(1), 1-11.

Chapter 5. Underlying Limitations behind Impedance Rise and Capacity Fade of Single Crystalline Ni-rich Cathodes Synthesized via a Molten-Salt Route

Luqman Azhari[1], Zifei Meng[1], Zhenzhen Yang[2], Guanhui Gao[3], Yimo Han[3], Yan Wang[1]

1 Department of Materials Science and Engineering, Worcester Polytechnic Institute, 100 Institute Road, Worcester, MA, 01609, USA

2 Chemical Science and Engineering Division, Argonne National Laboratory, 9700 S. Cass Avenue, Lemont, Illinois 60439, United States

3 Rice Electron Microscopy Center, Rice University, 6100 Main Street, Houston, Texas, USA 77005

Published as: Azhari, L., Meng, Z., Yang, Z., Gao, G., Han, Y., & Wang, Y. (2022). Underlying Limitations behind Impedance Rise and Capacity Fade of Single Crystalline Ni-rich Cathodes Synthesized via a Molten-Salt Route. Journal of Power Sources

Layered oxide $LiNi_xMn_yCo_zO_2$ (NMC) cathodes are often synthesized as polycrystalline secondary particles, composed of primary particles 50-200nm in size. Due to intergranular fracture stemming from volume changes of randomly oriented primary particles during charge/discharge, the synthesis of larger single-crystalline cathodes is of high interest. In this work, molten salt assisted growth of micron-sized Ni-rich crystals is achieved, with excellent crystallinity, low cation mixing, and negligible impurities. However, electrochemical performance is compromised by high surface reactivity resulting in decomposition of electrolyte and subsequent formation of a thick CEI layer. While intergranular fracture is eliminated, planar

gliding and severe intragranular fracture along the (003) plane occurs in the high voltage region within the first few formation cycles and is associated primarily with the H2 to H3 structural transitions. In addition, H2 to H3 transitions are highly irreversible with cyclic voltammograms revealing polarization growth within 5 cycles. As a result, the single-crystalline material exhibited markedly reduced available capacity and enhanced capacity fade from sharp impedance growth compared to its polycrystalline counterpart. This work furthers a fundamental understanding into the limitations of single-crystalline Ni-rich cathodes, and the obstacles required to be overcome in order to benefit from the advantages offered by the single-crystalline morphology.

5.1 Introduction

Layered oxide nickel-rich NMC cathodes composed of the composition $LiNi_xMn_{1-x-y}Co_yO_2$, with $x > 0.6$, are expected to be implemented for next generation commercial lithium-ion batteries. Specifically, "NMC811", with the composition of $LiNi_{0.8}Mn_{0.1}Co_{0.1}O_2$, is of significant interest; with a high practical specific capacity of 200mAh/g, low cost due to decreased cobalt content, and high discharge potential of 3.8 V (vs Li/Li^+), and it has the potential to meet the rising energy requirements for electric vehicles, drones, and personal electronics of the near future[1–4]. However, increasing the nickel content of NMC cathodes to this extent poses significant obstacles that need to be addressed, specifically regarding calendar life and safety. Ni-rich cathode materials can suffer from capacity loss from transition metal (TM) migration to lithium sites during cycling[4–7], gas evolution from Ni^{4+} reactivity with conventional electrolytes in the highly charged state[8], surface reconstruction from the layered R-3m to spinel and highly resistive rock-salt phases[9,10], transition metal dissolution and electrode cross-talk[11,12], and

intergranular cracking from large anisotropic volume changes during high levels of delithiation[10]. Most of these issues are exacerbated when using higher cutoff voltages above 4.3V due to the high valence state of Ni^{4+} and occurrence of the H2 to H3 transition around this region[13].

Of the various degradation mechanisms listed above, intergranular cracking has been highlighted as a major issue that should be addressed[14–16]. Intergranular cracking, also known as "electrochemical shock," typically occurs during high voltage cycling and is attributed to large and sudden anisotropic volume changes in the *c* lattice parameter associated with the H2 to H3 transition[17]. In-situ XRD data in other studies involving Ni-rich NMC have well documented an expansion in the *c* lattice parameter during delithiation until 4.3V, after which a sudden contraction and shrinkage of the crystal lattice along the (003) direction occurs[13]. This mechanism is due to the gradual electronic repulsion of the oxygen slabs and decreased shielding from Li^+ ions during initial delithiation, followed by collapse of the layer under higher state of charge from increased Ni-O covalency and loss of Li pillaring[13,18]. Subsequent intergranular fracture can lead to the development of microcracks, which can expose the interior of the particle to electrolyte penetration, leading to increased levels of surface-initiated degradation mechanisms, subsequent increase in impedance, and electrical disconnection in severe cases. This degradation mechanism is especially prevalent in NMC powders synthesized through conventional high-throughput coprecipitation methods, where the final products are secondary particles 8-16 μm in diameter and composed of many randomly oriented individual primary particles 100-200nm in size[19]. In these polycrystalline materials, intergranular fracture is well

documented and exacerbated when increasing the nickel content or upper cutoff voltage[17,18,20,21].

To mitigate or completely remove the impact of intergranular fracture, an increasingly popular method is to synthesize powders composed of large single crystals of NMC instead of polycrystalline secondary particles. To achieve this, previous studies have utilized a variety of different synthesis methods, ranging from molten salt flux growth[22–24], high energy ball milling[25–27], chemical etching of secondary particles[28] , and high temperature sintering[29] . Different particle sizes and morphologies can be obtained based on a variety of experimental parameters such as sintering temperature, flux, oxygen and lithium chemical activity, and time[30]. Successful growth of single crystalline NMC622 was demonstrated using a combination of molten salt and high temperature synthesis[22,29]. Dahn et al. have also demonstrated a variety of single crystal NMC532 and NMC622 cathodes using high temperature calcination combined with grinding and sieving, although electrochemical performance was subpar compared to their polycrystalline analogues[25,31,32]. To date, single crystal NMC has been shown to have superior cycling performance due to the absence of cracking[22] as well as reduced electrode crosstalk from higher surface to volume ratio[33]. In addition, Zhao et al. demonstrated that single crystal NMC622 pouch cells exhibited significantly reduced transition metal dissolution and gas evolution compared to polycrystalline counterparts[34]. However, it is even more challenging to synthesize Ni-rich single crystal cathodes such as NMC811 due to a generally lower optimum calcination temperature[35]. Increasing the calcination temperature is generally required to facilitate solid state growth, but also facilitates the formation of undesirable NiO and excessive cation mixing[35]. While some works have demonstrated successful synthesis of Ni-rich single

crystal cathodes, they require the use of ball milling or other mechanical pulverization of agglomerates[27,36].

In this work, we demonstrate synthesis of single-crystalline Ni-rich cathode powders ~1-2μm in size using a combination of high temperature synthesis, excess Li, and molten salt flux. The resulting cathode powders exhibit excellent crystallinity, with lower levels of cation mixing and increased Ni^{3+}/Ni^{2+} surface compositions. The use of molten salt flux reduces size distribution inhomogeneity and agglomeration, with the excess molten salt flux easily washed away using deionized water. Despite the crystallinity and surface quality of the initial material, we demonstrate that Ni-rich single crystalline cathodes with dominant (012) facets exhibit higher surface reactivity resulting in the formation of a thicker cathode electrolyte interphase. The H2 to H3 transition in the high voltage is shown to be much more irreversible compared to the polycrystalline counterpart, with increasing polarization and intragranular cracking along the weaker basal plane observed within the first few cycles. Lastly, rapid increases in charge transfer overpotentials occur beyond moderate levels of delithiation, which is not observed in the polycrystalline counterpart. Overall, these mechanisms limit the reversible capacity and long-term stability of the single-crystalline Ni-rich cathode and will require further tuning through dopants or morphology control to become competitive with traditional polycrystalline cathodes.

5.2 Experimental Methods

5.2.1 Synthesis of polycrystalline NMC811

To prepare polycrystalline NMC811 cathodes (“PC811”), spherical hydroxide precursors are first synthesized using a coprecipitation procedure based on a prior study[37]. A solution of

transition metal sulfates in the targeted ratio (Ni:Mn:Co = 8:1:1) is added dropwise into a stirring glass jacketed reactor under nitrogen atmosphere. Ammonia is added to the reactor to reduce the coprecipitation reaction rate as a chelating agent. The pH is maintained at 11±0.1 using a solution of sodium hydroxide, which also functions as the precipitating agent/counter anion. After a fixed reaction time, the hydroxide product is collected, rinsed with deionized water, and dried thoroughly to remove excess water. The obtained powder is then mixed thoroughly with lithium hydroxide in a 1:1.05 molar ratio to account for lithium volatilization and calcined at 450° C. The powder is then removed and gently ground again to homogenize possible lithium concentration irregularities, followed by a subsequent calcination at 775°C under flowing oxygen.

5.2.2 Synthesis of single-crystalline NMC811

Single crystalline NMC811 ("SC811") is synthesized via a molten-salt method using the same hydroxide precursors described in the previous section. The hydroxide powder is mixed with 50mol% excess lithium hydroxide and a eutectic mixture of lithium sulfate and sodium sulfate (0.62-0.38)[38]. The eutectic composition has a melting point of approximately 580°C, and sulfate-based fluxes are effective for the dissolution of oxides compared to other potential salt systems[38–40]. In a previous study on the molten salt growth of lead magnesium niobates, the oxide solubility using a Li_2SO_4-Na_2SO_4 mixture was nearly one order of magnitude higher than that of chloride flux[40]. It is understood that growth occurs via a dissolution-recrystallization mechanism which dissolves smaller oxide particles to facilitate the growth of larger particles through Ostwald ripening processes, with the molten flux allowing for faster mass transport than

simple solid-state growth[24]. The presence of the larger alkali Na^+ ions in the flux composition is also critical in molten salt growth by being more effective solvating O^{2-} anions than Li^+ [41].

The mixture is calcined using a two-step high temperature/low temperature profile similar to a previous study[29]; the sample is subject to a shorter calcination at 900°C for 2 hours, followed by a longer 13-hour soak time at 775°C to ensure good crystallinity. The collected sample is typically in the form of a "brick," which is then ground gently, followed by ultrasonic washing in deionized water to remove the water-soluble salts. The resulting powder is then dried at 100°C in a vacuum oven for several hours, followed by an annealing step at 650°C for 5hrs under flowing oxygen, which is necessary to recover surface damage from the washing process and improve electrochemical performance[22–24,42].

5.2.3 Electrode/Half-Cell Fabrication

To form electrodes, PC811 or SC811 powder is mixed with Super C65 carbon black as a conductive additive and PVDF dissolved in NMP (6wt%) as a binder. The slurry is composed of 80wt% of active material, 10wt% carbon black, and 10wt% PVDF. The resulting slurry is cast onto a 15μm thick Al foil using a 150μm doctor blade and dried at 70°C in air for several hours until the surface appears dry, followed by drying overnight in a vacuum oven at 120°C to remove residual solvents and possible moisture. Afterwards the electrode is calendered to an approximate total thickness of 35-40μm, punched into 12mm discs, and assembled into 2032-coin cells in an argon-filled glovebox with lithium metal as the anode, 1.0M $LiPF_6$ in EC/EMC (3:7 weight ratio) as the electrolyte, and a Celgard separator. Active mass loadings are calculated to be in the range of 3.5-4.3mg/cm^2.

5.3 Characterization Methods

X-ray diffraction (XRD) profiles were obtained using a PANalytical Empyrean X-ray Diffractometer (Cu Kα, λ = 1.5409Å radiation source, and step size of 0.0167°/step). Analysis of the XRD profiles was performed using Rietveld refinement technique via Fullprof Suite to determine crystallographic lattice parameters, degree of cation mixing, and $I_{(003)}/I_{(104)}$ ratios, using R-3m space group as the structural reference. Surface morphology, qualitative chemical information, and elemental distribution of the cathode powders were examined using SEM and EDS analysis via a JEOL JSM-7000F SEM at 10kV accelerating voltage. Chemical compositions were determined through ICP-OES via a Perkin-Elmer Optima 8000. High-resolution transmission electron microscopy (HRTEM) is performed using a Titan cubed Themis 300 at 300 kV, with EDS mapping performed in STEM mode. X-ray photoelectron spectra (XPS) analysis is performed via a PHI 5000 VersaProbe II system (Physical Electronics). Individual scans across the Li 1s, O 1s, C 1s, Co 2p3, Mn 2p3, Ni 2p3, and F 1s binding energies were collected at a pass energy of 23.50eV and electron escape angle of 45^{o} to the sample plane. Ar-ion milling for 2 minutes at 4kV was utilized to remove the surface material and probe subsurface regions less than ~100nm from the surface. Relevant XPS spectra were deconvoluted and fitted using XPSPeak software to examine the surface oxidation states of the powder in the as-synthesized state and electrodes taken from disassembled cells after 100 cycles.

Galvanostatic charge/discharge cycling was conducted at ambient room temperature on a LANDT CT2001A from 2.8-4.5 V at a C/2 rate. Electrochemical performance was also examined under different current loads of C/10, C/5, C/2, 1C, 2C, 3C, and C/10. Cyclic

voltammetry (CV) and electrochemical impedance spectroscopy (EIS) were obtained using a Bio-logic SAS VMP3 multi-channel Potentiostat maintained at 30°C. CV and EIS data were obtained for cells before and after cycling. CV profiles were obtained using a scan rate of 0.1 mV/s from 2.8-4.5V vs. Li/Li^+. EIS was obtained using a 10mV sinusoidal amplitude from 1MHz to 20mHz. Cells were subjected to a constant voltage hold at the desired SOC/voltage for approximately 2 hrs before EIS analysis to ensure the electrode was at the desired SOC. Galvanostatic intermittent titration technique (GITT) was utilized to determine SOC dependent lithium diffusion coefficients and polarization and was conducted using a C/10 current pulse for 0.5hrs, followed by 1.5hrs of resting time. GITT measurements for each sample were collected across one full charge cycle and discharge cycle.

5.4 Results and Discussion

5.4.1 Morphology and Crystallinity

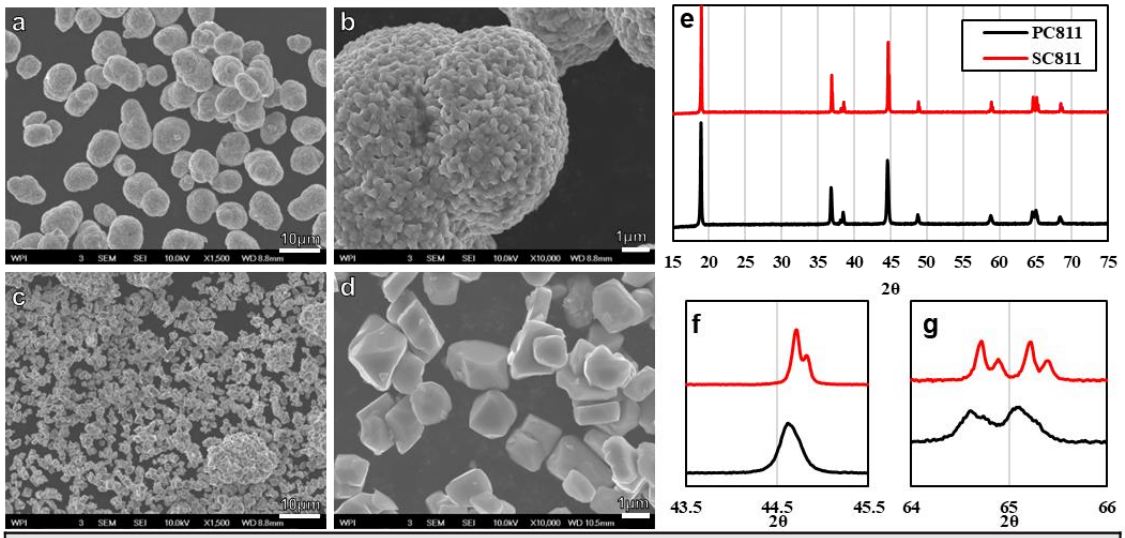

h

Sample	*a,b* (Å)	*c* (Å)	$FWHM_{(003)}$ (θ)	$FWHM_{(104)}$ (θ)	Ni_{Li} (%)	$I_{(003)}/I_{(104)}$	*c/a*	χ^2
PC811	2.8699	14.2025	0.1558	0.2621	3.19%	1.61	4.945	2.56
SC811	2.8664	14.1911	0.0848	0.0901	2.39%	1.53	4.951	3.67

Figure 30: SEM images of as-synthesized PC811 (a,b) and SC811 powders (c,d). SC811 powders are observed to form in octahedral shapes dominated by (001) and (012) surfaces, although other shapes are occasionally observed. (e) Powder XRD profiles for PC811 and SC811. (f,g) Selected 2θ ranges of the (104) and (108/110) peaks, respectively, demonstrating the smaller FWHM and well separated Kα doublet peaks of SC811 compared to PC811. (h) Table of relevant crystallographic parameters, obtained from Rietveld Refinement of XRD profiles

The morphology of PC811 and SC811 are examined with SEM in **Figures 30a-d** and demonstrates the contrasting size and shape distribution between the polycrystalline and single crystalline NMC811. Like previous works, PC811 is composed of spherical secondary particles ~8-10μm in diameter and consisting of elongated block-like primary particles ~50-200μm in size[43]. SC811 is composed primarily of 1-2μm crystals with well-defined facets. The cathode crystal shape is observed to be mostly composed of octahedral-shaped crystals which, based on

DFT calculations for equilibrium shapes of NMC from a study by Zhu et al., is assumed to be enclosed mostly by (012) facets[30]. Such shapes are expected to form when sintering under high oxygen and lithium activity, which was achieved through use of excess Li and flowing oxygen conditions[30]. High temperature and excess Li were found to be necessary to synthesize single crystalline NMC811, as reducing the upper temperature to 825°C was found to still retain the highly polycrystalline morphology [**Figure S1e**]

The use of 10 mol% Li_2SO_4-Na_2SO_4 flux was sufficient in producing well separated single crystals with consistent size and shape, due to the solubility of oxides in sulfate molten salts[39]. Although SC811 samples synthesized without the use of molten salt flux still resulted in large crystal sizes, the resulting powder exhibited severe agglomeration and wider particle size distribution due to the lack of molten salt flux [**Figure S1a-d**]. This is also indicated from **Figure S2**, where the d50 and specific surface area of single crystal samples prepared without sulfate flux is noticeably higher than that with 10 mol% sulfate flux, indicative of increased agglomeration and wider particle size distributions. It also is worth noting that increasing the excess LiOH is effective in reducing agglomeration and breaking apart secondary particles, as LiOH in excess will also function as a molten salt flux [**Figure S3**]. An increase in the sulfate flux content to 50 mol% expectedly retains the well separated and narrower size distribution, demonstrated in **Figure S1f**. However, the average size is noticeably reduced due to the increased diffusion length and oxide solvation. Therefore, by controlling the different variables of high temperature synthesis, excess Li, and molten salt flux type and concentration, 1-2μm sized octahedral single crystals of NMC811 with narrow size distribution and less agglomeration could be obtained.

Both PC811 and SC811 exhibit no noticeable impurity phases, shown in the selected XRD profiles in **Figure 30e-g**. Both XRD patterns display the typical characteristic peaks of the hexagonal α-$NaFeO_2$ layered structure of R-3m space group, with excellent crystallinity as made evident by the clear splitting of the (006)/(102) and (108)/(110) peaks[28]. SC811 exhibits superior long-range ordering due to the larger single-crystalline nature; the full-width half maximum (FWHM) of selected peaks are noticeable smaller, consistent with Scherrer relationship between crystallite size and peak width[44]. Moreover, doublet peaks can be observed due to reflections from both Cu $K\alpha_1$ and $K\alpha_2$ wavelengths, while such resolution cannot be observed in PC811 due to peak broadening. Both samples retain the expected composition based on ICP data in **Table S1**, with no lithium deficiency.

From the XRD refinement data in the table in **Figure 30h**, SC811 exhibits slightly smaller lattice parameters compared to PC811. In addition, SC811 samples have noticeably lower cation mixing than PC811, with only 2.39% cation mixing in the Li layer compared to 3.19% for PC811. The decreased cation mixing implies less Ni^{2+} in the Li layer for SC811, which would also correspond to the slightly smaller lattice parameters. The low cation mixing is further indicated by the higher *c/a* ratio for SC811 and excellent (003)/(104) intensity ratios for both samples. While the (003)/(104) ratio for SC811 is slightly lower than PC811, despite the lower cation mixing determined through Rietveld refinement, this difference is attributed to the faceted nature of SC811 with the preferred orientation during sample packing likely influencing the (003) and (104) peak intensities. The lower cation mixing can be understood when considering that the flux-assisted process allows for enhanced transport of the metal cations, along with dissolution

and recrystallization suppressing the amount of nickel ions settling into lithium sites under a sufficiently oxidizing atmosphere. Thus, the demonstrated synthesis method can achieve excellent crystallinity with low cation mixing. The addition of excessive amounts of sulfate flux results in a decline in crystallinity, as evidenced by the higher degree of cation mixing determined in **Figure S4** for samples prepared with 50 mol% sulfate flux.

5.4.2 Surface Composition and Structure

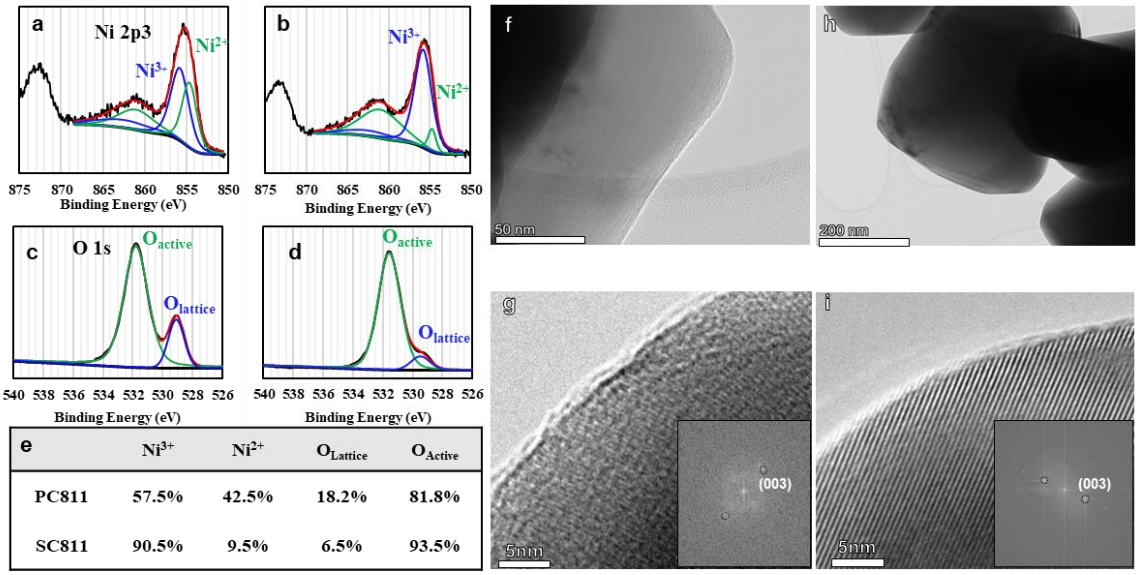

e	Ni^{3+}	Ni^{2+}	$O_{Lattice}$	O_{Active}
PC811	57.5%	42.5%	18.2%	81.8%
SC811	90.5%	9.5%	6.5%	93.5%

Figure 31: Ni 2p3 and O1s binding energies for (a, c) PC811 and (b, d) SC811 as-synthesized powders, with deconvoluted peaks. A SC811 particle was prepared by FIB to obtain a cross section for EDS and for obtaining a sufficiently thin particle section (e) Contribution of deconvoluted peaks to the overall signal. HAADF and HRTEM imaging of a primary particle edge for (f,g) PC811 and (h,i) SC811. FFT patterns in the inset are both indexed to the (003) lattice fringes of the layered R-3m structure. FFT points are circled for clarity

The surface composition and structure are probed using XPS and TEM techniques. Despite using sulfate fluxes containing sodium, no significant sodium, sulfur, or aluminum impurity can be detected for SC811 [**Figure S5**], demonstrating the effectiveness of the water washing and

annealing procedure to remove the soluble sulfate flux. As shown in **Figure 31a and 31b**, the Ni 2p3 spectra can be deconvoluted into 4 peaks centered around 855.76, 854.6, 861, and 862.5 eV[45,46]. Contributions from Ni^{2+} and Ni^{3+} oxidation states correspond to peaks at 855.76 eV and 854.6 eV, respectively, while others represent satellite peaks. Ni^{2+} exists on the surface of Ni-rich NMC as the higher energy surface is sensitive to ambient conditions and lattice lithium can react with moisture and carbon dioxide to form a residual lithium layer along with a corresponding reduction of nickel at the surface/subsurface region. By comparing the integrated area for each peak, an estimate of the nickel valence state ~5nm from the surface can be obtained. A higher fraction of Ni^{3+} is typically associated with better ordering, surface stability, and less cation mixing, as nickel should exist mostly in the 3+ oxidation state in pristine NMC811[47,48]. As shown in the table in **Figure 31e** of the areal contributions of individual peaks to the total integrated area, PC811 has a significantly higher percentage of Ni^{2+} (42.5%) compared to SC811 samples (9.5%), indicating a much more pristine surface structure for SC811 with less inherent surface reconstruction. It also suggests that cation mixing is easier to occur in PC811 samples than SC811 samples, which is consistent with XRD refinement results. For O1s spectra in **Figure 31c and 31d**, there are two distinct peaks observed at positions of 531.9 and 529 eV[49]. The peak at 531.9 eV represents higher energy active oxygen (O_{active}), and the peak at 529.3 eV corresponding to lattice-bonded oxygen ($O_{lattice}$)[49]. According to the table in **Figure 31e**, the percentage of $O_{lattice}$ in SC811 samples is moderately less than that in PC811 samples, indicating that there are more defects or broken bonds on the surface of SC811 samples, which may be a result of the more reactive (012) facets of the octahedral morphology. While the O_{active} is also considered to be present in the form of residual lithium such as Li_2CO_3, XPS analysis and deconvolution of the carbon 1S binding energies indicate similar levels of carbonate content,

indicating that the difference in O_{active} is attributed to the higher energy facets [**Figure S6**]. This is also confirmed from the HAADF and HRTEM imaging of a particle edge for as-synthesized PC811 and SC811 samples in **Figures 31f-i**, which show similar thicknesses of residuals along with clear lattice fringes. Cross sectional EDS mapping also verifies that transition metal distribution is homogenous across the entire particle, with no significant segregation [**Figure S7**].

5.4.3 Electrochemical Performance

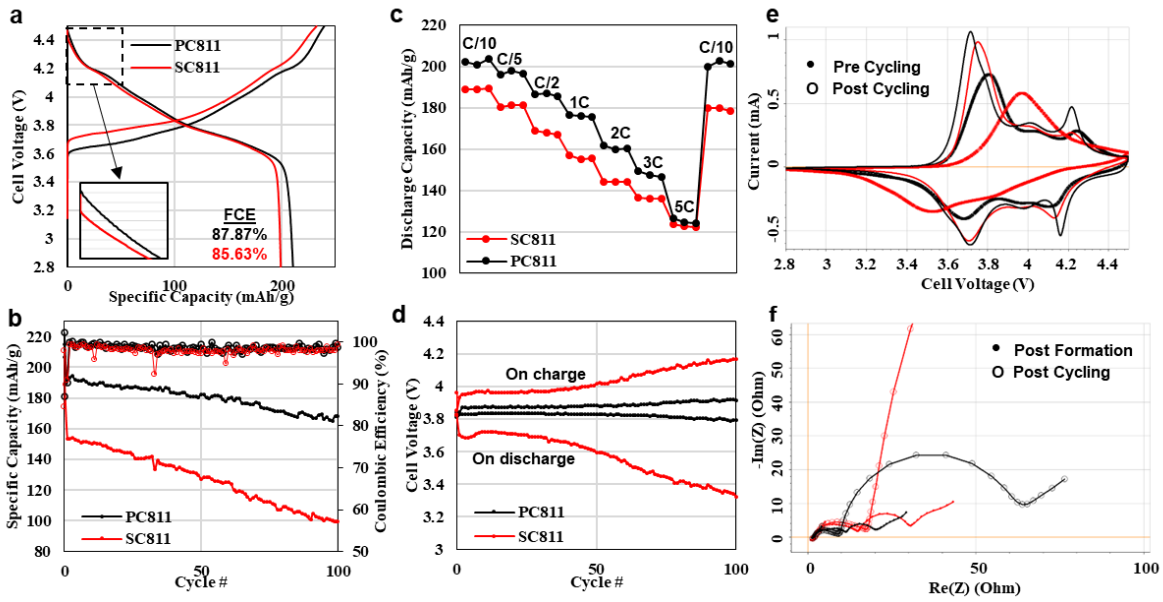

Figure 32: Electrochemical analysis of half-cells for PC811 (black) and SC811 (red). (a) First charge/discharge cycle and first coulombic efficiency, (b) galvanostatic charge/discharge cycling at 0.5C, (c) rate performance between 2.8-4.5V, (d) median charge and discharge voltage over cycling, (e) cyclic voltammetry curves before and after cycling, (f) electrochemical impedance curves before and after cycling. Inset in figure a demonstrates the higher initial potential drop of SC811 compared to PC811

While both SC811 and PC811 exhibit similar first coulombic efficiencies between 85-88% with similar voltage profiles and plateaus, SC811 suffers from a noticeably higher potential drop of

83mV upon first discharge, compared to 40mV for PC811 [**Figure 32a**]. In addition, the first discharge capacity is noticeably lower at 199mAh/g vs 211 for PC811. Upon cycling at a C/2 rate, shown in **Figure 32b**, the reversible capacity of SC811 drops even lower to around 160mAh/g with a capacity fade that is more severe compared to PC811, which was somewhat unexpected due to the intended improvement in regard to intergranular fracture.

The loss in accessible capacity is also observed at different rates of charge/discharge, with SC811 typically exhibiting a specific capacity 10-25mAh/g lower than its polycrystalline counterpart [**Figure 32c**]. However, this is not the case for 5C, where it is observed that both samples exhibit the same reversible capacity of ~125mAh/g. When examining the individual capacity-voltage curves for both the 3C and 5C rate, it becomes evident from the single slope at 5C that both PC811 and SC811 go through only the H1 → M and possibly M → H2 transitions due to the increased mass transfer overpotential and restricted voltage operation range. At 3C however, a plateau exists near 4V on discharge and 4.3V on charge and are associated with the H2 → H3 transitions which contribute an additional capacity. In contrast, this plateau is not observed for SC811 at 3C and the capacity is subsequently lower. These observations indicate that the performance limitation and low capacity of SC811 relative to PC811 is mostly associated with the H2 → H3 transition at high voltage and is investigated further in this work.

The increased rate of capacity fade from C/2 long term cycling is associated with a steady increase in cell polarization, which is demonstrated by the respective increase or decrease in the median charge or discharge voltage during extended cycling, shown in **Figure 32d, e,** which also shows an initially higher voltage difference that develops after the first formation cycles. While

the cyclic voltammetry curves of PC811 shows a moderate increase in peak-to-peak width and peak broadening after 100 cycles, the redox pairs associated with the H1 → M, M → H2, and H2 → H3 transitions are still observable[13]. This is in stark contrast to cycled SC811, where only the first set of redox peaks are observed with significant peak-to-peak width and broadening, indicating the loss of electrochemically active phases[50]. Electrochemical impedance spectra (EIS) obtained before and after cycling demonstrates an immense increase in the charge transfer resistance of SC811 compared to PC811, as evidenced by the larger second semi-circle at median frequency[51].

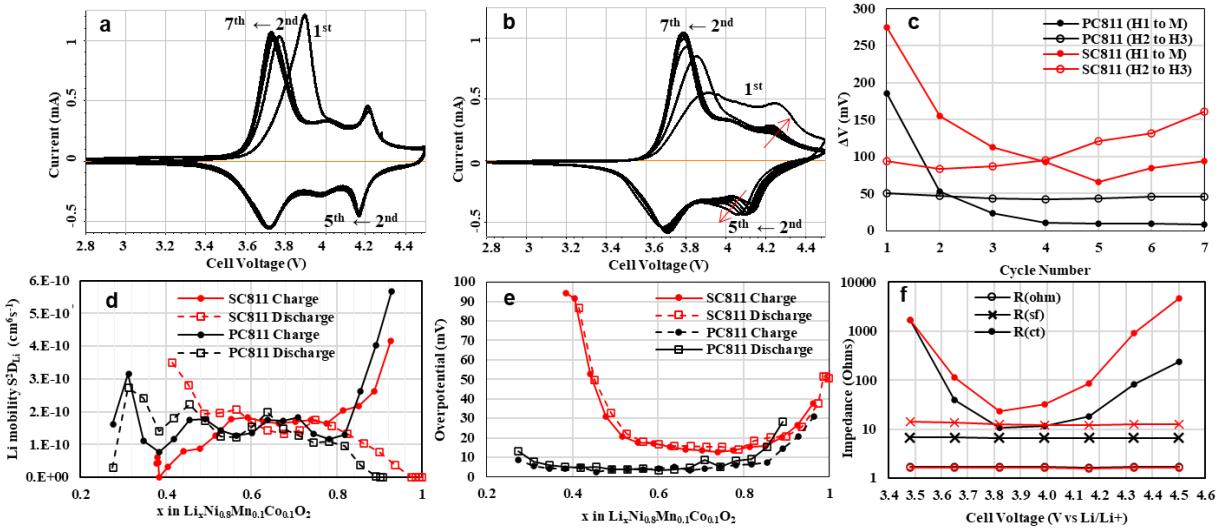

Figure 33: Cyclic voltammograms of the initial charge/discharge and four subsequent voltammograms for (a) PC811 and (b) SC811, with (c) redox pair polarization plotted vs cycle number. (d) Lithium diffusion coefficients and (e) overpotential vs SOC determined through GITT analysis. (f) Electrochemical impedance values of PC811 and SC811 across different SOC obtained from EIS curve fitting

To probe possible degradation mechanisms, cyclic voltammograms of the first 7 cycles are shown in **Figure 33a and b**, using a slow scan rate of 0.1mV/s. For both samples, anodic peaks can be observed in the first charge cycle at values above 3.8V before settling at a lower voltage that is generally more reversible. This higher anodic peak under first charge is typically observed

and is attributed to the oxidation of residual surface impurities, surface reconstruction, and subsequent formation of a CEI layer[52,53]. This can also be considered the "activation" of the NMC cathode. While PC811 has one clear anodic peak at 3.9V, SC811 takes several cycles with lower intensity peaks before the main redox peak shifts to the expected reversible value around 3.75-3.8V. Additionally, there is also an increased initial anodic peak for the H2 → H3 redox pair, which is not observed for PC811, suggesting that the formation of the CEI layer and electrolyte decomposition is distinctly different than PC811 and may be thicker compared to that of PC811[54,55]. More notably is the difference between the peak-to-peak width of the redox peaks associated with the H2 → H3 transition, which occurs between ~4.0-4.2V. While PC811 shows exceptional reversibility of the H2 → H3 transition, as evidenced by the well overlapping CV curves, SC811 shows an initially larger polarization which begins to increase within the first seven cycles. This is clearly shown in **Figure 33c**, where the peak-to-peak width of H2→H3 redox pair grows at a significantly faster rate for SC811, demonstrating the rapid irreversibility of these transitions. By the sixth cycle, it is also observed that the H1 → M redox peaks already begin to increase in polarization, again in significant contrast to the stable peak positions of PC811 and consistent with the lower capacity and faster capacity fade of SC811 observed from extended cycling.

GITT measurements shown in **Figure 33d** demonstrate no noticeable difference in the lithium diffusion coefficient between PC811 and SC811, indicating that although SC811 naturally has longer diffusion pathways, it is not considered a significant limiting factor concerning electrochemical performance. However, by analyzing the overpotential upon the application of the current pulse, a clear difference can be observed in the high SOC range [**Figure 33e, S9].**

While SC811 generally shows overpotential during current application compared to PC811, a strong increase is observed after 50% delithiation, where the values for SC811 rises from a low of ~15mV to 90mV at 40% delithiation. In comparison, the overpotential for PC811 stays well below 20mV across the entire SOC range beyond 20% delithiation. The overpotential associated with the immediate IR drop upon current pulse is associated with phenomena occurring at fast time scales, primarily ohmic and charge transfer overpotentials[56]. By examining the EIS curves at different SOC in **Figure 33f**, it is evident that while R_{sf} and R_{ohm} for PC811 and SC811 remain stable across all tested voltages, the same cannot be said for R_{ct}. While R_{ct} for both samples start at similar values in the fully discharged state, and decreases upon initial low levels delithiation, R_{ct} for SC811 begins to increase much more rapidly than PC811 above 4.0V. The EIS results support the observations from GITT analysis and imply that SC811 is severely limited by high impedance, particularly in the high voltage region associated with the H2 to H3 transition. Interestingly, cycling cells only to an upper voltage cutoff of 4.0 V to avoid the severe impedance rise results in similar capacity and retention between SC811 and PC811 [**Figure S11**].

5.4.4 Surface Composition at high SOC

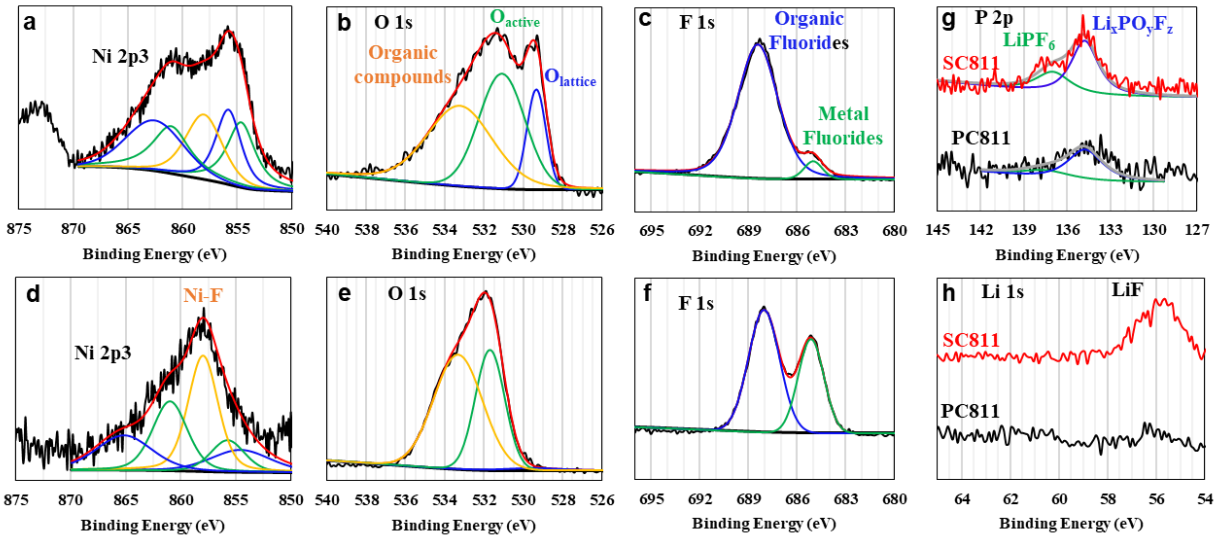

Figure 34: Ni 2p3, O 1s, and F 1s XPS spectra from (a-c) PC811 and (d-f) SC811 electrode surfaces from disassembled half-cells after holding at 4.5V. (g,h) P 2p and Li 1s XPS spectra the charged electrodes.

In order to further determine mechanisms for the rapid impedance growth of SC811 samples, XPS analysis of both SC811and PC811 samples at the high voltage of 4.5 V are conducted, examining both the surface and subsurface region. Both samples were initially subjected to two formation cycles, before charging to 4.5 V and subsequent disassembly. To analyze the subsurface components of PC811 and SC811 samples, the surface layers are removed by Ar ion polishing for 2 minutes at 4 kV. The XPS of Ni 2p3 binding energies for both PC811 and SC811 samples are almost the same as shown in **Figure S12a and b**. It is worth noting that the Ni^{2+} contribution has increased for both samples, which is expected due to the formation of a cation mixing/surface reconstruction layer upon charge/discharge. It is also evident that SC811 forms a thicker CEI layer; in **Figure S12c-f**, Mn 2p3 and Co 2p3 peaks can only be detected after ion polishing for SC811 samples. In contrast, Mn 2p3 and Co 2p3 signals for PC811 can still be

observed before polishing, indicating that the CEI layer is relatively thinner after the first formation cycles and under high SOC than for SC811.

To determine the components of the surface layer, XPS spectra of Ni 2p3, O 1s, F 1s, P 2p, and Li 1s are analyzed. As shown in **Figure 34a and 34d**, the appearance of a peak at 857.8 eV is observed and is attributed to the decomposition of electrolyte and subsequent formation of NiF_2 surface species[57]. The XPS of Ni 2p3 binding energies of PC811 are relatively unchanged when compared to after polishing. However, the XPS of Ni 2p3 for the SC811 surface is dominated by the NiF_2 peak, suggesting higher severity of electrolyte decomposition, and confirming the development of a thicker CEI layer just after formation cycles at high charge, with lattice Ni-O contributions barely observable. The development of higher amounts of metal fluorides is also shown in the F 1s spectra in **Figure 34c and f**, with noticeably higher metal fluoride signal compared to the organic fluoride signal that comes from the PVDF binder. Meanwhile, in **Figure 34b and 34e**, the $O_{lattice}$ cannot be detected at the surface of SC811 in the charged state while it is still observable for PC811, which also indicates the difference of the CEI thickness. There is a new peak, representing the organic compounds, can be observed in the spectra of O 1s, at the position of 533 eV and is likely due to some residual electrolyte[58].

Examination of the Li 1s and P 2p, and Li 1s in **Figure 34g and h** further reveals extensive formation of CEI surface species. A significantly higher peak in the Li 1s and P 2p spectra related to LiF and $Li_xPO_yF_z$ is observed for SC811 compared to PC811, respectively. These residual surface species are well documented to be highly ionically resistive[59], and thus, with more surface species forming on the surface for SC811, the impedance and polarization growth

of SC811 samples gradually increase during cycling, consistent with CV and EIS analysis. The difference in the CEI growth rate must be attributed to the higher surface reactivity of SC811, due to the known higher energy of the (012) facet compared to other possible facets and demonstrated by the higher O_{active} contribution.

5.4.5 Structural Integrity vs SOC

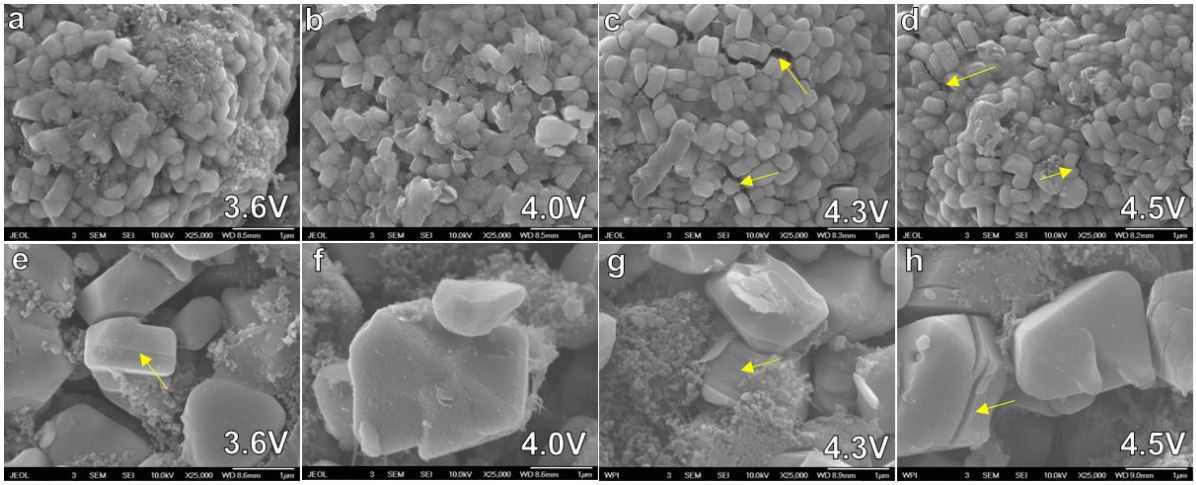

Figure 35: SEM images of (a-d) PC811 and (e-h) SC811 electrodes retrieved from disassembled cells after holding at various upper cutoff voltage. Intragranular cracks in PC811 can be observed to being at 4.3V, whereas gliding planes or intergranular cracks can be clearly seen spanning the entire length of the single crystalline grains. Note that all cells were subjected to 1 formation cycle between 2.8-4.5V before holding at target voltage.

Besides the thick CEI layer growth, intragranular cracking is also a possible reason for the fast-increasing impedance of SC811 samples, due to the generation of additional surfaces for electrolyte penetration and possible electrical disconnection. As shown in **Figure 35**, cracks in both PC811 and SC811 samples occur at voltages at 4.3V and higher and are analyzed by SEM. When the voltage is less than 4.0V, little to no cracks were observed for both samples **[Figure 35a, b, e, and f**]. Once the voltage reaches 4.3V, obvious cracks can be observed on the PC811 samples in the form of intergranular cracks along grain boundaries, as shown in **Figure 35c**, with

most of the cracks being recoverable upon discharge as shown in **Figure 35a**. For SC811 samples, rather than intergranular cracking, intragranular cracking and planar gliding can be observed in **Figures 35g, 35h** and are assumed to be mainly along the weaker (003) basal plane, which becomes more mechanically compromised at higher levels of delithiation[60,61]. The retaining effects of planar gliding was observed for several crystals after lithiation [**Figure 35e**]. Overall, it is demonstrated that at a high voltage state, significant amounts of intergranular in the case of polycrystalline NMC811, or intragranular cracking in the case of single-crystalline NMC811, can occur even just after the first formation cycle. No cracking of the individual primary particles is observed for the polycrystalline samples, as slip planes are held in place due to the neighboring grain boundary network[61,62]. The long-term impacts of these contrasting mechanisms differ from each other; intergranular cracking is limited to only the grain boundaries and would expectedly crack along the same grain boundaries during cycling, eventually leading to microcrack propagation. In contrast, intragranular cracking or planar gliding affects the (003) basal plane, which can occur multiple times in different locations along a single crystal cathode particle, running parallel to each other. With each cycle, numerous new surfaces are possibly exposed to electrolyte penetration and surface-initiated reactions. This contrast between intragranular and intergranular fracture is likely a defining feature that contributes to the rapid impedance growth and fast capacity fade for SC811.

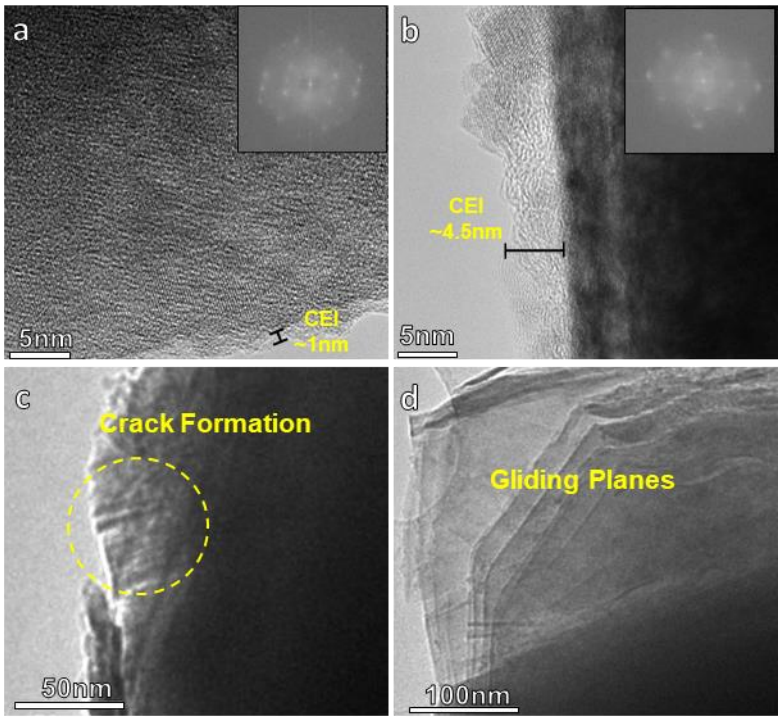

Figure 36: TEM images of (a) PC811 and (b-d) SC811 taken from electrodes charged and held at 4.5V after one formation cycle. Surface reconstruction is observed for both samples based on the FFT patterns in the inset. The occurrence of intragranular fracture and planar gliding is evident for SC811

The previously proposed mechanisms of CEI layer growth and intragranular cracking on PC811 and SC811 samples are further confirmed by HRTEM. PC811 and SC811 samples charged to 4.5V after the first formation cycle are examined in **Figure 36**. From **Figure 36a and b**, it was observed that the CEI layer for SC811 samples is noticeably thicker (~5nm) than that of PC811 samples (~1nm), consistent with conclusions drawn from XPS results and would result in the poorer electrochemical performance of SC811 compared to PC811. Meanwhile, in **Figure 36c and d,** evidence of intragranular cracking and planar gliding is observed. While the severity of planar gliding observed in **Figure 36d** is likely exacerbated by TEM sample preparation techniques (ultrasonic dispersion in NMP and ethanol), it is further indication of the anisotropic structural instability of Ni-rich single crystal cathodes, which occurs within the first cycle during

high voltage regions and results in further exposure to electrolyte penetration and expected detrimental surface reactivity.

5.5 Conclusion

In summary, a facile molten salt assisted synthesis approach towards single crystalline NMC811 is demonstrated. The addition of excess lithium and high temperature was necessary for crystal growth, with the use of alkali sulfate minimizing agglomeration. The resulting cathode material composed of 1-2um crystals with significant octahedral faceting exhibits excellent crystallinity, surface nickel valence, and minimal impurities. However, the higher reactivity of the surface due to the dominant (012) facets compared to its polycrystalline counterpart leads to the formation of a thick CEI layer within the first few formation cycles which dramatically increases the charge transfer resistance as demonstrated by the large polarization drops during GITT analysis and probed using CV and EIS techniques. Lithium diffusion was not found to be a significant limiting factor. In addition, the single crystal cathode is susceptible to intragranular cracking, especially within the high voltage region above 4.2V associated with the H2 → H3 transition, exhibiting significant irreversibility and increasing polarization again within just the first few cycles. The intragranular cracking is preceded by planar gliding of the (003) basal planes, which can occur across the entire length of the NMC particle and expose new surfaces to electrolyte with each cycle. The irreversibility and capacity loss mainly associated with the high voltage region may also be influenced by surface/bulk strain issues limiting proper lithium intercalation and rendering significant fractions of the material inactive, which has been proposed as a general limitation of Ni-rich cathodes and would require further study[63].

In order to develop high performing single-crystalline Ni-rich cathodes, these obstacles must be overcome, with the use of dopants or coatings as a possible solution, a variety of which is already demonstrated for polycrystalline morphologies[64–68]. Future work should focus on coating selection and methodology, and/or dopant selection and concentration with an objective towards stabilizing the single-crystal cathode surface. Modification approaches must achieve the formation of a thinner and stable CEI as well as better H2 → H3 reversibility. Recent work by Fan et al. utilized a coating of a NASICON-type $Li_{1.4}Y_4Ti_{1.6}(PO_4)_3$ onto single crystal Ni-rich cathode powder to form a both protective and ionic conductive network with moderate Ti-doping, which is a promising approach[69]. The utilization of other types of dominant facets should also be studied, although other works imply that the (012) facet is the most suitable for high-capacity Ni-rich crystals[30]. This work demonstrates some limitations of single crystalline morphology of Ni-rich cathodes and provides guidance towards improvement and the development of Ni-rich cathodes for next generation lithium-ion batteries.

5.6 Acknowledgements

This work was made possible under the financial support of the Ford Motor Company University Research Project. BET and PSD analysis was conducted with assistance from Ascend Elements. XPS analysis was conducted by Dr. Yang at the Chemical Science and Engineering Division at Argonne National Lab. TEM EDS mapping was conducted with assistance by Dr. Gao and Dr. Han at the Rice Electron Microscopy Center at Rice University. Additional TEM analysis was conducted with assistance from Dr. Wentao Liang from the Kostas Advanced Nano-Characterization Facility (KANCF), Northeastern University Innovation Campus of Burlington Massachusetts (ICBM).

5.7 References

[1] Ding, Y., Cano, Z. P., Yu, A., Lu, J. & Chen, Z. Automotive Li-Ion Batteries: Current Status and Future Perspectives. *Electrochemical Energy Reviews* **2**, 1–28 (2019).

[2] Gourley, S. W. D., Or, T. & Chen, Z. Breaking Free from Cobalt Reliance in Lithium-Ion Batteries. *iScience* **23**, 101505 (2020).

[3] Muralidharan, N. *et al.* Next-Generation Cobalt-Free Cathodes – A Prospective Solution to the Battery Industry's Cobalt Problem. *Advanced Energy Materials* vol. 12 (2022).

[4] Xia, Y., Zheng, J., Wang, C. & Gu, M. Designing principle for Ni-rich cathode materials with high energy density for practical applications. *Nano Energy* **49**, 434–452 (2018).

[5] Duan, J. *et al.* Building Safe Lithium-Ion Batteries for Electric Vehicles: A Review. *Electrochemical Energy Reviews* vol. 3 (2020).

[6] Wang, X., Ding, Y., Deng, Y. & Chen, Z. Ni-Rich/Co-Poor Layered Cathode for Automotive Li-Ion Batteries: Promises and Challenges. *Advanced Energy Materials* **10**, 1903864 (2020).

[7] Kim, J. *et al.* Prospect and Reality of Ni-Rich Cathode for Commercialization. *Advanced Energy Materials* **8**, 1702028 (2018).

[8] Gan, Q. *et al.* Revealing Mechanism of Li_3PO_4 Coating Suppressed Surface Oxygen Release for Commercial Ni-Rich Layered Cathodes. *ACS Applied Energy Materials* **3**, 7445–7455 (2020).

[9] Yang, C. *et al.* Bulk and surface degradation in layered Ni-rich cathode for Li ions batteries: Defect proliferation via chain reaction mechanism. *Energy Storage Materials* **35**, 62–69 (2021).

[10] Ryu, H.-H., Park, G.-T., Yoon, C. S. & Sun, Y.-K. Microstructural Degradation of Ni-Rich $Li[Ni_xCo_yMn_{1-x-y}]O_2$ Cathodes During Accelerated Calendar Aging. *Small* **14**, 1803179 (2018).

[11] Klein, S. et al. Demonstrating Apparently Inconspicuous but Sensitive Impacts on the Rollover Failure of Lithium-Ion Batteries at a High Voltage. ACS Applied Materials & Interfaces 13, 57241–57251 (2021).

[12] Kasnatscheew, J. et al. Changing Established Belief on Capacity Fade Mechanisms: Thorough Investigation of LiNi 1/3 Co 1/3 Mn 1/3 O 2 (NCM111) under High Voltage Conditions. The Journal of Physical Chemistry C 121, 1521–1529 (2017).

[13] Märker, K., Reeves, P. J., Xu, C., Griffith, K. J. & Grey, C. P. Evolution of Structure and Lithium Dynamics in $LiNi_{0.8}Mn_{0.1}Co_{0.1}O_2$ (NMC811) Cathodes during Electrochemical Cycling. *Chemistry of Materials* **31**, 2545–2554 (2019).

[14] You, B. *et al.* Research Progress of Single-Crystal Nickel-Rich Cathode Materials for Lithium Ion Batteries. *Small Methods* **5**, 2100234 (2021).

[15] Zeng, W. *et al.* Single-crystal high-nickel layered cathodes for lithium-ion batteries: advantages, mechanism, challenges and approaches. *Current Opinion in Electrochemistry* **31**, 100831 (2022).

[16] Langdon, J. & Manthiram, A. A perspective on single-crystal layered oxide cathodes for lithium-ion batteries. *Energy Storage Materials* **37**, 143–160 (2021).

[17] Park, K.-J. *et al.* Degradation Mechanism of Ni-Enriched NCA Cathode for Lithium Batteries: Are Microcracks Really Critical? *ACS Energy Letters* **4**, 1394–1400 (2019).

[18] Teichert, P., Eshetu, G. G., Jahnke, H. & Figgemeier, E. Degradation and Aging Routes of Ni-Rich Cathode Based Li-Ion Batteries. *Batteries* **6**, 8 (2020).

[19] Bao, W. *et al.* Simultaneous Enhancement of Interfacial Stability and Kinetics of Single-Crystal $LiNi_{0.6}Mn_{0.2}Co_{0.2}O_2$ through Optimized Surface Coating and Doping. *Nano Letters* **20**, 8832–8840 (2020).

[20] Li, J. *et al.* Comparison of Single Crystal and Polycrystalline $LiNi_{0.5}Mn_{0.3}Co_{0.2}O_2$ Positive Electrode Materials for High Voltage Li-Ion Cells. *Journal of The Electrochemical Society* **164**, A1534–A1544 (2017).

[21] Trevisanello, E., Ruess, R., Conforto, G., Richter, F. H. & Janek, J. Polycrystalline and Single Crystalline NCM Cathode Materials—Quantifying Particle Cracking, Active Surface Area, and Lithium Diffusion. *Advanced Energy Materials* **11**, 2003400 (2021).

[22] Qian, G. *et al.* Single-crystal nickel-rich layered-oxide battery cathode materials: synthesis, electrochemistry, and intra-granular fracture. *Energy Storage Materials* **27**, 140–149 (2020).

[23] Kim, Y. Lithium Nickel Cobalt Manganese Oxide Synthesized Using Alkali Chloride Flux: Morphology and Performance As a Cathode Material for Lithium Ion Batteries. *ACS Applied Materials & Interfaces* **4**, 2329–2333 (2012).

[24] Kimijima, T., Zettsu, N. & Teshima, K. Growth Manner of Octahedral-Shaped $Li(Ni_{1/3}Co_{1/3}Mn_{1/3})O_2$ Single Crystals in Molten Na_2SO_4. *Crystal Growth & Design* **16**, 2618–2623 (2016).

[25] Li, H., Li, J., Ma, X. & Dahn, J. R. Synthesis of Single Crystal $LiNi_{0.6}Mn_{0.2}Co_{0.2}O_2$ with Enhanced Electrochemical Performance for Lithium Ion Batteries. *Journal of The Electrochemical Society* **165**, A1038–A1045 (2018).

[26] Cheng, E. J. *et al.* Mechanical and physical properties of LiNi0.33Mn0.33Co0.33O2 (NMC). *J Eur Ceram Soc* **37**, 3213–3217 (2017).

[27] Zheng, L., Bennett, J. C. & Obrovac, M. N. All-Dry Synthesis of Single Crystal NMC Cathode Materials for Li-Ion Batteries. *Journal of The Electrochemical Society* **167**, 130536 (2020).

[28] Ma, X. *et al.* A universal etching method for synthesizing high-performance single crystal cathode materials. *Nano Energy* **87**, 106194 (2021).

[29] Qian, G. *et al.* Temperature-Swing Synthesis of Large-Size Single-Crystal $LiNi_{0.6}Mn_{0.2}Co_{0.2}O_2$ Cathode Materials. *Journal of The Electrochemical Society* **168**, 010534 (2021).

[30] Zhu, J. & Chen, G. Single-crystal based studies for correlating the properties and high-voltage performance of $Li[Ni_xMn_yCo_{1-x-y}]O_2$ cathodes. *Journal of Materials Chemistry A* **7**, 5463–5474 (2019).

[31] Li, H. *et al.* Synthesis of Single Crystal $LiNi_{0.88}Co_{0.09}Al_{0.03}O_2$ with a Two-Step Lithiation Method. *Journal of The Electrochemical Society* **166**, A1956–A1963 (2019).

[32] Li, J. *et al.* Comparison of Single Crystal and Polycrystalline $LiNi_{0.5}Mn_{0.3}Co_{0.2}O_2$ Positive Electrode Materials for High Voltage Li-Ion Cells. *Journal of The Electrochemical Society* **164**, A1534–A1544 (2017).

[33] Klein, S. et al. Prospects and limitations of single-crystal cathode materials to overcome cross-talk phenomena in high-voltage lithium ion cells. Journal of Materials Chemistry A 9, 7546–7555 (2021).

[34] Zhao, W. et al. Assessing Long-Term Cycling Stability of Single-Crystal Versus Polycrystalline Nickel-Rich NCM in Pouch Cells with 6 mAh cm −2 Electrodes. Small 18, 2107357 (2022).

[35] Ronduda, H. *et al.* On the Sensitivity of the Ni-rich Layered Cathode Materials for Li-ion Batteries to the Different Calcination Conditions. *Nanomaterials* **10**, 2018 (2020).

[36] Yang, C. Superior Cycle Stability of Single Crystal Nickel-Rich Layered Oxides with Micron-Scale Grain Size as Cathode Material for Lithium Ion Batteries. *International Journal of Electrochemical Science* 5031–5041 (2020) doi:10.20964/2020.06.03.

[37] Azhari, L., Arsenault, R., Gao, G. & Wang, Y. Modified Nickel-Rich Cathodes via Conformal Nanoparticle Coating of Precursors Using a Single Reactor Process. *ACS Applied Energy Materials* **4**, 14618–14627 (2021).

[38] FactSage. FTsalt. FACT Salt Phase Diagrams. https://www.crct.polymtl.ca/fact/documentation/FTsalt/FTsalt_Figs.htm, 2022 (accessed May 23rd 2022).

[39] Xiao, X., Hayashi, F., Yubuta, K., Selloni, A. & Teshima, K. Effects of Alkali Cations and Sulfate/Chloride Anions on the Flux Growth of {001}-Faceted β-Li_2TiO_3 Crystals. *Crystal Growth & Design* **17**, 1118–1124 (2017).

[40] Yoon, K. H., Cho, Y.-S., Lee, D.-H. & Kang, D.-H. Powder Characteristics of Pb(Mg1/3Nb2/3)O3 Prepared by Molten Salt Synthesis. Journal of the American Ceramic Society 76, 1373–1376 (1993).

[41] Cortese, A. J. et al. Oxygen Anion Solubility as a Factor in Molten Flux Crystal Growth, Synthesis, and Characterization of Four New Reduced Lanthanide Molybdenum Oxides: Ce 4.918(3) Mo 3 O 16 , Pr 4.880(3) Mo 3 O 16 , Nd 4.910(3) Mo 3 O 16 , and Sm 4.952(3) Mo 3 O 16. Crystal Growth & Design 16, 4225–4231 (2016).

[42] Zhang, F. *et al.* Surface regulation enables high stability of single-crystal lithium-ion cathodes at high voltage. *Nature Communications* **11**, 3050 (2020).

[43] Zheng, Z. *et al.* High Performance Cathode Recovery from Different Electric Vehicle Recycling Streams. *ACS Sustainable Chemistry & Engineering* **6**, 13977–13982 (2018).

[44] Zhang, X. *et al.* Minimization of the cation mixing in Li1+x(NMC)1−xO2 as cathode material. *Journal of Power Sources* **195**, 1292–1301 (2010).

[45] Zhang, R. *et al.* Understanding fundamental effects of Cu impurity in different forms for recovered LiNi0.6Co0.2Mn0.2O2 cathode materials. *Nano Energy* **78**, 105214 (2020).

[46] Fu, Z., Hu, J., Hu, W., Yang, S. & Luo, Y. Quantitative analysis of Ni2+/Ni3+ in Li[NixMnyCoz]O2 cathode materials: Non-linear least-squares fitting of XPS spectra. *Applied Surface Science* **441**, 1048–1056 (2018).

[47] Yeh, N.-H. et al. Controlling Ni 2+ from the Surface to the Bulk by a New Cathode Electrolyte Interphase Formation on a Ni-Rich Layered Cathode in High-Safe and High-Energy-Density Lithium-Ion Batteries. ACS Applied Materials & Interfaces 13, 7355–7369 (2021).

[48] Lv, C. et al. Revealing the degradation mechanism of Ni-rich cathode materials after ambient storage and related regeneration method. Journal of Materials Chemistry A 9, 3995–4006 (2021).

[49] Wang, T. *et al.* Tuning the Li/Ni Disorder of the NMC811 Cathode by Thermally Driven Competition between Lattice Ordering and Structure Decomposition. *The Journal of Physical Chemistry C* **124**, 5600–5607 (2020).

[50] Liang, L. *et al.* Nasicon-Type Surface Functional Modification in Core–Shell $LiNi_{0.5}Mn_{0.3}Co_{0.2}O_2$@$NaTi_2(PO_4)_3$ Cathode Enhances Its High-Voltage Cycling Stability and Rate Capacity toward Li-Ion Batteries. *ACS Applied Materials & Interfaces* **10**, 5498–5510 (2018).

[51] Saunders, L., Wang, J. & Stimming, U. Evaluating single-crystal and polycrystalline NMC811 electrodes in lithium-ion cells via non-destructive EIS alone. *Journal of Applied Electrochemistry* (2022) doi:10.1007/s10800-022-01713-x.

[52] Robert, R., Bünzli, C., Berg, E. J. & Novák, P. Activation Mechanism of $LiNi_{0.80}Co_{0.15}Al_{0.05}O_2$: Surface and Bulk Operando Electrochemical, Differential Electrochemical Mass Spectrometry, and X-ray Diffraction Analyses. *Chemistry of Materials* **27**, 526–536 (2015).

[53] Grenier, A. *et al.* Reaction Heterogeneity in $LiNi_{0.8}Co_{0.15}Al_{0.05}O_2$ Induced by Surface Layer. *Chemistry of Materials* **29**, 7345–7352 (2017).

[54] Jeyakumar, J., Wu, Y.-S., Wu, S.-H., Jose, R. & Yang, C.-C. Surface-Modified Quaternary Layered Ni-Rich Cathode Materials by Li_2ZrO_3 for Improved Electrochemical Performance for High-Power Li-Ion Batteries. *ACS Applied Energy Materials* **5**, 4796–4807 (2022).

[55] Ma, R. *et al.* Tuning Cobalt-Free Nickel-Rich Layered $LiNi_{0.9}Mn_{0.1}O_2$ Cathode Material for Lithium-Ion Batteries. *ChemElectroChem* **7**, 2637–2642 (2020).

[56] Chen, Y. *et al.* Revealing the Rate-Limiting Electrode of Lithium Batteries at High Rates and Mass Loadings. *SSRN Electronic Journal* (2022) doi:10.2139/ssrn.4117009.

[57] Lee, Y.-M. *et al.* Interfacial Origin of Performance Improvement and Fade for 4.6 V $LiNi_{0.5}Co_{0.2}Mn_{0.3}O_2$ Battery Cathodes. *The Journal of Physical Chemistry C* **118**, 10631–10639 (2014).

[58] Edström, K., Gustafsson, T. & Thomas, J. O. The cathode–electrolyte interface in the Li-ion battery. *Electrochimica Acta* **50**, 397–403 (2004).

[59] Soloy, A. *et al.* Effect of Particle Size on $LiNi_{0.6}Mn_{0.2}Co_{0.2}O_2$ Layered Oxide Performance in Li-Ion Batteries. *ACS Applied Energy Materials* **5**, 5617–5632 (2022).

[60] Bi, Y. *et al.* Reversible planar gliding and microcracking in a single-crystalline Ni-rich cathode. *Science (1979)* **370**, 1313–1317 (2020).

[61] Stallard, J. C. *et al.* Effect of Lithiation upon the Shear Strength of NMC811 Single Crystals. *Journal of The Electrochemical Society* **169**, 040511 (2022).

[62] Stallard, J. C. et al. Mechanical properties of cathode materials for lithium-ion batteries. Joule 6, 984–1007 (2022).

[63] Xu, C. *et al.* Bulk fatigue induced by surface reconstruction in layered Ni-rich cathodes for Li-ion batteries. *Nature Materials* **20**, 84–92 (2021).

[64] Park, K.-J. *et al.* Improved Cycling Stability of $Li[Ni_{0.90}Co_{0.05}Mn_{0.05}]O_2$ Through Microstructure Modification by Boron Doping for Li-Ion Batteries. *Advanced Energy Materials* **8**, 1801202 (2018).

[65] Gao, Y., Park, J. & Liang, X. Comprehensive Study of Al- and Zr-Modified $LiNi_{0.8}Mn_{0.1}Co_{0.1}O_2$ through Synergy of Coating and Doping. *ACS Applied Energy Materials* **3**, 8978–8987 (2020).

[66] Steiner, J. D. *et al.* Targeted Surface Doping with Reversible Local Environment Improves Oxygen Stability at the Electrochemical Interfaces of Nickel-Rich Cathode Materials. *ACS Applied Materials & Interfaces* **11**, 37885–37891 (2019).

[67] Li, H. *et al.* Stabilizing nickel-rich layered oxide cathodes by magnesium doping for rechargeable lithium-ion batteries. *Chemical Science* **10**, 1374–1379 (2019).

[68] Han, B. *et al.* From Coating to Dopant: How the Transition Metal Composition Affects Alumina Coatings on Ni-Rich Cathodes. *ACS Applied Materials & Interfaces* **9**, 41291–41302 (2017).

[69] Fan, X. et al. In situ inorganic conductive network formation in high-voltage single-crystal Ni-rich cathodes. Nature Communications 12, 5320 (2021).

Chapter 6. Recommendations for Future Work

In this work we have demonstrated different approaches towards improving the electrochemical performance of Ni-rich cathode materials, utilizing techniques that are commercially viable such as coprecipitation and doping methods. The underlying limitations of Ni-rich cathode materials during aqueous slurry processing and in the single crystal morphology have also been explored. However, the continued improvement and study of Ni-rich cathode materials can be pursued further.

6.1 Beyond NMC811 to ultra-nickel-rich cathodes

While NMC811 is often seen as the next step in next-generation commercial lithium-ion batteries, there has been an uptick in publications on layered oxide cathodes with nickel content greater than 80%. Such chemistries are occasionally referred to as "ultra-high nickel rich" and can effectively be considered doped versions of lithium nickel oxide ($LiNiO_2$, "LNO"), due to the nickel content approaching values $\geq 95\%$ in some cases [1-5]. These compositions are advantageous as they further reduce the cobalt content, which makes the cathode material naturally cheaper in raw materials costs. In addition, these compositions expectedly exhibit high capacities of over 200mAh/g when charged to an upper cutoff voltage of 4.3V vs Li/Li^+ due to the nickel content [4]. A secondary advantage which is often not highlighted is that as nickel content increases, the resulting composition typically requires lower sintering temperatures to achieve a desirable crystallinity and electrochemical performance than that of chemistries that contain more manganese or cobalt, as shown in **Figure 37a**. For example, most studies revolving around LNO or other ultra-high nickel rich compositions utilize sintering temperatures between

640-720°C [1-3,5-7]. In comparison, NMC111 and NMC622 are typically sintered at temperatures over 800°C [9,10]. Thus, this provides an additional economic benefit from an industry perspective, as the operation of high temperature furnaces is inherently energy intensive. However, it should be noted that nickel rich compositions are best synthesized in oxygen-rich atmospheres, which does result in additional operation costs compared to simple sintering in ambient air [11].

As has been established, as nickel content further increases, the electrochemical and thermal stability is worsened. In the case of LNO, degradation is far more severe than that of NMC811, with capacity fade to near end of life occurring several fold faster [4,6]. Previous work attributes the faster capacity fade to an even more accelerated surface-initiated degradation and phase transformations to spinel and rock-salt like structures [12]. TOF-SIMS analysis of the NiF_3^- signal by the Manthiram group indicated that ultrahigh nickel-rich compositions were more susceptible to acidic attack based on the following reaction: [12-14]

$$4HF + LiMO_2 \rightarrow MF_3^- + LiF + 2H_2O \qquad (14)$$

There are also unique bulk changes that occur with ultra-high nickel rich compositions; Li and Manthiram utilized in-situ XRD of $LiNi_{0.94}Co_{0.06}O_2$ to observe the structural changes during charge and discharge, and found that the (003) peak during the H2 to H3 transition exhibited a two-phase region, with the new $(003)_{H3}$ peak appearing and coexisting with the gradual disappearance of the $(003)_{H2}$ peak [12]. The phenomenon was also observed at lower SOC, when observing the (101) peak during the H1 to H2 transitions. This was in stark contrast to NMC811, where only a single peak with smooth transition from H1 to H2 and H2 to H3 was observed (**Figure 37b, c)**. This degree of "smoothness" in structural rearrangement during

charge/discharge is considered to be a factor in the fast degradation of ultra-nickel-rich cathode, as the existence of two phase regions would lead to larger lattice mismatch and generated strain within the cathode particles. This manifests as accelerated secondary particle pulverization and loss of crystallinity, with electrolyte continuously penetrating into the interior of the secondary particle. The Manthiram group demonstrated this by physical examination of electrodes after extended cycling of 1500 cycles, where ultrahigh nickel compositions retained nearly no intact secondary particles in contrast to NMC811 with moderate cracking **(Figure 37d, e)** [12]. Such work clearly demonstrates the increased mechanical vulnerability of ultrahigh nickel-rich cathodes. It should also be noted that pure LNO is typically difficult to synthesize with proper stoichiometry, as it is vulnerable to moderate levels of cation mixing during initial synthesis [14,15]. Therefore, it is imperative to add sufficient excess lithium and ensure a highly oxidizing atmosphere, and or with dopants to induce proper ordering.

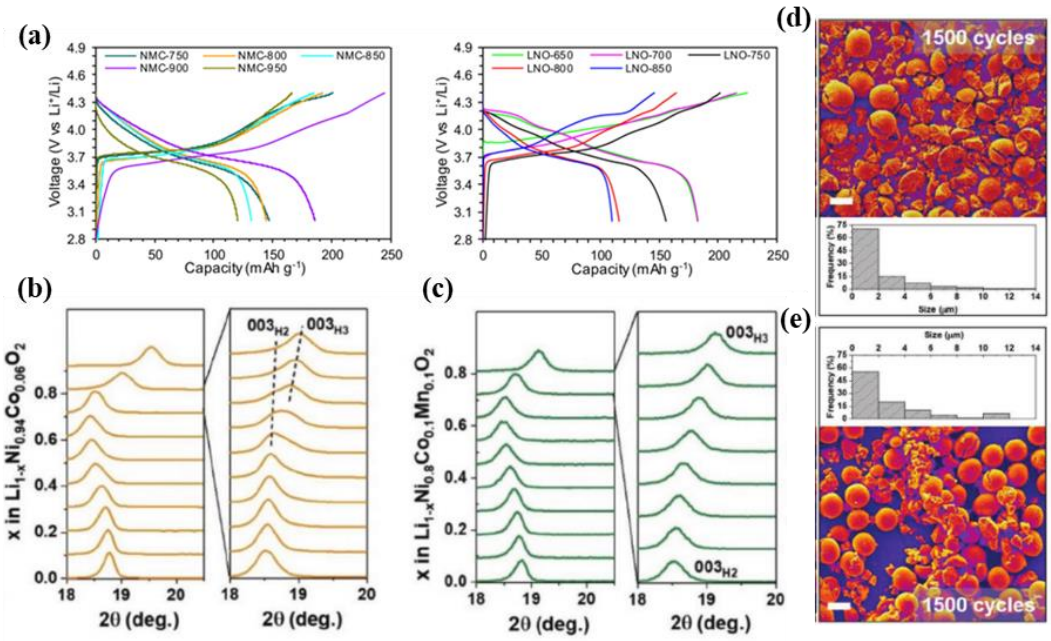

Figure 37: (a) Relationship between different calcination temperatures and first charge/discharge capacity for NMC622 (left) and LNO (right), demonstrating higher ideal temperature for lower Ni content, taken from Ref. [8]. (b) In-situ XRD data of the (003) peak of $LiNi_{0.94}Co_{0.06}O_2$ and (c) NMC811 during first charge, revealing a two-phase region for the former, taken from Ref. [12]. (d) Cross section images and particle size analysis of $LiNi_{0.94}Co_{0.06}O_2$ and (e) NMC811 after extended cycling, taken from Ref. [12]

6.1.1 Current work in ultra-nickel rich cathodes and doping

Like NMC811, current work in ultra-nickel rich cathodes typically utilize coating and/or doping mechanisms to stabilize the structure. The Manthiram group has demonstrated several cobalt free cathode compositions, each with nickel contents varying between 89 to 94% [16-18]. Electrochemical performance or stability was improved using a variety of methods such as composition tuning [17], coating via phosphoric acid treatment or polymers [1], and boron oxide-based coatings [19]. Other groups have also utilized compositions with the addition of titanium or other high valence metal elements such as Al [20], Zr [21], and Ta [22].

Dopants are especially important due to the bulk structural issues that occur during lithiation/delithiation, and additional research should be centered around utilizing the optimum dopants and possible co-dopants. To maintain the high nickel composition, dopants should be able to have significant effects on the host properties when added in only minor amounts (< 5mol%), to prevent excessive substitution of electrochemically active components. This differs than that of cobalt and manganese, which have electrochemical activity and are useful in improving performances when added in larger amounts due to their high solid solubility with nickel in the R-3m structure [23,24]. Cationic dopants are often added as solid precursors during the initial calcination step and can be added either to the lithium site or transition metal site, with the preferential dopant site typically dependent on the approximate matching of ionic radii.

A variety of cation dopants are well demonstrated for various NMC compounds, such as Al, Zr, B, Ta, Mg, Fe, Cu, Sn, and more [23-29]. In the case of boron and tantalum, dopants were found to be effective in altering grain growth, with primary particles growing in a thinner, elongated structure (**Figure 38a**) [23,26]. This microstructural modification with preferential orientation was better suited for alleviating volume changes during cycling and were successful in suppressing capacity fade for NMC811. Elements with similar ionic radius to lithium can stabilize the structure as a "pillar ion," as is the case with Mg which can dope on either the Ni or Li site depending on the concentration (0.72Å vs 0.76Å for Li) [30]. In such a case, these ions are electrochemically inactive and suppress the large volume contraction observed at high SOC (**Figure 38b, c**). Elements such as Al and other transition elements can also improve performance by inhibiting Ni^{2+} migration and subsequent phase transformations, improving ionic conductivity, increasing critical temperature, and reducing heat release, and increasing the

overall bond dissociation energy in the MO_6 octahedra to inhibit oxygen release (**Figure 38d**) [29,31].

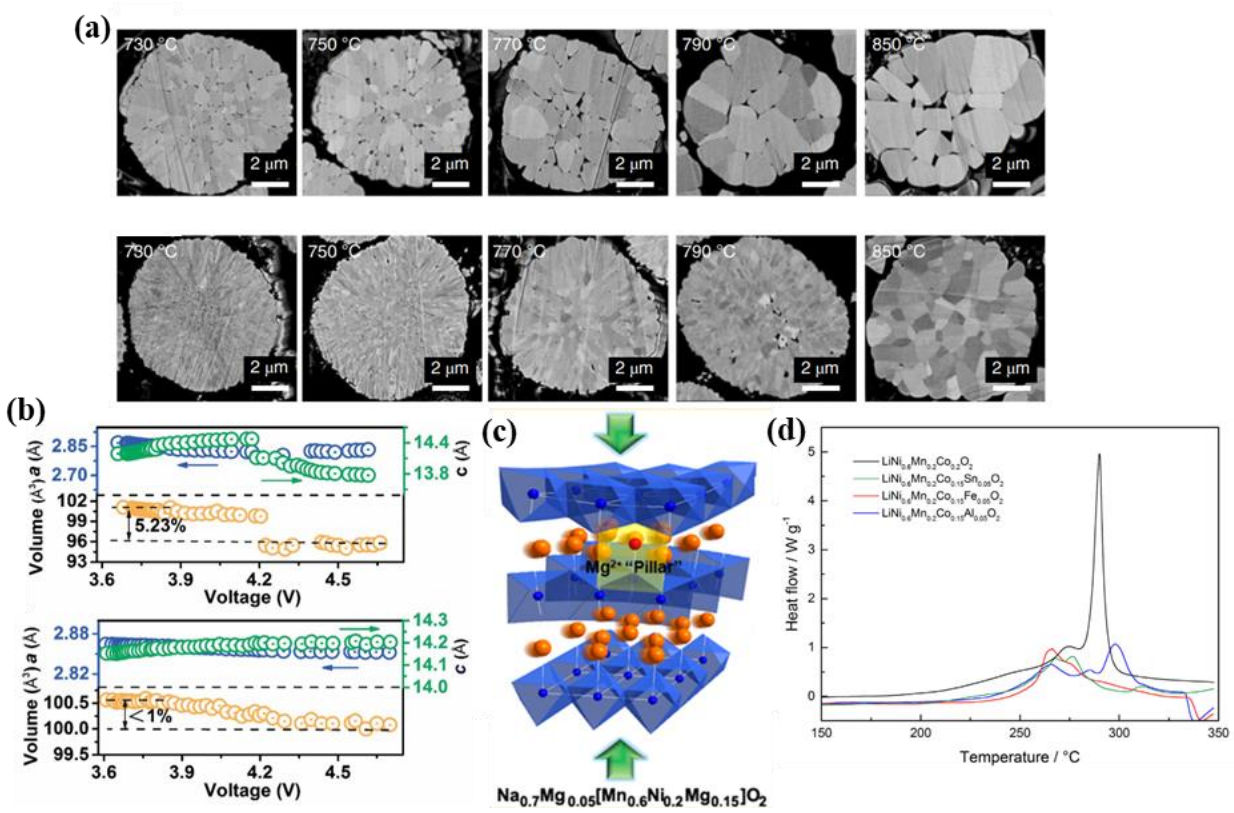

Figure 38: (a) SEM image of the primary particle microstructure of undoped NMC90 (top row) and 1mol% Ta-doped NMC90 (bottom row), taken from Ref. [23]. (b) Difference in contraction severity of the c lattice parameter of NMC811 (top) and $LiNi_{0.90}Co_{0.07}Mg_{0.03}O_2$ (bottom), taken from Ref. [38]. (c) Illustration of the pillaring effect of Mg ions on a layered oxide cathode, taken from Ref. [30]. (d) Improvement in thermal stability of Ni-rich cathodes by reduction of peak heat flow due to use of different dopants, taken from Ref. [29].

6.1.2 Mg & B Co-doped NMC95

Co-doping is a relatively recent development for layered oxides and may be beneficial in improving the desirable properties of LNO. Several works have studied co-doping of Al or Na cations and F anions on Li-rich layered oxides, demonstrating that such dopants can provide their individual benefits while mitigating potential negative effects of the other dopant [35-37]. In the

mentioned work, co-doping led to improvements in both conductivity and structural stability. However, for Ni-rich NMC compositions or LNO, co-doping has been mostly focused on dual cation implementation, rather than combined cation/anion dopants.

In this work, we utilize a combination of Mg and B dopants in doping $LiNi_{0.95}Mn_{0.025}Co_{0.025}O_2$ (NMC95). The undoped cathode material shows excellent initial capacity ~200mAh/g when cycled from 2.8-4.3V but is demonstrated to have rapid capacity fade. Magnesium is well studied dopant and is effective in improving the capacity retention of the NMC cathode. However, only small amounts can be added due to a significant detrimental impact to reversible capacity from Mg acting as obstacles toward Li diffusion [39]. The use of boron as a dopant for NMC cathodes is relatively recent, with most studies having been conducted within the past few years. Small additions of boron are effective in modifying the primary particle growth into a preferred orientation by decreasing the energy of the (003) plane [40]. In addition, the small boron ion (0.27Å vs 0.76 Å and 0.56 Å for Li^+ and Ni^{3+}, respectively) resides within the tetrahedral sites of the TM-O or Li-O octahedra [40]. Studies focused on boron doping find that reversible capacity increases due to expansion of the Li slab layer, along with improved capacity retention from the radial orientation of primary particles [23,40-42]. By combining the two dopants into the NMC95, a cathode with superior capacity retention while retaining good reversible capacity can be achieved, with particularly improved performance when cycled at an elevated temperature of 60˚C.

6.1.3 Synthesis of NMC95

NMC95 precursors were synthesized using a hydroxide-based co-precipitation reaction. In short, a 1.8M solution of transition metal sulfates in the desired ratio (95mol% $NiSO_4$, 2.5mol% $MnSO_4$, and 2.5mol% $CoSO_4$ was added dropwise into a double jacked reactor stirring at 650RPM and kept at 55°C under a nitrogen atmosphere. The reactor pH was maintained at 11.0 ± 0.2 using a solution of 5M NaOH, which also provides the counter anion for precipitation. Ammonia is also fed into the reactor as a chelating agent to control the reaction rate for the formation of dense, secondary particles of good size distribution. The reaction is allowed to run for a total of 8hrs before being collected and rinsed with deionized water to remove remaining ammonia, sodium hydroxide, and/or sulfate compounds, before being dried at 100 °C in a vacuum oven overnight. The final product consists of metal hydroxide spherical particles approximately 8um in diameter.

To produce the final lithiated cathode, a mixture of LiOH-H_2O and the hydroxide precursor are mixed thoroughly by mortar and pestle in an Li:TM molar ratio of 1.05:1.0. The mixture is intially sintered at 450°C for 5hrs in air, hollowed by gentle mixing to homogenize any areas of local Li excess. The powder is then calcined at 725°C for 15hrs under 50sccm of flowing oxygen to produce the final lithiated cathode powder. The powder is stored in an argon-filled glovebox to prevent degradation of the material due to moisture and other reactive compounds in the ambient environment.

6.1.4 Synthesis of Mg, B doped NMC95

1mol% Mg-doped NMC95 (1Mg-NMC95) is synthesized similarly to the undoped precursor. The initial metal sulfate solution however, is composed of a 1.8M solution with a ratio of

94.05mol% $NiSO_4$, 2.475mol% $MnSO_4$, 2.475mol% $CoSO_4$, and 1.0mol% $MgSO_4$. The reaction conditions and calcination conditions are unchanged.

For 1mol% B-doped NMC95 (1B-NMC95), the undoped hydroxide precursor is mixed thoroughly with LiOH and boric acid. The molar ratio of Li:TM:B was maintained at 1.05:1.00:0.01. To obtain good distribution of boron throughout the powder, ethanol as added to the mixture, which was stirred constantly until complete evaporation of the ethanol solvent. The following mixture is sintered using the same process as NMC95 and 1Mg-NMC95. The co-doped 1Mg-1B-NMC95 sample is prepared using the same process for 1B-NMC95, while using the precursor synthesized for 1Mg-NMC95.

6.1.5 Characterization Methods

Surface morphologies were analyzed via scanning electron microscopy (SEM) analysis using a JEOL JSM-7000F SEM with a 10 kV accelerating voltage. X-ray diffraction (XRD) profiles of the as-synthesized powders were obtained using a PANalytical Empyrean X-ray Diffractometer with a Cu Kα radiation source ($\lambda = 1.5406$ Å). Crystallographic lattice parameters and percentage of cation mixing were determined through the Rietveld refinement method via FullProf Suite software, using the R-3m space group as the structural reference and assuming only a single phase. Elemental compositions were determined through inductively coupled plasma optical emission spectrometry (ICP-OES), via a Perkin-Elmer Optima 8000 ICP-OES system.

Electrochemical charge/discharge cycles were conducted either at ambient room temperature or at 60°C in a controlled oven on a LANDT CT2001A from 2.8-4.3V (specific capacity set to

200mAh/g). Extended cycling of cells was conducted at a charge/discharge rate of 1C for up to 100 cycles. Rate performance was tested using rates of C/10, C/5, C/2, 1C, 2C, and 3C. Cyclic voltammetry (CV) profiles and electrochemical impedance spectra (EIS) were obtained using a Bio-logic SAS VMP3 multi-channel Potentiostat maintained at 30°C. CV and EIS data were obtained for cells before and after cycling. CV profiles were obtained at a scan rate of 0.1mV/s between 2.8-4.3 V vs. Li/Li^+. EIS was obtained using a 5mV sinusoidal amplitude from 1MHz to 20mHz. Galvanostatic intermittent titration technique (GITT) was utilized to determine lithium diffusion coefficients and was conducted using a C/10 current pulse for 0.5hrs, followed by 1.5hrs of resting time. GITT measurements for each sample were collected across one full charge cycle.

6.1.6 Results and Discussion

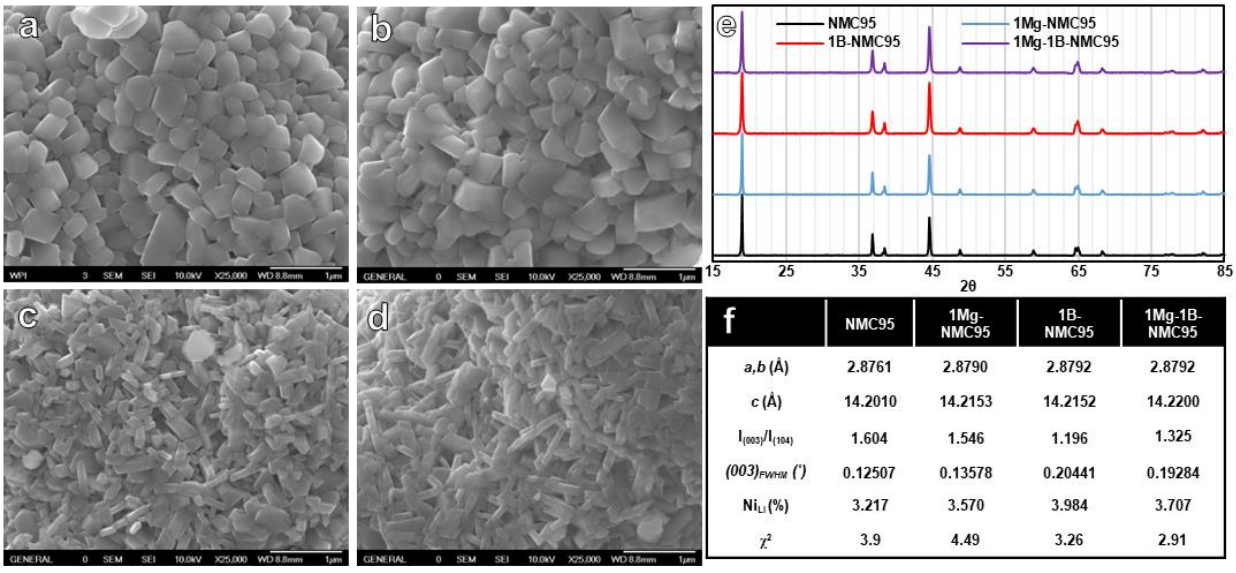

f	NMC95	1Mg-NMC95	1B-NMC95	1Mg-1B-NMC95
a,b (Å)	2.8761	2.8790	2.8792	2.8792
c (Å)	14.2010	14.2153	14.2152	14.2200
$I_{(003)}/I_{(104)}$	1.604	1.546	1.196	1.325
$(003)_{FWHM}$ (°)	0.12507	0.13578	0.20441	0.19284
Ni_{Li} (%)	3.217	3.570	3.984	3.707
χ^2	3.9	4.49	3.26	2.91

Figure 39: Surface morphology of (a) NMC95, (b) 1Mg-NMC95, (c) 1B-NMC95, (d) 1Mg-1B-NMC95 and (e) XRD profiles and (f) calculated crystallographic parameters via Rietveld Refinement

The morphology of each sample is shown in **Figure 39a-d**. From the undoped NMC95, the primary particles are composed of block-like crystals ~200nm in size. The addition of 1mol% of Mg does not appear to affect the primary particle shape, as shown in **Figure 39b**. However, the addition of 1mol% of B had a clear effect on primary particle growth. As shown in **Figure 39c, d**, the addition of boron resulted in thin, elongated primary particles with high anisotropy. Even for the co-doped sample, the effect of boron is significant and dominates primary particle formation. Based on past literature, it is understood that growth along the (003) direction is suppressed due to the reduction of the (003) surface energy [40]. Cross sections of fractured particles in **Figure 40** also show that boron-doped samples possess the radially oriented surface primary particles, consistent with previous work [40-42]. 1Mg-NMC95, however, shows no noticeable difference in the internal secondary particle structure compared to NMC95.

XRD profiles and determined lattice parameters in **Figure 39e, f**. Mg was assigned to occupy the transition metal sites, while B was assigned to occupy tetrahedral interstitial sites. All samples are well indexed to the R-3m layered structure and exhibit no noticeable secondary impurity phases. The addition of either Mg and B or the co-doped was found to increase the *a/b* lattice parameters by approximately 0.003Å compared to the undoped cathode. The *c* lattice parameter was also found to increase for both 1Mg-NMC95 and 1B-NMC95 by ~ 0.015Å, and 0.020Å for the co-doped 1Mg-1B-NMC95. Increases in the lattice parameter are attributed to the larger cation in the case of Mg^{2+} (0.72Å vs 0.56Å for Ni^{3+}), or distortion of the crystal structure in the case of B, which was previously demonstrated to increase the interslab distance [41]. The FWHM of the (003) peak for both 1B-NMC95 and 1Mg-1B-NMC95 are significantly larger than that of NMC95 and 1Mg-NMC95, consistent with the smaller crystallite size observed from SEM

imaging. Cation mixing across all samples are similar, between 3-4% Ni_{Li}, with the doped samples generally increasing the degree of cation mixing. Compared to Mg, the addition of boron led to larger increases in cation mixing, which can also be attributed to defects and distortions caused by the insertion of B atoms into the interstitial sites.

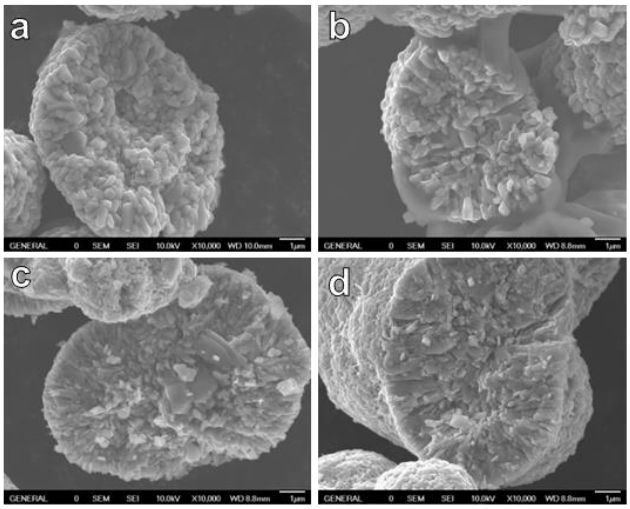

e	NMC95	1Mg-NMC95	1B-NMC95	1Mg-1B-NMC95
Li	1.029	1.042	1.096	1.030
Ni	0.957	0.957	0.957	0.957
Mn	0.021	0.021	0.021	0.021
Co	0.022	0.022	0.022	0.022
Mg	0.000	0.008	0.00	0.009
B	0.000	0.00	0.017	0.018

Figure 40: Cross sections of (a) NMC95, (b) 1Mg-NMC95, (c) 1B-NMC95, and (d) 1Mg-1B-NMC95. (e) Chemical composition derived from ICP-OES. B concentrations are higher than expected but may be higher due to error in the standards for low concentration.

Figure 40 reveals the effects of Mg and B on the internal microstructure of the secondary particles. For the most part, the addition of Mg has no observable impact on the internal morphology or microstructure, with **Figure 40a and b** having an interior of block-like primary particles with no preferred orientation. However, the addition of boron atoms results in a radially aligned internal structure, with thinner primary particles. This is consistent with previous observations on the influence of boron doping on the internal microstructure [40-42]. In addition, elemental analysis by ICP-OES reveals that the targeted compositions are mostly achieved, with no lithium deficiencies. The concentration of boron in the samples appears higher than expected and may be attributed to either the error in the ICP standards and calculated concentrations at

such low B concentration, or error in measuring the amount of boric acid due to the extremely low amounts needed per gram of precursor (6.7mg/1g hydroxide precursor for 1mol% doping).

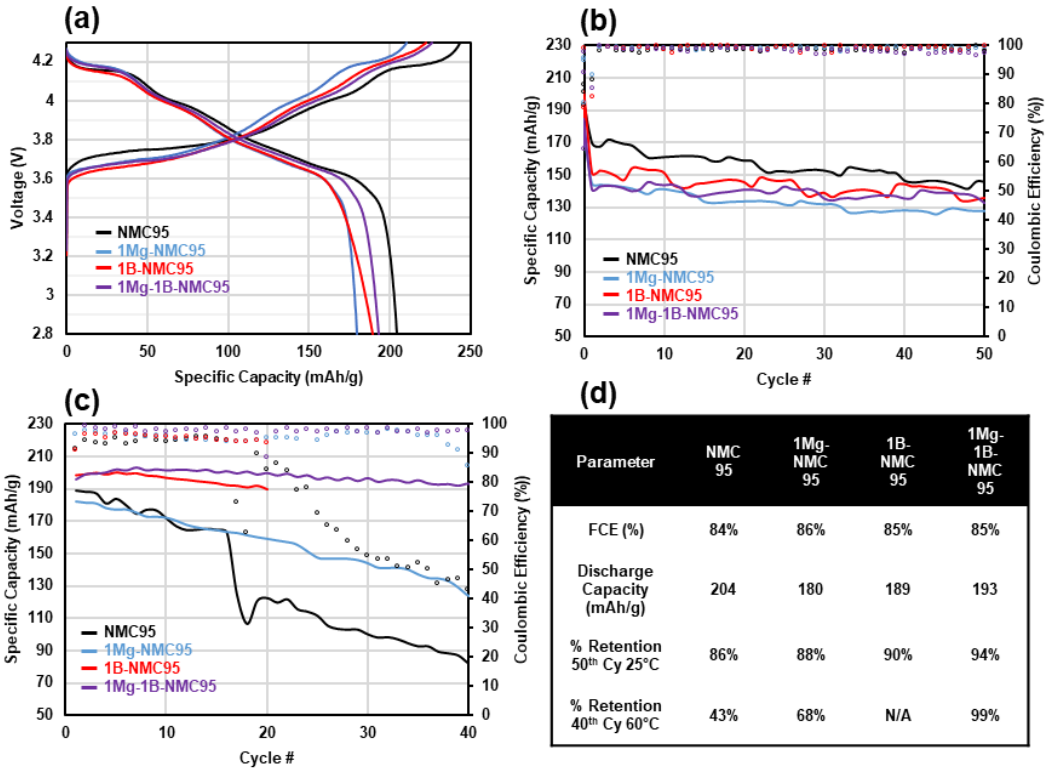

Parameter	NMC 95	1Mg-NMC 95	1B-NMC 95	1Mg-1B-NMC 95
FCE (%)	84%	86%	85%	85%
Discharge Capacity (mAh/g)	204	180	189	193
% Retention 50th Cy 25°C	86%	88%	90%	94%
% Retention 40th Cy 60°C	43%	68%	N/A	99%

Figure 41: (a) First charge/discharge cycle at 0.1C. (b) Capacity retention under 1C cycling from 2.8-4.3V at 25˚C. (c) Capacity retention under 1C cycling from 2.8-4.3V at 60˚C. (d) Tabulated results of first cycle and capacity retention

The electrochemical performance in half-cell 2032-type coin cells of the fabricated samples is shown in **Figure 41**. The first formation cycle in **Figure 41a** demonstrates that all doped samples exhibit reduced reversible capacity; the undoped NMC95 has an initial reversible capacity of 204mAh/g, while the doped samples range from 180-190mAh/g. The addition of Mg significantly reduces the availability capacity, which is consistent with previous observations and due to the presence of some Mg ions in the Li layer acting as pillars and obstacles towards Li

diffusion [44]. It is also worth noting that the addition of boron also found to reduce the reversible capacity, contrary to previous works that reported improved capacity due to an increase of the *c* lattice parameter [41]. It is suspected that the reduction in capacity is due a suboptimal doping concentration.

The capacity retention of samples at both room temperature and at 60°C are shown in **Figures b and c**. While the initial 1C capacity of the doped samples are expectedly reduced compared to NMC95, the capacity retention is noticeably improved; after 50 cycles, NMC95 retains only 86% of its original 1C capacity, while the co-doped 1Mg-1B-NMC95 retains 94% of its capacity. Solely Mg or B doping also improved the capacity retention, but not to the degree of the co-doped sample. A much more significant difference is observed at high temperature cycling, where NMC95 degrades dramatically within the first 40 cycles, with rapid capacity fade followed by abrupt decrease in the coulombic efficiency, suggesting a combination of uncontrolled SEI growth and intergranular cracking. 1Mg-NMC95 shows improved capacity retention, specifically regarding the stability of the coulombic efficiency, but still suffers from significant capacity fade, with only 68% of its original capacity after 40 cycles. In contrast, both 1B-NMC95 and 1Mg-1B-NMC95 exhibit significantly improved capacity and capacity retention. Both B-doped samples have an initial 1C capacity of 200mAh/g, with a stabile coulombic efficiency near %100. The co-doped 1Mg-1B-NMC95 shows much better capacity fade of 0.23mAh/g-cy vs 0.53mAh/g-cy for 1B-NMC95, suggesting the effectiveness of the co-doping.

6.1.7 Conclusion

Pushing the Ni-content further to the LNO composition is a clear path towards higher capacity and lower cost cathodes, so long as the severe degradation mechanisms are addressed. In this preliminary work, we demonstrate the feasibility of doping NMC95, which contains 95mol% Ni and only 2.5mol% of Co and Mn. Notable microstructural tuning at both the surface and interior are achieved using boron dopants, resulting in a microstructure better suited to resist particle fracture. While capacity was moderately reduced compared to the undoped material during room temperature operation, the Mg and B co-doped sample exhibited dramatically improved capacity and capacity retention over the undoped and single element doped counterparts. The improvement is suggested to be due to the dual dopants, which can suppress volume change and subsequent cracking and SEI growth. However, further analysis is needed, particularly in the post-mortem condition, to elucidate the benefits of Mg and B co-doping of NMC95.

6.2 Doping for Ni-rich Single Crystal Cathodes

Due to the inherent bulk instability of Ni-rich single crystal NMC cathodes, the incorporation of dopants is necessary to suppress planar gliding and intragranular fracture mechanisms. Based on work related to polycrystalline cathodes, Ti is a suitable dopant that improves the mechanical integrity of the secondary particle while also providing improved surface stability [43].

Preliminary results incorporating Ti into single crystal NMC811 (Ti-SC811) demonstrates that dopant concentrations as low as 1mol% is effective in improving the reversibility of the H2 to H3 transition and suppress the high charge transfer resistance in the delithiated state [**Figure 42**].

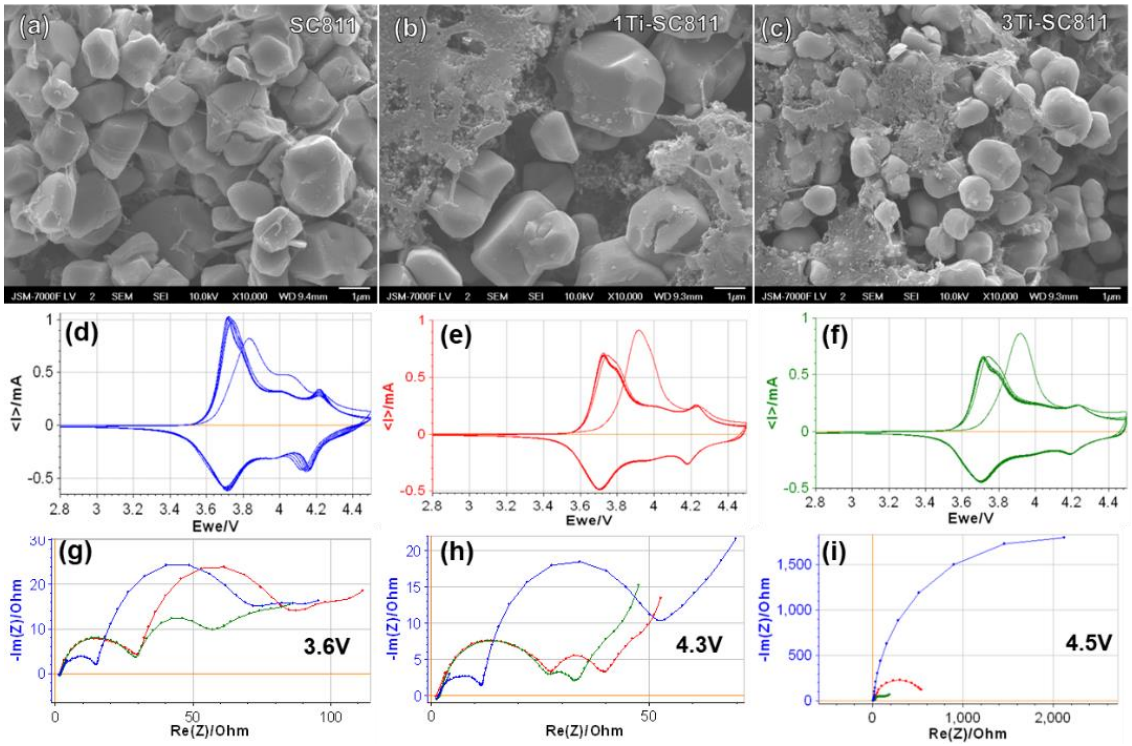

Figure 42: (a-c) SEM images of cathodes taken from disassembled cells, charged to 4.5V vs Li/Li+. (d-f) Cyclic voltammograms of the first 7 cycles, using a scan rate of 0.1mV/s. (g-i) Nyquist plots at selected states of charge

Exploration of Ti and optimum concentrations may improve the capacity retention to that or acceptable levels. The investigation of other dopants may also be suitable for improving Ni-rich single crystal cathodes and suppressing the degradation mechanisms observed in this work.

6.3 Analysis of Single Crystal Cathodes at the Electrode Level

We also recognize that further research is necessary on the optimization of electrode processing of single crystal cathodes and determining how preferred shape size, and orientation may affect the electronic network of the final dried cathode. Processing parameters such as slurry viscosity and optimum electrode drying processes may in fact differ between spherical polycrystalline powders and the faceted single crystals. Techniques to study tortuosity and electrode porosity

such as transmission X-ray tomography and mercury porosimetry would be exceptionally useful in discerning the differences between polycrystalline and single crystalline electrode processing.

6.4 Nanocoating Selection for Coated Precursors

The effective precipitation of an Mn-based nanoparticle coating layer on Ni-rich hydroxide precursors was able to improve performance while utilizing an industrially viable method. We recognize that other nanoparticle coatings can be produced using a similar route and may potentially offer better performance improvement for the Ni-rich cathode. Transition metal hydroxides such as $Al(OH)_3$, $Mg(OH)_2$, and $Cr(OH)_3$ are among several compounds with relatively low solubility products which should facilitate the feasible precipitation of nanoparticles, with the corresponding oxides having demonstrated various degrees of cathode improvement in past works [45-47]. Exploration into utilizing the 2-step coprecipitation process with pH modulation for synthesizing in-situ nanocoatings could be tested. Continued optimization of this process at scaled-up levels should also be taken into consideration.

6.5 Aqueous Processing of Modified, Coated Ni-rich Cathode

Aqueous processing remains a desirable milestone in battery cathode development, and while not practical for untreated Ni-rich cathode powders, cathode modifications may inhibit the pulverization of polycrystalline secondary particles. Besides, surface modifications already appear to be necessary for practical utilization of Ni-rich cathodes beyond 80% nickel. The impact of various coatings or dopants on inhibiting water-initiated surface damage and particle pulverization would be a fruitful area of work. Optimized single crystal morphologies for aqueous processing may also be an area of interest due to the lack of secondary particle structure.

6.6 Cobalt-free Ultrahigh Ni-rich Cathodes

While NMC95 is composed of only 2.5mol% cobalt, the next step in further reducing materials cost while also avoiding potential supply chain issues is to completely remove cobalt from the cathode composition design. Effectively, this delves into the realm of doped LNO cathodes. The addition and optimization of highly influential dopants with low solid solubilities is necessary for the realization and resurging study into the commercial viability of LNO cathodes.

6.7 References

[1] Xie, Q., & Manthiram, A. (2020). Long-life, ultrahigh-nickel cathodes with excellent air storage stability for high-energy density lithium-based batteries. *Chemistry of Materials*, *32*(17), 7413-7424.

[2] Zhang, Y., Li, H., Liu, J., Zhang, J., Cheng, F., & Chen, J. (2019). LiNi 0.90 Co 0.07 Mg 0.03 O 2 cathode materials with Mg-concentration gradient for rechargeable lithium-ion batteries. *Journal of materials chemistry A*, *7*(36), 20958-20964.

[3] Yoon, C. S., Ryu, H. H., Park, G. T., Kim, J. H., Kim, K. H., & Sun, Y. K. (2018). Extracting maximum capacity from Ni-rich Li [Ni 0.95 Co 0.025 Mn 0.025] O 2 cathodes for high-energy-density lithium-ion batteries. *Journal of materials chemistry A*, *6*(9), 4126-4132.

[4] Ryu, H. H., Park, K. J., Yoon, C. S., & Sun, Y. K. (2018). Capacity fading of Ni-rich Li [Ni x Co y Mn1–x–y] O2 (0.6≤ x≤ 0.95) cathodes for high-energy-density lithium-ion batteries: bulk or surface degradation?. *Chemistry of materials*, *30*(3), 1155-1163.

[5] Li, J., Chang, C. H., & Manthiram, A. (2019). Toward Long-Life, Ultrahigh-Nickel Layered Oxide Cathodes for Lithium-Ion Batteries: Optimizing the Interphase Chemistry with a Dual-Functional Polymer. *Chemistry of Materials*, *32*(2), 759-768.

[6] Mesnier, A., & Manthiram, A. (2020). Synthesis of LiNiO2 at Moderate Oxygen Pressure and Long-Term Cyclability in Lithium-Ion Full Cells. *ACS Applied Materials & Interfaces*, *12*(47), 52826-52835.

[7] Zhang, X., Zou, L., Cui, Z., Jia, H., Engelhard, M. H., Matthews, B. E., Cao, X., Xie, Q., Wang, C., Manthiram, A., Zhang, J.G., & Xu, W. (2021). Stabilizing ultrahigh-nickel layered oxide cathodes for high-voltage lithium metal batteries. *Materials Today*, *44*, 15-24.

[8] Ronduda, H., Zybert, M., Szczęsna-Chrzan, A., Trzeciak, T., Ostrowski, A., Szymański, D., Wieczorek, W., Rarog-Pilecka, W., & Marcinek, M. (2020). On the Sensitivity of the Ni-rich Layered Cathode Materials for Li-ion Batteries to the Different Calcination Conditions. *Nanomaterials*, *10*(10), 2018.

[9] Xiao, Y., Liu, T., Liu, J., He, L., Chen, J., Zhang, J., Luo, P., Lu, H., Wang, R., Zhu, W., Hu, Z., Teng, G., Xin, C., Zheng, J., Liang, T., Wang, F., Chen, Y., Huang, Q., & Chen, H. (2018). Insight into the origin of lithium/nickel ions exchange in layered Li (NixMnyCoz) O2 cathode materials. *Nano Energy*, *49*, 77-85.

[10] Ahmed, S., Nelson, P. A., Gallagher, K. G., Susarla, N., & Dees, D. W. (2017). Cost and energy demand of producing nickel manganese cobalt cathode material for lithium ion batteries. *Journal of Power Sources*, *342*, 733-740.

[11] Zheng, J., Xiao, J., & Zhang, J. G. (2016). The roles of oxygen non-stoichiometry on the electrochemical properties of oxide-based cathode materials. *Nano Today*, *11*(5), 678-694.

[12] Li, J., & Manthiram, A. (2019). A Comprehensive Analysis of the Interphasial and Structural Evolution over Long-Term Cycling of Ultrahigh-Nickel Cathodes in Lithium-Ion Batteries. *Advanced Energy Materials*, *9*(45), 1902731.

[13] Li, J., Li, W., You, Y., & Manthiram, A. (2018). Extending the service life of high-Ni layered oxides by tuning the electrode–electrolyte interphase. *Advanced Energy Materials*, *8*(29), 1801957.

[14] Bianchini, M., Roca-Ayats, M., Hartmann, P., Brezesinski, T., & Janek, J. (2019). There and back again—the journey of LiNiO2 as a cathode active material. *Angewandte Chemie International Edition*, *58*(31), 10434-10458.

[15] Delmas, C., Menetrier, M., Croguennec, L., Saadoune, I., Rougier, A., Pouillerie, C., Prado, G., Gune, M., & Fournes, L. (1999). An overview of the Li (Ni, M) O2 systems: syntheses, structures and properties. *Electrochimica Acta*, *45*(1-2), 243-253.

[16] Kim, Y., Seong, W. M., & Manthiram, A. (2021). Cobalt-free, high-nickel layered oxide cathodes for lithium-ion batteries: Progress, challenges, and perspectives. *Energy Storage Materials*, *34*, 250-259.

[17] Li, W., Lee, S., & Manthiram, A. (2020). High-Nickel NMA: A Cobalt-Free Alternative to NMC and NCA Cathodes for Lithium-Ion Batteries. *Advanced Materials*, *32*(33), 2002718.

[18] Lee, S., Li, W., Dolocan, A., Celio, H., Park, H., Warner, J. H., & Manthiram, A. (2021). In-Depth Analysis of the Degradation Mechanisms of High-Nickel, Low/No-Cobalt Layered Oxide Cathodes for Lithium-Ion Batteries. *Advanced Energy Materials*, *11*(31), 2100858.

[19] Xie, Q., Li, W., Dolocan, A., & Manthiram, A. (2019). Insights into boron-based polyanion-tuned high-nickel cathodes for high-energy-density lithium-ion batteries. *Chemistry of Materials*, *31*(21), 8886-8897.

[20] Park, T. J., Kang, S. H., Kim, C., & Son, J. T. (2013). Electrochemical Properties of LiNi0. 90Co0. 05Al0. 05O2/LiFe0. 9Mn0. 1PO4/C Blended Cathode for Lithium Ion Batteries. *Chemistry Letters*, *42*(10), 1320-1322.

[21] Park, K., Ham, D. J., Park, S. Y., Jang, J., Yeon, D. H., Moon, S., & Ahn, S. J. (2020). High-Ni cathode material improved with Zr for stable cycling of Li-ion rechargeable batteries. *RSC Advances*, *10*(45), 26756-26764.

[22] Rossen, E., Jones, C. D. W., & Dahn, J. R. (1992). Structure and electrochemistry of LixMnyNi1− yO2. *Solid State Ionics*, *57*(3-4), 311-318.

[23] Kim, U. H., Park, G. T., Son, B. K., Nam, G. W., Liu, J., Kuo, L. Y., Kaghazchi, P., Yoon, C.S, & Sun, Y. K. (2020). Heuristic solution for achieving long-term cycle stability for Ni-rich layered cathodes at full depth of discharge. *Nature energy*, *5*(11), 860-869.

[24] Rougier, A., Saadoune, I., Gravereau, P., Willmann, P., & Delmasa, C. (1996). Effect of cobalt substitution on cationic distribution in LiNi1− y CoyO2 electrode materials. *Solid State Ionics*, *90*(1-4), 83-90.

[25] Ren, Z., Shen, C., Liu, M., Liu, J., Zhang, S., Yang, G., Huai, L., Liu, X., Wang, D., & Li, H. (2020). Improving LiNi0. 9Co0. 08Mn0. 02O2's cyclic stability via abating mechanical damages. *Energy Storage Materials*, *28*, 1-9.

[26] Park, K. J., Jung, H. G., Kuo, L. Y., Kaghazchi, P., Yoon, C. S., & Sun, Y. K. (2018). Improved cycling stability of Li [Ni0. 90Co0. 05Mn0. 05] O2 through microstructure

modification by boron doping for Li-ion batteries. *Advanced energy materials*, *8*(25), 1801202.

[27] Lipson, A. L., Durham, J. L., LeResche, M., Abu-Baker, I., Murphy, M. J., Fister, T. T., Wang, L., Zhou, F., Liu, L., Kim, K., & Johnson, D. (2020). Improving the Thermal Stability of NMC 622 Li-Ion Battery Cathodes through Doping During Coprecipitation. *ACS applied materials & interfaces*, *12*(16), 18512-18518.

[28] Jeon, J. E., Park, K. R., Kim, K. M., Ahn, C., Lee, J., Yu, D. Y., Bang, J., Oh, N., Han, H., & Mhin, S. (2021). Effect of Cu/Fe addition on the microstructures and electrical performances of Ni–Co–Mn oxides. *Journal of Alloys and Compounds*, *859*, 157769.

[29] Eilers-Rethwisch, M., Winter, M., & Schappacher, F. M. (2018). Synthesis, electrochemical investigation and structural analysis of doped Li [Ni0. 6Mn0. 2Co0. 2-xMx] O2 (x= 0, 0.05; M= Al, Fe, Sn) cathode materials. *Journal of power sources*, *387*, 101-107.

[30] Wang, Q. C., Meng, J. K., Yue, X. Y., Qiu, Q. Q., Song, Y., Wu, X. J., Fu, Z.W., Xia, Y.Y., Shadike, Z., Xu, J., Yang, X.Q., & Zhou, Y. N. (2018). Tuning P2-structured cathode material by Na-site Mg substitution for Na-ion batteries. *Journal of the American Chemical Society*, *141*(2), 840-848.

[31] Guilmard, M., Rougier, A., Grüne, M., Croguennec, L., & Delmas, C. (2003). Effects of aluminum on the structural and electrochemical properties of LiNiO2. *Journal of Power Sources*, *115*(2), 305-314.

[32] Kong, F., Liang, C., Longo, R. C., Yeon, D. H., Zheng, Y., Park, J. H., Doo, S.G., & Cho, K. (2016). Conflicting roles of anion doping on the electrochemical performance of Li-ion battery cathode materials. *Chemistry of Materials*, *28*(19), 6942-6952.

[33] Kumar, S. K., Ghosh, S., & Martha, S. K. (2017). Synergistic effect of magnesium and fluorine doping on the electrochemical performance of lithium-manganese rich (LMR)-based Ni-Mn-Co-oxide (NMC) cathodes for lithium-ion batteries. *Ionics*, *23*(7), 1655-1662.

[34] Zhang, N., Stark, J., Li, H., Liu, A., Li, Y., Hamam, I., & Dahn, J. R. (2020). Effects of fluorine doping on nickel-rich positive electrode materials for lithium-ion batteries. *Journal of The Electrochemical Society*, *167*(8), 080518.

[35] Jamil, S., Yousaf, A. B., Yoon, S. H., Han, D. S., Yang, L., Kasak, P., & Wang, X. (2021). Dual cationic modified high Ni-low co layered oxide cathode with a heteroepitaxial interface for high energy-density lithium-ion batteries. *Chemical Engineering Journal*, *416*, 129118.

[36] Zeng, X., Wu, J., & Hu, Q. (2016). Effects of magnesium and chlorine co-doping on the structural and electrochemical performance of the spinel LiMn2O4 cathode materials. *Micro & Nano Letters*, *11*(12), 789-791.

[37] Liu, X., Chen, Q., Li, Y., Chen, C., Zeng, W., Yuan, M., Wang, R., & Xiao, S. (2019). Synergistic modification of magnesium fluoride/sodium for improving the electrochemical performances of high-nickel ternary (NCM811) cathode materials. *Journal of The Electrochemical Society*, *166*(14), A3480.

[38] Li, H., Zhou, P., Liu, F., Li, H., Cheng, F., & Chen, J. (2019). Stabilizing nickel-rich layered oxide cathodes by magnesium doping for rechargeable lithium-ion batteries. *Chemical science*, *10*(5), 1374-1379.

[39] Li, H., Zhou, P., Liu, F., Li, H., Cheng, F., & Chen, J. (2019). Stabilizing nickel-rich layered oxide cathodes by magnesium doping for rechargeable lithium-ion batteries. Chemical science, 10(5), 1374-1379.

[40] Roitzheim, C., Kuo, L. Y., Sohn, Y. J., Finsterbusch, M., Möller, S., Sebold, D., ... & Fattakhova-Rohlfing, D. (2021). Boron in Ni-Rich NCM811 Cathode Material: Impact on Atomic and Microscale Properties. *ACS Applied Energy Materials*, *5*(1), 524-538.

[41] Wu, C. Y., Bao, Q., Tsai, Y. T., & Duh, J. G. (2021). Tuning (003) interplanar space by boric acid co-sintering to enhance Li+ storage and transfer in Li (Ni0. 8Co0. 1Mn0. 1) O2 cathode. *Journal of Alloys and Compounds*, *865*, 158806.

[42] Liu, Y., Fan, X., Luo, B., Zhao, Z., Shen, J., Liu, Z., ... & Ou, X. (2021). Understanding the enhancement effect of boron doping on the electrochemical performance of single-crystalline Ni-rich cathode materials. *Journal of Colloid and Interface Science*, *604*, 776-784.

[43] Steiner, J. D., Cheng, H., Walsh, J., Zhang, Y., Zydlewski, B., Mu, L., ... & Lin, F. (2019). Targeted surface doping with reversible local environment improves oxygen stability at the electrochemical interfaces of nickel-rich cathode materials. *ACS applied materials & interfaces*, *11*(41), 37885-37891.

[44] Gomez-Martin, A., Reissig, F., Frankenstein, L., Heidbüchel, M., Winter, M., Placke, T., & Schmuch, R. (2022). Magnesium Substitution in Ni-Rich NMC Layered Cathodes for High-Energy Lithium Ion Batteries. Advanced Energy Materials, 12(8), 2103045.

[45] Gao, Y., Park, J., & Liang, X. (2020). Comprehensive study of Al-and Zr-modified LiNi0. 8Mn0. 1Co0. 1O2 through synergy of coating and doping. ACS Applied Energy Materials, 3(9), 8978-8987.

[46] Laskar, M. R., Jackson, D. H., Xu, S., Hamers, R. J., Morgan, D., & Kuech, T. F. (2017). Atomic layer deposited MgO: A lower overpotential coating for Li [Ni0. 5Mn0. 3Co0. 2] O2 cathode. ACS applied materials & interfaces, 9(12), 11231-11239.

[47] Phillip, N. D., Armstrong, B. L., Daniel, C., & Veith, G. M. (2020). Role of surface acidity in the surface stabilization of the high-voltage cathode LiNi0. 6Mn0. 2Co0. 2O2. ACS omega, 5(25), 14968-14975.

Chapter 7. Relevant Publications, Patents, and Presentations

Azhari, L., Arsenault, R., Gao, G., & Wang, Y. (2021). Modified Nickel-Rich Cathodes via Conformal Nanoparticle Coating of Precursors Using a Single Reactor Process. ACS Applied Energy Materials, 4(12), 14618-14627.

Azhari, L., Zhou, X., Sousa, B., Yang, Z., Gao, G., & Wang, Y. (2020). Effects of Extended Aqueous Processing on Structure, Chemistry, and Performance of Polycrystalline $LiNi_xMn_yCo_zO_2$ Cathode Powders. *ACS Applied Materials & Interfaces*, 12(52), 57963-57974.

Azhari, L., Bong, S., Ma, X., & Wang, Y. (2020). Recycling for All Solid-State Lithium-Ion Batteries. *Matter*, *3*(6), 1845-1861.

Azhari, L., Meng, Z., Yang, Z., Gao, G., Han, Y., & Wang, Y. Underlying Limitations Behind Impedance Rise and Capacity Fade of Single Crystalline Ni-Rich Cathodes Synthesized Via a Molten-Salt Route. Available at SSRN 4162770. *(Accepted to Journal of Power Sources)*

Azhari, L., Sousa, B., Ahmed, R., Yang, Z., Gao, G., Han, Y., and Wang, Y., Stability Enhancement and Microstructural Modification of Ni-rich Cathode via partial addition of Lithium Halide Salts *(Submitted to ACS Applied Materials & Interfaces)*

Ma, X., **Azhari, L**., & Wang, Y. (2021). Li-ion battery recycling challenges. *Chem*.

Bong, S., **Azhari, L**., & Wang, Y. (2021). Laser Ablation Inductive Coupled Plasma Mass Spectroscopy (LA-ICP-MS) Analysis on Lead-Acid Battery System: Development of Evaluation Method of Sub-ppm Metal Impurity Elements. *Journal of Sustainable Metallurgy*, 1-10.

Ma, X., Hou, J., Vanaphuti, P., Yao, Z., Fu, J., **Azhari, L**., Liu, Y., & Wang, Y. (2022). Direct upcycling of mixed Ni-lean polycrystals to single-crystal Ni-rich cathode materials. *Chem*.

Vanaphuti, P., **Azhari, L**., Ma, X., Liu, Y., Hou, J., Tompsett, G. A., Yang, Z., & Wang, Y. (2022). Upgrading the Performance and Stability of Lithium, Manganese-Rich Layered Oxide Cathodes with Combined-Formic Acid and Spinel Coating Treatment. *Batteries & Supercaps*, *5*(4), e202100377.

Zheng, Y., **Azhari, L**., Meng, Z., Gao, G., Han, Y., Yang, Z., and Wang, Y., The Effect of Phosphate Impurity on Recovered $LiNi_{0.6}Co_{0.2}Mn_{0.2}O_2$ Cathode Material via Hydrometallurgy Method *(Submitted to ACS Applied Materials & Interfaces)*

Azhari, L., Wang, Y., & Arsenault, R. (2021). *Cathode Material Stabilization* (Joint Application: Ford Global Technologies, LLC and Worcester Polytechnic Institute. FMC10162PUS (84381918).

Appendix

A. Supplementary Information for Chapter 2

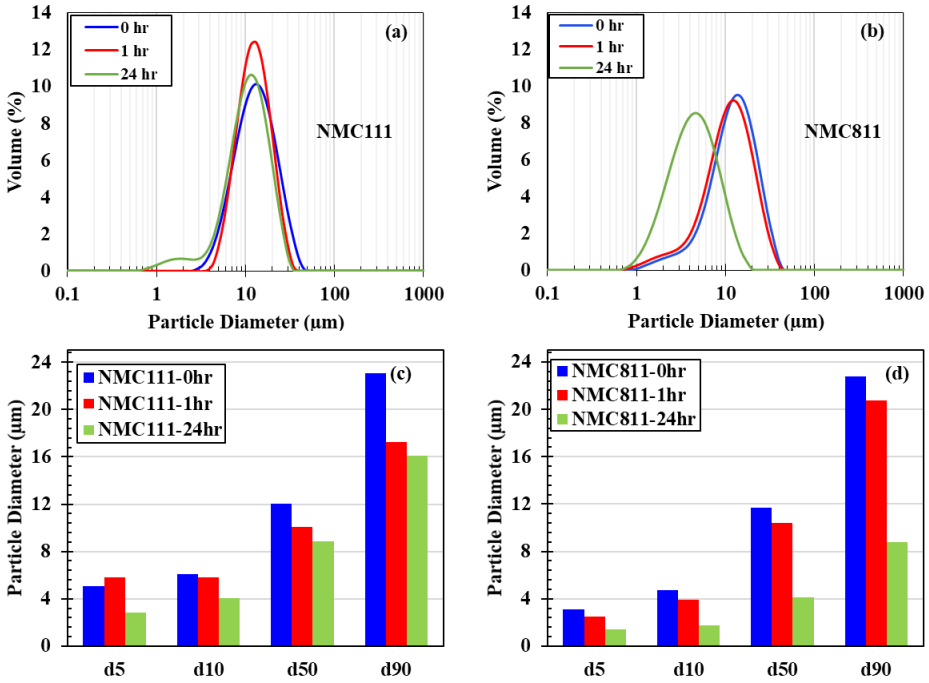

Figure S1: (a, b) Particle size distributions of NMC111 and NMC811 stirred in water at 500rpm at 10wt% solids loadings, respectively. (c, d) d5/d10/d50/d90 for the corresponding NMC111 and NMC811 samples.

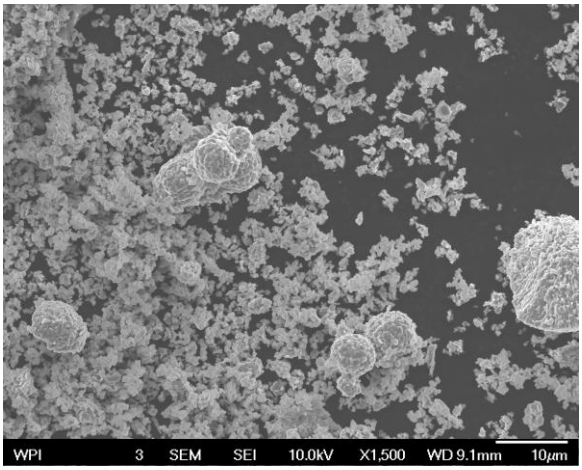

Figure S2: NMC811, stirred in DI water for 24hrs at 1000RPM.

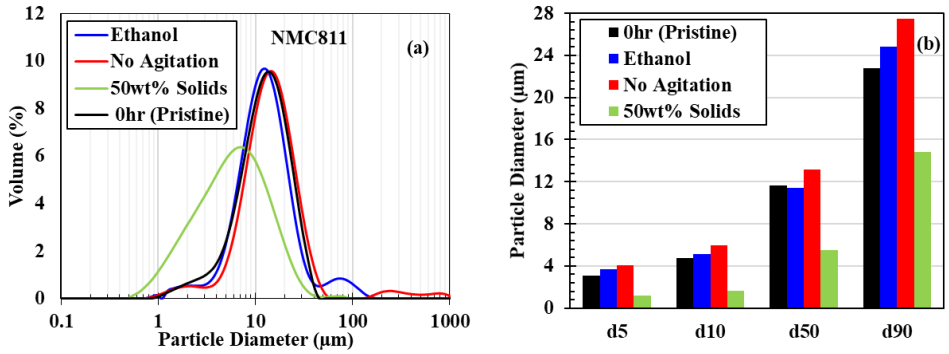

Figure S3: (a) Particle size distributions and (b) d5/d10/d50/d90 for NMC811 under different solution treatment conditions.

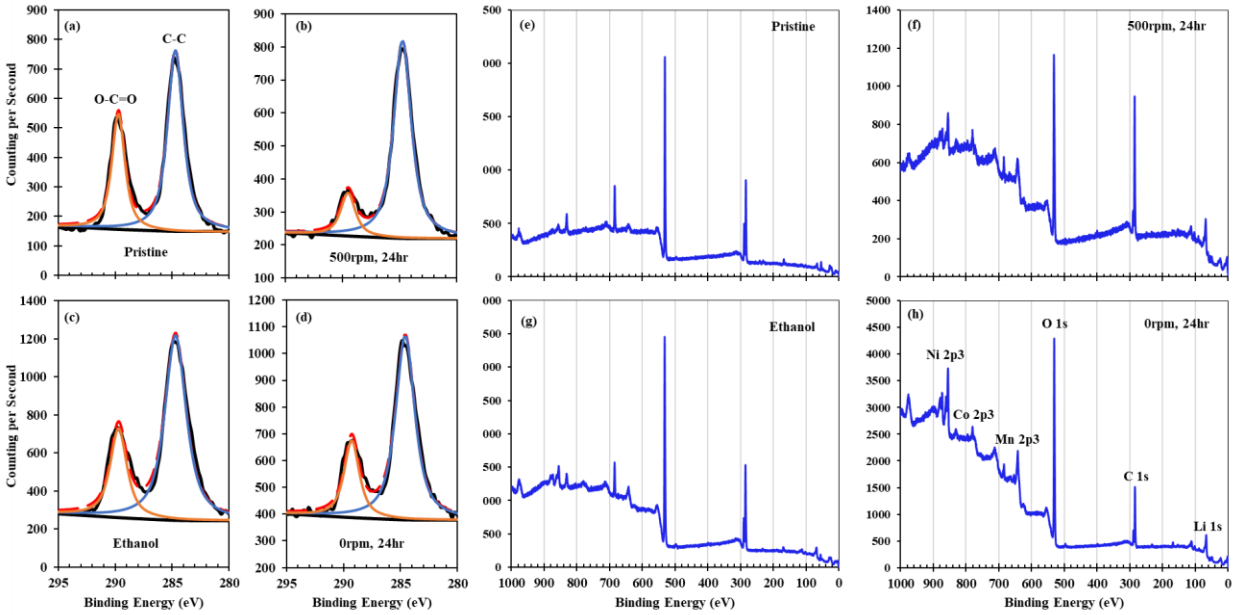

Figure S4: (a-d) XPS spectra of carbon 1s. (e-h) Survey scans of each NMC sample used to obtain atomic compositions of the surface. Carbon 1s XPS spectra shows significantly lower carbonate signal for water treated samples. Carbonate signal for water and ethanol treated samples may be attributed to a mixture of newly formed lithium and nickel carbonate species

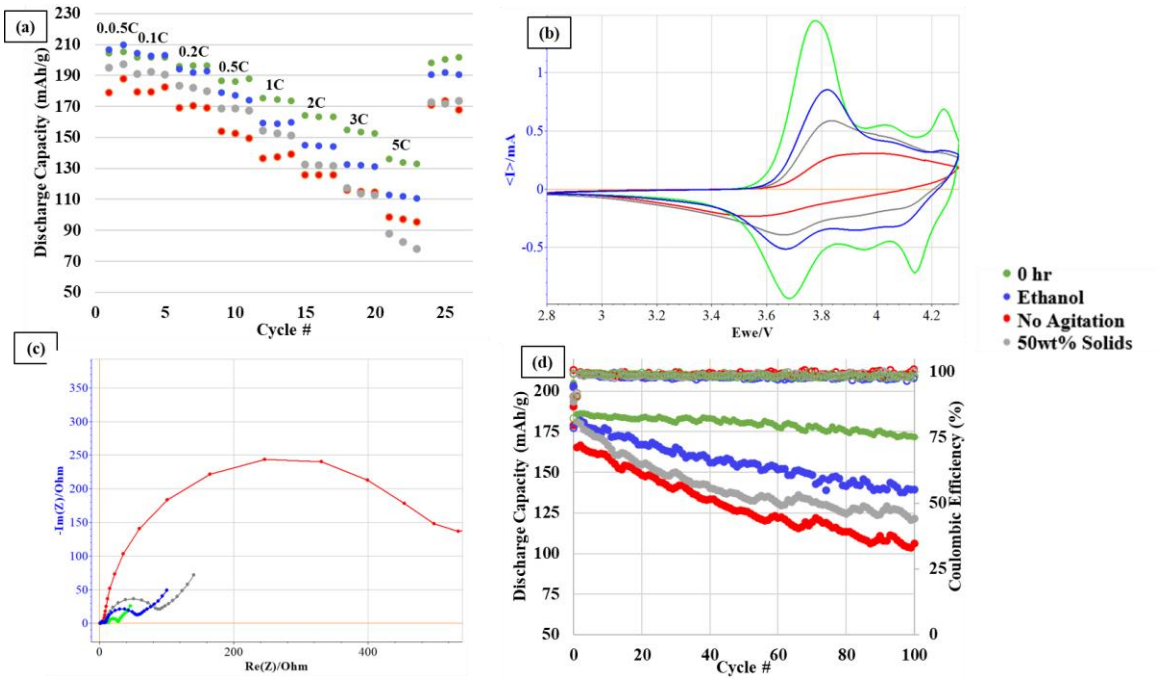

Figure S5: (a) Rate performance, (b) CV data post formation, (c) EIS data post formation, and (d) Cycling data of NMC811 in DI water for 24hrs with no stirring, NMC811 stirring for 24hrs in ethanol, and NMC811 stirring for 24hrs at 50wt% solids.

B. Supplementary Information for Chapter 3

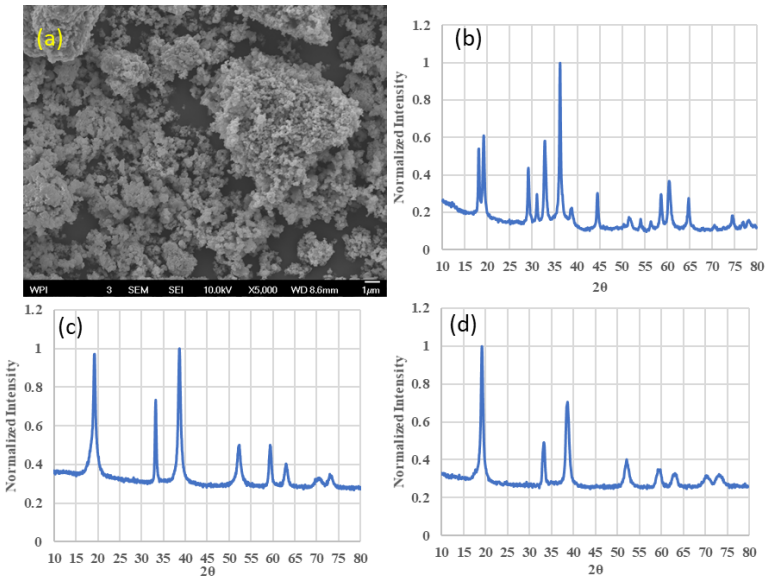

Figure S1: SEM (a) and XRD profile (b) of co-precipitation of only MC91 feedstock. XRD profile of precursor powder for (c) NMC811 and (d) C-NMC811

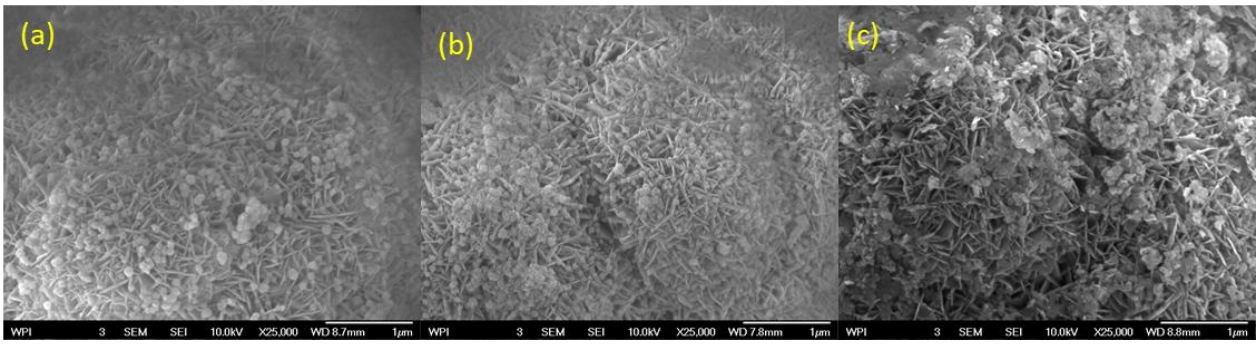

Figure S2: Coated NMC based on a 1hr coating time, and at different pH of (a) pH=9, (b) pH=10.3, (c) pH=12.5

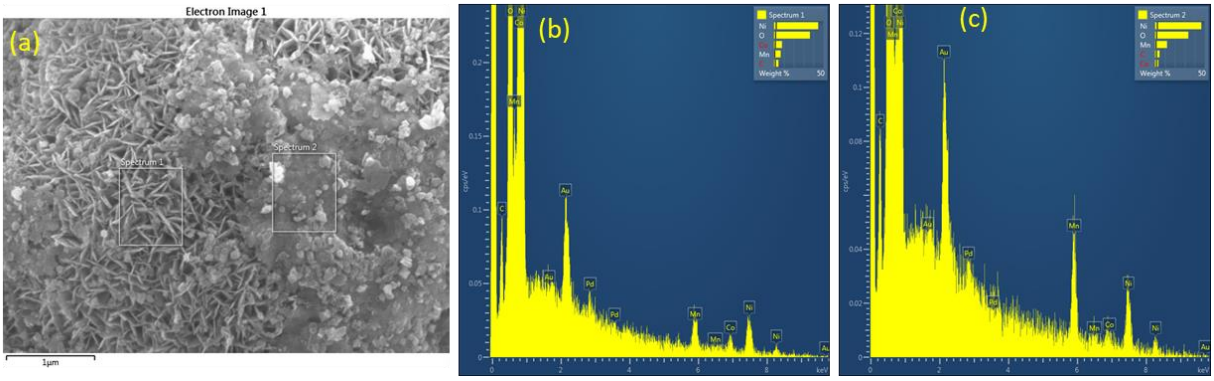

Figure S3: (a) Precursor morphology of C-NMC811, showing patchy areas of thick coating. (b) EDS of area of less coating and (c) thick coating

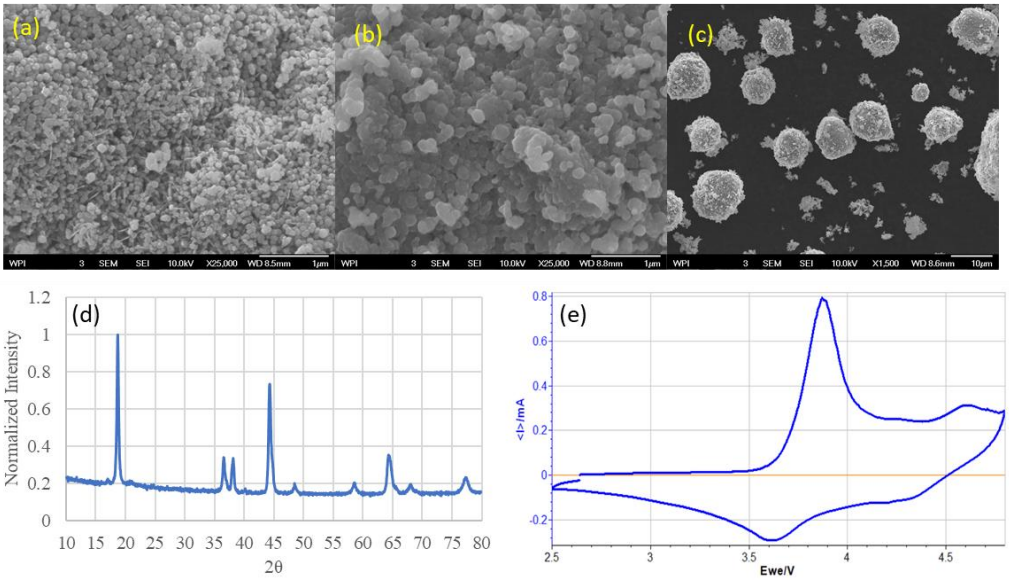

Figure S4: (a) Morphology of NMC811 precursor and (b, c) sintered cathode coated for 4 hrs. (d) XRD profile and (e) initial CV of the sintered cathode. XRD shows subpar R-3m crystallinity and I(003)/I(104) ~ 0.88. CV shows peak ~4.6V, characteristic of activation of LiMn2O3 phase in lithium-manganese rich layered oxide

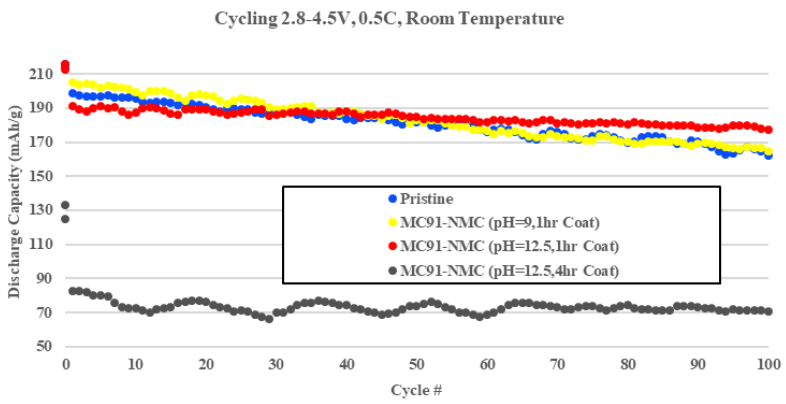

Sample	Ni	Mn	Co	Mol% Coating	Wt% Coating
NMC811	0.813	0.093	0.094	12.36	21.47
pH=9 1hr Coat	0.764	0.132	0.104	1.51	2.88
pH=12.5 1hr Coat	0.746	0.150	0.104	3.05	5.75
pH=12.5, 4hr Coat	0.628	0.273	0.099	12.36	21.47

Figure S5: Cycling data and ICP data for different coated NMC samples

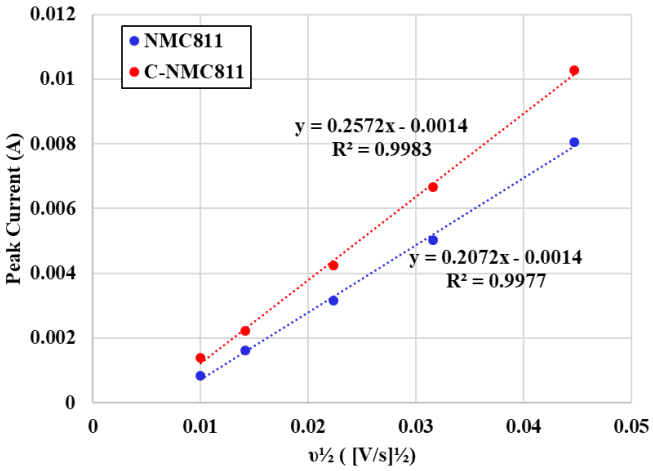

$$i_p = 0.4463(F^3/RT)^{1/2} n^{3/2} A D_o^{1/2} C_o^* v^{1/2}$$

Figure S6: Plot of Randles-Sevcik relationship between NMC811 and C-NMC811 after 100 cycles at room temperature. Higher slope of C-MC811 indicates a higher lithium diffusion coefficient.

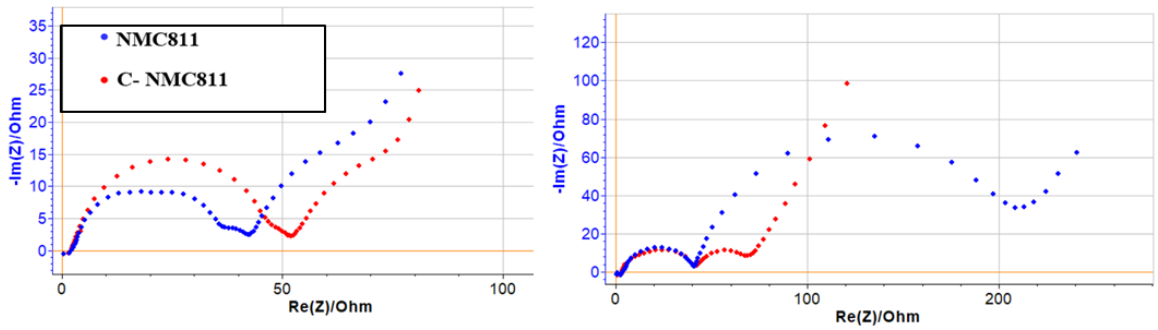

Figure S7: EIS of NMC811 and C-NMC811 probed at different state of charge of 3.8V (left) and 4.3V (right) after two initial formation cycles from 2.8-4.3V

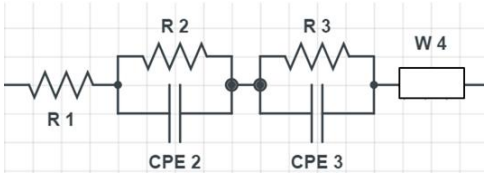

Figure S8: Equivalent circuit model for EIS

It is well documented that Ni-rich NMC suffers from significant volume changes during high voltage cycling, with the *c* lattice parameter affected the most. **Figure S9** shows that during delithiation, the *c* lattice parameter for both NMC811 and C-NMC811 initially increases in value. This is typically attributed to an increase in repulsion between the oxygen layers as lithium ions leave the structure, while the slight decrease in the *a* lattice parameter occurs due to the oxidation of transition metal ions [1, 2]. This behavior occurs until 4.3V, where a sharp decrease in the *c* lattice parameter beyond its initial value is observed for both samples, which has been previously observed and corresponds to a collapse of the lithium layer under the high degree of delithiation. This is usually attributed to an increase in impedance and reduced lithium diffusion of Ni-rich NMC in the highly charged state [49]. In this case, the coating does not prevent this collapse, and thus improvements in capacity retention and suppression of impedance

growth are inferred to derive solely from suppressed reactivity between the Ni-rich material and electrolyte.

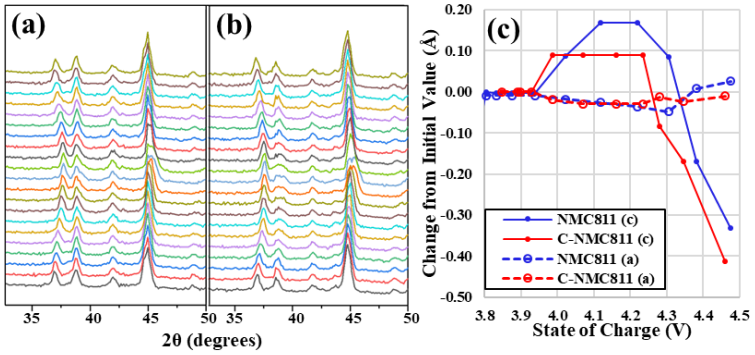

Figure S9: Selected range of in-situ XRD data of (a) NMC811 and (b) C-NMC811 from 3.6-4.5V. (c) Change in *a* and *c* lattice constants of NMC811 and C-NMC811 during charge cycle

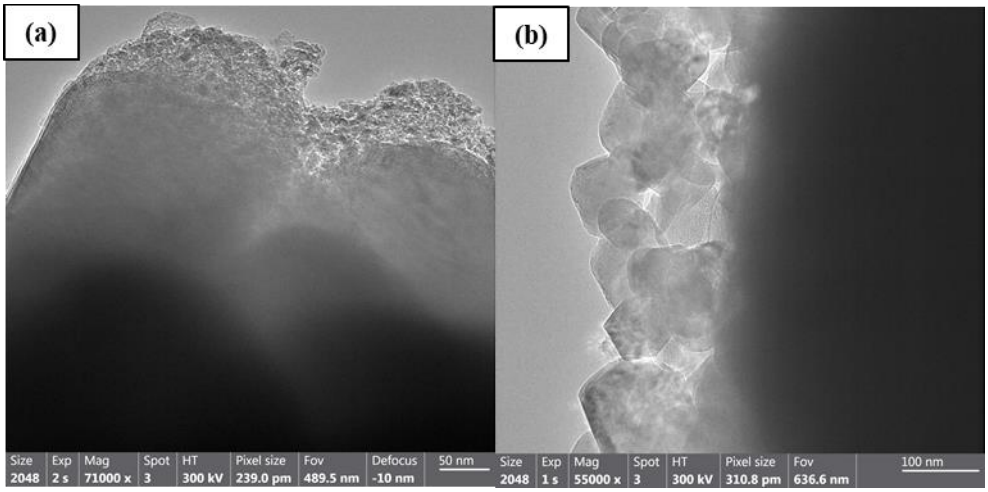

Figure S10: TEM images of (a) NMC811 and (b) C-NMC811 after long term exposure to air, showing buildup of residual compounds on NMC81l, while the surface of C-NMC811 has no visible residue

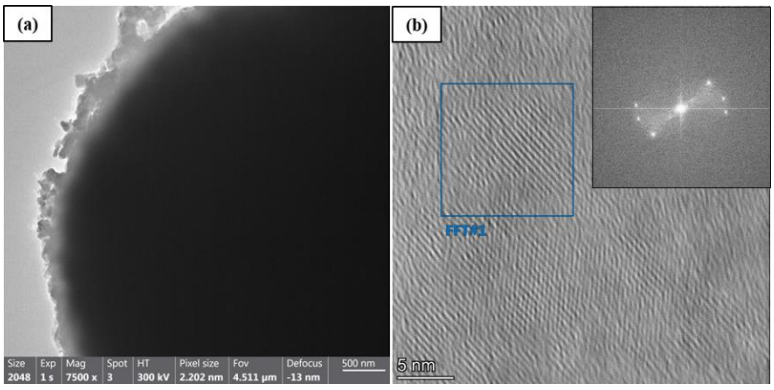

Figure S11: (a) TEM images of C-NMC811 revealing a surface layer of Mn-rich nano particles. (b) High magnification of a selected surface particle, with corresponding FFT pattern in the inset

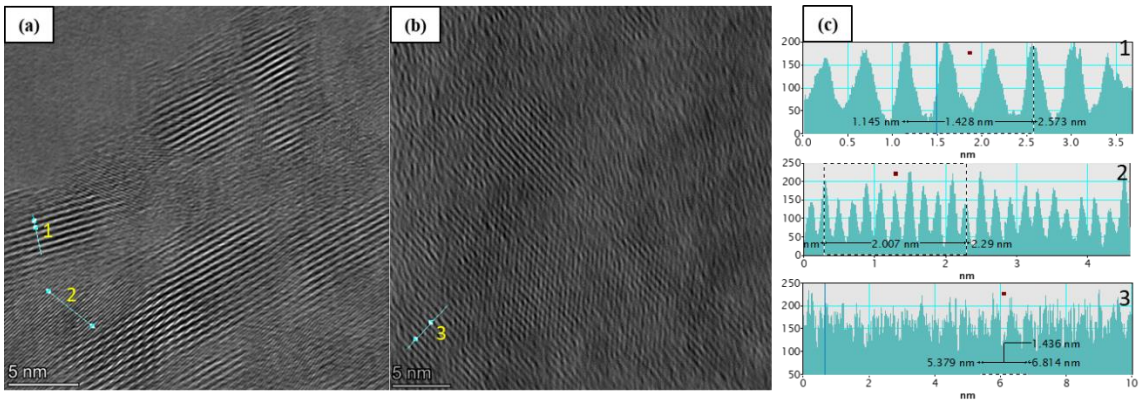

Figure S12: STEM-HAADF images of (a) NMC811 and (b) C-NMC811 after long term exposure to ambient air. (c) corresponding interplanar spacing by intensity line profiles

C. Supplementary Information for Chapter 4

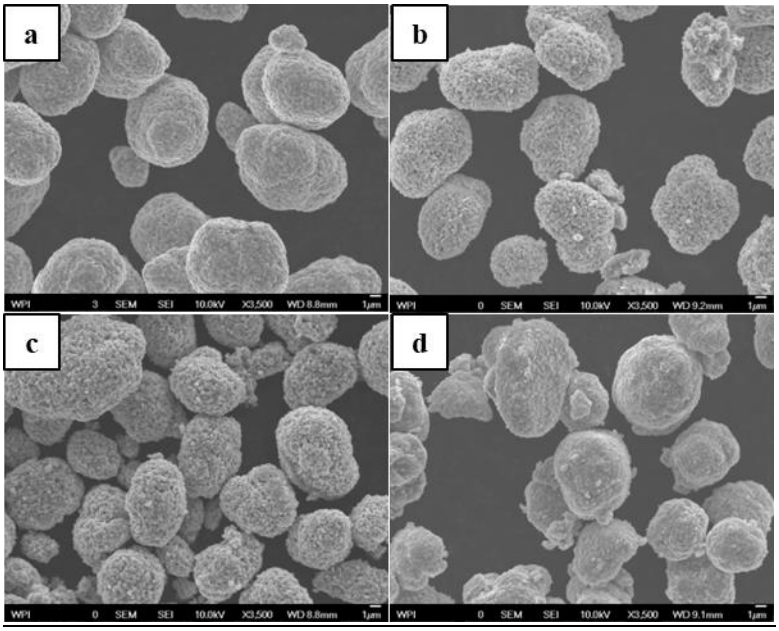

Figure S1: Low magnification image of (a) PR, (b) 5Br, (c) 5Cl, and (d) 5F, demonstrating spherical secondary particle shapes approximately 10um in diameter. Scale bar is set to 1µm

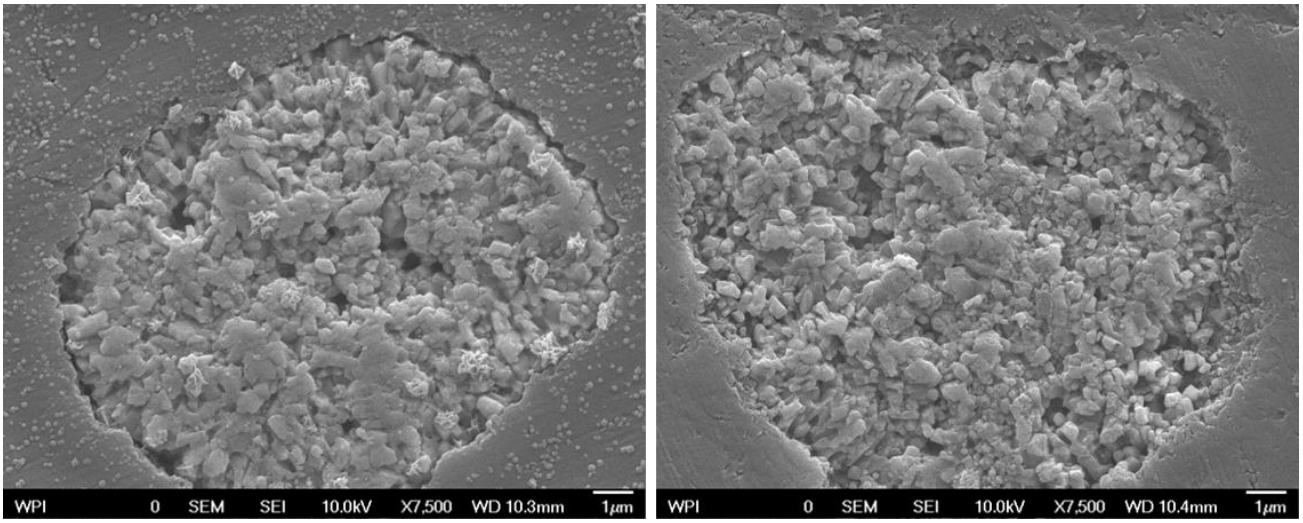

Figure S2: Enlarged SEM image of cross sections for PR (left) and 5Br (right)

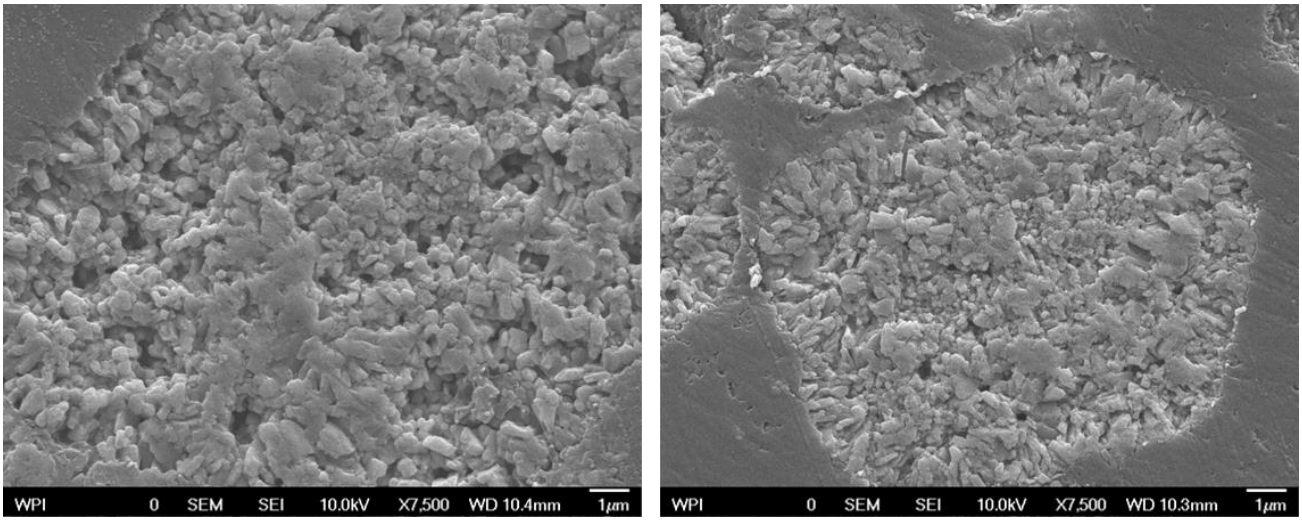

Figure S3: Enlarged cross section for 5Cl (left) and 5F (right)

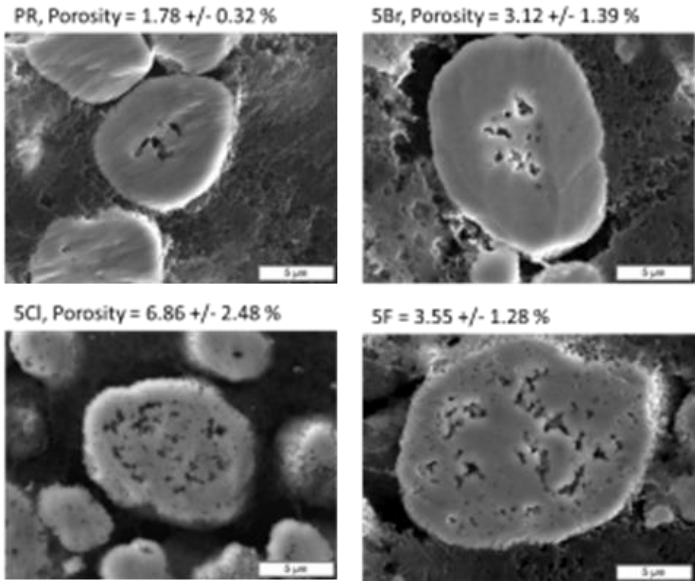

Figure S4: Ar-ion polished cross sections of PR, 5Br, 5Cl, and 5F samples. Porosity analysis was collected on a set of 15 particles. Due to the smaller set of samples, the results may not as representative as those inferred from combined PSA and BET analysis. Scale bar is set to 5µm

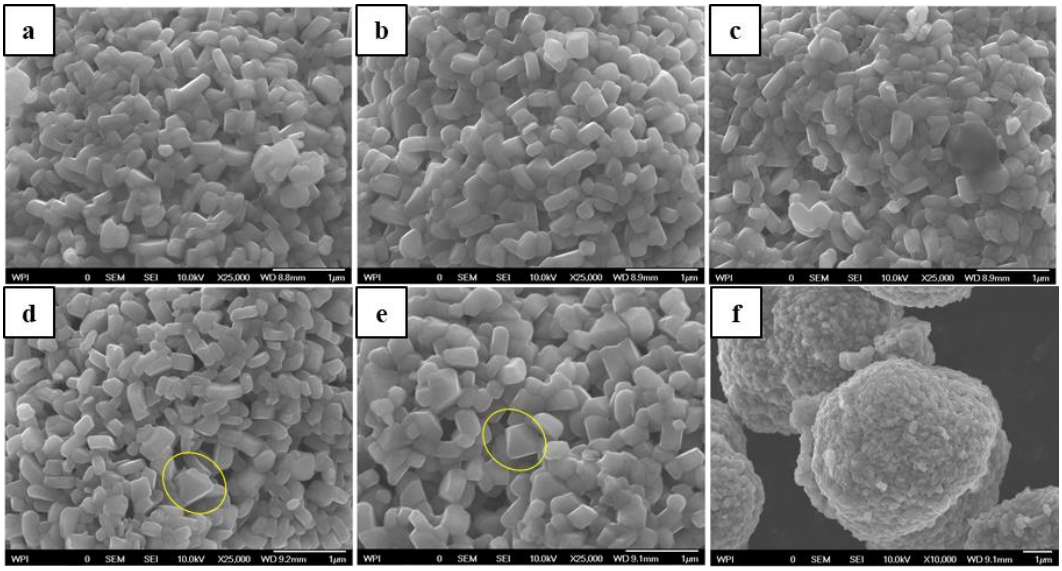

Figure S5: SEM images of the particle morphology of 2mol% doped Br (a), Cl (b), and F (c) and 8mol% doped Br (d), Cl (e), and F (f). And increasing fraction of Br or Cl results in much more porous secondary particles, while F maintains a densified structure. Circled particles are of faceted primary particles developed from molten salt assisted growth. Scale bars are set to 1µm

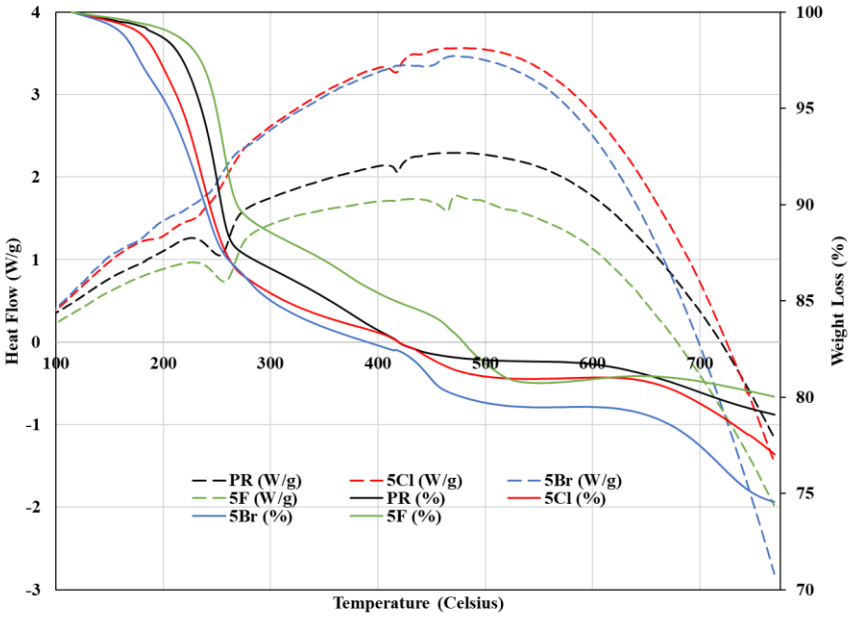

Figure S6: TGA and DSC curves across the entire heating range of 100 to 775 Celsius

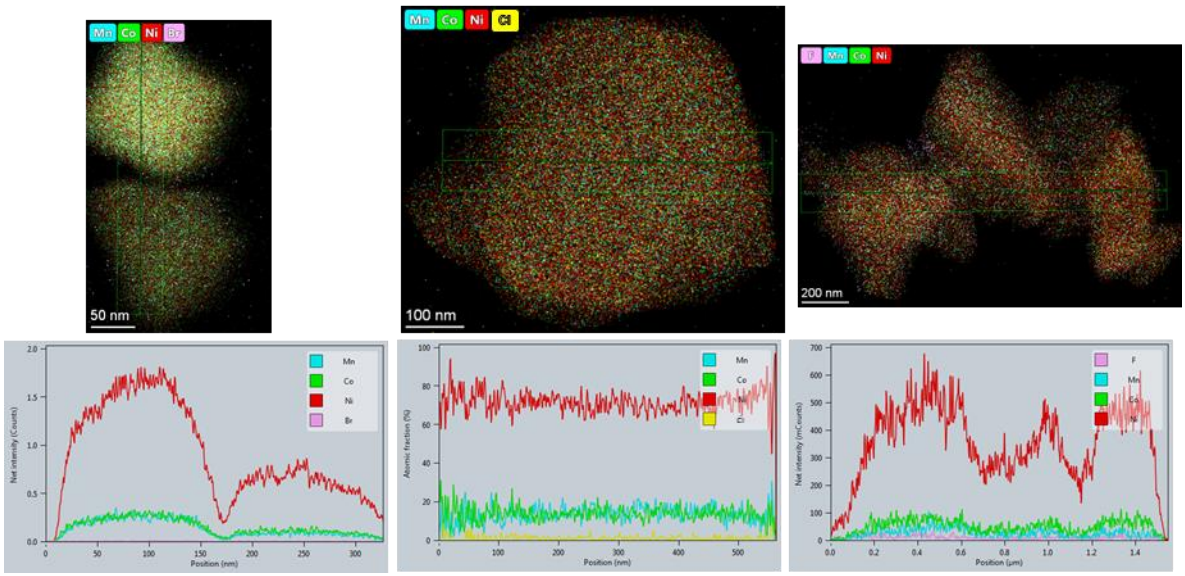

Figure S7: EDS mapping and line scans of 5Br, 5Cl, and 5F

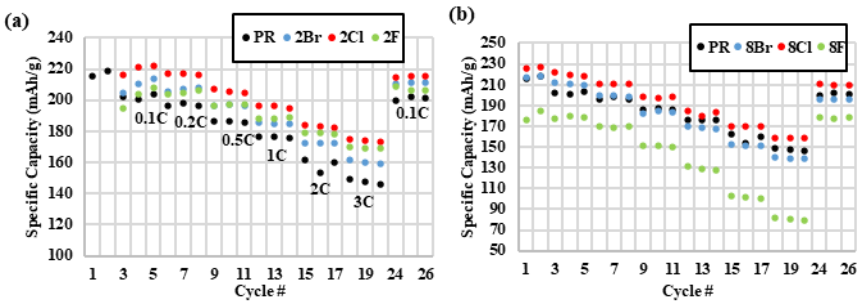

Figure S8: Rate performance of (a) 2mol% doped samples and (b) 8mol% doped samples

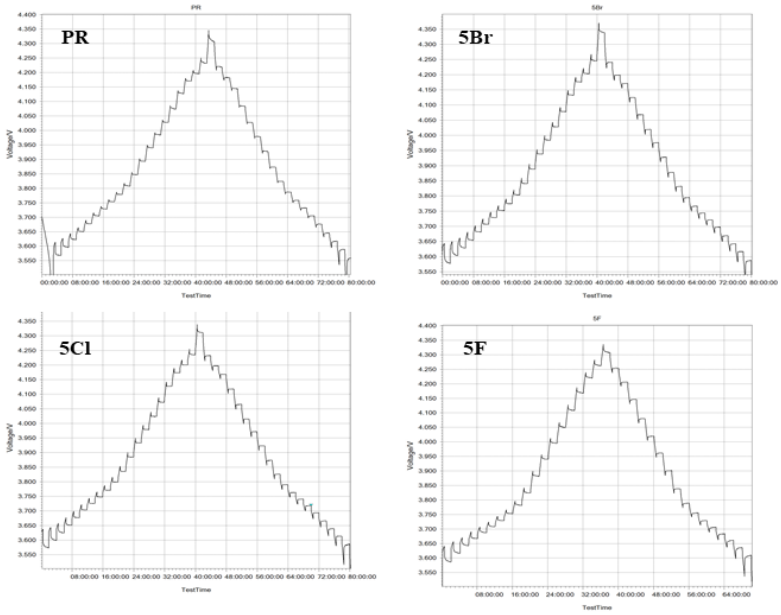

Figure S9: Raw GITT data for pristine and doped samples, collected after two formation cycles

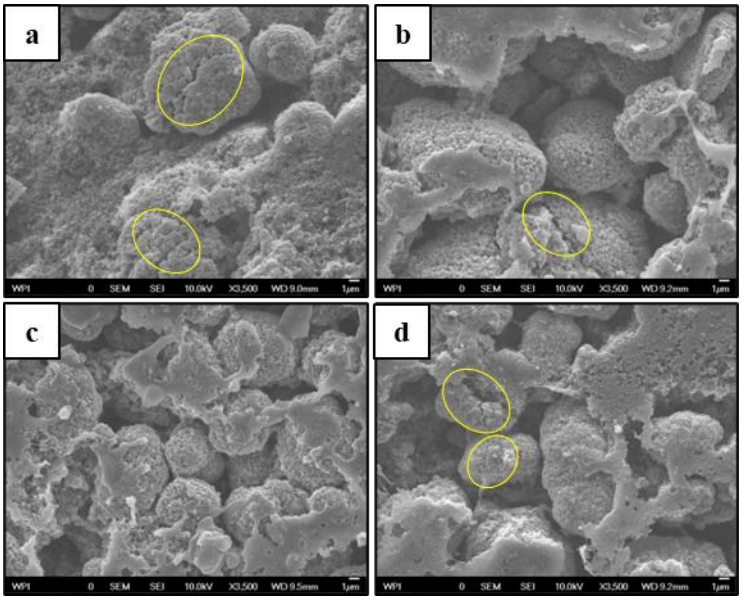

Figure S10: SEM images of (a) PR-811, (b) 5Br-811, (c) 5Cl-811, and (d) 5F-811 electrode films collected from disassembled half-cells after 100 cycles between 2.8-4.5V at C/2. Intergranular cracks observed are circled in yellow. Scale bars are set to 1µm

Table S1: D10, D50, and D90 determined from particle size analysis, from 2 runs, indicating no significant change in secondary particle size or distribution

Sample	Run #	D10	D50	D90
Pr	1	5.24	10.13	19.69
	2	5.25	10.19	19.95
5Cl	1	5.67	11.22	21.76
	2	5.72	11.12	22.36
5F	1	5.61	10.97	22.11
	2	5.78	11.18	21.63
5Br	1	6.1	11.91	23.98
	2	6.16	11.87	23.5

Table S2: Calculated compositions determined from ICP-OES analysis. Halogen content cannot be determined due to spectral peaks existing outside the range of the detector

	Li	Ni	Mn	Co
PR-811	1.054	0.809	0.093	0.098
5Br-811	1.027	0.810	0.092	0.098
5Cl-811	1.031	0.812	0.090	0.098
5F-811	1.021	0.810	0.092	0.098

Table S3: Contribution of deconvoluted XPS peaks to the total signal based on integrated area under the curve for as-synthesized samples

	Ni^{2+}	Ni^{3+}	$O_{Lattice}$	O_{Active}
PR-811	47.6%	52.4%	34.5%	65.5%
5Br-811	39.9%	60.1%	13.2%	86.8%
5Cl-811	39.4%	60.6%	46.3%	53.7%
5F-811	65.6%	34.4%	39.5%	60.5%

Table S4: Contribution of deconvoluted XPS peaks based on integrated area under the curve for cycled electrodes. The weighted contributions of peaks associated wtih Ni^{3+} and Ni^{2+} are compared with each other and not including the contribution from the NiF_2 signal

	Ni^{2+}	Ni^{3+}	$F_{Organic}$	F_{Metal}
PR-811	58.1%	41.9%	82.4%	17.6%
5Br-811	41.8%	58.2%	49.2%	50.8%
5Cl-811	30.2%	69.8%	39.8%	60.2%
5F-811	50.5%	49.5%	82.0%	18.0%

D. Supplementary Information for Chapter 5

NMC811 Hydroxide Precursor Formation

NMC811 precursors were synthesized using a hydroxide-based co-precipitation reaction. In short, a 1.8M solution of transition metal sulfates in the desired ratio (80mol% $NiSO_4$, 10mol% $MnSO_4$, and 10mol% $CoSO_4$ was added dropwise into a 1L double jacked reactor stirring at 650RPM and kept at 55°C under a nitrogen atmosphere. The reactor pH was maintained at 11.0 ± 0.2 using a solution of 5M NaOH, which also provides the counter anion for precipitation. A 3.5M solution of ammonia is also fed into the reactor as a chelating agent to control the reaction rate for the formation of dense, secondary particles of good size distribution. Metal sulfate and ammonia feeding rates were 0.55mL/min and 0.17mL/min, respectively. The reaction is allowed to run for a total of 8 hrs before being collected and rinsed with deionized water to remove remaining ammonia, sodium hydroxide, and/or sulfate compounds, before being dried at 100 °C in a vacuum oven overnight. The final product consists of metal hydroxide spherical particles approximately 8um in diameter.

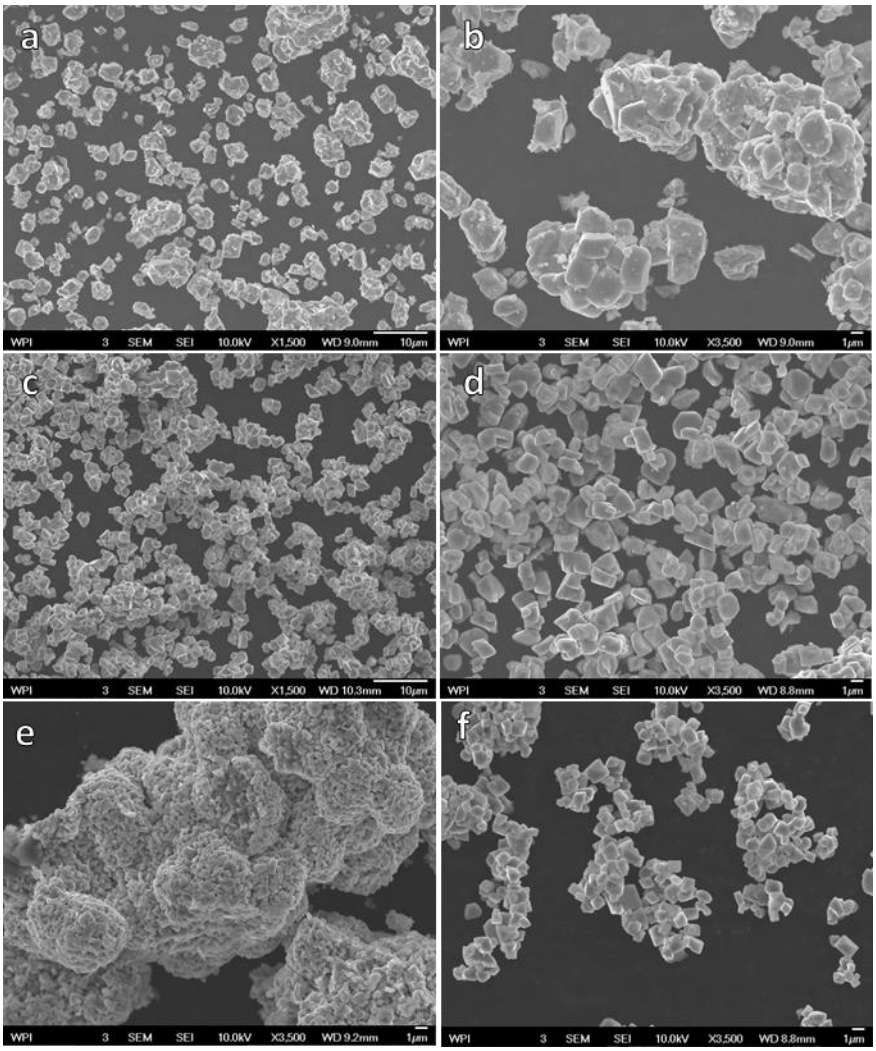

Figure S1: SC811 samples sintered with 50mol% excess LiOH and (a,b) without molten salt flux or (c,d) with 10mol% Li_2SO_4-Na_2SO_4 flux. Samples with molten salt flux are less agglomerated and generally more uniform in shape and size. (e) SC811 sample with 10mol% molten salt flux, with an upper temperature of 825°C. (f) SC811 sample with 50mol% molten salt flux.

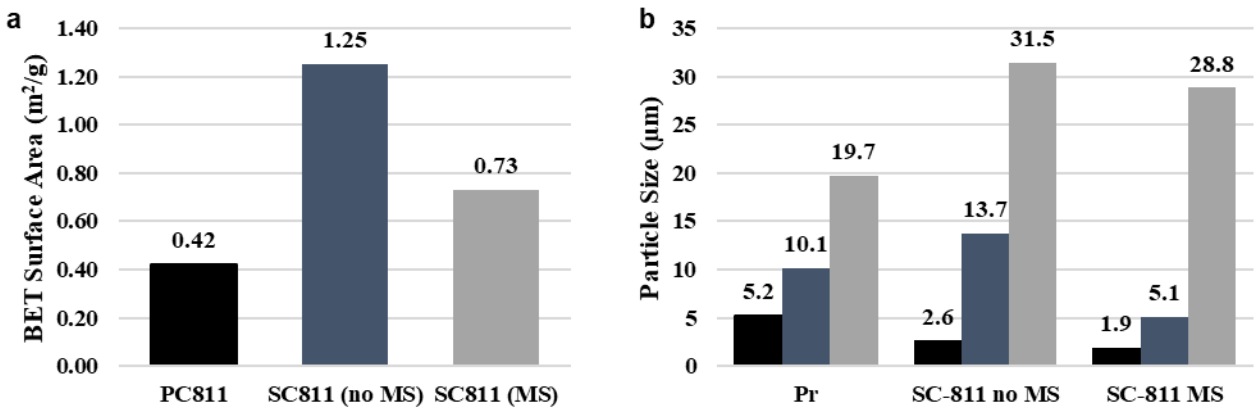

Figure S2: (a) BET surface area analysis and (b) particle size analysis of PC811 and SC811 powders

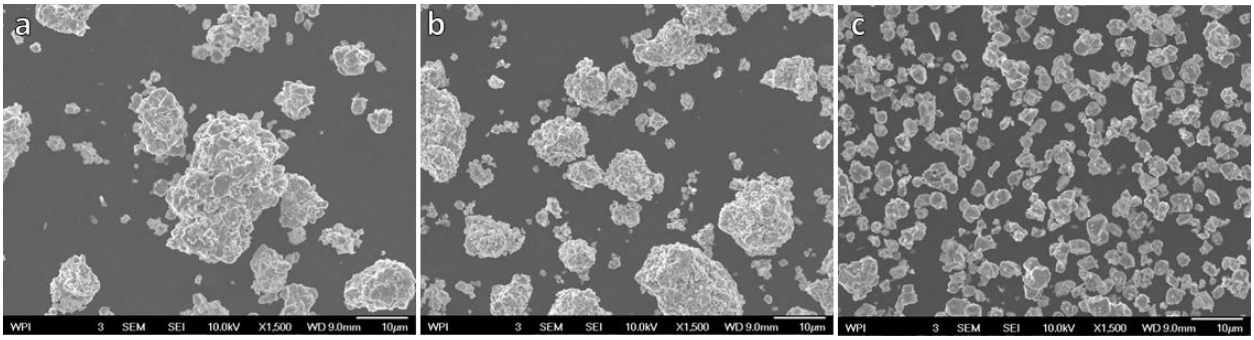

Figure S3: SC811 samples sintered using only (a) 5 mol%, (b) 20 mol%, and (c) 50 mol% excess LiOH, without the addition of sulfate flux

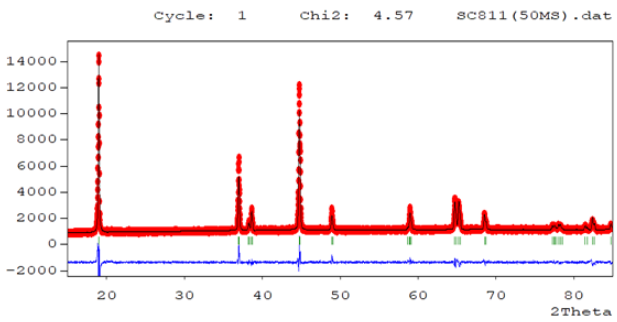

Sample	*a,b* (Å)	*c* (Å)	$FWHM_{(003)}$ (θ)	$FWHM_{(104)}$ (θ)	Ni_{Li} (%)	$I_{(003)}/I_{(104)}$	χ^2
SC811 (50% MS)	2.8699	14.2043	0.1504	0.1376	4.38%	1.22	4.57

Figure S4: Refined XRD profile of SC811 synthesized using 50 mol% sulfate flux, and refined lattice parameters

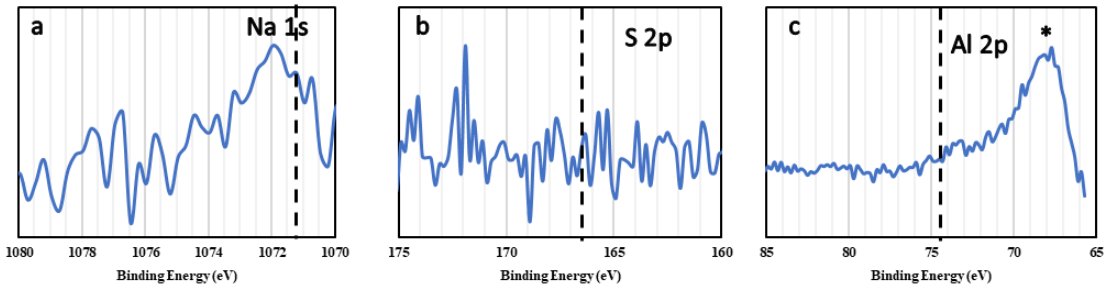

Figure S5: XPS spectra of potential impurities from molten salt flux and crucible. Negligible signals are observed. Asterisk in Al 2p XPS spectra is indicative of Ni 3p signal and not Al 2p. Dashed lines indicate where an expected XPS peak would be observed

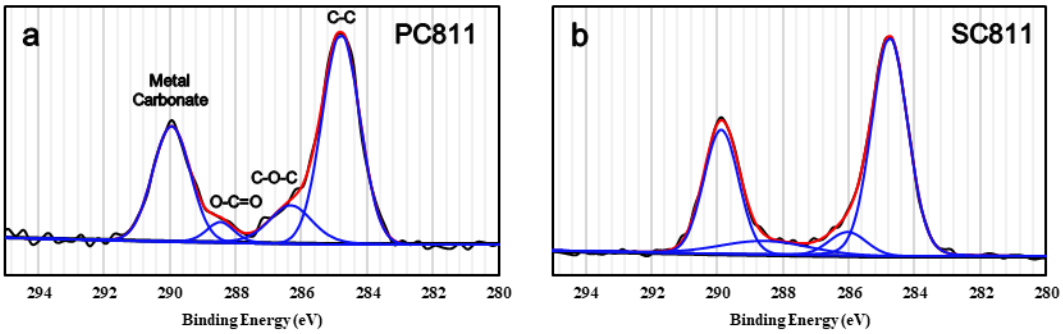

c

Sample	Carbon-Carbon	Organic Carbon	Metal Carbonate	MCO_3:Ni
PC811	53.7%	17.1%	29.2%	0.152
SC811	56.1%	14.3%	29.6%	0.127

Figure S6: XPS spectra of the carbon 1s binding energies for (a) PC811 and (b) SC811 powders in the as-synthesized condition. (c) Table of individual peak contribution to the overall signal, demonstrating no noticeable difference in lithium carbonate or other metal carbonate content. The ratio of the integrated intensity of the metal carbonate peak to nickel peaks are similar for both PC811 and SC811, further indicating similar levels of metal carbonate content

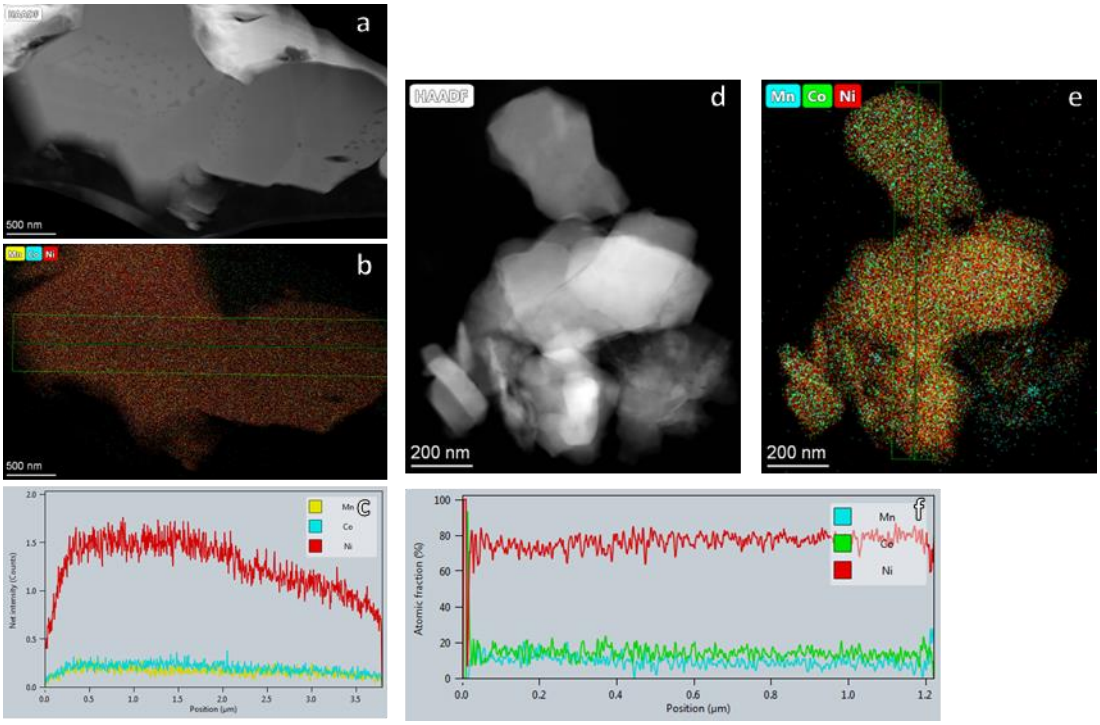

Figure S7: (a-c) EDS mapping and line scan of SC811 particle. (d-f) EDS mapping and line scan of PC811 particles. Elemental distribution is uniform across all samples, with no noticeable elemental segregation

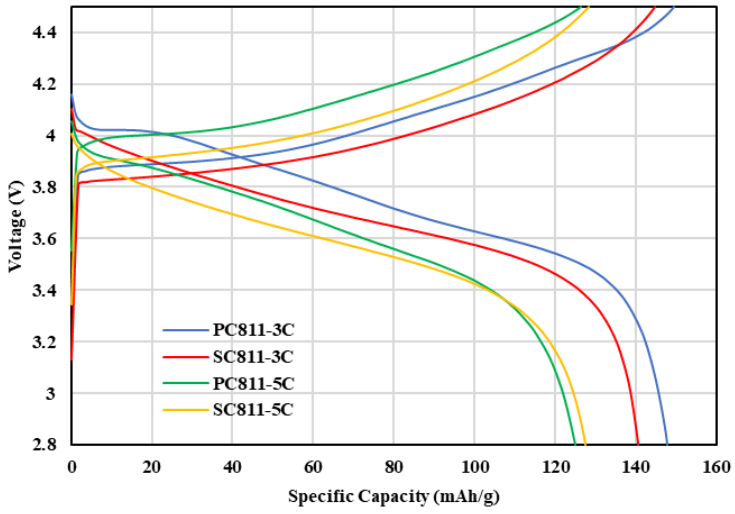

Figure S8: Capacity-Voltage plots of PC811 and SC811 at 3C and 5C charge/discharge rates

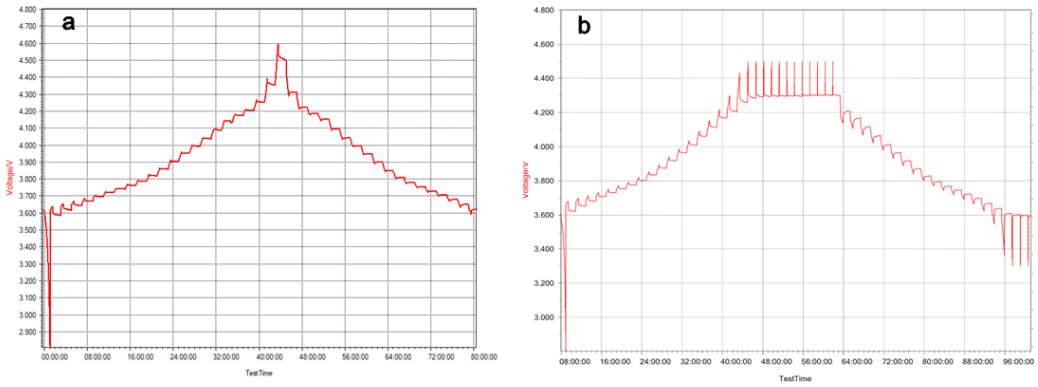

Figure S9: Raw GITT data for PC811 (left) and SC811 (right)

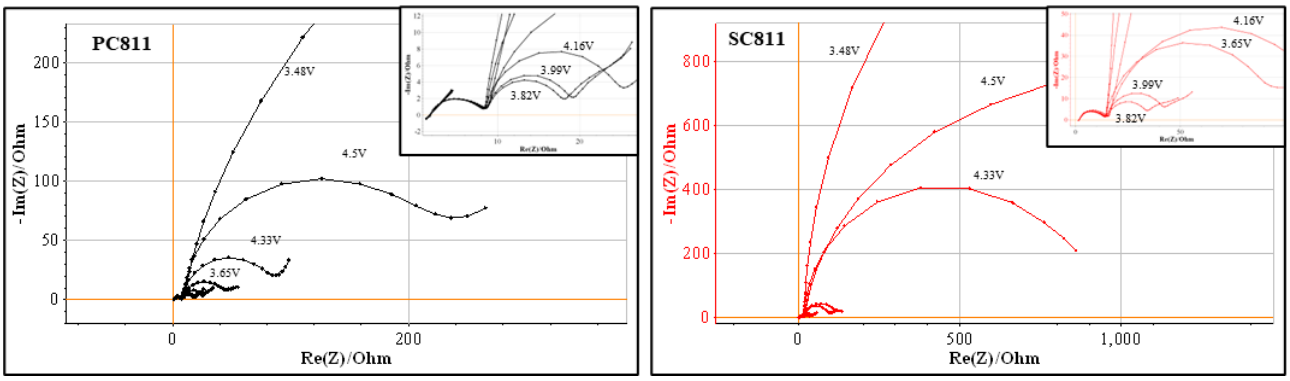

Figure S10: Raw EIS data from PC811 and SC811 taken after formation cycles

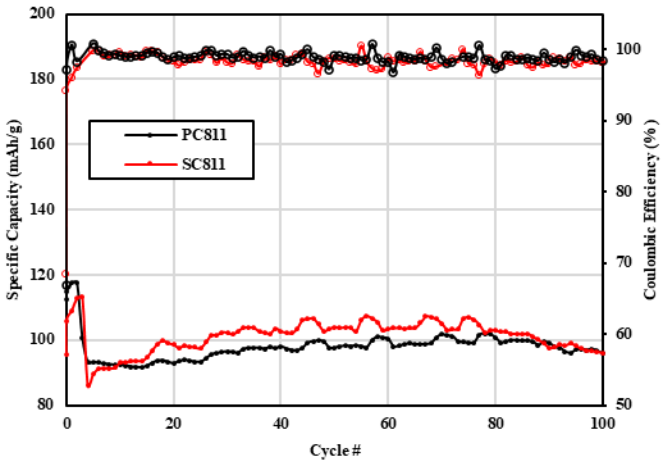

Figure S11: PC811 and SC811 cycled with an upper voltage cutoff of 4.0. Capacity and retention curves are similar for both samples

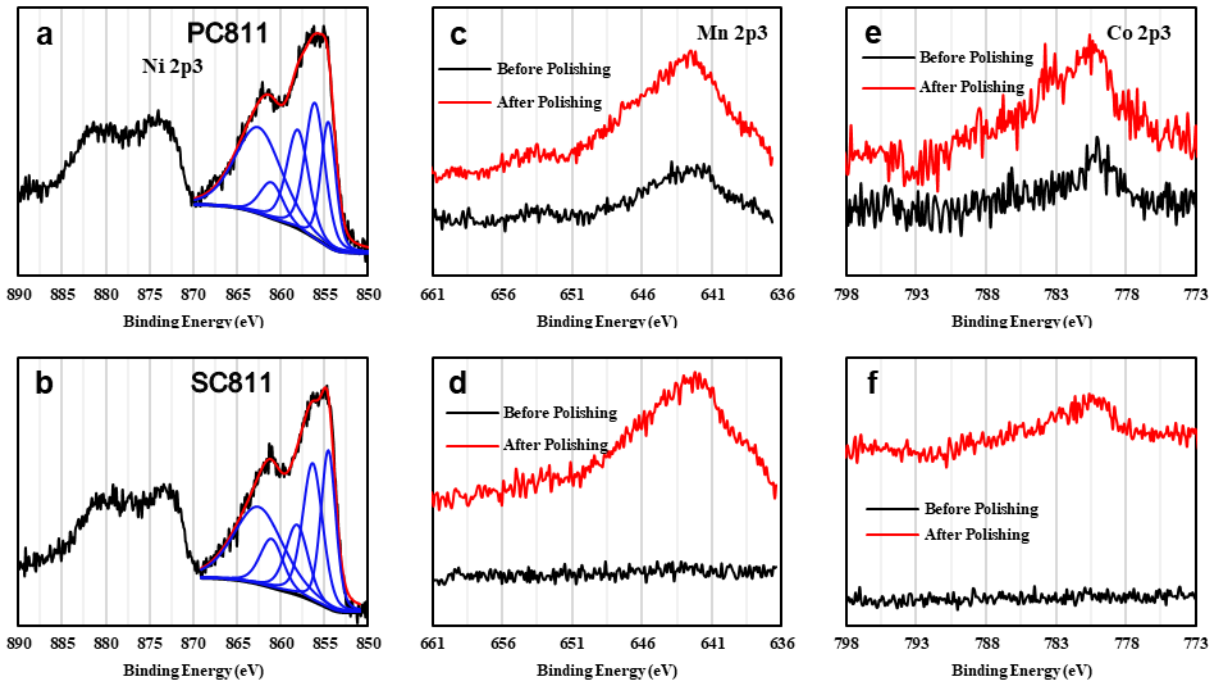

Figure S12: Ni 2p3 XPS profiles from (a) PC811 and (b) SC811 after ion polishing to remove the surface layer. Mn 2p3 and Co 2p3 XPS spectra before and after ion polishing for (c,e) PC811 and (d,f) SC811. Differences in XPS intensity confirm the development of a thicker coating for SC811 compared to PC811. Data collected on electrodes from disassembled half-cells after holding to 4.5V

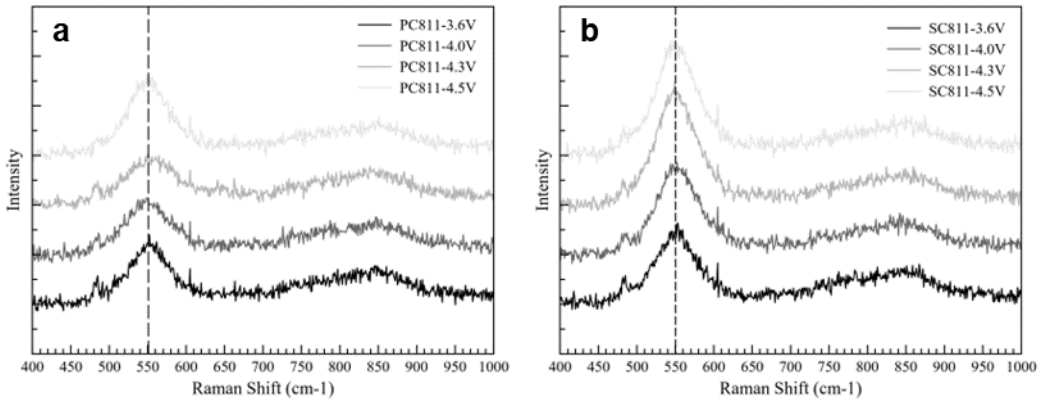

Figure S13: Ex-situ Raman spectroscopy of PC811 and SC811 electrodes held at targeted voltages before disassembly. The similarity in Raman shift between PC811 and SC811 indicate no change in the bulk structure due to the single crystalline structure

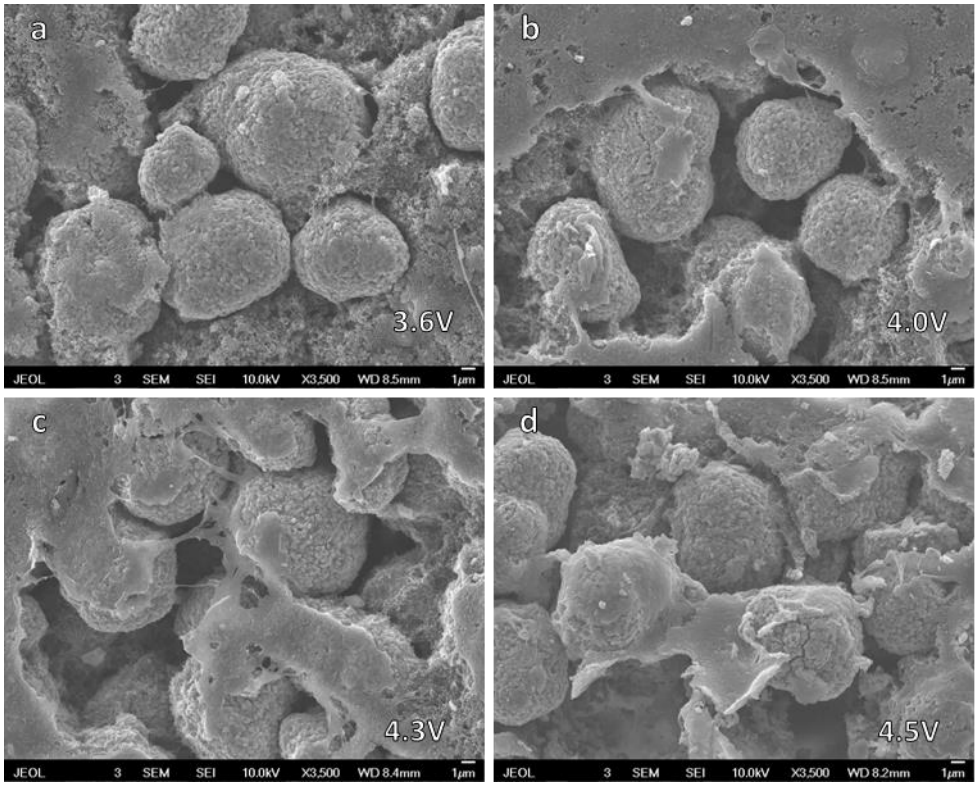

Figure S14: Lower magnification SEM images of PC811 under different SOC. Intergranular cracking beings to appear at 4.3V

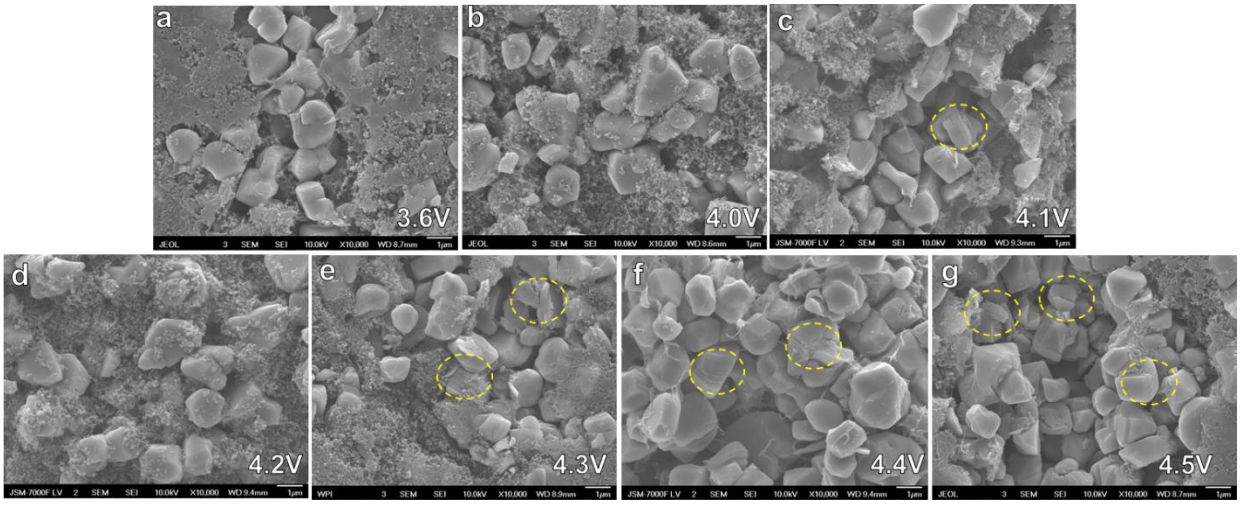

Figure S15: Lower magnification SEM images of SC811 under different SOC. Damaged areas related to intragranular fracture/planar gliding are circled

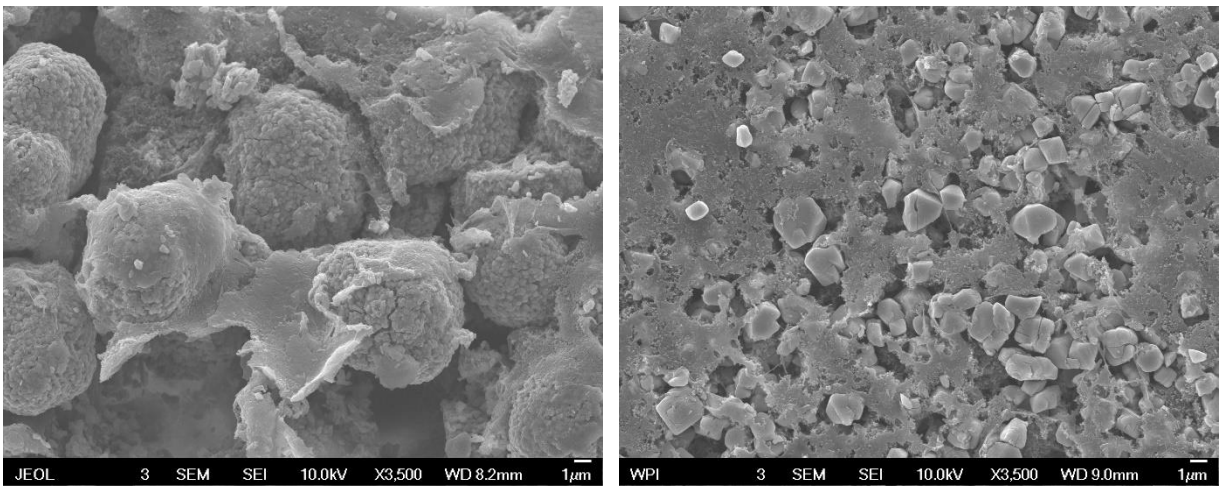

Figure S16: Lower magnification images of PC811 (left) and SC811 (right) from disassembled electrodes after holding at 4.5V. The majority of particles in SC811 display a series of parallel planar gliding or cracks

Table S1: ICP-OES Data of PC811 and SC811

Sample	Li	Ni	Mn	Co
PC811	1.074	0.809	0.093	0.098
SC811	1.104	0.799	0.096	0.106

References

[1] Dolotko, O., Senyshyn, A., Mühlbauer, M., Nikolowski, K., & Ehrenberg, H. (2014). Understanding structural changes in NMC Li-ion cells by in situ neutron diffraction. Journal of Power Sources, 255, 197–203.

[2] Märker, K., Reeves, P. J., Xu, C., Griffith, K. J., & Grey, C. P. (2019). Evolution of Structure and Lithium Dynamics in LiNi0.8Mn0.1Co0.1O2 (NMC811) Cathodes during Electrochemical Cycling. Chemistry of Materials, 31(7), 2545–2554.

[3] FTsalt (2022). FACT Salt Phase Diagrams. FactSage.